

UNIVERSITÉ DE GENÈVE

Département de radiologie

Centre Universitaire d'Informatique

FACULTÉ DE MÉDECINE

PD Dr H. Zaidi

FACULTÉ DES SCIENCES

Professeur S. Voloshynovskiy

---

# **Monte Carlo and experimental assessment of CT-based attenuation correction in PET**

## **THÈSE**

présentée à la Faculté des sciences de l'Université de Genève  
pour obtenir le grade de Docteur ès sciences, mention interdisciplinaire

par

Mohammad Reza AY

de

Shiraz, Iran

Thèse N° 3690

GENÈVE

Atelier de reproduction de la Section de physique

2005

## SUMMARY

**D**iagnosis, monitoring and follow-up in clinical oncology traditionally are based on high resolution computed tomography (CT) images. In recent years, functional positron emission tomography (PET) imaging using dedicated radiopharmaceuticals has been recognized as an important imaging modality and adjunct to CT images by providing complementary metabolic information. To overcome the challenges of aligning PET and CT images, acquired in different conditions and separate systems, hybrid PET/CT units have been designed and are commercially available since 2000. A PET/CT scanner combines premier technology from two imaging modalities, making it possible to reveal both anatomy and functional information in a single procedure.

PET/CT systems offer significant advantages over stand alone PET, including decreased scanning time and increased accuracy in tumour detectability. However, the use of CT images for attenuation correction of PET data is known to generate artefacts in the resulting PET images in some cases. The need to characterize quantitatively the effect of physical and physiological parameters such as contribution from x-ray scattered photons, tube voltage, tube current, contrast agents and metallic implants on CT-based attenuation correction (CTAC) spurred the development of an MCNP4C-based x-ray CT Monte Carlo simulator, which allows simulating fan- and cone-beam CT scanner geometries. Full simulation of x-ray tube, phantom and detectors with flat, single- and multi-slice configurations were considered. Detailed knowledge of x-ray spectra is required for Monte Carlo modelling of computed tomography systems and was the first step for benchmarking purposes. In addition, the spectra predicted by various computational methods were assessed by comparison with measured spectra with the aim of preparing an x-ray spectra database for the simulator. The comparative assessment of different computational models for prediction of x-ray spectra showed that despite the systematic discrepancy for some models, the difference between measured and calculated spectra for all computational models investigated in this study is not statistically significant.

The developed x-ray CT Monte Carlo simulator was validated using experimental measurements of various non-uniform phantoms with different shape and size on both clinical fan-beam and small-animal cone-beam CT scanners. There was good agreement between the simulated and measured projections and reconstructed images. Thereafter, it was extensively used in addition to experimental measurements performed on commercial PET and CT scanners to investigate potential artifacts and correction schemes when using CT-based attenuation correction on dual-modality PET/CT units.

After thorough review and analysis of the results related to the assessment of CT-based attenuation correction, the following general conclusions were drawn: (i) the contamination of CT

data with scattered radiation underestimates the attenuation correction factors for the cone-beam geometry; (ii) the tube current does not affect the accuracy of CTAC procedure to a visible or measurable extent; (iii) using a single calibration curve derived under standard scanning conditions during the CTAC procedure to images acquired at different tube voltages does not affect significantly the visual qualitative interpretation and quantitative analysis of PET emission images; (iv) the high concentration of contrast agents in CT images overestimates the apparent activity in the resulting PET images after applying attenuation correction, for which a generalized correction scheme was suggested; (v) the metallic leads used in deep brain stimulation techniques for the treatment of Parkinson's disease do not affect the accuracy of CT-based attenuation correction owing to their small size.

**Key words:** PET, x-ray CT, PET/CT, Monte Carlo simulation, attenuation correction, quantification, scattered radiation, contrast medium, tube voltage, tube current, metallic implants.

## Papers included in the thesis

This thesis is based on studies reported in the following original papers, referred to in the text by their Roman numerals. Published papers are reprinted by kind permission of the copyright owner.

- I. **M.R. Ay**, M. Shahriari, S. Sarkar, M. Adib, and H. Zaidi. Monte Carlo simulation of x-ray spectra in diagnostic radiology and mammography using MCNP4C. *Phys Med Biol* (2004), **49**: 4897-4917.
- II. **M.R. Ay**, S. Sarkar, M. Shahriari, D. Sardari, and H. Zaidi. Assessment of different computational models for generation of x-ray spectra in diagnostic radiology and mammography. *Med Phys* (2005), **32**: 1660-1675.
- III. **M.R. Ay** and H. Zaidi. Development and validation of MCNP4C-based Monte Carlo simulator for fan- and cone-beam x-ray CT. *Phys Med Biol* (2005), **50**: 4863-4885.
- IV. **M.R. Ay** and H. Zaidi. Assessment of errors caused by x-ray scatter and use of contrast medium when using CT-based attenuation correction in PET. Under revision *European Journal of Nuclear Medicine and Molecular Imaging* (2005).
- V. **M.R. Ay** and H. Zaidi. CT-based attenuation correction in neurological PET: evaluation of the effect of x-ray tube voltage on quantitative analysis. Submitted for publication in *Nuclear Medicine Communications* (2005).

## List of abbreviations

2D: two-dimensional  
3D: three-dimensional  
3DRP: 3D reprojection algorithm  
AC: attenuation correction  
ACF: attenuation correction factor  
AMCS: accelerated Monte Carlo simulator  
AP: attenuation profile  
CAC: calculated attenuation correction  
CT: computed tomography  
CTAC: CT-based attenuation correction  
CSDA: continuous slowing down approximation  
DAQ: data acquisition system  
DBS: deep brain stimulation  
DHCI: dual head coincidence imaging  
DICOM: digital imaging and communication in medicine  
EBCT: electron beam computed tomography  
ED: effective dose  
FBP: filtered backprojection  
FOV: field-of-view  
GTM: geometric transfer matrix  
HC: homogeneity coefficient  
HPD: hybrid photon detector  
HU: Hounsfield unit  
HVL: half value layer  
LAC: linear attenuation coefficient  
LOR: line of response  
MAC: mass attenuation coefficient  
MC: Monte Carlo  
MRI: magnetic resonance imaging  
MTM: measurement transmission method  
PBPET: panel based positron emission tomography  
PET: positron emission tomography  
PMT: photomultiplier tube  
PVC: partial volume correction  
RF: ripple factor  
RMSD: root mean square difference  
RNG: random number generator  
ROI: region of interest  
SC: scatter correction  
SCC: segmented contrast correction  
SNR: signal-to-noise ratio  
SPECT: single photon emission computed tomography  
SPR: scatter-to-primary ratio  
SSS: single scatter simulation  
VP: vector processor  
VOI: volume of interest

# Contents

*Summary*

*Papers included in this thesis*

*List of abbreviations*

<b>Résumé</b>	<b>1</b>
1. Introduction.....	1
2. Physique et instrumentation de l'imagerie TEP/TDM .....	2
3. La méthode de Monte Carlo appliquée à l'imagerie médicale .....	5
4. Modélisation des spectres à rayons X.....	7
5. Correction d'atténuation en TEP basée sur la TDM.....	8
6. Conclusions et développements futurs.....	10
<b>1. Introduction</b>	<b>11</b>
1.1 Medical imaging techniques.....	12
1.2 Dual-modality imaging devices.....	12
1.3 Purpose of this work.....	13
<b>2. PET/CT physics and instrumentation</b>	<b>14</b>
2.1 The physics of computed tomography (CT) .....	14
2.1.1 CT hardware components.....	15
2.1.2 CT design configurations.....	15
2.2 The Physics of positron emission tomography (PET) .....	17
2.2.1 PET components .....	18
2.2.2 Design configurations of PET scanners.....	18
2.3 Dual-modality PET/CT imaging .....	20
2.4 Limitations of quantitative PET imaging .....	20
2.4.1 Attenuation correction strategies in PET.....	20
2.4.2 CT-based attenuation correction in PET.....	21
<b>3. Monte Carlo modelling in medical imaging</b>	<b>23</b>
3.1 The Monte Carlo method.....	24
3.2 Monte Carlo computer codes used in this study.....	25
3.2.1 The MCNP version 4C (MCNP4C) code .....	25

3.2.2	The Eidolon program.....	27
3.3	Applications of the Monte Carlo method in medical imaging.....	28
<b>4.</b>	<b><i>Analytical and Monte Carlo x-ray spectra modelling</i></b>	<b>29</b>
4.1	Analytical models.....	29
4.1.1	Empirical models.....	29
4.1.2	Semi-empirical models .....	30
4.2	Monte Carlo modelling .....	30
4.3	Assessment of computational models .....	31
4.4	Relevance of x-ray spectra modelling in clinical and research setting .....	31
<b>5.</b>	<b><i>Development and validation of an x-ray CT simulator</i></b>	<b>32</b>
5.1	Motivations .....	32
5.2	Development strategy.....	32
5.3	Experimental validation.....	33
5.4	Applications of MC x-ray CT simulator.....	34
<b>6.</b>	<b><i>Sources of error and artefact in CT-based attenuation correction</i></b>	<b>35</b>
6.1	Misalignment between PET and CT images.....	35
6.2	Patient and respiratory motion.....	35
6.3	Truncation.....	36
6.4	Beam hardening and x-ray scattered radiation.....	36
6.5	Presence of contrast medium.....	36
6.6	Presence of metallic implants.....	37
6.7	Impact of tube voltage.....	37
6.8	Impact of tube current .....	38
<b>7.</b>	<b><i>Concluding remarks and future perspective</i></b>	<b>38</b>
7.1	Key conclusions.....	38
7.2	Future perspectives.....	40
	<i>Acknowledgements</i> .....	42
	<i>Publication list</i> .....	43
	<i>Bibliography</i> .....	45
	<b><i>Paper I</i></b>	<b>51</b>
	<b><i>Paper II</i></b>	<b>72</b>
	<b><i>Paper III</i></b>	<b>88</b>
	<b><i>Paper IV</i></b>	<b>111</b>
	<b><i>Paper V</i></b>	<b>139</b>

# RÉSUMÉ

L' imagerie médicale est née avec la découverte des rayons X par le professeur William Roentgen en 1895. Depuis, ces techniques d'exploration n'ont cessé de se développer pour donner naissance à l'imagerie isotopique incluant la tomographie par émission monophotonique (TEMP), la tomographie à rayons X ou tomodensitométrie (TDM), et l'imagerie par résonance magnétique nucléaire (IRMN). Le développement de systèmes d'imagerie hybride TEP/TDM est en pleine expansion. L'un des avantages principaux réside dans le fait que les données TEP sont intrinsèquement réalignées sur l'information anatomique fournie par la tomographie à rayons X sans nécessiter l'utilisation de marqueurs externes ou de contours internes.

## 1. Introduction

L'objectif principal de ce travail de thèse a été d'évaluer les sources d'erreurs et d'artefacts lorsque la correction d'atténuation appliquée au TEP est basée sur la génération actuelle des tomodensitomètres à coupe simple ou multiples et la génération future à base de détecteurs à écran plat (flat-panel) des systèmes d'imagerie hybrides TEP/TDM, en utilisant la simulation par la méthode de Monte Carlo et des données expérimentales et cliniques. Ce travail est basé sur cinq articles originaux pouvant être considérés comme des sujets de recherche à part entière:

1. Le code de calcul 'Monte Carlo N-particle' (MCNP4C) a été utilisé pour simuler les spectres à rayons X en radiodiagnostic et en mammographie. L'effet talon (talon d'anode) et des spectres en dehors de l'axe ont été déterminés pour différents angles d'anodes et de matériaux cibles. Les résultats de la simulation basée sur le code MCNP4C ont été comparés aux données mesurées et simulées par la méthode de Monte Carlo en utilisant le code EGS4 (**Article I**).
2. Différentes méthodes de calcul (empiriques, semi-empiriques et méthode de Monte Carlo) proposées pour la prédiction des spectres à rayons X aussi bien en radiodiagnostic qu'en mammographie ont été évaluées en effectuant des comparaisons avec les spectres mesurés. Cette comparaison inclut plusieurs figures de mérite, notamment l'évaluation qualitative et quantitative de la forme spectrale, les courbes de transmission, et d'autres paramètres physiques quantitatifs, de même que la dose absorbée et effective au fantôme adulte hermaphrodite ORNL. Après validation des différents modèles, une base de données de spectres à rayons X a été créée et utilisée dans le simulateur TDM développé (**Article II**).

3. Un simulateur TDM basé sur le code MCNP4C a été développé pour simuler aussi bien un TDM à rayons X avec une configuration à coupe simple ou multiples (jusqu'à 64 coupes) qu'un détecteur à écran plat. Le simulateur a été validé par confrontation des simulations avec des mesures expérimentales de différents fantômes non uniformes de tailles variables acquises avec un TDM clinique et un dédié à l'imagerie du petit animal (**Article III**). Le simulateur a été largement utilisé afin d'investiguer les artefacts potentiels et les méthodes de correction lors de l'utilisation de la correction d'atténuation basée sur la TDM sur les scanners hybrides TEP/TDM.
4. L'impact du rayonnement diffusé en TDM sur la précision de la correction d'atténuation basée sur la TDM a été investigué aussi bien pour un TDM clinique à coupes multiples que pour un prototype à base de détecteur à écran plat en utilisant le simulateur développé basé sur le code MCNP4C. L'influence de l'injection d'agents de contraste sur la correction d'atténuation basée sur la TDM a été étudiée par simulations moyennant la méthode de Monte Carlo ainsi qu'une étude expérimentale employant le fantôme striatal anthropomorphique (Radiology Support Devices, Inc., Long Beach, CA). Par ailleurs, nous avons aussi étudié l'effet des fils métalliques utilisés lors des stimulations cérébrales profondes dans le traitement de la maladie de Parkinson sur la précision de la correction d'atténuation basée sur la TDM (**Article IV**).
5. Nous avons investigué l'impact de l'utilisation d'une seule courbe de calibration pour la conversion des images TDM en cartes d'atténuation et de différentes intensités de courant des tubes à rayons X sur la précision de la correction d'atténuation basée sur la TDM pour des images acquises à différentes tensions du tube en procédant à des analyses quantitatives des cartes d'atténuation créées, des facteurs de correction d'atténuation générés et des données d'émission TEP neurologiques reconstruites en utilisant des études expérimentales et des études cliniques (**Article V**).

La première section de ce manuscrit consiste en une introduction aux techniques d'imagerie médicale, notamment à l'imagerie hybride ainsi que les objectifs de notre travail de recherche. Nous introduisons à la section 2 la technique de tomographie par émission de positons, celle de la tomographie à rayons X et celle de l'imagerie hybride TEP/TDM ainsi que l'instrumentation qui leur est associée. Nous décrivons également les limitations de l'imagerie TEP quantitative et les algorithmes de correction des effets d'atténuation. Dans la section 3, les principes de la méthode de Monte Carlo sont présentés, suivis par une revue des différents domaines d'application de cette technique en imagerie médicale, en particulier TDM et TEP. La section 4 expose la modélisation analytique et par la méthode de Monte Carlo des spectres à rayons X. La 5ème section est consacrée au développement et à la validation d'un simulateur CT à rayons X. Dans la section 6, nous présentons les sources d'erreurs et artefacts lors de la correction des effets d'atténuation basée sur la TDM. Finalement, les conclusions principales et une suite à cette recherche sont présentées dans la section 7.

## 2. Physique et instrumentation de l'imagerie TEP/TDM

L'imagerie séquentielle TEP/TDM est rendue possible par l'utilisation d'un système hybride intégrant à la fois un TEP et un TDM. Un seul lit est utilisé pour l'acquisition séquentielle des données TDM puis des données TEP. Depuis l'introduction du TEP/TDM dans le domaine clinique, de nombreux progrès ont été effectués aussi bien au niveau de la technologie TEP que TDM. Ces progrès ont été incorporés dans les générations actuelles des scanners TEP/TDM.

La tomographie par émission de positons est une modalité bien établie de formation d'images de radio-traceurs qui offre la possibilité de faire des mesures quantitatives des processus

physiologiques et biochimiques *in vivo*, mais aussi de fournir un outil diagnostique clinique utile. Plusieurs facteurs affectent la qualité des images et l'exactitude des données obtenues à partir d'une acquisition en TEP. Ceux-ci incluent les propriétés physiques des détecteurs, la conception et les performances du tomographe, la compensation des effets d'atténuation et du rayonnement diffusé, et l'algorithme de reconstruction.

Le traceur injecté aux patients est un émetteur  $b^+$ . Une fois émis, le positon effectue un court parcours dans le milieu, puis s'annihile avec un électron. Du fait de la conservation de l'énergie et de la quantité de mouvement, cette annihilation s'accompagne de l'émission de deux photons antiparallèles d'une énergie de 511 keV. Ces rayonnements sont ensuite détectés au niveau des couronnes de détecteurs. La question que l'on est en droit de se poser est de savoir si les deux photons détectés au niveau de la couronne sont issus de la même annihilation. Les photons émis lors d'une annihilation atteindront les détecteurs avec une différence de temps très faible. On se fixe alors un seuil temporel, et si le laps de temps séparant l'arrivée des deux photons est en dessous de ce seuil, les photons sont considérés comme détectés simultanément. Cette détection correspond à un événement. Si le temps qui sépare l'arrivée des deux photons est supérieur au seuil, l'événement produit par la paire de photons n'est pas accepté. Deux photons détectés presque simultanément déterminent une ligne de coïncidence (ou ligne de réponse), sur laquelle l'annihilation est supposée s'être produite. C'est aussi la ligne où a eu lieu la désintégration du noyau, au parcours du  $b^+$  près.

La couronne entourant l'objet est constituée d'un ensemble de détecteurs ou cristaux scintillateurs et d'un nombre défini de photomultiplicateurs. De plus, on définit pour chaque détecteur l'ensemble des autres détecteurs qui peuvent réagir en coïncidence avec lui. Cette ouverture définit le champ de vue transaxial correspondant à une zone de reconstruction à l'intérieur de la couronne.

Les données brutes sont le résultat de la comptabilisation des événements (deux photons détectés en coïncidence), avec une information supplémentaire de localisation sur la ligne de coïncidence si l'on dispose du temps de vol (temps séparant l'arrivée du premier photon de celle du second). À l'acquisition, on récupère donc soit les projections soit les événements en mode liste. Toutefois, à l'enregistrement des données, la caméra effectue une transformation en une géométrie équivalente où les coïncidences sont classées selon leur direction dans une barrette de détecteurs fictifs (ensemble de détecteurs correspondant à une même direction).

L'imagerie TEP, la correction de l'atténuation, la correction de la diffusion, la fusion d'images et les caméras à semi-conducteurs sont tous des secteurs susceptibles de bénéficier d'améliorations matérielles. Il est vraisemblable que les mérites relatifs des caméras à coïncidence et des systèmes TEP spécialisés entraîneront des améliorations pour les deux technologies, puisqu'elles s'orientent toutes deux vers un système à haute résolution abordable pour la TEP. En proposant de meilleurs rendements et des coûts inférieurs, l'utilisation de la TEP se généralisera avec la plus grande disponibilité du fluorodésoxyglucose (FDG) et des autres produits pharmaceutiques à base de F-18. Les caméras à scintillation peuvent tirer profit des cristaux épais partiellement pixélisés disponibles auprès des principaux fabricants de cristaux de caméra. Ces cristaux améliorent l'efficacité de détection à des taux d'énergie supérieurs, et réduisent la perte de résolution spatiale si l'énergie est plus faible. Les caméras à scintillation, notamment les systèmes double tête à grand champ, présentent de faibles rapports de comptage réellement aléatoires, ce qui limite le rendement clinique de ces systèmes et justifie leur disparition du marché des technologies TEP.

Les systèmes TEP à rendement supérieur et à faible coût présentent des obstacles en ce qui a trait au coût et à l'efficacité de l'imagerie à plus grandes surfaces dans la direction axiale du

patient. Les systèmes proportionnels multiconducteurs au gaz TDAE (tétrakis diméthylamino éthylène) avec résolutions temporelles de 3 à 4 nanosecondes largeur à mi-hauteur (LMI) sont des candidats possibles pour l'imagerie de surface. Les systèmes d'évaluation de l'atténuation poursuivent leur essor, tandis que les qualités relatives des systèmes en utilisation et en développement continuent à faire l'objet de controverses. De récentes percées ont permis l'ajout aux caméras à scintillation d'unités de tomographie aux rayons X pour les applications d'atténuation et de fusion d'images. D'autres progrès sont prévus pour produire des cartes d'atténuation plus précises et réduire les coûts de fonctionnement.

Les caméras à semi-conducteurs les plus prometteuses à ce jour reposent sur les cristaux de tellure de cadmium et de zinc (CdZnTe). Il s'agit réellement d'une caméra à semi-conducteurs, convertissant le photon gamma en électricité en proportion directe avec l'énergie entreposée dans le cristal, et ce, sans scintillation lumineuse intermédiaire ni conversion lumineuse subséquente en électricité par photomultiplicateur ou photodiode. Cette façon de faire procure une meilleure résolution énergétique, et la résolution spatiale est définie par la taille des cristaux présentés en réseau. Par contre, le coût est aussi proportionnel à la taille des cristaux et augmente rapidement au fur et à mesure que la surface à visualiser s'accroît. Une unité commerciale à petite surface a été présentée, puis retirée et remplacée par un système de scintillateur pixelé avec photodiodes. L'avenir des caméras à semi-conducteurs doit encore faire ses preuves.

En contraste, la tomographie à rayons X est une modalité d'imagerie qui produit des images tomographiques représentant les propriétés d'atténuation des rayons X du corps. A la différence de la tomographie conventionnelle, la TDM n'est pas sensible aux interférences provenant des structures du patient se trouvant en dehors de la partie imagée. Ceci est réalisé en irradiant uniquement des parties (coupes) fines du patient. Comparé à la radiographie planaire, les images TDM présentent un meilleur contraste, à savoir qu'il est possible de distinguer des différences très faibles d'atténuation des tissus.

Deux étapes sont nécessaires pour l'obtention d'une image TDM. La première étape est constituée par les mesures physiques d'atténuation des rayons X traversant le patient en différentes directions et la seconde consiste en des calculs mathématiques des coefficients d'atténuation linéaire  $\mu$ . Le système d'acquisition de données est composé d'une rangée de plusieurs centaines de petits détecteurs séparés les uns des autres et qui sont placés du côté opposé du patient.

La TDM à rayons X est composée de trois éléments principaux: le portique, la table sur laquelle est couché le patient et la console. Le portique est une structure mobile qui contient le tube à rayons X comprenant des collimateurs et des filtres, des détecteurs, le système d'acquisition de données (SAD), des composants de rotation incluant le système 'slip ring' et toute l'électronique associée. Dans les anciens systèmes, le générateur haute tension qui fournit la puissance au tube à rayons X était à l'extérieur du portique, tandis que dans la nouvelle génération de TDMs, le générateur est monté sur la composante de rotation à l'intérieur du portique et tourne avec le tube à rayons X. Le faisceau de rayons X produit après atténuation dans l'anode traverse la filtration inhérente du tube, le collimateur primaire, le filtre 'bow tie', le collimateur secondaire, le filtre additionnel et le patient. Les photons transmis à travers le patient sont recueillis par le récepteur ou le détecteur d'images. Une fois que le détecteur génère le signal analogue ou électrique, il est dirigé vers le SAD. Le signal analogue produit par le détecteur est un signal faible et doit être amplifié afin d'être analysé par la suite. L'amplification et la digitalisation du signal électrique sont réalisées par le SAD, qui est situé dans le portique juste après le système de détection.

Le signal numérique produit par le SAD est transféré à un processeur qui est placé à l'intérieur de la console. Le processeur exécute des algorithmes mathématiques à grande vitesse afin de

permettre la reconstruction des images. Le dernier composant du TDM est la table sur laquelle repose le patient. Celle-ci est constituée d'un matériel qui ne produit pas d'artefacts d'atténuation durant l'acquisition des images. De nombreuses tables sont conçues à base de fibres de carbone.

La technologie actuelle de tomодensitométrie hélicoïdale réalise l'acquisition de 4 à 64 coupes par rotation, réussissant ainsi à balayer entièrement la poitrine ou l'abdomen en quelques secondes. Les détecteurs à écran plat à large champ (de 30 à 40 cm sur l'axe des z) et les techniques de reconstruction du faisceau conique permettront de balayer ces régions en 0,5 à 1 seconde (en une seule rotation). Cela aura pour effet de révolutionner la TDM en permettant une visualisation en temps quasi réel de toutes les régions du corps avec une résolution spatiale isométrique.

Le traitement guidé par l'image exige que les images, provenant souvent de différentes modalités, soient enregistrées les unes avec les autres, avec les images du patient et avec les images fournies par un système de repérage des instruments dans le corps humain. Les organes, les tissus et les lésions doivent être délimités sur les images et celles-ci doivent être affichées, pour être consultées par le chirurgien, dans un format convivial et de manière à ne pas déranger les activités de la salle d'opération. Dans le but de représenter adéquatement le tissu humain auquel l'image correspond, les données numériques doivent être rendues à haute résolution, et l'équipement informatique doit permettre de manipuler ces données en temps réel.

Le diagnostic et le suivi oncologique sont traditionnellement basés sur la tomographie à rayons X. Cependant, ces dernières années, l'imagerie fonctionnelle TEP a été reconnue comme étant une modalité d'imagerie importante parallèlement à la TDM en fournissant des informations métaboliques complémentaires dans de nombreuses applications oncologiques. L'imagerie hybride TEP/TDM a été proposée permettant ainsi de surmonter les difficultés d'alignement des images TEP et TDM acquises indépendamment.

Bien que de nombreuses études aient démontré la supériorité de l'imagerie au FDG par rapport aux images de TDM dans l'évaluation des patients oncologiques, les techniques d'imageries fonctionnelles et anatomiques sont complémentaires. La TDM ou l'IRM sont nécessaires pour la localisation précise des lésions et pour démontrer leurs relations avec les organes et vaisseaux adjacents. Idéalement, les images fonctionnelles et anatomiques devraient être interprétées conjointement. Ceci peut se faire en les interprétant l'une à côté de l'autre ou en utilisant des logiciels pour superposer les images. Des logiciels fiables ont été développés pour recaler les images multimodales de structures rigides comme le crâne et le cerveau, cependant ces techniques ne fonctionnent pas aussi bien pour l'imagerie du corps entier.

Le scanner TEP/TDM combine la technologie des deux modalités d'imagerie (TEP et TDM), permettant ainsi de donner des informations détaillées sur l'anatomie du patient ainsi que sur les processus biologiques au niveau moléculaire des organes et tissus internes à partir d'une seule procédure non invasive. Le module TEP/TDM est à l'heure actuelle l'outil d'imagerie le plus puissant permettant la localisation, l'évaluation et le monitoring thérapeutique notamment des cancers de la sphère ORL.

### **3. La méthode de Monte Carlo appliquée à l'imagerie médicale**

La modélisation mathématique du processus d'acquisition est nécessaire pour l'évaluation de divers paramètres des systèmes d'imagerie médicale nucléaire puisque aucune solution analytique

n'est possible pour la résolution de l'équation de transport décrivant l'interaction des photons avec les structures atténuantes non-uniformes du corps humain et les géométries complexes de détection.

Les techniques de Monte Carlo sont devenues populaires dans différents domaines de la physique médicale bénéficiant de systèmes de calcul puissants mis à la disposition de la communauté scientifique durant ces dernières années. En particulier, elles ont été intensivement appliquées pour simuler des processus physiques stochastiques et pour estimer des paramètres physiques difficilement mesurables par des techniques expérimentales. Les innovations médicales nucléaires récentes, telles que la TEMP, la TEP, et l'imagerie hybride TEP/TDM se prêtent parfaitement à la modélisation par la méthode de Monte Carlo en raison de la nature stochastique des processus d'émission, de transport et de détection des rayonnements. Les facteurs qui ont contribué à une utilisation plus large incluent des modèles améliorés des procédés de transport de radiation, du caractère pratique de l'application avec le développement des techniques d'accélération et l'amélioration de la vitesse des ordinateurs. Les propriétés statistiques des données de projection simulées doivent être proches de celles obtenues par un imageur TEP ou TDM.

Dans ce travail de thèse, nous avons utilisé pour générer des sets de données TEP/TDM réalismes, le simulateur que nous avons développé basé sur le code de calcul MCNP4C permettant de modéliser aussi bien un tomodynamomètre à coupes multiples qu'un détecteur à écran plat et le programme de simulation *Eidolon* dédié à la simulation des tomographes TEP opérant en mode 3D. Dans ce qui suit, une description brève des codes Monte Carlo MCNP4C et *Eidolon* est présentée.

MCNP est un code Monte Carlo tout usage pouvant être employé pour le transport des neutrons, photons, et d'électrons ou pour le transport couplé de neutrons/photons/électrons. Il traite une configuration 3-D arbitraire des matériaux dans une cellule géométrique définie par des surfaces de second degré et des tores elliptiques du quatrième degré. Relativement aux photons, le code tient compte du rayonnement diffusé cohérent et incohérent, de la possibilité d'émission fluorescente après absorption photoélectrique, de la production de paires avec l'émission locale du rayonnement d'annihilation et de la production de bremsstrahlung. Les sections efficaces d'interaction par effet photoélectrique sont basées sur les travaux de Strom et Israel, tandis que les sections efficaces d'interaction par diffusion sont prises des tabulations ENDF. Un modèle de ralentissement continu 'continuous slowing down' est utilisé pour le transport d'électrons ou des positons, des rayons X des couches K, et du bremsstrahlung, mais n'incluant pas les champs externes ou auto-induits. Pour suivre un électron à travers une perte d'énergie significative, le code MCNP divise le chemin de l'électron en plusieurs étapes. Ces étapes sont définies de telle manière à être suffisamment longues afin d'éviter de nombreuses collisions (ainsi les théories de la diffusion multiple sont valides) mais suffisamment courtes pour que la perte d'énergie moyenne à n'importe quelle étape soit petite (pour satisfaire les approximations nécessaires pour les théories de diffusion multiple).

Pour le transport des électrons, MCNP traite le prélèvement des photons de rayonnement par freinage à chaque sous étape du parcours d'un électron. La table des probabilités de production est employée pour déterminer si un photon de rayonnement par freinage sera créé. Pour améliorer l'efficacité du transport des électrons et photons, deux cartes (PHYS:P et PHYS:E) sont mises en application dans MCNP pour polariser certains paramètres physiques tels que la production des électrons secondaires par les photons (IDES), la dispersion logique (NOCOH), la distribution angulaire de rayonnement par freinage (IBAD) et la production des rayons X caractéristiques (XNUM). La valeur par défaut pour ce dernier paramètre (XNUM = 1) résulte en un nombre analogue de voies prélevées. Si XNUM > 0, le nombre de photons produits est XNUM multiplié par le nombre qui serait produit dans le cas analogue, et un ajustement correspondant de poids est

réalisé. Le réglage de XNUM à zéro arrête la production des photons de rayon X par des électrons. Le simulateur TDM ainsi développé a été validé en comparant les résultats du modèle à des mesures expérimentales moyennant des TDM commerciaux utilisés en clinique et pour l'imagerie chez le petit animal (**Article III**).

La première version du simulateur de Monte Carlo, *Eidolon*, a été implémentée en Objective-C, un langage de programmation orienté-object basé sur la norme ANSI C en utilisant l'environnement de développement NextStep 3.3. Afin de faciliter la possibilité d'ajouter de façon incrémentale des fonctionnalités au programme, une conception modulaire comportant des éléments ou des modules chargés dynamiquement a été adoptée. Le bloc fonctionnel de base est une classe type qui permet d'accéder à des objets, de les examiner, les ajuster, les créer et les détruire à l'aide d'un inspecteur graphique. Ceci a été alors employé pour mettre en application une classe pour les sources, les détecteurs et un modèle du milieu atténuant ainsi que des classes paramétriques simples pour les sinogrammes et l'image de référence pour visualiser et sauvegarder les données produites. Le simulateur de Monte Carlo permet de simuler diverses configurations des modules d'acquisition de données TEP et d'obtenir une information détaillée sur les différents processus se produisant dans le fantôme et les détecteurs. Par exemple, le spectre d'énergie, la fonction de dispersion ponctuelle et la fraction de diffusé peuvent être obtenus. Le code permet également de séparer les différents événements qui composent les photons détectés: les événements primaires, les événements diffusés, ..etc., et de faire une investigation détaillée sur la distribution spatiale et énergétique des événements diffusés qu'il serait difficile, voire impossible à obtenir en utilisant les techniques expérimentales actuelles. Le simulateur a été validé en comparant les résultats du modèle à des mesures expérimentales ainsi que des études cliniques.

#### 4. Modélisation des spectres à rayons X

La connaissance détaillée du spectre des rayons X produit par un tube est nécessaire pour l'optimisation mathématique de la modélisation et la conception des systèmes radiologiques en général, la TDM en particulier. Cependant, la mesure directe des spectres exige un équipement cher et une attention et planification soignées pendant les mesures expérimentales. Puisque la mesure directe des spectres de rayons X requiert du temps et demeure une tâche difficile, les premières tentatives pour modéliser par ordinateur des spectres de rayons X ont commencé il y a plusieurs décennies et représentent toujours un secteur actif de recherche et développement. Généralement, des modèles de prédiction de spectres en radiodiagnostic et en mammographie peuvent être divisés en trois catégories principales: empiriques, semi-empiriques et modélisation par la méthode de Monte Carlo. Dans cette section, une brève vue d'ensemble des différents modèles informatiques pour la génération des spectres de rayons X est présentée.

Les modèles empiriques sont basés sur l'utilisation de données expérimentalement mesurées pour le développement de modèles permettant la prédiction des spectres de rayons X. Les premières tentatives basées sur l'utilisation de données mesurées se sont basées sur la reconstruction des spectres de rayons X moyennant les données de transmission. Il a été proposé que les spectres de rayons X pourraient être déterminés à partir des mesures de transmission à l'aide de matériel relativement simple se composant seulement d'un débitmètre et de quelques filtres. La simplicité de cette méthode comparée aux mesures expérimentales rigoureuses exigeant des spectromètres chers et une attention particulière pour la mesure directe des spectres de rayons X a attiré l'attention de plusieurs chercheurs. Pendant les trois dernières décennies, plusieurs groupes ont commencé à approcher une solution satisfaisante pour la reconstruction des spectres de rayons X à partir des données mesurées de transmission en utilisant la transformée de Laplace, les méthodes itératives, l'inversion directe de matrices et les réseaux de neurones. Un autre modèle

empirique basé sur l'interpolation par des polynômes pour la génération des spectres de rayons X en radiodiagnostic et en mammographie a également été proposé. Ces modèles sont basés sur l'utilisation de résultats mesurés et d'un modèle mathématique pour interpoler des spectres de rayons X. Les modèles semi-empiriques sont basés sur les théories de la mécanique quantique de la production de rayons X et de rayonnement par freinage. Ces techniques sont mises en application par dérivation mathématique suivie de certaines modifications pour ajuster les paramètres des équations en utilisant des spectres mesurés.

Les calculs par la méthode de Monte Carlo reposent sur le transport direct des électrons et des photons générés dans la cible et les filtres. L'utilisation de la méthode de Monte Carlo pour la simulation et le transport de particules chargées et non chargées est maintenant reconnue comme la méthode la plus précise pour la prédiction des spectres de rayons X, conséquence de la modélisation précise de la physique de l'interaction rayonnement-matière et l'incorporation des données physiques d'interactions appropriées.

Dans l'**Article I**, le code de calcul MCNP4C a été utilisé pour simuler des spectres à rayons X en radiologie diagnostique et en mammographie. L'effet talon (talon d'anode) a été étudié et des spectres en dehors de l'axe ont été déterminés pour différents angles d'anodes et de matériaux cibles. Les résultats de la simulation basée sur le code MCNP4C ont été comparés aux données mesurées et simulées par la méthode Monte Carlo basée sur EGS4. Par ailleurs, différentes méthodes de calcul (empiriques, semi-empiriques et méthode de Monte Carlo) proposées pour la prédiction des spectres à rayons X aussi bien pour le radiodiagnostic que pour la mammographie ont été évaluées en effectuant des comparaisons avec les spectres mesurés (**Article II**). Après validation des différents modèles, une base de données spectrale à rayons X a été créée et utilisée dans le simulateur TDM développé (**Article III**).

## 5. Correction d'atténuation en TEP basée sur la TDM

Les études précédentes souffrent des limites de la méthode de reconstruction des images. La méthode de rétroprojection conventionnellement utilisée amplifie le bruit de fond, dégradant la qualité des images. De nouveaux algorithmes de reconstruction ont été développés pour la reconstruction des images tomographiques, en utilisant une méthode itérative qui augmente le rapport signal/bruit de fond. Les effets du mode d'acquisition (2D versus 3D), de l'algorithme de reconstruction (rétroprojection versus reconstruction itérative) et de la correction d'atténuation ont été largement étudiés. L'absence de correction d'atténuation est un autre problème des études précédentes. Cette correction a été discutée extensivement dans les revues récentes.

Une proportion importante des photons de 511 keV est atténuée par les tissus du patient. L'atténuation est un phénomène non isotrope dans l'organisme, qui varie en fonction de la composition et de l'épaisseur des milieux traversés, ainsi que de l'énergie des photons. Les images obtenues en TEP, en l'absence de correction du phénomène d'atténuation, sous-évaluent les fixations profondes. Les effets de l'atténuation sont plus sévères si nous utilisons la technique de coïncidence que si nous utilisons celle du TEMP. Ceci est dû au fait que les deux photons résultant du procédé d'annihilation doivent traverser le champ de vue pour atteindre les détecteurs sans interaction. Les effets d'atténuation produisent des régions irrégulières et des distorsions des structures très radioactives. Une étude avec des fantômes a comparé les images FDG obtenues avec la technique du TEMP et de la TEP et a démontré que la correction de l'atténuation améliore la qualité et le contraste des images. Une correction doit être mise en œuvre pour restituer une image représentative de la distribution du traceur. Pour y parvenir, une mesure de transmission, réalisée avec une source externe, permet de connaître la distribution des coefficients d'atténuation

au sein du patient. Pour limiter la durée d'examen et éviter des problèmes de repositionnement, il est souhaitable d'effectuer la mesure de transmission au moment de la mesure des images d'émission. Plusieurs méthodes sont employées pour réaliser des mesures de transmission, elles utilisent des sources de germanium-68 ( $^{68}\text{Ge}$ ), de césium-137 ( $^{137}\text{Cs}$ ) ou un tube à rayons X. Le temps de mesure peut être réduit et compensé par des traitements informatiques adaptés. Ces derniers exploitent des techniques de segmentation des structures d'atténuation différentes, à partir des images de transmission bruitées et/ou biaisées. La valeur correcte du coefficient d'atténuation linéaire à 511 keV est alors affectée à chaque structure.

La distribution des coefficients d'atténuation peut aussi être mesurée au moyen d'un examen TDM réalisé par des rayons X. La possibilité de coupler un TEP et un TDM a déjà été évaluée depuis de nombreuses années, à l'université de Pittsburgh. Actuellement, tous les constructeurs proposent des systèmes qui réalisent cette double acquisition. L'intérêt réside dans l'obtention d'une image de transmission de très bonne résolution spatiale dans un temps très court, permettant de réduire la durée des examens. Ce gain en résolution dans l'image de transmission doit se traduire par une meilleure correction du phénomène d'atténuation au sein des petites structures atténuantes et hyperactives, qui ne sont pas « vues » par les mesures de transmission réalisées avec des sources radioactives. Cependant, l'apport de cette acquisition TDM dépasse très largement le problème de la correction d'atténuation, puisqu'elle apporte en plus une localisation anatomique précise des lésions.

La correction d'atténuation en TEP, associée à la correction des autres phénomènes physiques, permet de comparer les niveaux de fixation des différentes lésions. Elle permet une meilleure visualisation des lésions profondes, et facilite la localisation des lésions, grâce à des images plus représentatives de la fixation du traceur au sein des différents organes: ceci est particulièrement marqué pour l'interface entre le foie et les poumons. Par ailleurs, la correction d'atténuation constitue une étape essentielle pour la mise en œuvre de la quantification des études. Ceci est particulièrement important pour évaluer l'efficacité d'un traitement en cancérologie.

La correction d'atténuation présente certains avantages pour l'interprétation clinique des images, le plus important étant l'amélioration de la délimitation des repères anatomiques aidant à localiser plus précisément les lésions. C'est l'une des raisons pour lesquelles les images corrigées sont plus faciles à interpréter que celles sans correction d'atténuation. Un autre avantage est la possibilité de calculer la valeur de SUV (Standardized uptake value) si le système utilisé pour obtenir les images est calibré, ce qui est en général le cas des tomographes TEP dédiés, mais pas celui des caméras scintigraphiques hybrides. Le calcul de la valeur de SUV peut-être utile dans certaines situations cliniques particulières, par exemple la distinction des nodules pulmonaires malins et bénins quand leur taille est supérieure à deux fois la résolution du système d'imagerie. Une autre situation clinique pouvant bénéficier du calcul de la valeur de SUV est l'évaluation de la réponse thérapeutique des lésions malignes. Toutefois, les images corrigées pour l'atténuation ont souvent un bruit de fond plus important que les images non corrigées, ce qui est un désavantage. L'augmentation du bruit de fond dépend de la méthode utilisée pour générer la correction d'atténuation. La correction d'atténuation peut-être calculée pour les structures ayant une forme et un contenu prévisible comme le cerveau. La correction calculée est indépendante du patient; les méthodes de calcul ne peuvent être appliquées aux images du corps entier, le contenu interne étant asymétrique et les formes variables d'un patient à l'autre. Pour le corps entier, diverses méthodes ont été développées pour mesurer la correction nécessaire, utilisant des sources radioactives de transmission extérieures au patient. Dans ce cas, la qualité des images avec correction d'atténuation dépend essentiellement de la précision avec laquelle les images de transmission et d'émission sont superposées, et donc de la position du patient sur la table lors des deux séances d'imagerie, ainsi que de ses mouvements involontaires. Des études diverses comparant des images

de TEP avec et sans correction ont conclu que celle-ci n'améliorait pas le nombre de lésions détectées. Par contre, les études les plus récentes ont montré que la correction d'atténuation permet la détection d'un plus grand nombre de lésions sur les images de la TEP.

Dans ce travail de thèse, nous avons étudié en détail l'impact du rayonnement diffusé en TDM ainsi que l'injection d'agents de contraste sur la précision de la correction d'atténuation basée sur la TDM en utilisant des données simulées par le code MCNP4C ainsi que des données expérimentales et cliniques (**Article IV**). Par ailleurs, nous avons étudié l'impact de l'utilisation d'une seule courbe de calibration et de différentes intensités de courant des tubes à rayons X sur la précision de la correction d'atténuation basée sur la TDM pour des images acquises à différentes tensions du tube en procédant à des analyses quantitatives des cartes d'atténuation créées, des facteurs de correction d'atténuation générés et des données d'émission TEP neurologiques reconstruites en utilisant des études expérimentales sur fantôme et des études cliniques (**Article V**).

## 6. Conclusions et développements futurs

Dans les sections présentées de cette thèse, nous avons vu comment il était possible à l'aide des images TDM de corriger l'atténuation des images fournies par la caméra TEP et de comprendre tous les paramètres mis en jeu qui limitent la précision d'une telle correction. En ce qui concerne la mise en oeuvre, nous nous sommes surtout penché sur la définition des caractéristiques générales de la formation des images en TDM et leur conversion en une carte d'atténuation à 511 keV en tenant compte des paramètres physiques et physiologiques qui induisent des erreurs lors de la conversion.

En conclusion, nous avons apporté une contribution spécifique au développement d'un outil de simulation de la TDM par la méthode de Monte Carlo basé sur le code à usage général MCNP4C ainsi que son application pour l'évaluation des limitations de la correction d'atténuation en imagerie TEP moyennant des cartes d'atténuation générées par la TDM.

Une des applications potentielles du simulateur consiste en la génération de données pour tester et évaluer les algorithmes de reconstruction et correction de rayonnement diffusé en TDM pour les nouvelles générations de caméras hybrides TEP/TDM. Dans cette thèse, nous nous sommes intéressés à l'étude de l'atténuation des photons et sa correction. L'utilisation du simulateur TDM nous a apporté des informations complémentaires importantes pour l'évaluation d'effets physiques et physiologiques difficiles à modéliser dans des mesures expérimentales. Ceci nous a permis d'évaluer les performances d'une méthode qui tient compte de la présence d'agents de contraste développée par un autre groupe de recherche, et sa généralisation dans cette thèse. En conséquence, notre travail ouvre des perspectives intéressantes à la compréhension des phénomènes liés à la dégradation des images TDM et leur propagation aux images TEP lors de la correction d'atténuation. Il serait souhaitable de pouvoir implémenter d'une manière efficace le simulateur sur une plateforme parallèle ou une grille de calcul pour diminuer le temps de calcul et d'explorer plus en détail des alternatives aux méthodes conventionnelles de correction du rayonnement diffusé en TDM et de la présence d'agents de contraste et de prothèses ou implants métalliques en adaptant les algorithmes proposés dans la littérature à des cas plus complexes.

## 1. Introduction

Diagnostic imaging began in the first decade of the 20<sup>th</sup> century after discovery of x-rays by Professor Roentgen. The development of radiology as a first imaging technique grew at a good pace until World War II. Extensive use of x-ray imaging during the second World War, and the advent of the digital computer and new imaging modalities like ultrasound, magnetic resonance imaging and nuclear medicine have combined to create an explosion of diagnostic imaging techniques in the past 25 years.

For the first fifty years of radiology, the primary examinations involved creating an image by focusing x-rays through the body part of interest and directed onto a single piece film inside a special cassette. In the earliest days, a head x-ray could require up to 11 minutes of exposure time. The next development involved the use of fluorescence screens and special glasses so that physicians could see x-ray images in real time. In 1955, the x-ray image intensifier was developed and allowed the pick up and display of x-ray movies using TV cameras and monitors. The image intensifier opened the way for a new radiographic sub-specialty known as angiography to allow the routine imaging of blood vessels and the heart. Digital imaging techniques were implemented in the 1970's with the first clinical use and acceptance of computed tomography (CT) developed by Godfrey Hounsfield in 1972. Hounsfield's original CT scan took hours to acquire a single slice of image data and more than 24 hours to reconstruct this data into a single image. Today's state-of-the-art CT systems can acquire up to 64 slices in less than a second and reconstruct the images instantly.

The first nuclear medicine studies were done in the 1940's, where the spatial information about radioactive source distributions within the brain were produced using a single detector positioned at various locations around the head. Ben Classen improved this method in the 1950's when he invented the rectilinear scanner. In the late 1950's, Hal Anger invented the scintillation camera using a single NaI(Tl) crystal and PMT array for single photon emission computed tomography (SPECT). Kuhl and Edward were the first to present tomographic images produced using the Anger Camera in 1963. Rapid progress occurred during the 1970's. Beginning in the 1980's and continuing till today, there has been rapid expansion in nuclear medicine techniques.

The development of positron emission tomography (PET) covered many decades and included contributions from many scientists. The first medical applications for positron annihilation were made and reported by William H. Sweet in 1951. This was a simple brain probe that utilized coincidence to localize brain tumours. Gordon L. Brownell along with William H. Sweet developed and built the first probe using two opposite scintillator detectors with NaI(Tl) crystal in 1952. The first PET scanners were produced in the early 1960's using a ring of 32 NaI(Tl) detectors. The following generation of PET scanners reduced detector size and added additional rings to allow for simultaneous acquisition of multiple slices. In the late 1970's, marketing finally began making these machines the first commercially available.

The use of ultrasound in medicine began during and shortly after the World War II. The work of Dr. Dussik in 1942 on transmission ultrasound investigation of brain resulted in the first published work on medical ultrasonics. However, for various practical reasons, ultrasound only became widely available in medicine in the 1970's.

The history of magnetic resonance imaging (MRI) can be traced to 1946, when Felix Bloch and Edward Purcell discovered the magnetic resonance phenomenon independently and both of

them were awarded the Nobel Prize in 1952. Magnetic resonance imaging was initially researched in the early 1970's and the first MRI prototype was tested on clinical patients in 1980. Finally, MRI was cleared for commercial clinical availability by the FDA in 1984.

### 1.1. Medical imaging techniques

Clinical diagnosis is often supported by several imaging modalities which provide complementary information. Generally, this information can be classified as anatomical or functional. Diagnosis, staging and re-staging of cancer, as well as the monitoring and planning of cancer treatment, has traditionally relied on anatomic imaging like CT and MRI. One of the disadvantages of anatomical imaging techniques is their inability to characterize the tumour. Lesions need to be characterized whether they are benign or malignant and if malignant it would be helpful to know whether proliferation is slow or fast. Necrotic, scar and inflammatory tissue often cannot be differentiated from malignancy based on anatomic imaging alone. Anatomical imaging has high sensitivity for detection of structural changes, but a low specificity further characterization of these abnormalities. SPECT and PET are imaging techniques that provide information on physiology rather than anatomy. These modalities have been used for evaluation of tumour metabolism, difference between tumour recurrence and radiation necrosis, detection of hypoxic areas of the tumour, and other functional imaging [1].

There are many instances in which it would be desirable to integrate the information obtained from two modalities of the same patient. The poor anatomical resolution of PET and SPECT images can be improved by integration with high resolution images delivered by CT or MRI. The resulting image could be named as hybrid image. Figure 1 shows a transaxial slice from human chest acquired with different modalities, left (CT, anatomical information), middle (PET, functional information) and right (PET/CT, fusion of anatomical and functional information).

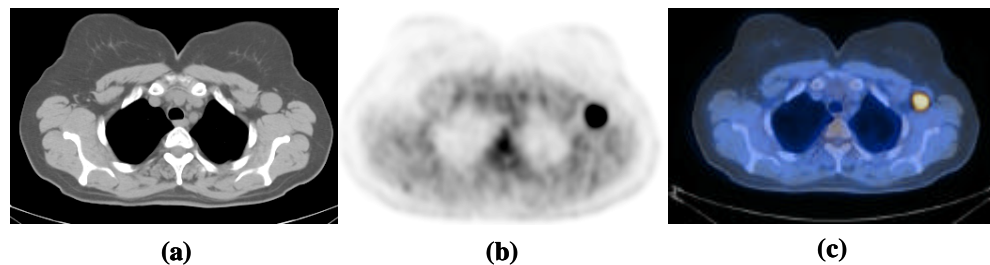


**Fig. 1.** Transaxial slice from chest acquired with different modalities: (a) CT; (b) PET; and (c) hybrid PET/CT.

### 1.2 Dual-modality imaging devices

From advances in x-ray film and cassettes to the introduction of computers and digital images, diagnostic imaging has never stopped reinventing its technology to improve patient care. Today, diagnostic imaging is one of the cusps of explosive growth in an arena known as hybrid imaging. This technology melds two independent imaging modalities, typically a procedure that demonstrates an organ's function and metabolism with one that depicts the organ's anatomy, to produce a diagnostically and clinically superior study.

Historically, the first dual-modality device was a combination of SPECT and CT. The pioneering work by Hasegawa *et al.* [2] and Lang *et al.* [3] combined anatomical and functional images by using a single detector for both modalities. In addition, the x-ray CT images were used to provide an attenuation map for attenuation correction of SPECT data [4]. The first commercial SPECT/CT produced by GE Medical Systems (Milwaukee, WI) was introduced in 1999 [5].

Although the idea of combining PET and CT was proposed in 1994, the first prototype dedicated PET/CT scanner was installed in the University of Pittsburgh Medical Center in 1998 [6]. The prototype was developed in collaboration with CTI PET systems (Knoxville, TN) and the first commercial system approved by FDA was presented at the 2000 Society of Nuclear Medicine meeting in St. Louis. Thereafter, GE Medical Systems (Milwaukee, WI) introduced a PET/CT system, now named Discovery LS, at the 2000 Radiological Society of North America (RSNA) meeting in Chicago and Philips Medical Systems (Milville, TN) presented their version of combined PET/CT, the Gemini, at the RSNA meeting in 2001. Combined PET/CT scanners have been in production for less than 5 years and the technology is undergoing rapid evolution. The introduction of new geometrical designs, scintillator crystals and fast electronics in PET components and in parallel increasing the number of detector rows and reduction of rotation time in CT scanners will potentially increase the performance of PET/CT scanners [7].

In principle all advantages of a PET/CT scanner could be replicated by PET/MRI; however, there are several major problems to combine PET and MRI technology in an integrated system. One obvious problem is that the radiation of interest, photons for PET and radiofrequency in MRI, come from opposite ends of the electromagnetic spectrum and there is no single detection system that can be used for both modalities. Besides putting the two machines in one cover, similar to the current PET/CT scanners design is problematic because of the incompatibility of currently used technologies in PET and MRI [8].

### 1.3. Purpose of this work

The main motivation behind this thesis was the assessment of sources of error and artefact when using CT-based attenuation correction (CTAC) on current (multi-row detector) and future (flat-panel detector) generation of dual-modality PET/CT systems using Monte Carlo simulations, experimental measurements and clinical data. This thesis is based on five original papers which will be referred by their Roman numerals in the text. The following paragraphs summarize the content of this thesis:

1. The general purpose Monte Carlo N-particle radiation computer code (MCNP4C) was used for the simulation of x-ray spectra in diagnostic radiology and mammography. The anode heel effect and off-axis x-ray spectra were assessed for different anode angles and target materials. The results of MCNP4C-based simulation were compared with EGS4-based Monte Carlo simulations and measured results (**Paper I**).
2. Different computational methods (empirical, semi-empirical and Monte Carlo) proposed for prediction of x-ray spectra both in diagnostic radiology and mammography were assessed by comparison with measured spectra. The comparative assessment encompasses many figures of merit including qualitative and quantitative assessment of spectra shape, the difference in K x-ray yield, transmission curves, half value layer as well as absorbed dose and effective dose imparted to the adult ORNL hermaphroditic phantom. After validation of models, an x-ray spectra database was created and used in the developed CT simulator (**Paper II**).

3. A MC x-ray CT simulator based on the Monte Carlo N-particle radiation transport code (MCNP4C) was developed for simulation of both fan- and cone-beam x-ray CT scanners with single-slice, multi-slice (up to 64 slices) and flat-panel detector configurations. The simulator was validated through comparison with experimental measurements of different non-uniform phantoms with varying sizes on both a clinical and a small-animal CT scanner. The simulator was extensively used to investigate potential artefacts and correction schemes when using CTAC on dual-modality PET/CT scanners (**Paper III**).
4. The impact of x-ray scattered radiation on the accuracy of CTAC was investigated for both a clinical-multi slice and prototype flat-panel detector-based x-ray CT scanner using the developed MCNP4C-based CT simulator. The influence of contrast medium on CTAC was studied by Monte Carlo simulations and experimental studies using the RSD (Radiology Support Device Inc., Long Beach, CA) anthropomorphic striatal phantom. The effect of metallic leads used in deep brain stimulation (DBS) techniques for treatment of Parkinson's disease on CTAC was also investigated (**Paper IV**).
5. The impact of using a single calibration curve and different tube currents on the accuracy of CTAC for images acquired at different tube voltages was investigated through quantitative analysis of created attenuation maps ( $\mu$ maps), generated attenuation correction factors (ACFs) and reconstructed neurological PET emission data using experimental phantom and clinical studies (**Paper V**).

In section 2, a general overview of PET/CT physics and instrumentation is presented and different attenuation correction strategies in PET outlined. Section 3 introduces the applications of Monte Carlo modelling in medical imaging and Monte Carlo codes used in this study. In section 4, the methodological basis for analytical and Monte Carlo x-ray spectra modelling is presented and followed by a discussion of the relevance of x-ray spectra modelling in clinical and research settings. Section 5 gives the general motivation, the development strategy and experimental validation of our MCNP4C-based x-ray CT simulator. In section 6, the sources of error and artefact in CT-based attenuation correction are presented. Finally, key conclusions and suggested continuation of this research are presented in section 7.

## 2. PET/CT physics and instrumentation

In current PET/CT designs, the two scanners (PET and CT) are physically separate with the CT position anterior of the PET, in the same cover. The advantage of this minimal hardware integration is that each system can use the latest technology, independently. In the last five years, since the introduction of PET/CT in clinical area, there have been significant advances in both CT and PET technology and consequently these advances become incorporated into current generation PET/CT scanners [7].

### 2.1. The physics of computed tomography (CT)

X-ray computed tomography is an imaging modality that produces cross-sectional images representing the x-ray attenuation properties of the body. Unlike conventional tomography, CT does not suffer from interference from structures in the patient outside the slice being imaged. This is achieved by irradiating only thin slices of the patient. Compared to planar radiography, CT

images have superior contrast resolution, i.e, they are capable of distinguishing very small differences between tissues attenuation.

Two steps are necessary to derive a CT image: firstly, physical measurements of the attenuation of x-rays traversing the patient in different directions; and secondly mathematical calculations of the linear attenuation coefficients,  $\mu$  all over the slice. The patient remains on the examination table while the x-ray tube rotates in a circular or spiral orbit around the patient in a plane perpendicular to the length-axis of the patient. The data acquisition system is an array of several hundred small separate detectors placed on the opposite side of the patient. The arrangements of the x-ray tube and detectors have changed over the years as will be discussed in the following sections.

When readings from the detectors have been stored in the scanner's computer, the tube is rotated to another angle and a new projection profile is measured. After a complete rotation, it is possible to calculate the average linear attenuation coefficient,  $\mu$  for each pixel. This procedure is called image reconstruction from measured projections. In modern CT scanners, images consist of  $512 \times 512$  pixels representing the CT number, which is expressed in Hounsfield Units (HU). The CT number is defined as:

$$CT\ number = \frac{\mu - \mu_{H_2O}}{\mu_{H_2O}} \times 1000 \quad (1)$$

Where  $\mu$  is the average linear attenuation coefficient for the material in a given pixel. With this definition, air and water have a CT number of -1000 HU and 0 HU, respectively.

### 2.1.1 CT hardware components

The CT scanner consists of three major components: gantry, patient table or couch and consol. The gantry is a movable frame that contains the x-ray tube including collimators and filters, detectors, data acquisition system (DAQ), rotational components including slip ring system and all associated electronics. In the old CT systems, the high voltage generator that supplied power to the x-ray tube was outside the gantry while in the new generation of CT scanners the generator is mounted on the rotational component inside the gantry and rotate with the x-ray tube. The produced x-ray beam after attenuation in the anode passes through the tube's inherent filtration, primary collimator, bow-tie filter, secondary collimator, additional filter and patient. The transmitted photons through the patient are collected by the image receptor or detector. Once the detector generates the analog or electrical signal, it is directed to the data acquisition system. The analog signal generated by the detector is a weak signal and must be amplified to further be analyzed. Amplifying and digitizing the electrical signal is the task performed by the DAQ. The DAQ is located in the gantry right after the detector system.

The digital signal produced by the DAQ is transferred to an array processor placed inside the console. The array processor is a specialized high speed computer designed to execute mathematical algorithms for the purpose of image reconstruction. The final component of a CT scanner is the patient table or couch, which should be made with materials that will not cause artefacts during scanning. Many CT tables are made of carbon fibre material [9].

### 2.1.2 CT design configurations

The general classification of CT scanners is based upon the arrangement of components and the mechanical motion required for collecting the data. The different scanner design configurations are categorized in four generations.

*First generation.* In the first CT scanners' design, a single x-ray source and a single detector cell collect all the data for a single slice. The source and detector are rigidly coupled and the pencil beam is translated across the patient to obtain a set of parallel projection measurements at one angle. The source/detector pair is then rotated slightly and a subsequent set of measurements are obtained during a translation past the patient. This process is repeated for each projection angle. Because of the translation and rotation process, this geometry is referred to as a translate/rotate scanner.

*Second generation.* Because the x-ray source emits radiation over a large angle, the efficiency of measuring projections was greatly improved by using multiple detectors. The source and the array of detectors are translated as in a first generation system, but since the beam measured by each detector is at a slightly different angle with respect to the object, each translation step generates multiple parallel ray projections. Since multiple projections are obtained during each translation past the patient, the second generation of CT scanners is significantly more efficient and faster than the original first generation scanner. This generation is also referred to as a translate/rotate scanner.

*Third generation.* With improvements in detector and data acquisition technology, it was possible to design a detector array with enough high spatial resolution cells to allow the simultaneous measurement of a fan-beam projection of the entire patient cross section. With such a large detector, it is no longer necessary for the tube-detector assembly to translate past the patient. Instead, the tube-detector assembly simply rotates around the object. The imaging process is significantly faster than first and second generation systems. However, very high performance detectors are needed to avoid ring artefacts and the system is more sensitive to aliasing than previous generations. Because both the tube and detector rotate, this generation is often referred to as rotate/rotate scanner geometry.

*Fourth generation.* Contemporary with the development of viable third generation systems and to avoid the sensitivity to ring artefacts, a design was developed using a stationary detector ring and a rotating x-ray tube. Because the reduced motion seemed consistent with a reduction in complexity, this geometry is known as the fourth generation. The stationary detector requires a large acceptance angle and is therefore more sensitive to scattered radiation than the third generation geometry. Fourth generation geometries also require a large number of detector cells and electronic channels (at a potentially higher cost) to achieve the same spatial resolution and dose efficiency as third generation systems. This system is referred to as rotate/stationary geometry.

Several other CT scanner geometries which have been developed do not precisely fit the above categories. However, there is no agreed-upon generation designation for them. In a fourth generation scanner, the detector ring is outside the circular path of the x-ray source. A CT system design was developed in which a circular detector ring is inside the source trajectory. This reduces the size of detector array and may lead to a more compact system. In this system, the detector array nutates so that the detectors do not obstruct the x-rays as they pass from the source to the object. In some texts, this is referred to as a fifth generation system.

In another design of CT scanners, both the x-ray tube anode and detectors are stationary. The anode, however, is a very large semicircle ring that forms an arc around the patient scan circle, and is a part of a very large, non-conventional x-ray tube. Instead of rotating an x-ray tube around the

patient, the system sweeps an intense electron beam across the stationary anode target. Because the electron beam can be moved very rapidly, this scanner can attain very rapid image acquisition rates. In the literature, this system has been referred to variably as fifth and sixth generation. It has also been described as stationary/stationary scanner. The terms of millisecond CT, ultrafast CT, and electron beam CT (EBCT) have also been used.

The slip-ring technology has had a great impact on CT system performance and utilization in 1991 (Fig. 2a). Whereas most previous conventional CT systems used a cable-take-up mechanism to deliver high voltage to the x-ray tube (and could rotate through perhaps 400-600 degrees before it had to stop), the use of slip-ring allows the continuous rotating of the x-ray tube. Scanners equipped with this technology are generally referred to as spiral CT scanners. Speed and spatial resolution have been significantly improved with the development of multi-slice CT technology in 1998 (Fig. 2b). The multi-slice capability has been created by dividing each detector element into several smaller sub-elements that has its own complete data acquisition electronics [10]. Although the multi-slice technology started with dual slice scanners, nowadays 64 slice scanners are commercially available.

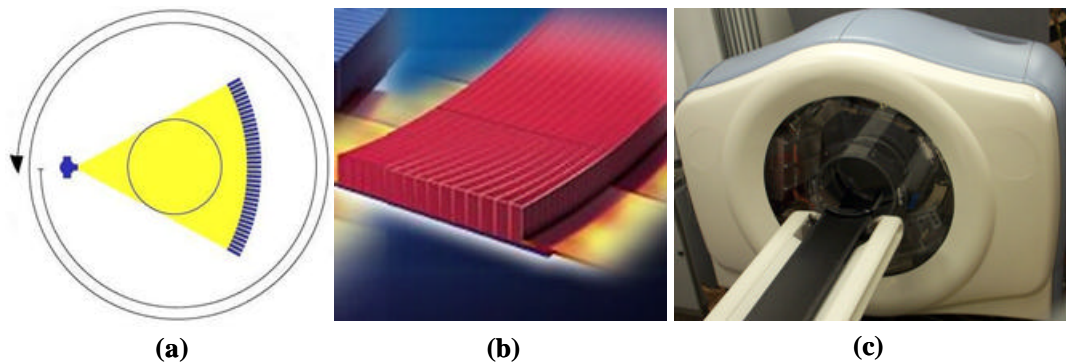


**Fig. 2.** (a) Continuous rotation with slip-ring technology. (b) Multi-slice detector. (c) Prototype human cone-beam CT scanner with flat-panel detector-based design.

Recently, with the introduction of flat-panel detectors, another generation of CT scanners named as cone-beam CT is under investigation. Whereas this generation of scanners is under development for human imaging, small animal cone-beam CT is commercially available. In this generation of CT scanners, the x-ray tube and flat-panel detector which is an areal detector move around the object in a similar way to the movement in third generation CT scanners. Unlike, single- and multi-slice CT scanners which cover a maximum of 4 cm of the object, cone-beam CT can cover more than 20 cm of the object in one rotation (Fig. 2c).

## 2.2 Physics of positron emission tomography (PET)

PET imaging relies on the nature of positron decay. When a nucleus undergoes positron decay, the result is a new nuclide with one fewer proton and one more neutron, as well as the emission of positron and a neutrino. As positrons pass through matter, they experience the same interactions as electrons, including loss of energy through ionization and excitation of nearby atoms and molecules. After losing enough energy and travelling a given distance in matter (depending the initial energy of the positron), the positron will annihilate with a nearby electron and two photons in opposite directions are emitted each with an energy of 511 keV (Fig. 3a). These photons are the basis of coincidence detection and coincidence imaging. PET imaging systems detect annihilation

events by means of several rings of photon detectors that surround the patient. When two matching photons originating from the same annihilation event are recorded within nanoseconds of each other, two opposite detectors register a coincidence event along the line between both detectors. The PET system then registers all lines of response between each detector pair registering a coincidence event during the scan. At the end of the acquisition, there will be areas of overlapping lines which indicate more highly concentrated areas of radioactivity, according to the tracer distribution within the patient body (Fig. 3b). Then the raw data can be reconstructed to create cross sectional images representing the radioactivity distribution into the tissues [11].

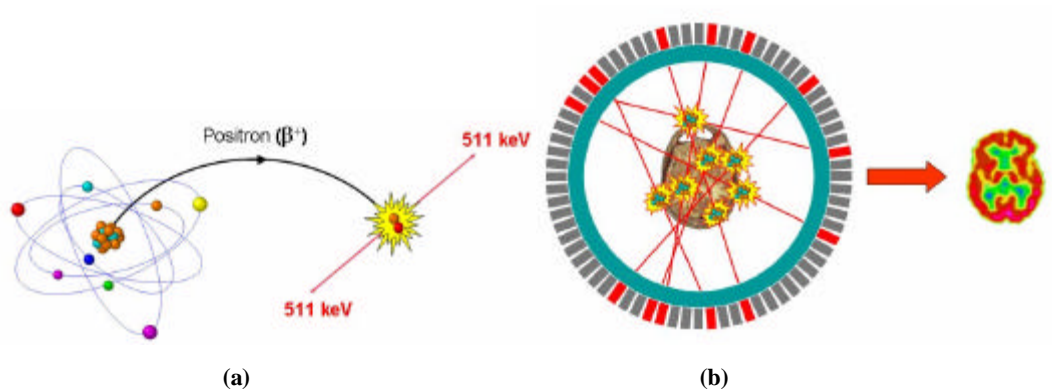


**Fig 3.** (a) Schematic representation of positron emission and annihilation. (b) Coincidence event detection in a cylindrical multiple-ring PET scanner.

### 2.2.1. PET components

The PET scanner consists of three major components: gantry, patient table or couch and console. The PET gantry contains detector blocks, collimators if any and front-end electronics. The detector blocks include scintillator crystals (such as BGO, LSO and GSO), photomultiplier tubes (PMT) and amplifiers. The blocks are grouped together to form a detector module (cassette). Modules are mounted in the gantry to form the detector ring. There are two types of shielding on the detector to reduce detecting scattered radiation: primary shield and collimator (septa). At the front and back of the detector ring are pieces of lead that make up the primary shield. This primary shield prevents detection of radiation from outside the field of view. While the primary shielding on the detector's outside helps prevent interference, the collimator ensures that radiation within the proper plane is detected. The collimator uses thin tungsten blades to make the walls of the collimator referred to as the septa. In some systems, the collimator is mounted on sliding rails inside the gantry. This allows the system to move the collimator out of the scanner field of view for high sensitivity 3D scanning. After scintillation, PET has electronics that analyze, validate and report the information. The first step in the electronics process is to analyze the PMT signals and determine location and energy. The PET system knows the  $Y$  value of a detected event because of the fixed rings. Then utilizing position of event detection and Anger logic, the PET front-end electronics determines  $X$  and  $Z$  positional values. PET table or couch should be made with material that will not cause artefacts during scanning. The operator's console allows the user to view the image on a monitor, transmit or store it digitally and print it out.

### 2.2.2. Design configurations of PET scanners

The development of positron emission tomography has attracted many strong personalities, great scientists, physicians and businessmen, many of whom have dedicated their entire lives to this technology. The history of PET is dynamic and is marked by many significant technological

advances. Generally, the geometrical design of PET scanners can be categorized in four classes: multiple full-ring, multiple partial-ring, hexagonal array and dual-head (Fig. 4). The multiple full-ring geometry is the most successful design that represents a reasonable compromise between maximizing system sensitivity and resolution while keeping detector dead-time and corruption from scatter and random coincidences at a reasonable level [12]. To lower the cost of dedicated multiple full-ring systems, Townsend *et al.* [13] developed a partial-ring PET tomograph since the crystals account for about 60% of the cost of full-ring PET tomographs. Another design configuration for fully 3D PET scanners is based on a hexagonal array of sodium iodide scintillation cameras [14]. Dual-head gamma cameras offer the capability of imaging in both single-photon and coincidence imaging [15].

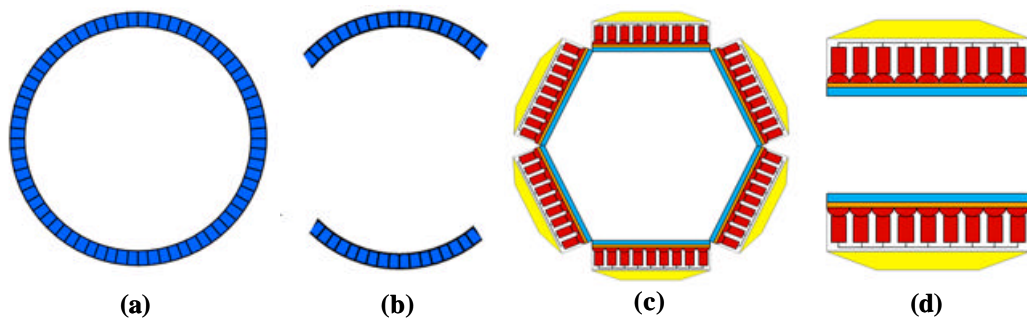


**Fig. 4.** Illustration of the range of different geometries of PET systems. **(a)** Multiple full-ring; **(b)** multiple partial-ring; **(c)** hexagonal array; **(d)** dual-head. The dual-head and partial-ring scanners require the rotation of the detectors to collect a full set of projection data.

More recently, sodium iodide scintillation detectors in the hexagonal configuration have been replaced with flat-panel LSO based detectors with a physical dimension of  $52 \times 36$  cm, including more than 10000 individual detector elements and a rotation speed of 30 rpm to acquire full data sets for 3D reconstruction [7]. One of the critical components of PET scanners is the scintillation crystal used in the detection system. The scintillation process involves the conversion of photons energy into visible light via interaction with a scintillating material. The characteristic of scintillation materials used in the design of PET cameras is summarized in Table 1.

**Table 1.** Characteristic of scintillation crystals under development and currently used in PET systems design.

Scintillator	BGO	LSO	GSO	LuAP	LaBr <sub>3</sub>	LYSO
Formula	$\text{Bi}_4\text{Ge}_3\text{O}_{12}$	$\text{Lu}_2\text{SiO}_5:\text{Ce}$	$\text{Gd}_2\text{SiO}_5:\text{Ce}$	$\text{LuAlO}_3:\text{Ce}$	$\text{LaBr}_3:\text{Ce}$	$\text{LuYSiO}_5:\text{Ce}$
Density (g/cc)	7.13	7.4	6.71	8.34	5.3	7.1
Light yield (photons/keV)	9	25	8	10	61	32
Effective Z	75	66	60	65	46.9	64
Principal decay time (ns)	300	42	60	18	35	48
Peak wavelength (nm)	480	420	440	365	358	420
Index of refraction	2.15	1.82	1.95	1.95	1.88	1.8
Photofraction (%) <sup>*</sup>	41.5	32.5	25	30.6	15	34.4
Attenuation length (cm) <sup>*</sup>	1.04	1.15	1.42	1.05	2.13	1.12
Energy resolution (%) <sup>*</sup>	12	9.1	7.9	11.4	3.3	7.1
Hygroscopic	No	No	No	No	Yes	No

<sup>\*</sup>@ 511 keV

### 2.3. Dual-modality PET/CT imaging

Diagnostic and follow-up in clinical oncology are traditionally based on CT. In recent years, however, functional imaging using PET has been recognized as an important imaging modality and adjunct to CT that provides complementary metabolic information in many oncological applications. To overcome the challenges of aligning independently acquired PET and CT image sets, several *ad hoc* concepts of integrating PET and CT imaging in a single device have been proposed [7].

The PET/CT scanner combines premier technology from two modalities, PET and CT, making it possible to reveal detailed anatomy and biological processes at the molecular level of internal organs and tissues from one single non-invasive procedure. The combined PET/CT scanner is the most powerful imaging tool available for localizing, evaluating and therapeutic monitoring of head and neck cancer and equally useful for other cancers that are difficult to pinpoint. Separately, CT and PET do not provide images with the necessary combination of clear structural definition and metabolic activity that is achieved with PET/CT [8]. Current PET/CT systems consist of a single, long-bore gantry with the individual PET and CT systems adjacent to one another (Fig. 5). In some systems, a single housing is placed over the two modules whereas in others the modules have separate covers, but are positioned very close to one-another.

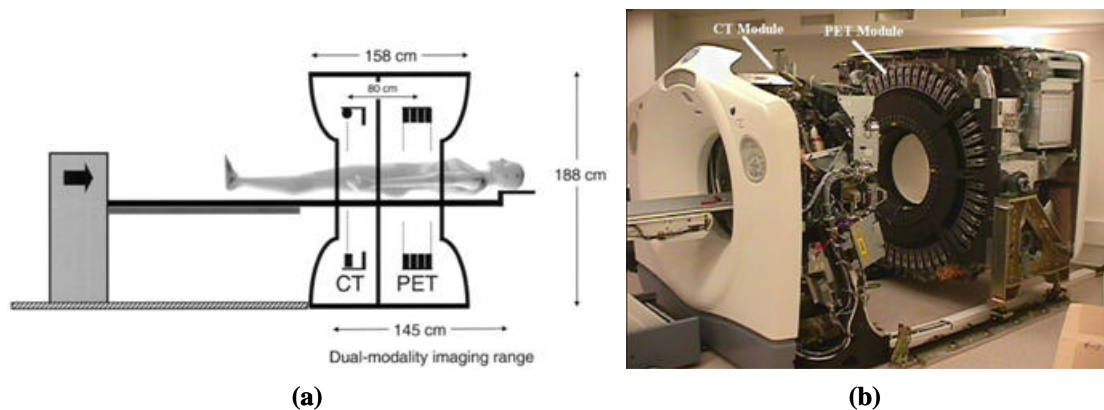


**Fig. 5.** (a) Schematic illustration of a PET/CT scanner. Reprinted with permission from ref. [7] (b) Individual PET and CT modules placed in one cover in a commercial PET/CT scanner.

### 2.4. Limitations of quantitative PET imaging

Several physical factors can degrade image quality and quantitative accuracy in PET. These factors include but are not limited to: scattered photons [16], physiological as well as patient motion [17], attenuation of photons [18], partial volume effect [19], parallax effect [20], positron range and non-collinearity [21]. The most important factor is attenuation of photons in tissues, which can affect both visual interpretation and quantitative accuracy of PET data [18]. Attenuation correction has been shown to improve image quality, lesion detection, staging and management of patients in clinical oncology compared to non-attenuation corrected images [22].

#### 2.4.1. Attenuation correction strategies in PET

Reliable attenuation correction methods for PET require determination of an attenuation map, which represents the spatial distribution of linear attenuation coefficients at 511 keV for the region

under study. After the attenuation map is generated, it can be incorporated into image reconstruction algorithms to correct the emission data for errors contributed by photon attenuation (Fig. 6). The methods for generating the attenuation maps can be categorized in two main classes: transmissionless methods and transmission-based methods [18].

Transmissionless correction methods are based on calculation of boundary and distribution of attenuation coefficients by means of approximate mathematical methods, statistical modelling for simultaneous estimation of attenuation and emission distribution and consistency conditions criteria. It is generally difficult to generate accurate attenuation map using transmissionless methods especially in whole-body imaging with more complex juxtapositions of media with different attenuation properties and irregular contours. Therefore, transmissionless techniques have limited value for clinical applications [18].

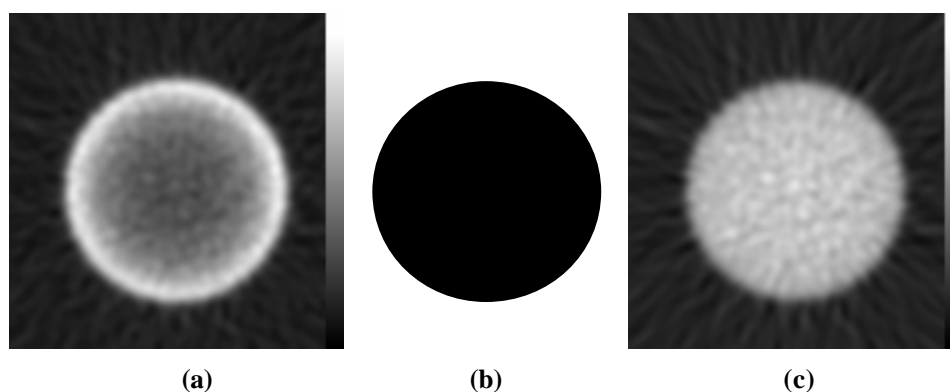


**Fig 6.** Illustration of reconstruction artefact resulting from lack of attenuation correction for uniform distribution of activity in a cylindrical phantom. **(a)** Reconstructed image without attenuation correction. **(b)** Uniform attenuation map at 511 keV. **(c)** Same slice as **(a)** after applying attenuation correction. Reprinted with permission from ref. [18].

In clinical applications, in which the attenuation coefficient distribution is not known *a priori*, and for areas of inhomogeneous attenuation such as the chest, more adequate methods (transmission-based methods) must be performed to generate the attenuation map. This includes transmission scanning using external radionuclide sources, x-ray CT scanning and segmented MRI data. In stand alone PET systems, the most widely used attenuation correction technique is radionuclide transmission scanning before (pre-injection), during (simultaneous) or after (post-injection) emission scan [23]. The use of x-ray CT scans offers the advantage of higher photon fluence rates and faster transmission scan, in addition to true anatomic imaging and localization capability that can not be obtained using radionuclide transmission scans [18]. The clinical use of MRI-based attenuation correction techniques is limited to brain imaging. In this method the T1-weighted MR images are realigned to preliminary reconstructed PET data using an automatic algorithm and then segmented to classify the tissues in different categories depending on their density and composition. Then the theoretical tissue-dependent attenuation coefficients are assigned to the related voxels in order to generate an appropriate attenuation map [24].

#### 2.4.2. CT-based attenuation correction in PET

Attenuation maps generated for attenuation correction have traditionally been obtained using external radionuclide sources. This process is identical conceptually to the process of generating CT images with an x-ray tube that transmits radiation through the body, with transmitted intensity recorded by an array of detector elements. The transmission data can then be reconstructed using a tomographic algorithm that inherently calculates the attenuation coefficients at each point in the

reconstructed slice. The reconstructed CT image contains pixel values that are related to the linear attenuation coefficient at that point in the patient, calculated from the effective CT energy at operational tube voltage of scanner. However, the attenuation map at 511 keV can be generated from the CT images to correct the PET emission data for photon attenuation [18]. CT-based attenuation correction offers four significant advantages [25]: first, the CT data will have much lower statistical noise; second, the CT scan can be acquired much more quickly than a radionuclide transmission scan; third is ability to collect uncontaminated post-injection transmission scan and forth, using the x-ray transmission scan eliminates the need for PET transmission hardware and periodic replacement of  $^{68}\text{Ge}/^{68}\text{Ga}$  positron sources. A potential benefit not yet fully explored is the direct incorporation of anatomical information derived from the CT data into the PET image reconstruction process and correction for partial volume effect [26].

As noted above, CT inherently provides a patient-specific measurement of the linear attenuation coefficient at each point in the image. However, the linear attenuation coefficient measured with CT is calculated at the x-ray energy rather than at the 511 keV. It is therefore necessary to convert the linear attenuation coefficients obtained from the CT scan to those corresponding to the 511 keV (Fig. 7). Several conversion strategies have been developed including scaling [27], segmentation [25], hybrid (segmentation/scaling) [28], piece-wise linear scaling [29], and dual-energy decomposition methods [30]. In the following, a short description of the nominated methods is presented.

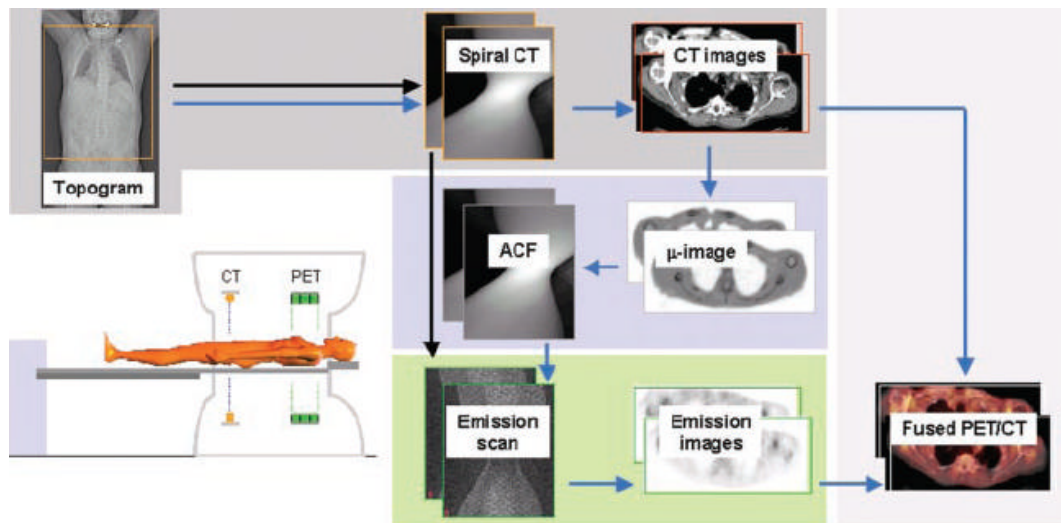


**Fig. 7.** Principle of CT-based attenuation correction method on commercial PET/CT scanners. Reprinted with permission from ref. [31].

*Scaling.* The scaling approach estimates the attenuation image at 511 keV by multiplying the CT image by the ratio of attenuation coefficients of water at CT and PET energies. A single effective energy is chosen to represent the CT spectrum, typically in the range of 50-80 keV [27].

*Segmentation.* This method forms the attenuation image at 511 keV by segmenting the reconstructed CT image into different tissue types. The CT image value for each tissue type is then replaced with appropriate attenuation coefficients at 511 keV. Typical choices for tissue types are soft tissue, bone, and lung [25].

*Hybrid.* This method appears to be the most promising and is based on a combination of the scaling and segmentation methods above using the fact that for most materials except bone, the ratio of the linear attenuation coefficient at any two photon energies is essentially constant [28].

*Piece-wise linear.* In this method, series of CT scans from a known material (e.g.  $K_2HPO_4$  solution) with different concentrations is performed. A calibration curve is then generated in which the measured CT number is plotted against the known attenuation coefficients at 511 keV. The resulting calibration curve is piece-wise linear and covers the range of linear attenuation coefficients commonly encountered in the body. It should be noted that most commercially available PET/CT scanners use the bi-linear calibration curve method [29].

*Dual-energy decomposition.* A technically challenging approach is to acquire the CT image at two different photon energies (e.g. 40 keV and 80 keV) and use these data to extract the individual photoelectric and Compton contributions to linear attenuation coefficients. The different contributions can then be scaled separately in energy [30].

In addition to the energy conversion, there are other issues that must be considered in using CT to generate attenuation maps for correction of emission data. CT fundamentally has a higher spatial resolution and is reconstructed in a finer image matrix than PET. Typically,  $512 \times 512$  CT images can be down-sampled to the same image format (e.g.  $64 \times 64$ ,  $128 \times 128$ ,  $256 \times 256$ ) as that used for reconstruction of PET emission data. CT images also must be smoothed with a Gaussian filter using an appropriate kernel to match the spatial resolution of emission data (Fig. 8) [18].

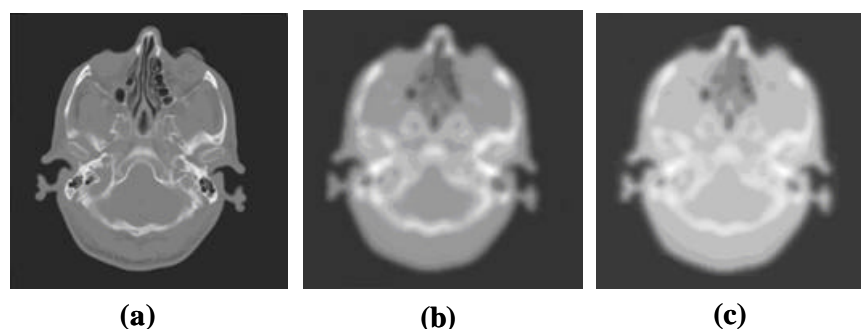


**Fig. 8.** (a) Original CT image acquired at 120 kVp with matrix size  $512 \times 512$ ; (b) the slice in (a) after down-sampling to  $128 \times 128$  and Gaussian smoothing with FWHM=6 mm. (c) Attenuation map of the slice in (b) at 511 keV converted using a bi-linear calibration curve.

### 3. Monte Carlo modelling in medical imaging

Radiation transport using the Monte Carlo method was first used in the 1940s for the design of atomic weapons. Although this technique made a slow entry in the field of medical physics in the 1970s and early 1980s, its applications in medical physics has had a great impact during the last decade with the advent of powerful computers. Nowadays, the Monte Carlo method is widely used for solving problems involving statistical processes and also generation of raw data for testing different correction and reconstruction algorithms in medical physics and biomedical engineering due to the stochastic nature of radiation emission, transport and detection processes [32]. In recent years, there has been an enormous increase and interest in the use of Monte Carlo techniques in the field of medical imaging including conventional and digital diagnostic radiology [33, 34], mammography [35] and x-ray CT [36-38] as well as nuclear imaging techniques including planar imaging [39], SPECT [40], PET [41] and optical coherent tomography [42]. However, due to

computer limitations, the method has not been lived up to its potential. Nevertheless, the increasing number of peer reviewed publications reporting the application of Monte Carlo methods in medical physics for different purposes proves the usefulness of Monte Carlo modelling.

### 3.1. The Monte Carlo method

The Monte Carlo method is a numerical solution to a problem that models an object interacting with other objects or their environment based upon simple object-object or object-environment relationship. It represents an attempt to model nature through direct simulation of the essential dynamics of the system under study. Monte Carlo simulation of radiation transport is considered to be one of the most accurate methods of modelling medical imaging chains of different modalities. The earliest application of the Monte Carlo method to radiation transport was undertaken by Spencer in 1948 [43] where he investigated the effect of polarization on multiple Compton scattering. Generally, the basic concept of Monte Carlo is to create a model as similar as possible to the real system under study and predict the interactions within the modeled system based on known probabilities of occurrence using random sampling of probability density functions for each event. The primary components of a Monte Carlo simulation method include the following [44]:

(i) *Probability density functions (pdfs)*. The physical system must be described by a set of pdfs. A pdf serves to represent a probability distribution in terms of integrals. Any function that is everywhere non-negative and whose integral from  $-\infty$  to  $+\infty$  is equal to one is a pdf.

(ii) *Random number generator (RNG)*. A source of random numbers uniformly distributed on the unit interval must be available. Most RNGs used in practice are based on mathematical formulations with extremely long periods and thus are repeatable. As such, the generated numbers are just pseudo-random.

(iii) *Sampling rules*. A prescription for sampling from the quantities of interest. The simplest sampling rule for particle transport problems is analog sampling which uses the natural probabilities governing various events occurrence. Particles are followed from event to event and the next event is always sampled (using the RNG) from a number of possible next events according to the natural event probabilities. This is called analog sampling because it is directly analogous to the naturally occurring transport. A non-analog sampling attempts to follow interesting particles more often than uninteresting ones. An interesting particle is one that contributes a large amount to the quantity (or quantities) that needs to be estimated. A non-analog sampling technique will have the same expected tallies as an analog technique if the expected weight executing any given random walk is preserved.

(iv) *Scoring*. The outcomes must be accumulated into overall tallies or scores for the quantities of interest.

(v) *Error estimation*. An estimate of the statistical error (variance) as a function of the number of trials and other quantities must be determined. The estimated relative error can be used to form confidence intervals about the estimated mean, allowing one to make a statement about what the true result is.

(vi) *Variance reduction techniques*. Methods for reducing the variance in the estimated solution to reduce the computational time of Monte Carlo simulations. Generally, there are four classes of variance reduction techniques ranging from the trivial to the most advanced methods: truncation

methods, population control methods, modified sampling methods and partially deterministic methods. When variance reduction techniques are used correctly, the efficiency of Monte Carlo calculations can increase significantly.

(vii) *Parallelization and vectorization algorithms*. This allows Monte Carlo methods to be implemented efficiently on sophisticated computer architectures.

An overview of the fundamentals of Monte Carlo techniques and their applications in medical physics and nuclear medical imaging can be found in [44, 45].

### 3.2. Monte Carlo computer codes used in this study

With the advent of powerful computers and parallel processing including Grid technology, the use of Monte Carlo techniques for radiation transport simulation has become the most popular method for modelling different medical imaging modalities. Several Monte Carlo programs including general purpose and dedicated codes have been developed for use in the field of medical physics, with many of them available in the public domain. Table 2 lists some of the general purpose and dedicated Monte Carlo codes used in the field of medical imaging together with a short description of their key features. In this study, our developed MCNP4C-based Monte Carlo x-ray simulator [37] for modelling both fan- and cone-beam CT scanners and the *Eidolon* dedicated 3D PET Monte Carlo simulator [41] were used to generate realigned PET/CT data sets. In the following, a short description of MCNP4C and *Eidolon* Monte Carlo computer codes is presented.

#### 3.2.1. The MCNP version 4C (MCNP4C) code

MCNP is a general purpose Monte Carlo code that can be used for neutron, photon, and electron or coupled neutron/photon/electron transport. It treats an arbitrary 3D configuration of materials in geometric cells bounded by first and second degree surfaces and fourth degree elliptical tori. For photons, the code takes account of incoherent and coherent scattering, the possibility of fluorescent emission after photoelectric absorption, absorption in pair production with local emission of annihilation radiation and bremsstrahlung production. The photoelectric cross sections are based on Storm & Israel [46] whereas the scattering cross sections are taken from ENDF tabulations [47]. A continuous slowing down model is used for electron transport that includes positrons, K-shell x-rays, and bremsstrahlung but does not include external or self induced fields. To follow an electron through a significant energy loss, the MCNP code breaks the electron's path into many steps. These steps are chosen to be long enough to encompass many collisions (so that multiple scattering theories are valid) but short enough so that the mean energy loss in any one step is small (so that the approximations necessary for multiple scattering theories are satisfied). Except for the energy loss and straggling calculation, the detailed simulation of the electron history takes place in the sampling of the substeps. The Goudsmit-Saunders theory is used to sample from the distribution of angular deflections, so that the direction of the electron can change at the end of each substep. For electron transport, MCNP addresses the sampling of bremsstrahlung photons at each electron substep. The table of production probabilities is used to determine whether a bremsstrahlung photon will be created [48]. To improve the efficiency of electron and photon transport, two cards (PHYS:P and PHYS:E) are implemented in MCNP for biasing some physical parameters such as production of secondary electrons by photons (IDES), coherent scattering (NOCOH), bremsstrahlung angular distribution (IBAD) and production of characteristic x-rays (XNUM). The default value for the latter (XNUM = 1) results in the analog number of tracks being sampled. If XNUM > 0, the number of photons produced is XNUM times the number that

would be produced in the analog case, and a corresponding weight adjustment is made. Setting XNUM to zero turns off the production of x-ray photons by electrons.

**Table 2.** Key features of some Monte Carlo codes used in medical imaging.

MC code	General description	Language
MCNP [49]/ MCNPX [50]	General purpose code. Coupled neutrons/photons/electrons transport in any material through user generalized geometry. Simulation of imaging systems not specifically included.	FORTRAN
EGS4 [51]/ EGSnrc [52]	General purpose code. Coupled photons/electrons transport in any material through user specified geometry. Simulation of imaging systems not specifically included. EGSnrc is an extended and improved version of EGS4.	MORTRAN
ITS [53]	General purpose code. Coupled photons/electrons transport in any material through user specified geometry. Simulation of imaging systems not specifically included.	FORTRAN
GEANT [54]	General purpose code. Coupled photons/electrons transport in any material through user specified geometry. Simulation of imaging systems not specifically included.	FORTRAN/C++
PENELOPE [55]	General purpose code. Coupled photons/electrons transport in any material through user specified geometry. Simulation of imaging systems not specifically included.	FORTRAN
FLUKA [56]	General purpose code. Coupled photons/electrons transport in any material through user specified geometry. Simulation of imaging systems not specifically included.	C/C++
ROSI [57]	EGS4-based MC package for simulation of x-ray imaging systems. The user interface of ROSI can be used for creation of simulation geometry. Simple predefined shape-based phantoms are available in the code.	C++
ViPRIS [34]	EGSnrc-based MC package for radiographic image optimization. The VIP-Man phantom has been implemented in this computer program as a voxelized phantoms.	MATLAB
Unnamed [58]	MC software package for x-ray imaging simulation. Photons transport in any material through shape- and voxel-based phantom.	C
MASTOS [59]	MC software package as mammography simulation tool for design optimization studies. Photons transport in any material through shape-based phantoms.	Unknown
MCMIS [60]	MC code for simulation of digital mammography systems. Photons transport in any material through shape-based phantoms.	Unknown
AMCS [36]	Accelerated MC simulator of small-animal micro-CT scanner. Photons transport in any material through shape- and voxel-based phantoms.	Unknown
CTmod [61]	A toolkit for MC simulation of CT scanners. Photons transport inside simple phantoms for cone-beam single-row detector configuration.	Unknown
Unnamed [37]	MCNP4C-based MC simulator for fan- and cone-beam x-ray CT. The GUI includes several shape- and voxel-based phantoms and x-ray spectra database.	MATLAB
SIMSET [62]	MC simulator for SPECT and PET imaging systems. Photons transport in material through voxel-based phantoms.	C
SIMIND [40]	MC simulator for SPECT imaging systems. Photons transport in any material through voxel-based phantoms.	FORTRAN
SIMSPECT [63]	MCNP-based MC simulator for SPECT imaging systems in shape- and voxel-based phantoms.	FORTRAN/C
MCMATV [64]	MC simulator for SPECT imaging systems. Photons transport in material through voxel-based phantoms.	FORTRAN
PETSIM [65]	MC simulator for PET imaging systems. Photons transport in material through shape-based phantoms.	FORTRAN
EIDOLON [41]	MC simulator for PET imaging systems. Photons transport in any material through shape- and voxel-based phantoms.	Objective-C
PET-EGS [66]	EGS4-based MC simulator for PET imaging systems in shape- and voxel-based phantoms.	FORTRAN/C
Unnamed [67]	MC simulator for SPECT imaging systems. Photons transport in material through shape-based phantoms.	FORTRAN/C
GATE [68]	GEANT4-based simulator for SPECT and PET imaging systems in shape- and voxel-based phantoms.	C++
PET-SORTEO [69]	MC simulator for PET imaging systems. Photons transport in any material through shape- and voxel-based phantoms.	C

In the first step of using MCNP code, the user should create an input file which contains information about the problem such as geometry specification, description of materials, and type of answer or tally and variance reduction techniques to be used. The geometry of MCNP treats an arbitrary three-dimensional configuration in Cartesian coordinate system. The number of cells in this code should be less than  $10^5$ . If this limit is exceeded when using the cell geometry, the lattice geometry should be used. The lattice uses a smaller number of cells but adds somewhat to the MCNP execution time. Important standard features that make MCNP very versatile and easy to use include a powerful general source and surface source, both geometry and output tally plotters, a rich collection of variance reduction techniques, a flexible tally structure and an extensive collection of cross-section data. For the purpose of decreasing computation time, MCNP takes advantage of parallel computer architectures. It is supported in multitasking mode on some mainframes and in multiprocessing mode on a cluster of workstations where distributed processing uses the Parallel Virtual Machine (PVM) software [49].

### 3.2.2. The *Eidolon* program

This program has been developed using modern software engineering techniques mainly for fully 3D PET imaging. The code has been written in Objective-C, an object oriented programming language based on ANSI C. The user interface allows the user to select scanner parameters such as the number of detector rings, detector material and sizes, energy discrimination thresholds and detector energy resolution (Fig. 9). It also allows choosing either a complex anthropomorphic phantom or a set of simple 3D shapes, such as parallelepiped, ellipsoid or cylinders for the annihilation sources and the scattering media, as well as their respective activity concentrations and chemical compositions. The model assumes a cylindrical array of detector crystals and known spatial distribution of annihilation sources and scatter phantoms. Radial samples are assumed to be equidistant, although ring curvature can be taken into account for sampling. Pairs of annihilation photons are generated uniformly within the source objects; they are tracked until extermination of their history either by interacting with scatter or detector objects, or by escaping the positron tomography geometry and field of view. Positron range, photon non-collinearity and effect of Anger logic have been included in the code. Photoelectric absorption as well as incoherent and coherent scattering are taken into account to simulate photon interaction with scatter and detector objects. Interaction cross-sections and scattering distributions are computed from parameterizations implemented in the GEANT simulation package or in the form of look-up table from more recent photon interaction libraries [70]. The Klein-Nishina angular distribution is used to sample the direction of the Compton scattered photons. The Marsaglia algorithm has been used to generate uniformly distributed pseudorandom numbers. Interaction within the scatter or detector objects can be switched on and off. In cases, interaction within detector objects is switch off, any photon impinging on the detector is assumed to deposit all its energy in the detector crystal. In other case, photon pairs are recorded once two photons resulting from one annihilation event have passed the energy window set for discrimination. Random coincidences are not simulated. The user has the possibility to view the reference source image and sinogram data set as they are generated and are periodically updated [41]. An implementation of the software on a high performance parallel platform was also reported [71]. Experimental and/or clinical validation of the *Eidolon* has been described in [41, 72].

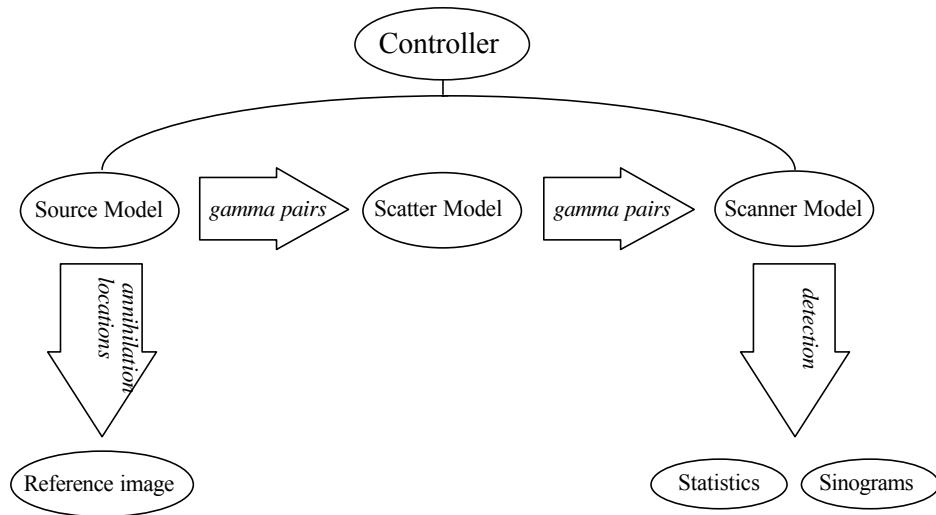


**Fig. 9.** A flow diagram showing the main components of *Eidolon* Monte Carlo simulator. Reprinted with permission from ref [41].

### 3.3. Applications of the Monte Carlo method in medical imaging

Monte Carlo methods have become the most popular tools for the investigation of different design parameters and correction schemes in medical imaging. MC calculations can be used to quantify the impact of different physical design parameters on overall imaging system performance and clinical image quality that can be difficult or even impossible to calculate by experimental measurements and theoretical analysis. In recent years, there has been an enormous increase and interest in the use of Monte Carlo techniques in the field of medical imaging. Recent nuclear medicine imaging innovations such as SPECT and PET as well as dual-modality imaging systems (PET/CT and SPECT/CT) are ideal for MC modelling because of the stochastic nature of radiation emission, transport and detection processes. Today's applications of MC techniques in the field of nuclear medicine imaging include detector modelling, optimization of imaging systems and collimator design and development, evaluation of image reconstruction and attenuation and scatter correction techniques [32]. MC simulation of detector response and efficiencies as function of detector material and geometry is one of the areas which has received considerable attention [73]. Design optimization and assessment of the impact of different physical factors on SPECT and PET systems performance using MC modelling is another active research area in nuclear medicine [74]. MC techniques have been extensively used for collimator design and assessment of their performance through calculation of sensitivity and spatial resolution trade-off [75]. MC simulations can be used for validation and evaluation of image reconstruction algorithms owing to the fact that it is possible to generate artefact-free raw data sets [76]. Another promising application of MC calculations in nuclear medicine imaging is quantification, validation and comparative evaluation of correction algorithms for attenuation and scatter corrections [77].

The application of Monte Carlo modelling in radiological imaging research including diagnostic radiology, mammography, angiography and computed tomography is an everlasting enthusiastic topic and still is an area of considerable interest. X-ray tube design and development of new target/filter combinations to improve image quality in radiological imaging using MC calculations is an active research area [78, 79]. The quantification of the impact of scattered radiation on image quality [80, 81] and evaluation of scatter removal strategies including

antiscatter grid design in radiology and optimization of septa length in CT is another application of MC modelling in radiological imaging [33, 82]. Monte Carlo simulators dedicated to radiological imaging (table 2) are powerful tools for evaluation of the effect of physical, geometrical and other design parameters on overall radiological imaging performance and resulting image quality [35, 61, 83-85]. Such programs could be used for detailed analysis of various parameters of the imaging chain in a controllable way, which is usually difficult or impossible to perform experimentally. Scattered radiation characterization is one such example. Monte Carlo modelling of detection systems including optimization of detector material and size, calculation of detection quantum efficiency and dynamic range, quantification of geometrical distortion and evaluation of detector response remain active areas of research and there are many relevant contributions to this domain [86, 87].

## 4. Analytical and Monte Carlo x-ray spectra modelling

A detailed knowledge of the x-ray spectra is necessary for mathematical modelling and design optimization of radiological imaging systems in general and x-ray CT in particular. However, the direct measurement of spectra required expensive equipment and careful attention and planning during the experimental measurement setup. Since direct measurement of x-ray spectra is time consuming and remains a difficult task, early attempts for computer modelling of x-ray spectra have begun several decades ago and still represent an active research area. Generally, x-ray prediction models in diagnostic radiology and mammography energy ranges can be divided into three main categories: empirical, semi-empirical and Monte Carlo. In this section, a brief overview of different computational models for generation of x-ray spectra is presented. Detailed information about the fundamentals of x-ray spectra modelling and available computer programs for generation of x-ray spectra are described in ref. [88].

### 4.1. Analytical models

Early attempts for analytical prediction of diagnostic x-ray spectra were pioneered by Kramers in 1923 [89]. This original work was sustained by several investigators and research groups and still is regarded as a worthwhile research topic. Generally, the analytical x-ray prediction models in diagnostic energy range can be divided in two categories: empirical and semi-empirical models.

#### 4.1.1. Empirical models

Empirical models are based on the use of experimentally measured data for development of models allowing the prediction of x-ray spectra. Early attempts based on using measured data relied on the reconstruction of x-ray spectra from transmission data [90]. He suggested that the x-ray spectra could be determined from transmission measurements using simple equipment consisting of only an exposure meter and some filters. The inherent simplicity of this method compared to more rigorous experimental measurements requiring expensive spectrometers and careful attention for direct measurement of x-ray spectra attracted the interest of many investigators. During the last three decades, several groups have begun to approach a satisfactory solution for reconstruction of x-ray spectra from measured transmission data using the Laplace transform, iterative methods, direct matrix inversion and neural networks [88]. Another empirical model based on interpolating polynomials was proposed by Boone *et al.* for generation of x-ray spectra in both diagnostic radiology [91] and mammography [92] energy ranges. These models are based on the use of measured results and a mathematical model for interpolating x-ray spectra.

### 4.1.2. Semi-empirical models

Semi-empirical models are based on quantum mechanics theory of bremsstrahlung x-ray production [93, 94] implemented by mathematical derivation followed by some tuning in the equations' parameters using measured spectra. The bremsstrahlung x-ray spectra in these models can be calculated by solving the mathematical expressions that depends to several factors such as anode's material, energy of electrons and the angle that electrons hit the anode. The earliest theoretical model of differential intensity of bremsstrahlung x-rays based on thick-target theory was introduced by Kramers [89]. This model was used extensively to calculate thick-target spectra even if it neglected electron backscatter and photon attenuation losses in target. This model was first modified to include target attenuation by Soole [95] and again by Birch and Marshal [93] to generate x-ray spectra that more closely matched experimental results. They used Green's formulation [96] with some modifications based on experimental measurements for predicting characteristic x-rays intensity. The contribution of electron backscatter from the target was included in this model by Iles [94]. Tucker *et al.* [97] modified the latter model by incorporating appropriate modelling to take into account the fact that x-rays are produced in different depths in the target depending on the incoming electron's energy. Moreover, they used Vignes and Dez [98] approach to estimate more accurately characteristic x-rays intensity. In parallel to the thick-target theory, the thin-target bremsstrahlung theory introduced by Sommerfeld [99] was corrected by Strom [100] for electron energy losses, electron backscatter losses and photon attenuation to obtain thick-target bremsstrahlung distribution comparable to measured spectra.

### 4.2. Monte Carlo modelling

Monte Carlo-based calculations of x-ray spectra use direct transport of electrons and generated photons in the target and filter. The use of the Monte Carlo method to simulate radiation and charged particles transport has become the most accurate method for prediction of x-ray spectra owing to the more accurate physics modelling and incorporation of appropriate cross section data [44]. Berger and Seltzer [101] developed the first Monte Carlo program for calculating bremsstrahlung spectra which included electron and photon multiple scattering. Their calculation for normal incidence of the electron beam on the target was in good agreement with measured data published by Placious [102]. The next Monte Carlo study for generation of x-ray spectra in diagnostic and therapeutic energy ranges was performed by Sundararaman *et al.* [103] based on the theoretical formulation of electron transport proposed by Berger in 1963 [104]. The comparison between their results and the spectra generated using Kramers's theory [89] showed good agreement for low tube voltages, but moderate agreement for high tube voltages especially at the spectral peak and near the K absorption edge [105]. The spectra calculated using the Monte Carlo method by Reiss and Steinle [106] in diagnostic energy range had excellent agreement with measured spectra. The Monte Carlo approach used for generation of x-ray spectra by Morin and Raeside [107] differed from the previous techniques in the sense that it relied on repeated sampling of an analytical photon energy intensity based on Kramer's theory [89] for generation of bremsstrahlung x-rays and thereafter adding the characteristic x-rays calculated by Raeside [105]. Early contributions to Monte Carlo generation of x-ray spectra for mammographic energy range were undertaken by Kulkarni and Supe [108] to simulate x-ray tubes equipped with molybdenum and tungsten targets. The advent of parallel computers and current generation PCs in the GHz range combined with the availability of high performance Monte Carlo codes in addition to the popularity of variance reduction techniques spurred the use of general purpose codes for the generation of x-ray spectra. Various general purpose codes including EGS4 [109], MCNP [78], ITS [110], PENELOPE [111] and GEANT [112] have been used by investigators to generate x-ray spectra in diagnostic and therapeutic energy range. A detailed description of the developed model

for Monte Carlo simulations of x-ray spectra using MCNP4C general purpose computer code is presented in **Paper I**.

### 4.3. Assessment of computational models

The aforementioned models for generation of x-ray spectra do not predict the same bremsstrahlung x-ray energy distribution and characteristic x-rays even for the same setup such as tube voltage, anode angle, filter thickness and material owing to the difference between the mathematical and physical formulations used. Although the x-ray spectra generated using the different models were individually validated against measured spectra using equipment available in the authors' labs, it is worth to compare the spectra generated using different models with similar widely distributed experimental spectra. The comparative assessment could be an asset to assess the impact of using one model or another on the outcome of complex simulation studies targeting imaging system performance or dosimetry. A few publications addressed the issue of comparing different computational models for generation of x-ray spectra [109, 110, 113-118]. Model validation and the strategy for comparative assessment of different computational models relies on rigorous selection of appropriate criteria and figures of merit such as spectra shape, attenuation curves (transmission data), half value layer (HVL), K x-ray yield, and imparted dose.

The spectra shape is the best parameter for qualitative visual assessment of potential differences between two spectra owing to the fact that it includes bremsstrahlung and characteristic x-rays. The quantitative evaluation of the differences between two spectra can be estimated through the root mean square difference (RMSD) or other statistical tests such as student's *t*-test or Chi-square. Attenuation curves (transmission data) and HVLs are standard indices of x-ray beam quality. The K x-ray yield indicates the contribution of characteristic x-rays to the spectra. Calculation of imparted dose estimates the impact of using spectra generated by different computational models on the outcome of dosimetry calculations. In addition to the aforementioned parameters used for comparative assessment of different computational models, the flexibility and robustness of each model with respect to generating the desired spectrum for a variety of parameters such as target material, target angle, additional filter, tube voltage ripple and energy bin should be considered. Empirical models are inherently limited in terms of target angle and filter material as well as tube voltage ripple in mammography energy range. Although semi-empirical models are more flexible compared to empirical models, they are generally limited to specific target materials, particular sets or combinations of additional filters and voltage ripples. Notwithstanding, there is no theoretical limitation for predicting x-ray spectra for the different parameters mentioned above using the Monte Carlo method, computer proficiency and computational time remain the challenges for widespread application of Monte Carlo simulations. The x-ray spectra generated by various computational models used in diagnostic radiology and mammography energy range have been assessed by comparison with measured data in **Paper II**.

### 4.4. Relevance of x-ray spectra modelling in clinical and research settings

Computer simulation of x-ray spectra is one the most important parts of simulation studies associated with radiation dose assessment, image quality optimization and imaging system design in the field of radiological sciences. The x-ray spectrum shape and quality strongly influence the dose distribution pattern, image quality and detector response. Thus, accurate simulation studies rely on accurate modelling of x-ray spectra. X-ray spectra modelling has been used extensively in many dosimetry and imaging simulation studies in the field of x-ray CT [87, 119] and

conventional radiology [120]. Moreover, the issue of grid performance assessment and design optimization based on computer simulation in diagnostic radiology and mammography is highly dependent on accurate x-ray spectra modelling [121]. Likewise, Monte Carlo calculation of absorbed dose as a function of target/filter combination, tube voltage and grid parameters is another active research area in radiological imaging that requires accurate x-ray spectra modelling [115, 119]. Generally, the application of x-ray spectra modelling in medical physics and particularly in radiological imaging is an everlasting enthusiastic and an area of considerable research interest.

## 5. Development and validation of an x-ray CT simulator

### 5.1. Motivations

Accurate and efficient simulation of x-ray CT scanners plays an important role in research studies. There are several sources of error and artefacts that affect clinical x-ray CT image quality. The assessment of their effect on image quality is generally commended with the aim to reduce their impact either by optimization of scanners' design or by devising appropriate image correction and reconstruction strategies. It has long been recognized that the ideal research tool for x-ray CT modelling is the Monte Carlo method. Though, to the best of our knowledge, at the time of this study, there exist only two dedicated MC-based CT simulator which can be used for the purpose of imaging chain modelling. The first is the accelerated Monte Carlo simulator (AMCS) which is a rapid MC-based micro-CT simulator dedicated for modelling of cone-beam small animal x-ray CT scanners [36]. Another MC x-ray CT simulator is *CTmod* which was used for simulation of single-slice detector configuration and has been used mainly for scatter modelling in the cone-beam geometry [61]. Both simulators have some limitations. In addition, their validation was limited to a specific geometry and the code is not general enough to extend its application to other geometries. The need to characterize quantitatively the effect of physical and physiological parameters such as contribution of scattered photons, tube voltage, tube current, contrast agent and metallic implants on CT-based attenuation correction in this study spurred the development of an MCNP4C-based x-ray CT Monte Carlo simulator, which allows simulating fan- and cone-beam CT scanner geometries with single-slice, multi-slice and flat-panel detector configurations. Detailed information about the development and validation of our MCNP4C-based x-ray CT simulator is presented in **Paper III**.

### 5.2. Development strategy

To use the advantages offered by extensively tested state-of-the-art general-purpose Monte Carlo codes in terms of versatility, published reports and long-term technical support and maintenance, our developed x-ray CT simulator was built on top of the MCNP4C general-purpose MC computer code, which serves as a core layer giving the opportunity to the developer to construct application-specific modules in a hierarchical architecture. Detailed MC radiation transport into the x-ray tube, bow-tie filter, collimator, phantom and detector is performed using MCNP4C with appropriate adjustment of physics treatment options implemented into the code.

In the first step of using MCNP4C code, the user should create an input file which contains information about the problem such as geometry specification, description of materials, type of answer or tally and variance reduction techniques to be used. The creation of input file in the

MCNP4C code using first and second degree surfaces is not an easy task, especially when dealing with the complex geometries typical of an x-ray CT scanner requiring an extremely large number of planes to create detector cells and septa. To solve this problem, a user interface program running under Matlab 6.5.1 (The MathWorks Inc., Natick, MA, USA) was developed by an easy to use concept. Basically, the user is asked to choose the x-ray CT scanner's design parameters. According to the information provided by the user, the interface program creates the scanner geometry as input file for MCNP4C. Since MCNP4C is not able to simulate gantry rotation, the geometry of each view is created in separate files and run sequentially [37]. After simulation of all views, the sinogram is created from detector outputs after blank scan correction in all views by the user interface program. The filtered back-projection reconstruction algorithm [122] has been implemented in the user interface program for image reconstruction of simulated data sets. Many other quantities such as absorbed dose, individual scatter and primary profiles can be also extracted from the created output file for each view. Figure 10 illustrate the principles and main components of the MCNP4C-based simulator as applied to model an x-ray CT imaging system.

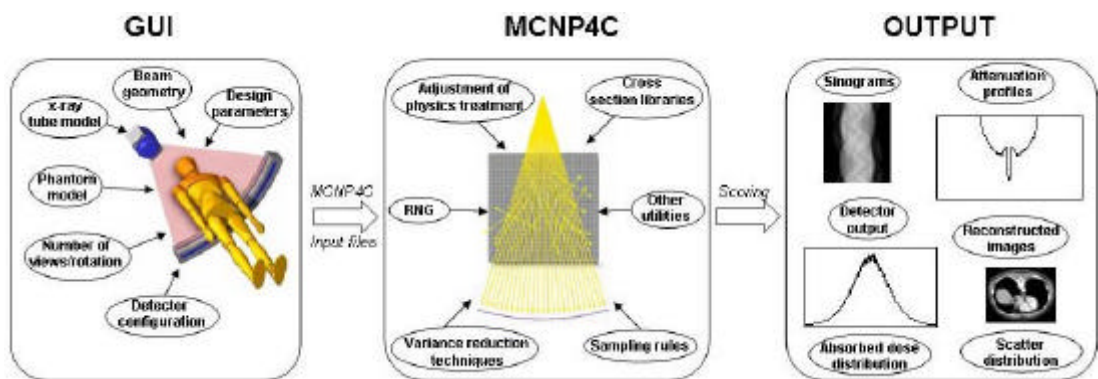


**Fig. 10.** Principles and main components of MCNP4C-based Monte Carlo program dedicated for simulation of x-ray CT imaging systems.

### 5.3. Experimental validation

Generally, before Monte Carlo simulated data can be trusted, the simulation model must be validated. According to the definition of the international standard on quality management systems (ISO 9000), validation is *“the confirmation through the provision of objective evidence that the requirements for a specific intended use or application have been fulfilled”*. Therefore different intended uses require different validation studies. We will first discuss the intended use of the MC model which underlines this validation study. In the validation study described in this work (**Paper III**), the intended use of the MC model is the assessment and quantification of the impact of different physical parameters on x-ray CT image quality and its propagation to CT-based attenuation correction in PET. The validity of the MCNP4C-based Monte Carlo simulator was verified by comparing the simulated and measured distributions from various uniform and non-uniform phantoms on both fan- and cone-beam x-ray CT scanners. The single-slice GE HiSpeed X/iF (General Electric Healthcare Technologies, Waukesha, WI, USA) fan-beam CT scanner and the cone-beam small-animal SkyScan 1076 (SkyScan, Aartselaar, Belgium) with flat-panel detector were used for experimental measurements. Good agreement between the simulated and measured projections and reconstructed images was observed.

After the experimental validation study, we concluded that the developed x-ray CT simulator is a powerful tool for evaluating the effect of physical, geometrical and other design parameters on

the performance of new generation CT scanners and image quality in addition to offering a versatile tool for optimizing the absorbed dose to patients and investigating potential artefacts and optimal correction schemes when using CT-based attenuation correction on dual-modality PET/CT units [5] in connection with ongoing research in our lab related to PET quantification using a dedicated PET Monte Carlo simulator [41].

#### **5.4. Applications of the MC x-ray CT simulator**

Today's applications of MC techniques in the field of x-ray CT imaging include performance assessment and optimization of design geometries and scanning parameters [37], scatter characterization and rejection strategies [38, 61], detector configuration and material [87], generation of data sets for testing reconstruction and beam hardening correction algorithms [123, 124] and absorbed dose calculations to assess radiobiological risk from CT scans. For the latter, the accuracy of MC simulations is well established for both axial [115] and spiral [125] scanning modes.

With the advent of multiple-row and flat-panel detector configurations in addition to the slip-ring technology, there have been rapid developments in the design of clinical and small-animal CT scanners including: x-ray tube specifications, geometrical magnification, detector configuration and dose management. MC simulations offer many advantages including the possibility of optimizing tube design, development of new target/filter combinations and calculation of off-axis spectra to improve image quality and reduce patient dose [78]. The optimization of geometrical magnification in x-ray CT, which depends on the source to detector and iso-center distance, is another application of Monte Carlo CT simulators. The optimal detector's element material and size, which depends on the balance between image resolution, patient dose and signal to noise ratio is another active research area where MC modelling plays an important role.

The corruption of projection data in x-ray CT with scattered radiation decreases low contrast detectability, reduces CT numbers and introduces cupping and streak artefacts in reconstructed images. Scatter removal is also mandatory in x-ray CT imaging because of the need to have clinically acceptable low contrast detectability. The assessment of the scatter component in fan- and cone-beam x-ray CT scanners is an active research area in quantitative imaging and there are many relevant contributions to this domain [38, 61, 81]. The most common technique used to reduce the detection of scattered radiation consists of using collimator plates inside the detector housing (septa) in multi-slice CT and antiscatter grids in flat-panel cone-beam CT scanners. The optimization of septa length and thickness (namely geometrical efficiency of detection system) as well as septa material is also being investigated through assessment of resulting scatter-to-primary ratio (SPR) using MC calculations. It has been shown that increasing the septa length could effectively reduce the contribution of scattered radiation, thus decreasing the SPR at the expense of more manufacturing constraint to avoid possible septa plates' vibration during the gantry rotation [37].

Analytical models for generation of transmission x-ray projections for testing image reconstruction and beam hardening correction algorithms can be used with some confidence for simple geometries and homogeneous objects; however, their application to more complex geometries and nonhomogeneous objects is complicated and prone to error. A more general and accurate approach for generation of data sets is to use MC simulations by paying special attention to the number of simulated events to reduce statistical uncertainties in the generated data sets.

## 6. Sources of error and artefact in CT-based attenuation correction

PET/CT systems offer significant advantages over stand alone PET including decreased overall scanning time and increased accuracy in tumour localization and detectability [5]. However, the use of CT images for attenuation correction of PET data is known to generate visible artefacts in the resulting PET images in some cases [18]. Commercial, CT reconstruction algorithms cannot account for the presence of metal implants, such as dental fillings or prostheses properly. This results in streak artefacts, which are propagated into PET images by the attenuation correction process [126-128]. The transformation of attenuation coefficients at x-ray energies to those at 511 keV works well for soft tissues, bone, and air, but not for dense CT contrast agents such as iodine or barium [129-131]. Mismatches due to uncoordinated respiration as well as patient movement result in incorrect attenuation-corrected PET images [132]. Truncation artefacts due to limited CT field-of-view are frequently observed in PET/CT imaging of large patients [31]. These artefacts, however, can be minimized or avoided by careful acquisition protocols or appropriate correction schemes [133]. In the following, an overview of different sources of error and artefact in CT-based attenuation correction is presented. Detailed assessment of some of these errors and artefacts are addressed in **Papers IV and V**.

### 6.1. Misalignment between PET and CT images

The advent of hybrid PET/CT systems has simplified image registration since the PET and CT data sets are collected sequentially on the same system without the need for the patient to move to another scanner. This removes the image registration problem induced by different patient set-up positions. Once the CT scan is complete, the patient couch is moved further into the gantry to commence the PET scan. The two data sets can be considered to be inherently registered; just the distance between the PET and CT positions needs to be taken into account. Generally, there are two registration issues that must be considered; first the misalignment of CT and PET modules during the installation of the PET/CT scanner owing to the fact that current PET/CT systems consists of individual PET and CT systems adjacent to one another. Second, is the flex of patient couch. As the couch is moved into the gantry toward the PET module after CT scanning, more of the patient's weight is taken by part of the couch that is unsupported by the base. For accurate image registration it is important that the degree of couch flex does not change as the patient is moved from CT to PET acquisition position. This would cause registration problems in PET/CT. More recently with the advent of pedestal/couch design configurations the degree of flex keeps constant regardless of how far the couch is moved into the gantry. This ensures that the vertical position of the patient is the same for the CT and PET acquisitions [134].

### 6.2. Patient and respiratory motion

Mismatches between CT and PET images due to the physiological motion (respiratory motion) as well as patient movement have been described as a source of potential artefacts of PET emission images obtained using CT-based attenuation correction [17]. Most of patient movement and positioning errors in PET/CT examinations may be overcome using immobilization tools [133]. Respiratory artefacts are particularly severe when standard breath-hold techniques with maximum inspiration are transferred directly from clinical CT standalone protocols to combined PET/CT without future adaptation. These artefacts are caused by the mismatches of anatomy of thoracic and abdominal organs at maximum inspiration in CT images versus the anatomy when averaging

over many respiratory cycles during the PET study [31]. Goerres *et al.* [135] have compared the accuracy of PET/CT image alignment in the thorax and abdomen. They reported normal expiration and free breathing to provide the best match in the thorax area in 53% and 23% of patients, respectively. The PET and CT alignment in the abdominal area was satisfactory in both protocols [136]. In the absence of available respiratory gating options, if the respiratory commands are not adequately followed by the patient, the reconstruction of emission data without attenuation correction is suggested [133].

### 6.3. Truncation

During CT imaging of obese patients and patients with their arms down, part of the anatomy may extend beyond the boundaries of the CT field of view (50 cm) and is not reconstructed in CT. This truncation artefact will propagate errors to the CT-based attenuation correction which is based on fully reconstructed CT images including all anatomies which appears in PET images. In the presence of truncation errors in CT images, the reconstructed emission images appear to be masked by the truncated CT. The tracer distribution is then only partially recovered outside the CT field of view as some bias of the reconstructed activity distribution inside the field of view is observed. There are two approaches for truncation artefact correction. In the software approach, several algorithms have been suggested to extend the truncated CT projections to recover truncated parts of the attenuation map [137]. In the hardware approach, most manufacturers offer PET/CT scanners with a patient port of 70 cm for both PET and CT modules to avoid truncation of CT images for most of the patients even with arms in down position [7].

### 6.4. Beam hardening and x-ray scattered radiation

The polyenergetic x-ray spectra used during CT imaging makes it subject to beam hardening artefact caused by the absorption of low energy x-rays as they pass through the patient's body. The direct consequence is that the linear attenuation coefficient calculated for thick body regions is lower than thin regions. This effect generates cupping and streak artefact in the reconstructed CT image and makes it not acceptable for diagnostic purposes. Furthermore, the resulting erroneous CT-based attenuation correction subsequently propagates the error to the calculated activity concentration in PET images [133]. Although beam hardening effect correction algorithms [138] implemented as part of CT reconstruction software, this effect is still visible when having the patient's arms in the field-of-view or for obese patients during CT scanning using standard whole-body PET/CT protocols [133].

The contamination of CT data with scattered radiation reduces reconstructed CT numbers and introduces cupping artefacts in the reconstructed images. This effect is more pronounced in next generation of CT scanners with large area flat-panel detector that seems to be candidates as CT module in next generation of PET/CT scanners with panel-based PET module [7]. The assessment of the impact of scattered radiation in both fan-beam (multi-slice) and cone-beam (flat-panel) CT images on the accuracy of CT-based attenuation correction is addressed in **Paper IV**.

### 6.5. Presence of contrast medium

Although diagnostic quality CT relies on the administration of oral or intravenous contrast agents to allow improved lesion delineation, the presence of positive contrast agents in dual-modality

PET/CT systems significantly overestimates the attenuation map in some cases and may generate artefacts during CTAC [129-131]. This is due to the high attenuation coefficient of these materials at the low effective energy of the corresponding x-ray spectra which results in high CT numbers in the region of contrast agent accumulation through misclassification with high density cortical bone [139]. Currently available algorithms for conversion from CT numbers to linear attenuation coefficients at 511 keV are based on the assumption that image contrast in the CT data is contributed by mixtures of air, soft tissue, and bone [29]. The presence of contrast medium complicates this process since two regions that have the same image contrast may indeed have different compositions, for example contributed by bone and soft tissue in one case and iodine/barium contrast and soft-tissue in another situation [5]. These artefacts are most severe in cases where the contrast media is concentrated, for example in abdominal imaging after the patient swallows a bolus of oral contrast. In this case, the higher densities contributed by the oral contrast media can lead to an overestimation of PET activity [18]. The in-depth analysis of the effect of contrast medium on CTAC method is presented in **Paper IV**.

## 6.6. Presence of metallic implants

Some candidate patients for PET/CT imaging have artificial metallic implants, such as artificial joints, metal braces in the spine, chemotherapy ports, hip prosthetic material, dental filling, pacemaker and ICD leads. In standard PET transmission scanning with radionuclides, metal implants causes a little or no artefact while these artefact can be significant in CT energies due to the significantly higher x-ray absorption of high-Z materials (e.g. metals) compared to the low-Z materials (e.g. tissues). The presence of streak artefacts caused by metallic implants in CT images may mislead the diagnosis of patients in PET/CT images, particularly when lesions are present in the very vicinity of metallic implants [133]. Several authors addressed the impact of using CTAC on quantitative analysis of PET/CT images in presence of dental metallic implants [126], hip prosthetic material [140], pacemaker and ICD leads [128]. **Paper IV** addresses the effect of metallic leads used in deep brain stimulation (DBS) techniques [141] for the treatment of Parkinson's disease on CTAC.

## 6.7. Impact of tube voltage

In general, the CT number values in CT images are approximately linearly related to the linear attenuation coefficient of the corresponding tissue type. However, it is well known that the CT images do not precisely correspond to a perfect linear attenuation map at a fixed energy due to the use of polyenergetic x-ray spectra. With the introduction of hybrid PET/CT systems in clinical setting, precise conversion from CT numbers derived from low energy polyenergetic x-ray spectra to linear attenuation coefficients (LACs) at 511 keV became essential in order to apply accurate CT-based attenuation correction to the PET data. Most commercially available PET/CT scanners use the bi-linear calibration curve method, which is generally calculated at a preset tube voltage (120-140 kVp). Since patient CT images may be acquired at different tube voltages depending on patient size and region under study and considering the fact that the CT number of a particular tissue is tube voltage dependent, it is hypothesized that the use of a single calibration curve calculated at a specific tube voltage for CT images acquired under different scanning conditions might propagate a significant uncertainty during the quantitative analysis of emission data when PET attenuation correction is based on CT. Bai *et al.* [29] argued that the slope of the bi-linear calibration curve for CT numbers higher than 0 HU is tube voltage dependent. Other studies reported on the relevance of deriving tube voltage dependent CTAC schemes for PET/CT [142].

**Paper V** addresses the impact of using a single calibration curve on the accuracy of CTAC when CT images are acquired in different tube voltages and vice versa, that is, acquiring CT images at standard tube voltages and varying the voltage for derivation of calibration curves.

## 6.8. Impact of tube current

It is well known that a high tube current improves CT image quality at the expense of increasing patient dose. It was reported that effective doses of 8.81 mSv and 18.97 mSv are delivered to the patient for a whole body scan in high-speed and high-quality mode, respectively [143]. This is in contrast to relatively low effective doses of 0.15 mSv and 0.08 mSv for thoracic and whole-body transmission scans using positron emitting  $^{68}\text{Ga}/^{68}\text{Ge}$  and single-photon emitting  $^{137}\text{Cs}$  radionuclide sources, respectively [18]. With the introduction of PET/CT systems, several questions had to be answered, one of them is “to which limit can the CT tube current be reduced while still yielding adequate  $\mu$ maps for attenuation correction of PET data?”. Kamel *et al.* [144] investigated the effect of varying tube current and showed that a low-current CT is sufficient for CTAC using comparative quantitative analysis of reconstructed clinical PET images. Likewise, a new pre-processing algorithm was proposed recently to use a single ultra-low dose CT scan for both attenuation map construction and lesion localization [145]. These topical developments combined with the lack of detailed studies investigating the effect of tube current and voltage on the quantitative analysis of non-clinical PET data where the ground truth is known motivated the work presented in **Paper V**.

## 7. Concluding remarks and future perspectives

From advances in x-ray film and cassettes to the introduction of computers and digital images, diagnostic imaging has never stopped reinventing its technology to improve patient care. Today, diagnostic imaging is one of the cusps of explosive growth in an arena known as dual-modality imaging. This technology melds two independent imaging modalities (PET and CT), typically a procedure that demonstrates an organ’s function and metabolism with one that depicts the organ’s anatomy, to produce a diagnostically and clinically superior study. Until recently, clinicians had to obtain physiological and anatomical information on separate machines and use special registration software to digitally superimpose the two images. Today, new PET/CT dual-modality equipments are capable of performing both types of examinations simultaneously, automatically merging the data to form a composite image. By uniting metabolic function with anatomic form, dual-modality imaging depicts the human body with a level of precision never achieved before. In addition, the use of CT images for CT-based attenuation correction in dual-modality systems allows to decrease the overall scanning time and to create a noise free attenuation map. However, the use of CT images for attenuation correction of PET data is known to generate visible artefacts in the resulting PET images in some cases.

In conclusion, let us review what concrete results have been achieved through the Monte Carlo and experimental assessment of CT-based attenuation correction in this thesis. What the implications of this work are in clinical and research environment, and which direction of future research work arise as its logical consequence.

### 7.1. Key conclusions

Monte Carlo simulation of x-ray spectra has been used extensively in different medical imaging applications including assessment of image quality, optimisation of system design and absorbed dose calculation. Although the simulation of x-ray spectra using the Monte Carlo method is time consuming, the generated x-ray spectra provides detailed information about particles' interaction with different target and filter combinations. This information is useful for x-ray tube design and development of new target/filter combinations to improve image quality in diagnostic x-ray imaging. The results of this study indicated that the MCNP4C general purpose Monte Carlo code with some small adjustment in the appropriate physics treatment cards is a useful tool for generating diagnostic radiology and mammography x-ray spectra and investigation of anode heel effect (**Paper I**).

Different computational methods based on empirical or semi-empirical models and sophisticated Monte Carlo calculations have been proposed for prediction of x-ray spectra both in diagnostic radiology and mammography. In this study, the spectra generated using different computational models were compared with measured spectra. Despite the systematic differences between the simulated and reference spectra for some models, the student's *t*-test and RMSD statistical analysis showed there is no statistically significant difference between measured and generated spectra for all computational models investigated in this study. Nevertheless, given the limited flexibility of the empirical and semi-empirical models, the spectra obtained through Monte Carlo modelling offer several advantages by providing detailed information about the interactions in the target and filters, which is relevant for the design of new target and filter combinations and optimization of radiological imaging protocols (**Paper II**).

Monte Carlo calculations can be used to quantify the impact of different physical design parameters on overall x-ray CT scanner performance and clinical image quality that can be difficult or even impossible to calculate by experimental measurements and theoretical analysis. The results of validation studies proved that our developed MCNP4C-based x-ray CT simulator is a powerful tool for evaluating the effect of physical, geometrical and other design parameters on the performance of new generation CT scanners and image quality in addition to offering a versatile tool for optimizing the absorbed dose to the patients and investigating potential artefacts and optimal correction schemes when using CT-based attenuation correction on dual-modality PET/CT scanners in connection with ongoing research in our lab related to PET quantification using the *Eidolon* PET Monte Carlo simulator (**Paper III**).

Quantitative image reconstruction in PET requires an accurate attenuation map of the object under study for the purpose of attenuation correction. The contamination of CT data with scattered radiation in CT-based attenuation correction is known to generate artefacts in the attenuation map and thus the resulting PET images. The contribution of x-ray scatter in CT images without x-ray scatter compensation during the CTAC procedure was quantified for commercially available multi-slice CT and prototype large area flat-panel detector-based cone-beam CT scanners. It was concluded that the magnitude of scatter in CT images for the cone-beam geometry is significant and might create cupping artefacts in reconstructed PET images during CTAC; however, its effect is small for current generation multi-slice fan-beam CT scanners using septa between detector elements, but should preferably be corrected during CT reconstruction to avoid quantification bias. These results substantiate the important role of antiscatter collimation and robust scatter correction algorithms which certainly will be implemented in future generation flat-panel based PET/CT scanners when used for quantitative measurements (**Paper IV**).

Although diagnostic CT relies on the administration of oral or intravenous contrast agents to allow improved lesion delineation, the presence of positive contrast agents in dual-modality PET/CT systems significantly overestimates the attenuation map in some cases and may generate

artefacts during CTAC. The results of Monte Carlo simulations and experimental measurements in this study showed that contrast-enhanced CT images may create visible artefacts in regions containing high concentrations of contrast medium. It should be noted that this study reports results from a limited set of computer simulations of realistic PET and CT systems combined with experimental measurements using validated techniques (**Paper IV**).

Artefacts in CTAC due to the presence of highly attenuating metallic implants can be associated with an incorrect scale factor when using the common bi-linear calibration curve technique. The impact of metallic DBS leads used for treatment of Parkinson's disease on CTAC was investigated in this study by inserting metallic leads in an appropriate region of the RSD striatal phantom's CT images. It was concluded that metallic leads do not create any visible or quantifiable artefacts in the reconstructed PET images owing to their small size (**Paper IV**).

With the introduction of hybrid PET/CT systems in clinical setting, precise conversion from CT numbers derived from low energy polyenergetic x-ray spectra to linear attenuation coefficients at 511 keV became essential in order to apply accurate CT-based attenuation correction to the PET data. The most common procedure requires a piece-wise linear calibration curve acquired under standard imaging conditions to convert the patient's CT image from low effective CT energy into an attenuation map at 511 keV. One of the aims of this thesis was to evaluate the effect of tube voltage and current on the accuracy of CTAC. It was concluded that firstly, using a single calibration curve derived under standard scanning conditions during the CTAC procedure to images acquired at different tube voltages does not affect significantly the visual qualitative interpretation and quantitative analysis of PET emission images, and secondly, the tube current do not affect the accuracy of CTAC procedure to a visible or measurable extent (**Paper V**).

## 7.2. Future perspectives

The primary motivation of this thesis was assessment of sources of error and artefacts on CT-based attenuation correction in dual-modality PET/CT systems using Monte Carlo simulations and experimental measurements. However, the conclusions described in this thesis suffer from the limited number of MC simulations and experiments performed. In the following paragraphs some research activities in continuum to this work are discussed.

One significant problem in the use of MCNP4C-based x-ray CT simulator developed in this study is the presence of statistical uncertainties (noise) in the final results. A simple way to decrease statistical uncertainties is to run MC simulations for sufficiently long time and use efficient variance reduction techniques. The acceleration of this simulator using parallelization, de-noising and hybrid simulation approaches is ongoing. Parallel implementation of MC calculations can be performed effectively owing to the fact the particle histories are completely independent from each other. Another approach to remove statistical fluctuations from noisy MC results is to use smoothing or de-noising algorithms. The other approach to speed-up x-ray CT modelling is to use hybrid approaches combining MC and analytical simulations. Optimal design and performance prediction of next generation panel-based PET/CT using the developed MCNP4C-based simulator is another active research area.

Since this study was carried out using separate PET and CT systems owing to the fact that a dedicated PET/CT (being install in our department) was not available at the time of this study, it was limited to the use of a neurological research brain phantom and clinical brain images, rather than an anthropomorphic whole-body phantom and whole-body clinical images, which might

impose a far greater challenge to the accuracy of attenuation correction due to the much larger attenuating volume, larger bony structures and more complex juxtapositions of media with different attenuating properties, e.g. lung/soft tissue/bone in the thorax. It is hard to predict whether the answers necessarily will be equivalent or the same conclusions will be reached in the clinical challenging situations mentioned above. Nevertheless, the same observations were reported in the literature for whole-body PET where attenuation correction is based on CT. Further investigation using whole-body data is guaranteed when the inline PET/CT system will be fully operational in our department.

The issue of whether the use of contrast medium in dual-modality PET/CT scanning produces medically significant artefacts is still controversial with some studies corroborating and others contradicting the fact that the presence of contrast medium can be a source of error and artefact when the CT data are used for attenuation correction of PET images. The quantification of a lower concentration threshold below which the use of contrast medium is risk-free proved to be a difficult task. The optimal quantity and route of administration of contrast medium and potential correction schemes are still open questions which require further research and development efforts. Developing an automatic segmentation algorithm for detection of contrast agent in the CT images is another active research area. Such algorithms will allow using the segmented contrast correction (SCC) method in clinical area.

## Acknowledgements

*The work behind this thesis was carried out at the Division of Nuclear Medicine, Geneva University Hospital. This thesis would not have been realized without the contributions and support of many people. I would like to express my sincere gratitude and appreciations to all of them. It is not practical to list all of those that have contributed because then I would be reciting names of many that I never met, but whose published work inspired me. Suffice it to say that to all those, Thank you!*

*In particular, I want to thank some people of special importance to me:*

*PD Dr Habib Zaidi, my main thesis advisor who invited me to join his laboratory. He gave me the opportunity to make a PhD as his assistant, and he always believed in my potentials. Habib is undoubtedly the person who contributed most to this work. Whenever I got stuck, he pulled me back on to the right track. He was more than an advisor should be. I am really indebted of his support and help for ever.*

*Professor Sviatoslav Voloshynovskiy, my thesis co-advisor, for continuous support and encouragement throughout the project and for solving numerous practical administrative problems.*

*Professor Abbas Alavi (University of Pennsylvania, USA) and Professor Jean-Phillipe Thiran (EPFL, Switzerland), for accepting to be part of jury and for their judicious comments and criticisms which significantly improved the quality of this thesis.*

*Dr. J.M. Boone, Dr. K.P. Ng, Dr. L.E. Wilkinson, Dr. G. Striling, Dr. M. Bhat, Dr. R. Nowotny, Dr. G.W. Allen, Dr. C. Lee, Dr. K. Van Ripper, Dr. Zbijewski, and Dr. O.G. Rousset who shared with us their data and programs.*

*I would like to thank all members of PET Instrumentation and Neuroimaging Laboratory, particularly, Frédéric Schoenahl, Torsten Ruest, and Nicolas Andreini to provide enjoyable working atmosphere, and also for putting their trust in me by allowing me to use their knowledge and skills. A special thank to Dr. Marie-Louise Montandon for her valuable support during the writhing and editing of this thesis.*

*I would like to thank my papers' reviewers in scientific journals for their constructive criticisms and suggestions. Their comments have contributed to remarkably improve the overall quality of my papers.*

*I thank all the personnel of the Division of Nuclear Medicine for a very enjoyable working atmosphere and their direct or indirect help.*

*A special thank to my parents and my wife's parents, relatives and friends, for their encouragements, and everlasting generosity. Without their love and support, this thesis would have not been possible at all.*

*Thanks to all "late-evening" and "week-end" working friends for pleasant company over the years.*

*Finally, and most of all I wish to thank my wife who could have not possibly supported me more, for her everyday support and encouragement, unbelievable patience and confidence. Thank you, Pardis for your sharing and caring.*

*This work was supported by the Swiss National Science Foundation under grant SNSF 3152A0-102143.*

## Publication List

### *Peer-reviewed Journal Publications*

1. **Ay, M.R.** and H. Zaidi, "CT-based attenuation correction in neurological PET: evaluation of the effect of x-ray tube voltage and current on quantitative analysis". Submitted for publication in the *Nucl Med Commun*, 2005.
2. **Ay, M.R.** and H. Zaidi, "Assessment of errors caused by x-ray scatter and use of contrast medium when using CT-based attenuation correction in PET". Under revision *European Journal of Nuclear Medicine and Molecular Imaging*, 2005.
3. H. Zaidi and **M.R. Ay**, "Current status and new horizons in Monte Carlo simulation of x-ray CT scanners". Submitted for publication in the *International Journal of Biomedical Engineering*, 2005.
4. **Ay, M.R.** and H. Zaidi, "Development and validation of MCNP4C-based Monte Carlo simulator for fan- and cone-beam x-ray CT". *Physics in Medicine and Biology*, 2005. **50**(20): p. 4863-4885.
5. **Ay, M.R.**, S. Sarkar, M. Shahriari, D. Sardari, and H. Zaidi, "Assessment of different computational models for generation of x-ray spectra in diagnostic radiology and mammography". *Medical Physics*, 2005. **32**(6): p. 1660-1675.
6. **Ay, M.R.**, M. Shahriari, S. Sarkar, M. Adib, and H. Zaidi, "Monte Carlo simulation of x-ray spectra in diagnostic radiology and mammography using MCNP4C". *Physics in Medicine and Biology*, 2004. **49**(21): p. 4897-4917.
7. **Ay, M.R.**, S. Sarkar, M. Shahriari, and P. Ghafarian, "Measurement of organ dose in abdomen-pelvis CT exam as a function of mA, KVp and scanner type by Monte Carlo method". *Iranian Journal of Radiation Research*, 2004. **1**(4): p. 187-194.

### *Proceeding and Conference Records*

1. **Ay, M.R.**, S. Sarkar, M. Shahriari, D. Sardari, and H. Zaidi. "MCNP4C-based Monte Carlo simulator for fan- and cone-beam x-ray CT: development and experimental validation". In *Proc. of the 14th International Conference of Medical Physics. Biomedizinische Technik*. 2005. Nuremberg, Germany, Sept. 14-17, 2005. **50 Suppl Part 1**: p. 360-361.
2. **Ay, M.R.**, S. Sarkar, M. Shahriari, D. Sardari, and H. Zaidi. "Comparative assessment of different computational models for generation of x-ray spectra in diagnostic radiology and mammography". In *Proc. IEEE Nuclear Science Symposium and Medical Imaging Conference*. 2004. Oct. 19-22, Rome, Italy. **4**: p. 4190-4194.

### *Published Abstracts*

1. **Ay, M.R.**, S. Sarkar, M. Shahriari, and P. Ghafarian. "Estimating of patient dose in abdomen-pelvis CT exam as a function of scan techniques in single and multi-slice speiral CT by Monte Carlo method". In *2th International Conference on Nuclear Science and Technology in Iran*. 2004. Apr. 27-30, Shiraz, Iran: p. 46.
2. **Ay, M.R.**, M. Adib, and H. Zaidi. "Development of a Monte Carlo simulation package for scintillation cameras operation in single photon and coincidence imaging mode". In *Annual Congress of the European Association of Nuclear Medicine (EANM03)*. 2003. Amsterdam, The Netherlands, Aug. 23-28: p. S326-S327.
3. **Ay, M.R.**, M. Shahriari, S. Sarkar, and P. Ghafarian. "Measurement of organ dose in abdomen-pelvis CT exams as a function of mA, KVp and scanner type by Monte Carlo method". In *3th International Conference of The Effect of Low and Very Low Doses of Ionizing Radiation on Human Health*. 2003. Oct. 21-23, Tehran, Iran: p. 53.
4. **Ay, M.R.** "Image fusion in nuclear medicine". In *The 7th Annual Meeting of Nuclear Medicine*. 2003. Tehran, Iran: p. 45.
5. **Ay, M.R.** "Steps toward building a PET center". In *The 6th Annual Meeting of Nuclear Medicine*. 2002. Mashhad, Iran: p. 29.
6. **Ay, M.R.** "Comparison of PET detectors". In *The 6th Annual Meeting of Nuclear Medicine*. 2002. Mashhad, Iran: p. 31.
7. **Ay, M.R.** and M.E. Ashrafi. "Providing software for PET (Coincidence) 3D simulation using Monte Carlo method". In *The International Conference on Radiation and its Role in Diagnosis and Treatment (FICR2000)*. 2000. Tehran, Iran, Oct. 14-18: p. 51.

### *Book Chapters*

1. **Ay, M.R.** and H. Zaidi, "Analytical and Monte Carlo modeling of x-ray spectra in mammography", in *Emerging Technologies in Breast Imaging and Mammography*, J.S. Suri, R.M. Rangayyan, and S. Laxminarayan, Editors. 2006, American Scientific Publishers: Valencia, CA. *in press*.
2. **Ay, M.R.**, "Introduction to PET and PET/CT systems", in *Comprehensive book on Radiology, Nuclear Medicine and Therapy Systems*, J. Shokohi, A.A. Ameri, and H.R. Sagha, Editors. 2003, Andishe Rafi Publisher: Tehran, Iran. p. 1757-1781.
3. **Ay, M.R.**, "Cyclotrons in nuclear medicine", in *Comprehensive book on Radiology, Nuclear Medicine and Therapy Systems*. J. Shokohi, A.A. Ameri, and H.R. Sagha, Editors. 2003, Andishe Rafi Publisher: Tehran, Iran. p. 1742-1756.

## Bibliography

- [1] P. A. Van den Elsen, E. D. Pol, and M. A. Viergever, "Medical image matching- A review with classification," *IEEE Trans. Eng. Med. Biol.*, vol. 12, pp. 26-39, 1993.
- [2] B. H. Hasegawa, B. Stebler, B. K. Rutt, A. Martinez, E. L. Gingold, C. S. Barker, K. G. Faulkner, C. E. Cann, and D. P. Boyd, "A prototype high-purity germanium detector system with fast photon-counting circuitry for medical imaging," *Med. Phys.*, vol. 18, pp. 900-909, 1991.
- [3] T. F. Lang, B. H. Hasegawa, S. C. Liew, J. K. Brown, S. C. Blankespoor, and S. M. Reilly, "Description of a prototype emission-transmission computed tomography imaging system," *J. Nucl. Med.*, vol. 33, pp. 1881-1887, 1992.
- [4] B. H. Hasegawa, T. F. Lang, J. K. Brown, S. M. Reilly, S. C. Blankespoor, S. C. Liew, B. M. W. Tsui, and C. Ramanathan, "Object-specific attenuation correction of SPECT with correlated dual-energy x-ray CT," *IEEE Trans. Nucl. Sci.*, vol. 40, pp. 1242-1252, 1993.
- [5] B. H. Hasegawa and H. Zaidi, "Dual-modality imaging: more than the some of its components," in *Quantitative analysis in nuclear medicine imaging*, H. Zaidi, Ed. New York: Springer, 2005, pp. 35-81.
- [6] T. Beyer, D. W. Townsend, T. Brun, P. E. Kinahan, M. Charron, R. Roddy, J. Jerin, J. Young, L. Byars, and R. Nutt, "A combined PET/CT scanner for clinical oncology," *J. Nucl. Med.*, vol. 41, pp. 1369-1379, 2000.
- [7] D. W. Townsend, J. P. J. Carney, J. T. Yap, and N. C. Hall, "PET/CT today and tomorrow," *J. Nucl. Med.*, vol. 45, pp. 4s-14s, 2004.
- [8] D. W. Townsend and S. R. Cherry, "Combining anatomy and function: the path to true image fusion," *Eur. Radiol.*, vol. 11, pp. 1968-1974, 2001.
- [9] S. C. Bushong, *Radiologic science for technologists: physics, biology and protection.*, Seventh Edition ed. St. Louis: Mosby Co, 1998.
- [10] A. F. Koppa, K. Klingenberg-Regn, M. Heuschmid, A. Kuttner, B. Ohnesorge, T. Flohr, S. Schaller, and C. D. Claussen, "Multislice computed tomography: Basic principles and clinical applications," *Electromedica*, vol. 68, pp. 94-105, 2000.
- [11] T. G. Turkington, "Introduction to PET instrumentation," *J. Nuc. Med. Technol.*, vol. 29, pp. 1-8, 2001.
- [12] D. Bailey, S. R. Meikle, and T. Jones, "Effective sensitivity in 3D PET: the impact of detector dead-time on 3D system performance," *IEEE Trans. Nucl. Sci.*, vol. 40, pp. 1180-1185, 1997.
- [13] D. W. Townsend, M. Wensveen, L. G. Byars, A. Geissbuhler, H. J. Tochon-Danguy, A. Christin, M. Defrise, D. L. Bailey, S. Grootenok, A. Donath, and et al., "A rotating PET scanner using BGO block detectors: design, performance and applications," *J. Nucl. Med.*, vol. 34, pp. 1367-76, 1993.
- [14] J. S. Karp, G. Muehlelehner, F. D. Mankof, C. E. Ordonez, J. M. Ollinger, M. E. Daube-Witherspoon, A. T. Haigh, and D. J. Beerbohm, "Continuous-slice PENN-PET: a positron tomograph with volume imaging capability," *J. Nucl. Med.*, vol. 31, pp. 617-27, 1990.
- [15] M. Bocher, A. Balan, Y. Krausz, Y. Shrem, A. H. R. Lonn, M. Wilk, and R. Chisin, "Gamma camera-mounted anatomical x-ray tomography: technology, system characteristics and first images," *Eur. J. Nuc. Med.*, vol. 27, pp. 619-627, 2000.
- [16] H. Zaidi and K. F. Koral, "Scatter modelling and compensation in emission tomography.," *Eur J Nucl Med Mol Imaging*, vol. 31, pp. 761-782, 2004.
- [17] M. Osman, C. Cohade, Y. Nakamoto, and R. L. Wahl, "Respiratory motion artifacts on PET emission images obtained using CT attenuation correction on PET-CT," *Eur. J. Nucl. Med.*, vol. 30, pp. 603-606, 2003.
- [18] H. Zaidi and B. Hasegawa, "Determination of the attenuation map in emission tomography," *J. Nucl. Med.*, vol. 44, pp. 291-315, 2003.
- [19] O. Rousset, Y. Ma, and A. C. Evans, "Correction for partial volume effect in PET: principal and validation," *J. Nucl. Med.*, vol. 39, pp. 904-911, 1998.
- [20] A. Braem, M. C. Llatas, E. Chesi, J. G. Correia, F. Garibaldi, C. Joram, S. Mathot, E. Nappi, M. R. Da Silva, F. Schoenahl, J. Seguinot, P. Weilhammer, and H. Zaidi, "Feasibility of a novel design of high resolution parallax-free Compton enhanced PET scanner dedicated to brain research," *Phys. Med. Biol.*, vol. 49, pp. 2547-2562, 2004.
- [21] A. Sanchez-Crespo, A. Andreo, and S. M. Larsson, "Positron flight in human tissues and its influence on PET image spatial resolution," *Eur. J. Nucl. Med.*, vol. 31, pp. 44-51, 2003.
- [22] L. Lonnet, I. Borbath, A. Bol, A. Coppens, M. Sibimana, R. Bausart, M. Defrise, S. Pauwels, and C. Michel, "Attenuation correction in whole body FDG oncological studies: the role of statistical reconstruction," *Eur. J. Nucl. Med.*, vol. 26, pp. 591-598, 1999.
- [23] D. L. Bailey, "Transmission scanning in emission tomography," *Eur. J. Nucl. Med.*, vol. 25, pp. 774-787, 1998.

- [24] H. Zaidi, M. L. Montandon, and D. O. Slosman, "Magnetic resonance imaging-guided attenuation and scatter corrections in three-dimensional brain positron emission tomography," *Med. Phys.*, vol. 30, pp. 937-48, 2003.
- [25] P. E. Kinahan, B. Hasegawa, and T. Beyer, "X-ray-based attenuation correction for positron emission tomography/computed tomography scanners," *Semin. Nucl. Med.*, vol. 34, pp. 166-179, 2003.
- [26] C. Comtat, P. E. Kinahan, J. A. Fessler, T. Beyer, D. W. Townsend, M. Defrise, and C. Michel, "Clinically feasible reconstruction of 3D whole-body PET/CT data using blurred anatomical labels," *Phys. Med. Biol.*, vol. 47, pp. 1-20, 2002.
- [27] T. Beyer, P. E. Kinahan, D. W. Townsend, and D. Sashin, "The use of X-ray CT for attenuation correction of PET data," *Proc. IEEE Nuclear Science Symposium and Medical Imaging Conference*, Rome, Italy, vol. 4, pp. 1573 - 1577, 1995.
- [28] P. E. Kinahan, D. W. Townsend, T. Beyer, and D. Sashin, "Attenuation correction for a combined 3D PET/CT scanner," *Med. Phys.*, vol. 25, pp. 2046-2053, 1998.
- [29] C. Bai, L. Shao, A. Da Silva, and Z. Zhao, "A generalized model for the conversion from CT numbers to linear attenuation coefficients," *IEEE Trans. Nucl. Sci.*, vol. 50, pp. 1510-1515, 2003.
- [30] M. J. Guy, I. A. Castellano-Smith, M. A. Flower, G. D. Flux, R. J. Ott, and D. Visvikis, "DETECT-dual energy transmission estimation CT - for improved attenuation correction in SPECT and PET," *IEEE Trans. Nucl. Sci.*, vol. 45, pp. 1261-1267, 1998.
- [31] T. Beyer, G. Antoch, S. P. Mueller, T. Egelhof, L. S. Freudenberg, J. F. Debatin, and A. Bockisch, "Acquisition protocol considerations for combined PET/CT Imaging," *J. Nucl. Med.*, vol. 45, pp. 25s-35s, 2004.
- [32] H. Zaidi, "Relevance of accurate Monte Carlo modeling in nuclear medical imaging.," *Med. Phys.*, vol. 26, pp. 574-608, 1999.
- [33] H. P. Chan, K. L. Lam, and Y. Z. Wu, "Studies of performance of antiscatter grids in digital radiography: effect on signal-to-noise ratio," *Med. Phys.*, vol. 17, pp. 655-64, 1990.
- [34] M. Winslow, X. G. Xu, and B. Yazici, "Development of a simulator for radiographic image optimization," *Comput. Methods Programs Biomed.*, vol. 78, pp. 179-190, 2005.
- [35] G. Spyrou, G. Tzanakos, G. Nikiforides, and G. Panayiotakis, "A Monte Carlo simulation model of mammographic imaging with x-ray sources of finite dimensions," *Phys. Med. Biol.*, vol. 47, pp. 917-933, 2002.
- [36] A. P. Colijn, W. Zbijewski, A. Sasov, and F. J. Beekman, "Experimental validation of a rapid Monte Carlo based micro-CT simulator," *Phys. Med. Biol.*, vol. 49, pp. 4321-4333, 2004.
- [37] M. R. Ay and H. Zaidi, "Development and validation of MCNP4C-based Monte Carlo simulator for fan- and cone-beam x-ray CT," *Phys. Med. Biol.*, vol. 50, pp. 4863-85, 2005.
- [38] A. P. Colijn and F. J. Beekman, "Accelerated simulation of cone beam X-ray scatter projections," *IEEE Trans. Med. Imaging*, vol. 23, pp. 584-590, 2004.
- [39] M. M. Dresser, "Scattering effects in radioisotopic imaging," in *University of Michigan, University Microfilm*. Ann Arbor, MI: University of Michigan, 1972.
- [40] M. Ljungberg and S. E. Strand, "A Monte Carlo program for the simulation of scintillation camera characteristics," *Comput. Methods Programs Biomed.*, vol. 29, pp. 257-272, 1989.
- [41] H. Zaidi, A. H. Scheurer, and C. Morel, "An object-oriented Monte Carlo simulator for 3D cylindrical positron tomographs," *Comput. Methods Programs Biomed.*, vol. 58, pp. 133-45, 1999.
- [42] A. Tycho, T. M. Jorgensen, H. T. Yura, and P. E. Andersen, "Derivation of a Monte Carlo method for modeling heterodyne detection in optical coherence tomography systems," *Appl. Opt.*, vol. 41, pp. 6676-91, 2002.
- [43] L. V. Spencer, "Polarization of multiply scattered gamma rays (unpublished)," National Bureau of Standards Interim Report on Contract with US Office of Naval Research, 1948.
- [44] H. Zaidi and G. Sgouros, "Therapeutic applications of Monte Carlo calculations in nuclear medicine," in *Medical Physics series, Series in Medical Physics and Biomedical Engineering*, C. G. Orton, J. A. E. Spaan, and J. G. Webster, Eds. Bristol: Institute of Physics Publishing, 2002.
- [45] M. Ljungberg, S. E. Strand, and M. A. King, *Monte Carlo calculations in nuclear medicine: Application in diagnostic imaging*. London: Institute of Physics Publishing, 1998.
- [46] E. Storm and H. I. Israel, "Photon cross-section from 0.001 to 100 MeV for elements 1 through 100," *Los Alamos Scientific Laboratory*, 1967.
- [47] J. H. Hubbell, W. J. Veigele, E. A. Briggs, R. T. Brown, D. T. Cromer, and R. J. Howerton, "Atomic form factors, incoherent scattering functions, and photon scattering cross-sections," *J. Phys. Chem. Ref. Data*, vol. 4, pp. 471-538, 1975.
- [48] H. G. Hughes, "Status of electron transport in MCNP," Los Alamos National Laboratory, NM, Los Alamos, NM LA-UR-97-1368, 1997.
- [49] J. F. Briesmeister, "MCNP - A general Monte Carlo Nparticle transport code. version 4C," Los Alamos National Laboratory, NM, Los Alamos, NM LA-13709-M, 2000.
- [50] J. S. Hendricks, G. W. McKinney, L. S. Waters, T. L. Roberts, H. W. Egdorf, J. P. Finch, H. R. Trellue, E. J. Pitcher, D. R. Mayo, M. T. Swinhoe, S. J. Tobin, F. X. Gallmeier, D. Jean-Christophe,

- W. B. Hamilton, and J. Lebenhaft, "MCNPX, VERSION 2.5.e," Los Alamos National Laboratory, NM, Los Alamos, NM LA-UR-04-0569, 2004.
- [51] W. R. Nelson, H. Hirayama, and D. W. O. Roger, "The EGS4 code system," Stanford Linear Acceleration Center, Stanford, 1985.
- [52] I. Kawrakow, E. Mainegra-Hing, and D. W. O. Rogers, "The EGSnrc Code System: Monte Carlo Simulation of Electron and Photon Transport," Ionizing Radiation Standards, National Research Council of Canada, Ottawa NRCC Report PIRS-701, 2003.
- [53] J. A. Halbleib, R. P. Kensek, G. D. Valdez, S. M. Seltzer, and M. J. Berger, "ITS: The Integrated TIGER Series of electron/photon transport codes - version 3.0," *IEEE Trans. Nucl. Sci.*, vol. 39, pp. 1025-1030, 1992.
- [54] R. Brun, F. Bruyant, M. Maire, A. C. McPherson, and P. Zancarini, "GEANT3," CERN, 1987.
- [55] F. Salvat and J. M. Fernandez-Varea, "PENELOPE- A code system for Monte Carlo simulation of electron and photon transport," Nuclear Energy Agency, Barcelona, 2003.
- [56] A. Fasso, A. Ferrari, and P. R. Sala, "Electron-photon transport in FLUKA: status," in *Proceedings of the Monte Carlo 2000 Conference*, A. Kling, Barao, F, Nakagawa, M, Tavora, L, Vaz, P, Ed. Berlin: Springer-Verlag, 2001, pp. 159-164.
- [57] J. Giersch, A. Weidemann, and G. Anton, "ROSI- an object-oriented and parallel-computing Monte Carlo simulation for X-ray imaging," *Nucl. Instr. Meth. A*, vol. 509, pp. 151-156, 2003.
- [58] D. Lazos, K. Bliznakova, Z. Kolitsi, and N. Pallikarakis, "An integrated research tool for X-ray imaging simulation," *Comput. Methods Programs Biomed.*, vol. 70, pp. 241-251, 2003.
- [59] G. Spyrou, G. Panayiotakis, and G. Tzanakos, "MASTOS: Mammography Simulation Tool for design Optimization Studies," *Med. Inform. Internet Med.*, vol. 25, pp. 275-93, 2000.
- [60] D. E. Peplow and K. Verghese, "Digital mammography image simulation using Monte Carlo," *Med. Phys.*, vol. 27, pp. 568-79, 2000.
- [61] A. Malusek, M. M. Seger, M. Sandborg, and G. Alm Carlsson, "Effect of scatter on reconstructed image quality in cone beam computed tomography: evaluation of a scatter-reduction optimisation function," *Radiat. Prot. Dosimetry*, vol. 114, pp. 337-340, 2005.
- [62] R. L. Harrison, S. D. Vannoy, D. R. Haynor, S. B. Gillispie, M. S. Kaplan, and T. K. Lewellen, "Preliminary experience with the photon history generator module for a public-domain simulation system for emission tomography," *IEEE Med. Imag. Conf.*, San Francisco, vol. Conf. Rec. IEEE Med. Imag. Conf., pp. 1154-1158, 1994.
- [63] J. C. Yanch and A. B. Dobrzeniecki, "Monte Carlo simulation in SPECT: Complete 3-D modeling of source, collimator and tomographic data acquisition," *IEEE Trans. Nucl. Sci.*, vol. 40, pp. 198-203, 1993.
- [64] M. F. Smith, C. E. Floyd, and R. J. Jaszczak, "A vectorized Monte Carlo code for modeling photon transport in SPECT," *Med. Phys.*, vol. 20, pp. 1121-1127, 1993.
- [65] C. J. Thompson, J. M. Cantu, and Y. Picard, "PETSIM: Monte Carlo program simulation of all sensitivity and resolution parameters of cylindrical positron imaging systems," *Phys. Med. Biol.*, vol. 37, pp. 731-749, 1992.
- [66] I. Castiglioni, O. Cremonesi, M. C. Gilardi, A. Savi, V. Bettinardi, G. Rizzo, E. Bellotti, and F. Fazio, "A Monte Carlo model of noise components in 3D PET," *IEEE Trans. Nucl. Sci.*, vol. 49, pp. 2297-2303, 2002.
- [67] D. De Vries and S. Moore, "Monte Carlo simulation of photon transport in gamma camera collimators," in *Monte Carlo calculations in nuclear medicine: Applications in diagnostic imaging.*, Series in Medical Physics and Biomedical Engineering, M. Ljungberg, S. E. Strand, and M. A. King, Eds. Bristol: Institute of Physics Publishing, 1998, pp. 125-144.
- [68] G. Santin, D. Strul, D. Lazaro, L. Simon, M. Krieguer, M. Vieira Martins, B. V., and C. Morel, "GATE: A Geant4-based simulation platform for PET and SPECT integrating movement and time management," *IEEE Trans. Nucl. Sci.*, vol. 50, pp. 1516-1521, 2003.
- [69] A. Reilhac, C. Lartizien, N. Costes, S. Sans, C. Comtat, R. N. Gunn, and A. C. Evans, "PET-SORTEO: a Monte Carlo-based simulator with high count rate capabilities," *IEEE Trans. Nucl. Sci.*, vol. 51, pp. 46-52, 2004.
- [70] H. Zaidi, "Comparative evaluation of photon cross section libraries for materials of interest in PET Monte Carlo simulations," *IEEE Trans. Nucl. Sci.*, vol. 47, pp. 2722-2735, 2000.
- [71] H. Zaidi, C. Labbe, and C. Morel, "Implementation of an environment for Monte Carlo simulation of fully 3-D positron tomography on a high-performance parallel platform," *Parallel Computing*, vol. 24, pp. 1523-1536, 1998.
- [72] H. Zaidi, "Comparative evaluation of scatter correction techniques in 3D positron emission tomography," *Eur. J. Nuc. Med.*, vol. 27, pp. 1813-1826, 2000.
- [73] D. Rogers, "More realistic Monte Carlo calculations of photon detector response functions," *Nucl. Instr. Meth. A*, vol. 199, pp. 531-548, 1982.
- [74] P. Gantet, J. P. Esquerre, B. Danet, and R. Guiraud, "A simulation method for studying scintillation camera collimators," *Phys. Med. Biol.*, vol. 35, pp. 659-669, 1990.

- [75] S. Webb, D. M. Binnie, M. A. Flower, and R. J. Ott, "Monte Carlo modelling of the performance of a rotating slit-collimator for improved planar gamma-camera imaging," *Phys. Med. Biol.*, vol. 37, pp. 1095-1108, 1992.
- [76] M. A. King, W. Xia, D. J. deVries, T. S. Pan, B. J. Villegas, S. Dahlberg, B. M. Tsui, M. H. Ljungberg, and H. T. Morgan, "A Monte Carlo investigation of artifacts caused by liver uptake in single-photon emission computed tomography perfusion imaging with technetium 99m-labeled agents," *J. Nucl. Cardiol.*, vol. 3, pp. 18-29, 1996.
- [77] H. Zaidi, "Scatter modelling and correction strategies in fully 3D PET," *Nucl. Med. Comm.*, vol. 22, pp. 1181-1184, 2001.
- [78] M. Ay, M. Shahriari, S. Sarkar, M. Adib, and H. Zaidi, "Monte Carlo simulation of x-ray spectra in diagnostic radiology and mammography using MCNP4C," *Phys. Med. Biol.*, vol. 49, pp. 4897-4917, 2004.
- [79] D. Dance, A. Thilander, M. Sandborg, C. Skinner, I. Castellano, and G. Carlsson, "Influence of anode/filter material and tube potential on contrast, signal-to-noise ratio and average absorbed dose in mammography: a Monte Carlo study," *Br. J. Radiol.*, vol. 73, pp. 1056-1067, 2000.
- [80] J. M. Boone, K. K. Lindfors, V. N. Cooper, and J. A. Seibert, "Scatter/primary in mammography: comprehensive results," *Med. Phys.*, vol. 27, pp. 2408-2416, 2000.
- [81] M. Endo, T. Tsunoo, N. Nakamori, and K. Yoshida, "Effect of scatter radiation on image noise in cone beam CT," *Med. Phys.*, vol. 28, pp. 469-474, 2001.
- [82] M. Sandborg, D. R. Dance, G. A. Carlsson, and J. Persliden, "Monte Carlo study of grid performance in diagnostic radiology: task dependent optimization for screen-film imaging," *Br. J. Radiol.*, vol. 67, pp. 76-85, 1994.
- [83] J. H. Siewerdsen and D. A. Jaffray, "Optimization of x-ray imaging geometry (with specific application to flat-panel cone-beam computed tomography)," *Med. Phys.*, vol. 27, pp. 1903-1914, 2000.
- [84] M. Sandborg, D. R. Dance, J. Persliden, and G. A. Carlsson, "A Monte Carlo program for the calculation of contrast, noise and absorbed dose in diagnostic radiology," *Comput. Methods Programs Biomed.*, vol. 42, pp. 167-180, 1994.
- [85] J. M. Boone, M. H. Buonocore, and V. N. Cooper, "Monte Carlo validation in diagnostic radiological imaging," *Med. Phys.*, vol. 27, pp. 1294-1304, 2000.
- [86] J. M. Boone, J. A. Seibert, J. M. Sabol, and M. Tecotzky, "A Monte Carlo study of x-ray fluorescence in x-ray detectors," *Med. Phys.*, vol. 26, pp. 905-916, 1999.
- [87] M. Khodaverdi, A. F. Chatziioannou, S. Weber, K. Ziemons, H. Halling, and U. Pietrzyk, "Investigation of different microCT scanner configurations by GEANT4 simulations," *IEEE Trans. Nucl. Sci.*, vol. 52, pp. 188-192, 2005.
- [88] M. R. Ay and H. Zaidi, "Analytical and Monte Carlo modeling of x-ray spectra in mammography," in *Emerging Technologies in Breast Imaging and Mammography*, J. S. Suri, R. M. Rangayyan, and S. Laxminarayan, Eds. Valencia, CA: American Scientific Publishers, 2006, *in press*.
- [89] H. A. Kramers, "On the theory of x-ray absorption and of the continuous x-ray spectrum," *Phil. Mag.*, vol. 46, pp. 836-871, 1923.
- [90] L. Silberstein, "Determination of the spectral composition of x-ray radiation from filtration data," *Opt. Soc. Am.*, vol. 22, pp. 265-280, 1932.
- [91] J. M. Boone and J. A. Seibert, "An accurate method for computer-generating tungsten anode x-ray spectra from 30 to 140 kV," *Med. Phys.*, vol. 24, pp. 1661-1670, 1997.
- [92] J. M. Boone, T. R. Fewell, and R. J. Jennings, "Molybdenum, rhodium, and tungsten anode spectral models using interpolating polynomials with application to mammography," *Med. Phys.*, vol. 24, pp. 1863-1874, 1997.
- [93] R. Birch and M. Marshall, "Computation of bremsstrahlung X-ray spectra and comparison with spectra measured with a Ge(Li) detector," *Phys. Med. Biol.*, vol. 24, pp. 505-517, 1979.
- [94] W. J. Iles, "The Computation of the bremsstrahlung x-ray spectra over an energy range 15 keV to 300 keV," National Radiological Protection Board March, 1987.
- [95] B. W. Soole, "A determination of x-ray attenuation analysis for approximating the intensity distribution at its point of origin of bremsstrahlung excited in a thick target by incident electrons of constant medium energy," *Phys. Med. Biol.*, vol. 21, pp. 369-389, 1976.
- [96] M. Green and V. E. Cosslett, "Measurements of K, L and M shell x-ray production efficiencies," *Br. J. Appl. Phys.*, vol. 1, pp. 425-436, 1968.
- [97] D. M. Tucker, G. T. Barnes, and D. P. Chakraborty, "Semiempirical model for generating tungsten target x-ray spectra," *Med. Phys.*, vol. 18, pp. 211-218, 1991.
- [98] A. Vignes and G. Dez, "Distribution in depth of the primary x-ray emission in anticathodes of titanium and lead," *B. J. Appl. Phys.*, vol. 1, pp. 1309-1322, 1968.
- [99] A. Sommerfeld, "Wellenmechanik," *Ann. Physik*, vol. 11, pp. 257-330, 1931.
- [100] E. Storm, "Calculated bremsstrahlung spectra for thick tungsten targets," *Phys. Rev.*, vol. A5, pp. 2328-2338, 1972.

- [101] M. J. Berger and S. M. Seltzer, "Bremsstrahlung and photoneutrons from thick tungsten and tantalum targets," *Phys. Rev. C* 2, vol. 2, pp. 621-631, 1970.
- [102] R. C. Placious, "Dependence of 50- and 100-keV Bremsstrahlung on Target Thickness, Atomic Number, and Geometric Factors," *J. App. Phys.*, vol. 38, pp. 2030-2038, 1968.
- [103] V. Sundararaman, M. A. Prasad, and R. B. Vora, "Computing spectra from diagnostic and therapeutic x-ray tubes," *Phys. Med. Biol.*, vol. 18, pp. 208-218, 1973.
- [104] M. J. Berger, "Monte Carlo Calculation of the penetration and diffusion of fast charged particles," in *Methods in Computational Physics*, vol. 1, B. Alder, S. Fernbach, and M. Rotenberg, Eds. New York: Academic Press, 1963, pp. 135-215.
- [105] D. E. Raeside, "Monte Carlo principles and application," *Phys. Med. Biol.*, vol. 21, pp. 181-197, 1976.
- [106] K. H. Reiss and B. Steinle, "Calculation of x-ray spectra in the diagnostic energy range, due regard being paid to scattered radiation," *Phys. Med. Biol.*, vol. 18, pp. 746-747, 1973.
- [107] R. L. Morin and D. E. Raeside, "Bremsstrahlung spectra sampling for Monte Carlo simulations," *Phys. Med. Biol.*, vol. 27, pp. 223-228, 1982.
- [108] R. N. Kulkarni and S. J. Supe, "Monte Carlo calculations of mammographic x-ray spectra," *Phys. Med. Biol.*, vol. 29, pp. 185-190, 1984.
- [109] M. Bhat, J. Pattison, G. Bibbo, and M. Caon, "Off-axis x-ray spectra: a comparison of Monte Carlo simulated and computed x-ray spectra with measured spectra," *Med. Phys.*, vol. 26, pp. 303-309, 1999.
- [110] K. P. Ng, C. S. Kwok, and F. H. Tang, "Monte Carlo simulation of x-ray spectra in mammography," *Phys. Med. Biol.*, vol. 45, pp. 1309-1318, 2000.
- [111] C. Bramouille, F. Husson, and J. P. Manens, "Monte Carlo (PENELOPE code) study of the x-ray beams from SL linacs (Elekta)." *Physica Medica*, vol. XVI, pp. 107-115, 2000.
- [112] M. J. Fix, H. Keller, and P. Ruegsegger, "Simple beam models for Monte Carlo photon beam dose calculations in radiotherapy," *Med. Phys.*, vol. 27, pp. 2739-1747, 2000.
- [113] J. P. Bissonnette and L. J. Schreiner, "A comparison of semiempirical models for generating tungsten target x-ray spectra," *Med. Phys.*, vol. 19, pp. 579-582, 1992.
- [114] M. Bhat, J. Pattison, G. Bibbo, and M. Caon, "Diagnostic x-ray spectra: a comparison of spectra generated by different computational methods with a measured spectrum," *Med. Phys.*, vol. 25, pp. 114-120, 1998.
- [115] M. Caon, G. Bibbo, and J. Pattison, "A comparison of radiation dose measured in CT dosimetry phantoms with calculations using EGS4 and voxel-based computational models," *Phys. Med. Biol.*, vol. 42, pp. 219-229, 1997.
- [116] L. E. Wilkinson, P. N. Johnston, and J. C. Heggie, "A comparison of mammography spectral measurements with spectra produced using several different mathematical models," *Phys. Med. Biol.*, vol. 46, pp. 1575-1589, 2001.
- [117] P. Meyer, E. Buffard, L. Mertz, C. Kennel, A. Constantinesco, and P. Siffert, "Evaluation of the use of six diagnostic X-ray spectra computer codes," *Br. J. Radiol.*, vol. 77, pp. 224-230, 2004.
- [118] M. R. Ay, S. Sarkar, M. Shahriari, D. Sardari, and H. Zaidi, "Assessment of different computational models for generation of x-ray spectra in diagnostic radiology and mammography," *Med. Phys.*, vol. 32, pp. 1660-1675, 2005.
- [119] J. M. Boone, V. N. Cooper, W. R. Nemzek, J. P. McGahan, and J. A. Seibert, "Monte Carlo assessment of computed tomography dose to tissue adjacent to the scanned volume," *Med. Phys.*, vol. 27, pp. 2393-2407, 2000.
- [120] L. Ben Omrane, F. Verhaegen, N. Chahed, and S. Mtimet, "An investigation of entrance surface dose calculations for diagnostic radiology using Monte Carlo simulations and radiotherapy dosimetry formalisms," *Phys. Med. Biol.*, vol. 48, pp. 1809-1824, 2003.
- [121] J. M. Boone, O. V. Makarova, V. N. Zyryanov, C. M. Tang, D. C. Mancini, N. Moldovan, and R. Divan, "Development and Monte Carlo analysis of antiscatter grids for mammography," *Technol. Cancer Res. Treat.*, vol. 1, pp. 441-447, 2002.
- [122] A. C. Kak and M. Slaney, *Principles of Computerized Tomographic Imaging*, Electronic Copy ed. New York: IEEE PRESS, 1999.
- [123] I. A. Elbakri and J. A. Fessler, "Statistical image reconstruction for polyenergetic X-ray computed tomography," *IEEE Trans. Med. Imaging*, vol. 21, pp. 89-99, 2002.
- [124] B. De Man, J. Nuyts, P. Dupont, G. Marchal, and P. Suetens, "Metal streak artifacts in x-ray computed tomography: a simulation study," *IEEE Trans. Nucl. Sci.*, vol. 46, pp. 691-696, 1999.
- [125] J. J. DeMarco, C. H. Cagnon, D. D. Cody, D. M. Stevens, C. H. McCollough, J. O'Daniel, and M. F. McNitt-Gray, "A Monte Carlo based method to estimate radiation dose from multidetector CT (MDCT): cylindrical and anthropomorphic phantoms," *Phys. Med. Biol.*, vol. 50, pp. 3989-4004, 2005.
- [126] E. Kamel, C. Burger, A. Buck, G. K. Von Schulthess, and G. Goerres, "Impact of metallic dental implants on CT-based attenuation correction in a combined PET/CT scanner," *Eur. Radiol.*, vol. 13, pp. 724-728, 2003.

- [127] G. W. Goerres, T. F. Hany, E. Kamel, G. K. Von Schulthess, and A. Buck, "Head and neck imaging with PET and PET/CT: artefacts from dental metallic implants," *Eur. J. Nucl. Med.*, vol. 29, pp. 367-370, 2002.
- [128] F. P. Diflippo and R. C. Brunken, "Do implanted pacemaker leads and ICD leads cause metal-related artifact in cardiac PET/CT?," *J. Nucl. Med.*, vol. 46, pp. 436-443, 2005.
- [129] G. Antoch, L. S. Freudenberg, T. Beyer, A. Bockisch, and J. F. Debatin, "To enhance or not enhance? 18F-FDG and CT contrast agents in dual-modality 18F-FDG PET/CT," *J. Nucl. Med.*, vol. 45, 2004.
- [130] E. V. Dizendorf, T. F. Hany, A. Buck, G. K. Von Schulthess, and C. Burger, "Cause and magnitude of the error induced by oral contrast agent in CT-based attenuation correction of PET emission studies," *J. Nucl. Med.*, vol. 44, pp. 732-738, 2003.
- [131] Y. Nakamoto, B. B. Chin, D. L. Kraitchman, L. P. Lawler, and R. L. Wahl, "Effect of nonionic intravenous contrast agents at PET/CT imaging: Phantom and Canine studies," *Radiology*, vol. 227, pp. 817-824, 2003.
- [132] G. Goerres, C. Burger, E. Kamel, B. Seifert, A. H. Kaim, A. Buck, T. C. Buehler, and G. K. Von Schulthess, "Respiration-induced attenuation artifact at PET/CT: technical considerations," *Radiology*, vol. 226, pp. 906-910, 2003.
- [133] A. Bockisch, T. Beyer, G. Antoch, L. S. Freudenberg, H. Kuhl, J. F. Debatin, and S. P. Mueller, "Positron emission tomography / computed tomography-Imaging protocols, artifacts, and pitfalls," *Mol. Imag. Biol.*, vol. 6, pp. 188-199, 2004.
- [134] D. Platten, "CT issues in PET/CT scanning," Medicines and Healthcare product Regulatory Agency (MHRA), London, 2004.
- [135] G. W. Goerres, E. Kamel, T. N. Heidelberg, M. R. Schwitter, C. Burger, and G. K. von Schulthess, "PET-CT image co-registration in the thorax: influence of respiration," *Eur. J. Nucl. Med. Mol. Imaging*, vol. 29, pp. 351-360, 2002.
- [136] G. W. Goerres, C. Burger, M. R. Schwitter, T. N. Heidelberg, B. Seifert, and G. K. von Schulthess, "PET/CT of the abdomen: optimizing the patient breathing pattern," *Eur. Radiol.*, vol. 13, pp. 734-9, 2003.
- [137] J. P. Carney, D. W. Townsend, P. E. Kinahan, T. Beyer, K. Kachelriess, B. De Man, and J. Nuyts, "CT-based attenuation correction: the effect of imaging with the arms in the field-of-view [abstract]," *J. Nucl. Med.*, vol. 42(suppl), pp. 56P-57P, 2001.
- [138] P. M. Joseph and C. Ruth, "A method for simultaneous correction of spectrum hardening artifact in CT images containing both bone and iodine," *Med. Phys.*, vol. 24, pp. 100-108, 1997.
- [139] S. A. Nehmeh, Y. E. Erdi, H. Kalaigian, K. S. Kolbert, T. Pan, H. Yeung, O. Squire, A. Sinha, S. M. Larson, and J. L. Humm, "Correction for oral contrast artifacts in CT attenuation-corrected PET images obtained by combined PET/CT," *J. Nucl. Med.*, vol. 44, pp. 1940-1944, 2003.
- [140] G. Goerres, S. I. Ziegler, C. Burger, T. Berthold, G. K. Von Schulthess, and A. Buck, "Artifacts at PET and PET/CT caused by metallic hip prosthetic material," *Radiology*, vol. 226, pp. 577-584, 2003.
- [141] B. L. Walter and J. L. Vitek, "Surgical treatment for Parkinson's disease," *Lacent Neurology*, vol. 3, pp. 719-728, 2004.
- [142] V. Rappoport, J. P. J. Carney, and D. W. Townsend, "CT tube-voltage dependent attenuation correction scheme for PET/CT scanners," IEEE Nuclear Science Symposium and Medical Imaging Conference, Oct. 19-22, Rome, Italy, vol. 6, pp. 3853-3857, 2004.
- [143] T. H. Wu, Y. H. Huang, J. J. S. Lee, S. Y. Wang, S. C. Wang, C. T. Su, L. K. Chen, and T. C. Chu, "Radiation exposure during transmission measurements: comparison between CT- and germanium-based techniques with a current PET scanner," *Eur. J. Nucl. Med.*, vol. 31, pp. 38-43, 2004.
- [144] E. Kamel, T. F. Hany, C. Burger, V. Treyer, A. H. R. Lonn, G. K. Von Schulthess, and A. Buck, "CT vs 68Ge attenuation correction in a combined PET/CT system: evaluation of the effect of lowering the CT tube current," *Eur. J. Nucl. Med.*, vol. 29, pp. 346-350, 2002.
- [145] J. Li, J. Hsieh, J. Colsher, C. Stearns, and A. H. R. Lonn, "Towards single ultra-low dose CT scan for both attenuation map creation and localization in PET-CT application," Proc. IEEE Nuclear Science Symposium and Medical Imaging Conference., Oct. 19-22, Rome, Italy, vol. 4, pp. 2396-2398, 2004.

# Paper I

*Phys Med Biol* **49**: 4897-4917

© Reprinted with Permission From  
Institute of Physics and IOP Publishing

## Monte Carlo simulation of x-ray spectra in diagnostic radiology and mammography using MCNP4C

M R Ay<sup>1,2</sup>, M Shahriari<sup>3</sup>, S Sarkar<sup>4</sup>, M Adib<sup>5</sup> and H Zaidi<sup>2</sup>

<sup>1</sup> Department of Physics and Nuclear Sciences, AmirKabir University of Technology, Tehran, Iran

<sup>2</sup> Division of Nuclear Medicine, Geneva University Hospital, 1211 Geneva, Switzerland

<sup>3</sup> Department of Nuclear Engineering, Shahid Beheshti University, Tehran, Iran

<sup>4</sup> Department of Medical Physics, Tehran University of Medical Science, Tehran, Iran

<sup>5</sup> TPP Co., GE Medical Systems, Iran Authorized Distributor, Tehran, Iran

E-mail: farshid.ay@tppgems.com

Received 16 March 2004

Published 8 October 2004

Online at [stacks.iop.org/PMB/49/4897](http://stacks.iop.org/PMB/49/4897)

doi:10.1088/0031-9155/49/21/004

### Abstract

The general purpose Monte Carlo N-particle radiation transport computer code (MCNP4C) was used for the simulation of x-ray spectra in diagnostic radiology and mammography. The electrons were transported until they slow down and stop in the target. Both bremsstrahlung and characteristic x-ray production were considered in this work. We focus on the simulation of various target/filter combinations to investigate the effect of tube voltage, target material and filter thickness on x-ray spectra in the diagnostic radiology and mammography energy ranges. The simulated x-ray spectra were compared with experimental measurements and spectra calculated by IPEM report number 78. In addition, the anode heel effect and off-axis x-ray spectra were assessed for different anode angles and target materials and the results were compared with EGS4-based Monte Carlo simulations and measured data. Quantitative evaluation of the differences between our Monte Carlo simulated and comparison spectra was performed using student's *t*-test statistical analysis. Generally, there is a good agreement between the simulated x-ray and comparison spectra, although there are systematic differences between the simulated and reference spectra especially in the K-characteristic x-rays intensity. Nevertheless, no statistically significant differences have been observed between IPEM spectra and the simulated spectra. It has been shown that the difference between MCNP simulated spectra and IPEM spectra in the low energy range is the result of the overestimation of characteristic photons following the normalization procedure. The transmission curves produced by MCNP4C have good agreement with the IPEM report especially for tube voltages of 50 kV and 80 kV. The systematic discrepancy for higher tube voltages is the result of systematic differences between the corresponding spectra.

(Some figures in this article are in colour only in the electronic version)

## 1. Introduction

Computer simulation of x-ray spectra is one of the most important tools for investigation of patient dose and image quality in diagnostic radiology imaging systems. Early attempts at predicting diagnostic x-ray spectra were undertaken by Kramers (1923). This pioneering work was sustained by several investigators and many research groups are still trying to find an accurate method for computer simulation of x-ray spectra owing to the fact that experimental measurement of x-ray spectra requires special equipment which is available only in a limited number of laboratories (Fewell and Shuping 1978, Fewell *et al* 1981, Laitano *et al* 1991, Antonuk *et al* 1997, Dance *et al* 2000, Wilkinson *et al* 2001). Fewell *et al* measured x-ray spectra with different target/filter combinations for over two decades and have published several measured spectra (Fewell and Shuping 1977, 1978, Fewell *et al* 1981). Since experimental measurement of x-ray spectra is time consuming and remains difficult, different methods for spectra prediction have been presented. These can be divided into three categories: empirical models (Fewell and Shuping 1977, Boone and Seibert 1997, Boone *et al* 1997), semi-empirical models (Birch and Marshall 1979, Boone 1988, Tucker *et al* 1991, Blough *et al* 1998) and Monte Carlo modelling (Kulkarni and Supe 1984, Acosta *et al* 1998, Bhat *et al* 1999, Verhaegen *et al* 1999, Ng *et al* 2000, Ben Omrane *et al* 2003, Verhaegen and Castellano 2002). Although, purely empirical and semi-empirical models remain the fastest methods for x-ray spectra prediction, the models proposed so far still have limitations which prevent their adoption for a large range of applications (Ay *et al* 2004). In addition, most of these models have preset target/filter combinations and thus do not allow investigation of newly developed material compositions on the quality of resulting x-ray spectra. Sophisticated Monte Carlo modelling was adopted as an alternative to overcome the limitations mentioned above. Nevertheless, the prediction of x-ray spectra using the Monte Carlo method is computer intensive and time consuming compared to empirical and semi-empirical models.

The use of the Monte Carlo method to simulate radiation transport has become the most accurate means of predicting the x-ray spectra even in complex geometries owing to more accurate physics modelling and incorporation of appropriate interaction cross section data (Zaidi and Sgouros 2002). Moreover, the method tracks the evolution of all secondary particles (and their descendants) generated by primary electrons. Using the Monte Carlo method, it is possible to transport electrons and photons inside the target and filter to obtain detailed information about the factors contributing to the production of the x-ray spectrum (Acosta *et al* 1998). For the purpose of Monte Carlo simulation of x-ray spectrum, some authors have used self-written or in house developed computer codes (Kulkarni and Supe 1984, O'Meara *et al* 1998), while others have used public domain general-purpose Monte Carlo codes such as EGS4 (Bhat *et al* 1998, 1999, Ben Omrane *et al* 2003), MCNP (Verhaegen *et al* 1999, Mercier *et al* 2000) and ITS (Ng *et al* 2000).

In this work, we used MCNP4C running on Pentium-based PC to simulate the diagnostic radiology and mammography x-ray tube with the aim of predicting the x-ray spectra with different combinations of target/filter such as W/Al, Mo/Mo and Mo/Rh using various tube voltages (between 50 and 140 kV in diagnostic radiology and 30 kV in mammography) and different anode angles (between 6° and 18°). The Be window and air between tube window and measurement point were simulated. This paper addresses particularly some aspects not sufficiently covered in previously published papers, namely the variation of the radiation output across the x-ray beam, the anode heel effect and off-axis spectra for different target angles both in diagnostic radiology and mammography. The main motivations behind the choice of this code are its wide use by the medical physics community, wide acceptance

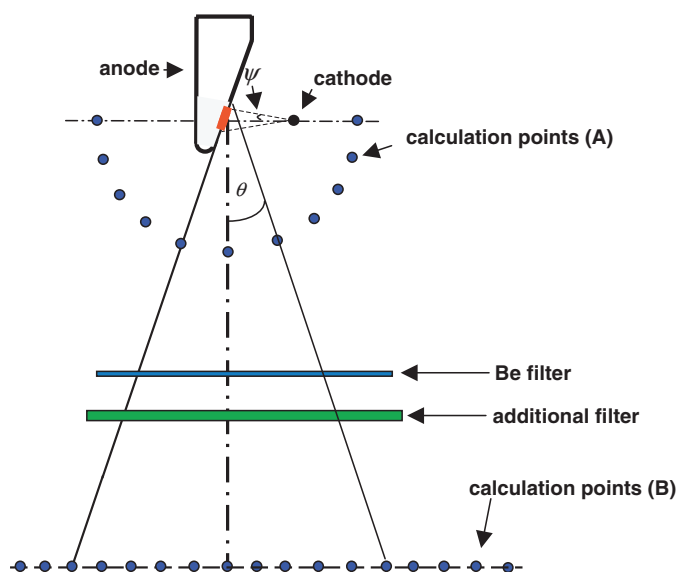


**Figure 1.** Geometry of the experimental set-up used for Monte Carlo simulation of x-ray spectra and assessment of anode heel effect. The position of detectors for calculation of exposure around the target (A) and anode heel (B) is also shown.

as an international standard for coupled particle transport having the best condensed history electron physics package and remarkable tally capabilities in addition to a powerful reporting system of statistical checks (Briesmeister 2000, Mercier *et al* 2000). The validity of MCNP4C simulated data was checked by comparing the calculated spectra, transmission curves and heel effect with the IPEM report number 78 (Cranley *et al* 1997), measured data (Fewell *et al* 1981, Bhat *et al* 1998, 1999, Pernieka *et al* 1997) and EGS4-based Monte Carlo simulations (Bhat *et al* 1999), respectively.

## 2. Material and methods

### 2.1. The MCNP4C code

MCNP is a general-purpose Monte Carlo code that can be used for neutron, photon and electron or coupled neutron/photon/electron transport (Briesmeister 2000). The code treats an arbitrary three-dimensional configuration of materials in geometric cells bounded by first and second degree surfaces and fourth degree elliptical tori. For photons transport, the code takes into account incoherent and coherent scattering, the possibility of fluorescent emission after photoelectric absorption and bremsstrahlung. The continuous slowing down approximation energy loss model is used for electron transport. To follow an electron through a significant energy loss, the MCNP4C code breaks the electron's path into many steps. These steps are chosen to be long enough to encompass many collisions (so that multiple scattering theories are valid) but short enough so that the mean energy loss in any one step is small (so that the approximations necessary for multiple scattering theories are satisfied). Except for the energy loss and straggling calculation, the detailed simulation of the electron history takes place in the sampling of the substeps. The Goudsmit–Saunderson theory is used to sample from the distribution of angular deflections, so that the direction of the electron can change at the end of each substep. For electron transport, MCNP addresses the sampling of bremsstrahlung photons at each electron substep. The table of production probabilities is used

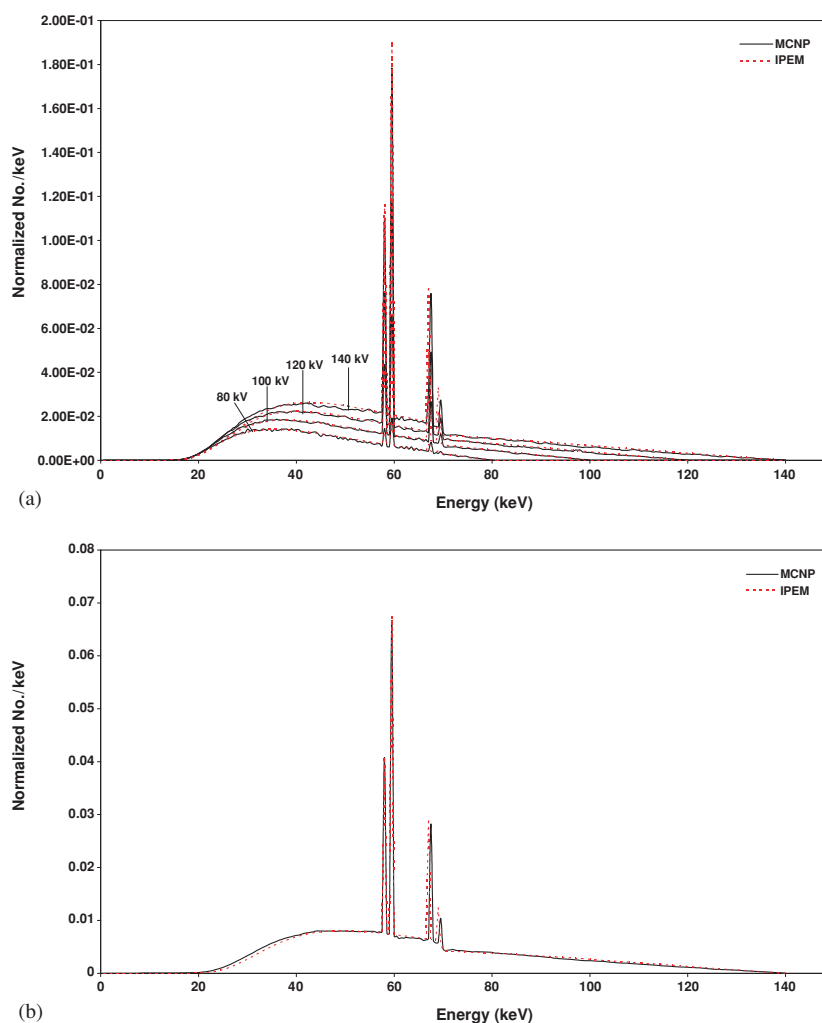


**Figure 2.** (a) Comparison of x-ray spectra produced by MCNP4C and IPEM report 78 for various tube voltages. (b) Same as (a) for 140 kV tube voltage with 0.1 mm Cu additional filter.

to determine whether a bremsstrahlung photon will be created (Hughes 1997). To improve the efficiency of electron and photon transport, two cards (PHYS:P and PHYS:E) are implemented in MCNP for biasing some physical parameters such as production of secondary electrons by photons (IDES), coherent scattering (NOCOH), bremsstrahlung angular distribution (IBAD) and production of characteristic x-rays (XNUM). The default value for the latter ( $XNUM = 1$ ) results in the analog number of tracks being sampled. If  $XNUM > 0$ , the number of photons produced is  $XNUM$  times the number that would be produced in the analog case, and a corresponding weight adjustment is made. Setting  $XNUM$  to zero turns off the production of x-ray photons by electrons.

## 2.2. Simulation of x-ray spectra using MCNP4C

The procedure of x-ray production consists of tracking a large number of electrons incident on the target until they are absorbed or emerge from it, and calculating the number of

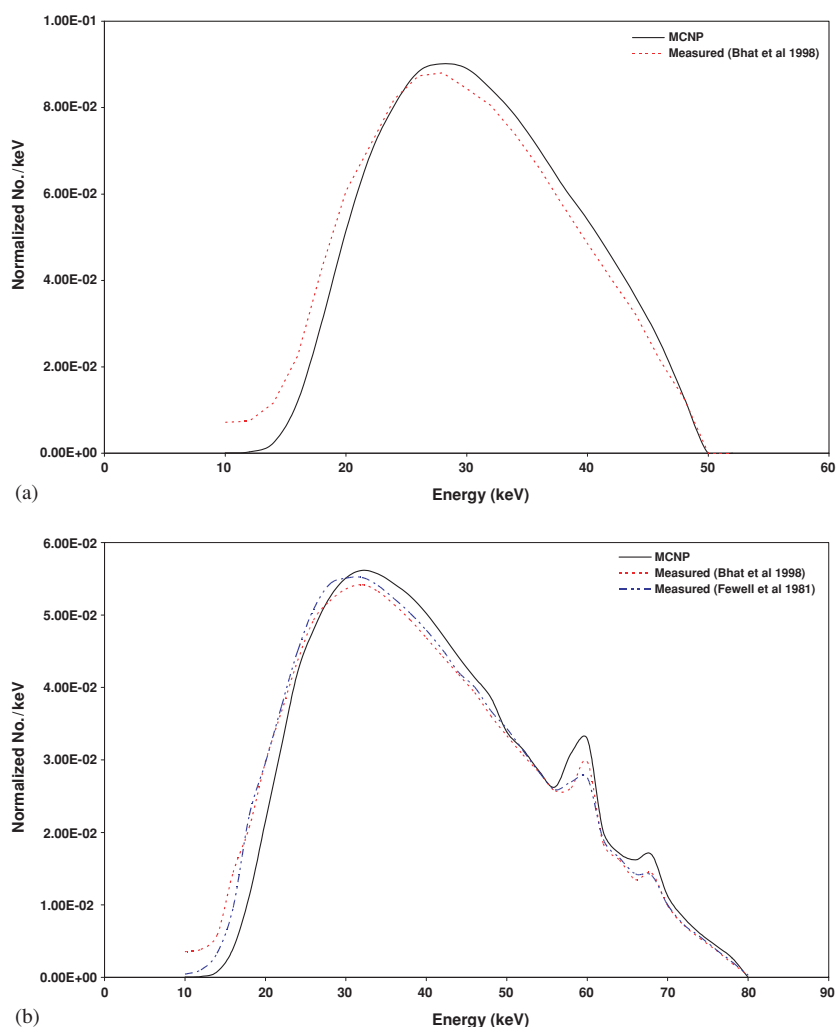


**Figure 3.** Comparison of x-ray spectra for various tube voltages produced by MCNP4C and measured data by Fewell *et al* (1981) and Bhat *et al* (1998). (a) 50 kV, (b) 80 kV, (c) 100 kV.

bremstrahlung and characteristic photons produced by them during their travel within the target (Kulkarni and Supe 1984). For simulation of x-ray spectra, MCNP4C was run in photon and electron mode (mode: P, E) using default values for PHYS:P and PHYS:E cards to enable full electron and photon transport (XNUM was modified in our experiments to investigate the intensity of produced characteristic photons).

The procedure starts with definition of an electron source (defined in our experiments as a point source) emitting the electrons with energy  $E$  within a solid angle  $\psi$  towards the target. The focal spot size on the target can be adjusted by changing this angle. Focal spot sizes of 0.3, 0.6 and 1.2 mm corresponding to the projection on the beam central axis of the large diameter of the ellipse covered by solid angle  $\psi$  on the target were investigated. Although the approximation of the focal spot shape by an ellipse is a rough estimation, it was considered reliable for the assessment of the influence of focal size on heel effect.

We have considered a constant energy for emitted electrons in most of the cases, although the effect of ripple in electrons energy was simulated in one experiment to study its effect on

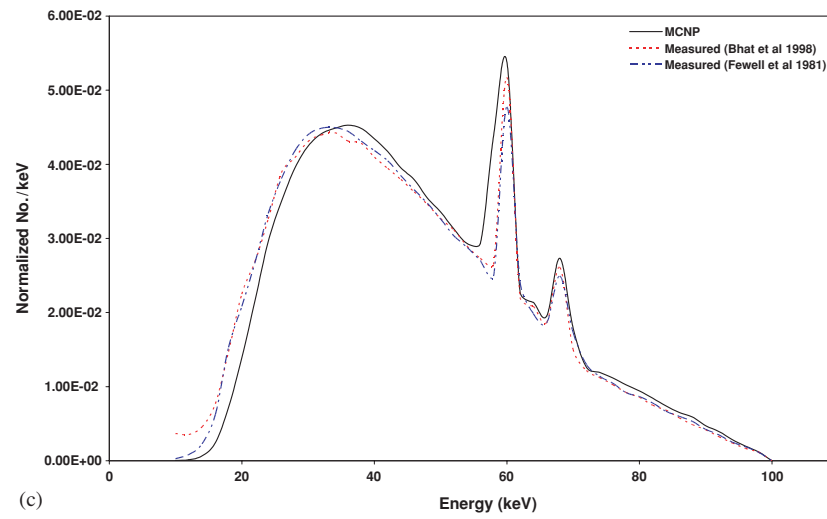


Figure 3. (Continued.)

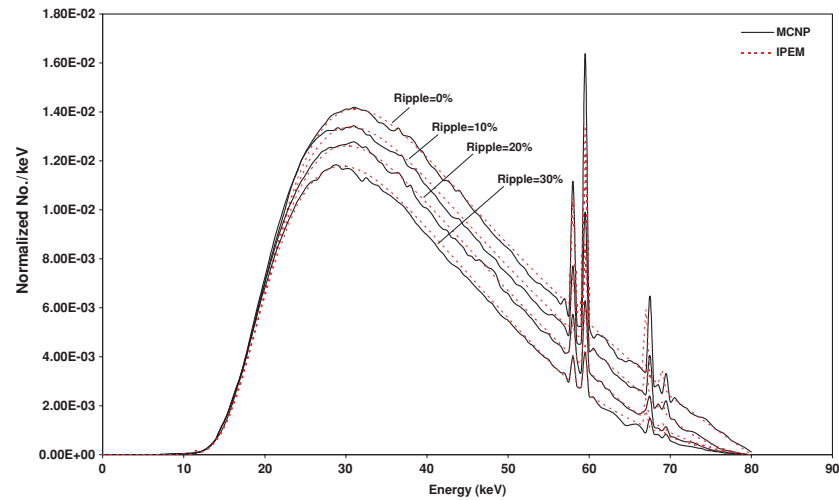


Figure 4. Comparison of x-ray spectra using various tube voltage ripple factors in 80 kV produced by MCNP4C and IPEM report 78.

the calculated spectra. To simulate ripple in MCNP4C, we used the following formulation for ripple factor and tube voltage (Boone and Seibert 1997):

$$\text{Ripple factor (RF)} = 100 \times \frac{kV_{\max} - kV_{\min}}{kV_{\max}}. \quad (1)$$

Thus, the energy of an electron before emission towards the target is sampled uniformly from tube voltage waveform with different ripple values:

$$kV(t) = kV_{\max} \left[ 1 - \frac{\text{RF}}{100} (1 - |\sin(\omega t)|) \right] \quad (2)$$

where  $t$  is time. When the ripple is neglected (i.e.  $\text{RF} = 0$ ),  $kV_{\max} = kV$ .

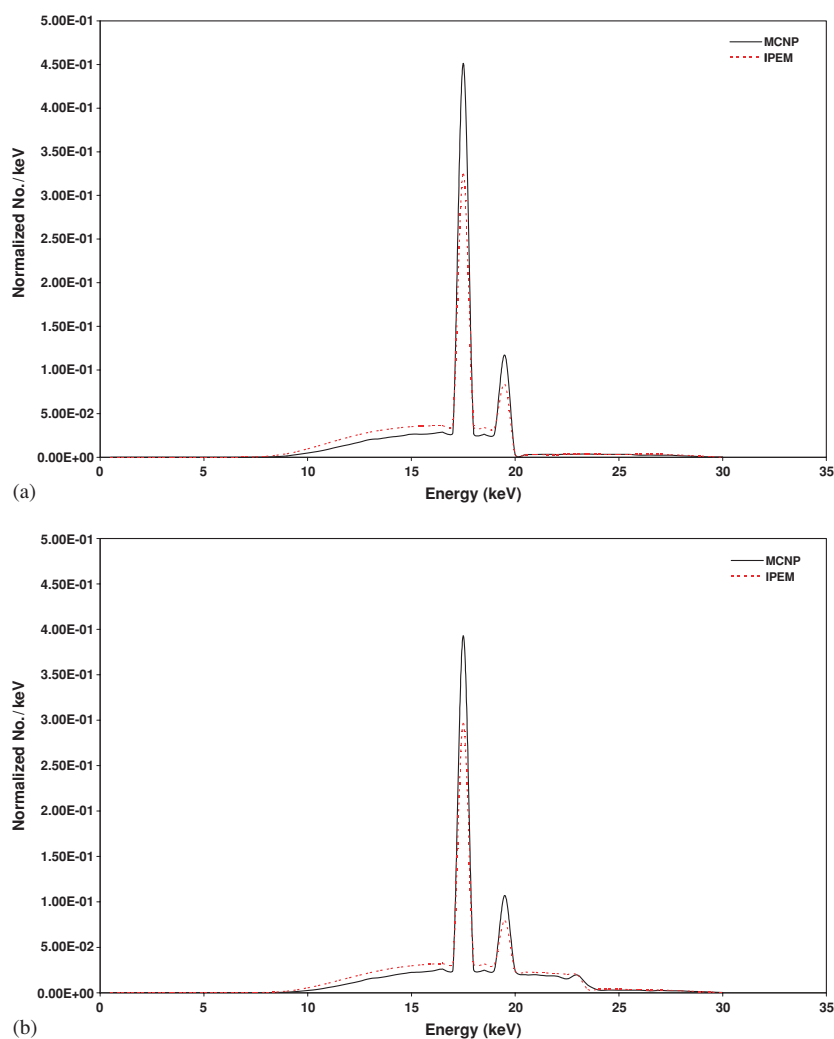


**Figure 5.** Comparison of 30 kV x-ray spectra produced by MCNP4C and IPEM report 78 for (a) Mo target with 0.5 mm Be and 0.03 mm Mo filter, (b) Mo target with 0.5 mm Be and 0.025 mm Rh and (c) W target with 0.5 mm Be and 1.2 mm Al.

When the electrons strike the target, the code transports the electrons inside the target material until they are stopped after losing their kinetic energy. During the electrons' transport, all bremsstrahlung and characteristic x-ray production is considered. The calculated spectrum is then normalized to the total number of photons in the spectrum. The experimental set-up used in our simulation was based on the RAD 60 x-ray tube (Varian Medical Systems, CA) material composition and target dimensions (figure 1).

MCNP4C simulations without applying variance reduction techniques require an unacceptably long time to produce statistically relevant results. Thus, a variance reduction technique known as point detector (F5 tally), belonging to the class of partially-deterministic variance reduction methods implemented in MCNP4C was used. In this method, the transport of particles towards the detector is replaced by a deterministic estimate of potential contribution to the detector (Briesmeister 2000). The point detector tally measures photon flux at a point

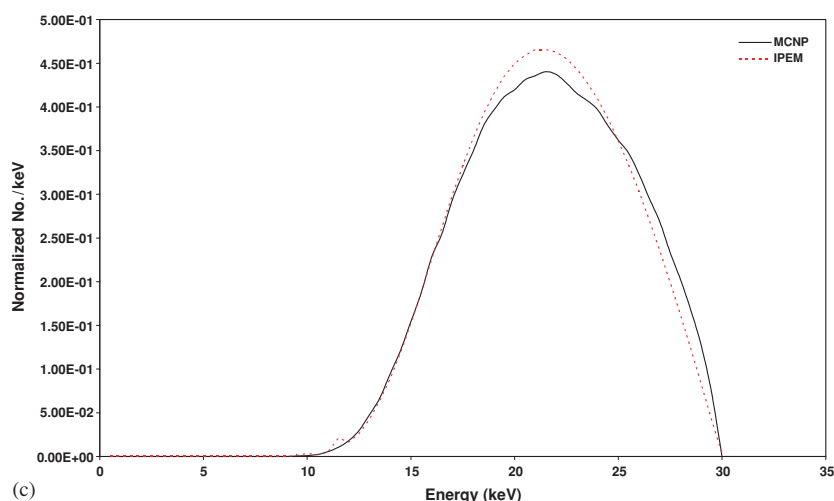


Figure 5. (Continued.)

(unit is photons  $\text{cm}^{-2}$  or  $\text{MeV cm}^{-2}$ ), which is normalized to be per starting particle. We used the unit photons  $\text{cm}^{-2}$  for spectra generation and  $\text{MeV cm}^{-2}$  for exposure assessment in the part related to investigation of anode heel effect. The point detectors were arranged in the calculation points *A* and *B* shown in figure 1 to calculate the exposure around the target and study anode heel effect. Note that the arrangement of point detectors for the calculation of exposure in the axis perpendicular to the anode–cathode axis is not shown. According to the MCNP user manual (Briesmeister 2000), an uncertainty of less than 5% is required for point detector tally (F5) to produce a generally reliable confidence interval. The maximum uncertainty regarding the number of produced photons within each energy bin of widths 0.5, 1 and 2 keV is less than 2% in our simulations, the magnitude of which depends on the number of simulated electrons (in our case  $4 \times 10^7$ ).

The x-ray beam is produced as electrons slow down in the anode and encounter some attenuation in the anode material depending on the anode angle and the beam direction. The x-rays propagate isotropically from the point of production, but the direction towards the Be window is the only one of interest for measurement of the x-ray spectra. After passing through the Be window, the x-ray spectrum passes through the additional filter material and air for further attenuation of the x-ray beam before the measurement point. Table 1 summarizes all the x-ray tube parameters investigated in the experiments carried out in this work. The simulated x-ray spectra using MCNP4C were compared with experimental measurements and spectra calculated by IPEM report number 78 described below. The comparative assessment encompassed calculation of transmission curves based on both computational models. The calculation of transmission curves involved running the code for different thicknesses of aluminium filter incrementing in 1 mm steps in radiology and 0.1 mm in mammography. To convert the photon spectra to kerma in air, the total number of transmitted photons in each energy bin for each thickness was multiplied by a related photon to kerma conversion factor (ICRU 1989) and then normalized relative to the air kerma without the filter being present.

Quantitative evaluation of the differences between Monte Carlo simulated and calculated spectra was performed using statistical analysis. The student's *t*-test values and the corresponding significance levels associated with the student's analysis (two-tailed test)

**Table 1.** Summary of x-ray tube parameters investigated in this work using MCNP4C-based Monte Carlo simulations.

Figure	Tube voltage (kV)	Target/Angle	Filter (mm)	FSD <sup>a</sup> (mm)
2a <sup>b</sup>	80–140	W/12°	1 Be/2.5 Al	750
2b <sup>b</sup>	140	W/12°	1 Be/2.5 Al/0.1 Cu	750
3a <sup>b</sup>	50	W/12°	1.2 Al	3500
3b <sup>b</sup>	80	W/12°	1.2 Al	3500
3c <sup>b</sup>	100	W/12°	1.2 Al	3500
4 <sup>b</sup>	80 (ripple 0–30%)	W/12°	1.2 Al	750
5a <sup>b</sup>	30	Mo/10°	0.5 Be/0.03 Mo	500
5b <sup>b</sup>	30	Mo/10°	0.5 Be/0.025 Rh	500
5c <sup>b</sup>	30	W/14°	0.5 Be/1.2 Al	750
6a,b <sup>b</sup>	30	Mo/10°	0.5 Be/0.03 Mo	500
7a <sup>c</sup>	50–140	W/12°	1.2 Al/0–20 Al	750
7b <sup>c</sup>	30	Mo/12°	1 Be/0.035 Mo/0–2 Al	500
8a,b,c <sup>b</sup>	100	W/12°	1.2 Al	3500
9a,b,c <sup>b</sup>	100	W/6°–14°	1.2 Al	750
10a <sup>d</sup>	100	W/12°	1.2 Al	3500
10b <sup>d</sup>	100	W/12°	1.2 Al	200
10c <sup>d</sup>	100	W/8°–12°	1.2 Al	750
11a <sup>d</sup>	80–140	W/6°–18°	1 Be/2.5 Al	750
11b <sup>d</sup>	25–35	Mo/6°–18°	0.5 Be/0.03 Mo	1000

<sup>a</sup> Distance between focal spot and measurement point.

<sup>b</sup> X-ray spectrum data.

<sup>c</sup> Transmission curve data.

<sup>d</sup> Radiation intensity data.

were calculated for the MCNP4C simulated spectra as compared to the IPEM report and experimental measurements. If the calculated *t*-value is greater than the critical *t*-value, the null hypothesis of no statistically significant difference (at the 95% confidence level) is rejected. It is worth pointing out that failure to prove statistically significant differences is not sufficient to confirm that the results are statistically identical. Generally, the paired *t*-test showed no statistically significant differences between the MCNP and IPEM spectra for all experiments performed in this work.

One unfortunate consequence of the line-focus principle is that the radiation intensity on the cathode side of the x-ray field is higher than that on the anode side. The intensity distribution falling on a plane at right angles on the axis of the window (e.g., a film or a screen) is not uniform owing to the anode heel effect (Bushong 1998). In our experiments, the anode heel effect and off-axis x-ray spectra were assessed for different anode angles and target materials and the results were compared with EGS4-based Monte Carlo simulations and measured data published by Bhat *et al* (1999).

### 2.3. IPEM report no. 78

The original version of the catalogue based on a semi-empirical model for computing x-ray spectra (Birch and Marshall 1979) was published in 1979 and provided essential data useful for applications in diagnostic radiology and mammography (Birch *et al* 1979). The current electronic version (Cranley *et al* 1997) contains sets of radiology and mammography x-ray spectra with much wider ranges than the previous version. This version uses the XCOM photon cross section library (Berger and Hubbell 1987) to calculate linear attenuation coefficients of various materials. The unattenuated photon spectra are given for tungsten targets, tube potential

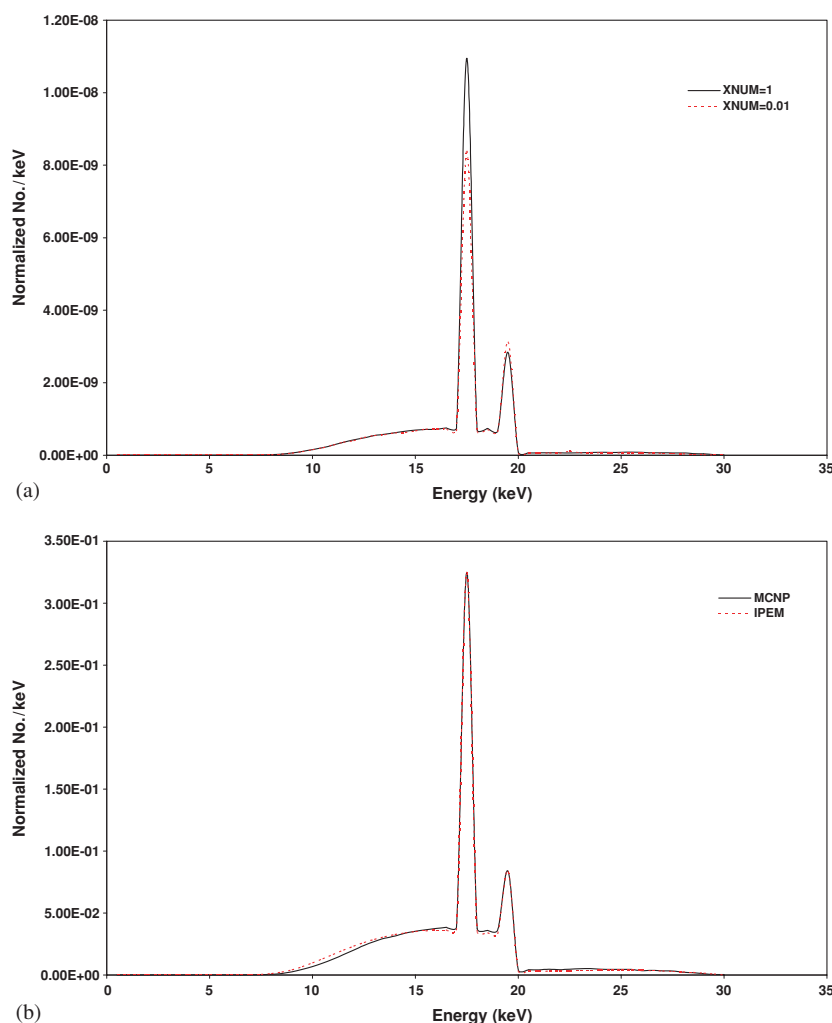


**Figure 6.** (a) Plots of 30 kV x-ray spectra simulated by MCNP4C for Mo target with 0.5 mm Be and 0.03 mm Mo filter produced for XNUM = 1 and 0.01. (b) Comparison between x-ray spectra produced by MCNP4C with XNUM = 1 and IPEM report 78 after manual setting of the intensity of characteristic photons in the MCNP4C spectra to match the value computed by IPEM.

from 30 kV to 150 kV, and target angles from  $6^\circ$  to  $22^\circ$ . The ripple value can be changed from 0 to 30%. Constant potential mammographic spectra are provided from 25 kV to 32 kV for molybdenum and rhodium targets for target angles ranging between  $9^\circ$  and  $23^\circ$ . All spectra are provided at energy bin width of 0.5 keV (Cranley *et al* 1997). The IPEM report 78 was used as reference to compare with the MCNP simulations because of its popularity and wide availability (Ng *et al* 2000).

### 3. Results and discussion

#### 3.1. X-ray spectra in diagnostic radiology and mammography

One of the most important parameters influencing the quality of the x-ray spectrum is filtration. The produced x-ray beam after attenuation in the target passes through the

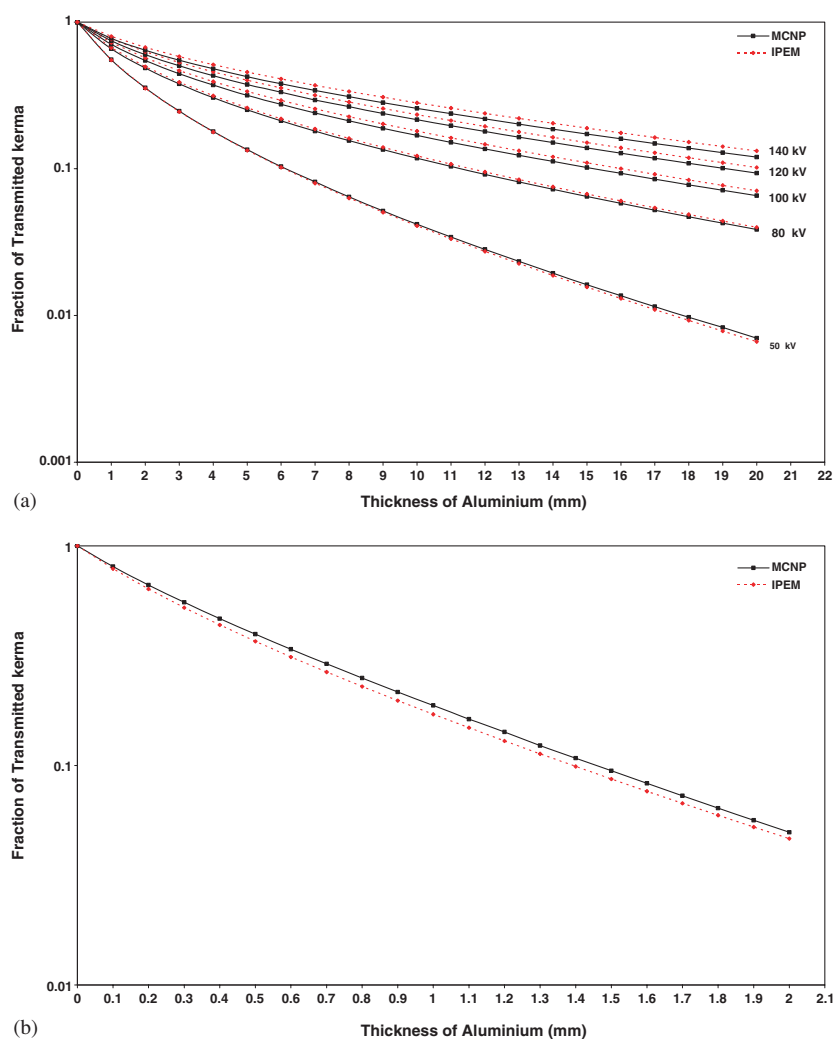


**Figure 7.** Comparison of transmission curves produced by MCNP4C and IPEM report 78 for (a) tungsten target between 50 and 140 kV and (b) molybdenum target at 30 kV.

tube's inherent filtration (e.g., Be window) and other filter materials (e.g., aluminium for the attenuation of soft x-rays). Figure 2(a) shows simulated x-ray spectra according to the set-up summarized in table 1 for different tube voltages and their comparison with IPEM report no. 78. The uncertainty achieved in figure 2(a) by simulating  $4 \times 10^7$  electrons is  $\sim 2\%$  and this value decreases to  $\sim 1\%$  in figure 2(b) by simulating  $1 \times 10^8$  electrons. Figure 2(b) shows the simulated x-ray spectrum and its comparison with the IPEM report no.78 for 140 kV tube voltage using a different filter combination, namely 2.5 mm Al, 1 mm Be and 0.1 mm Cu additional filter.

The x-ray spectrum shows significant tungsten  $K$  x-rays at 58, 59.5, 67.5 and 69 keV, the small shift in characteristic x-ray energy being the result of binning the data into 0.5 keV energy intervals. It can be seen that our results have good agreement with the IPEM report with small differences visible in the intensity of characteristic x-rays and the low energy range, namely between 20 and 40 keV. The intensity of  $K_{\alpha 1}$  (59 keV) and  $K_{\alpha 2}$  (58 keV) x-ray production by

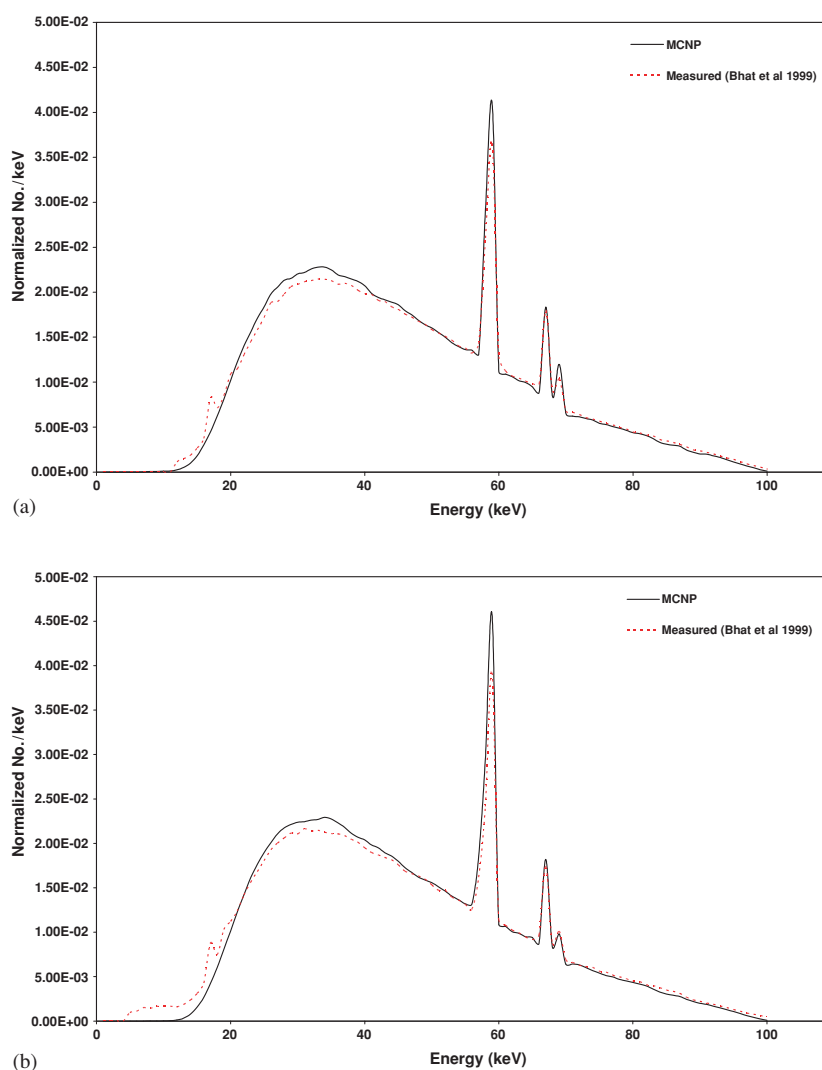


**Figure 8.** Comparison of simulated and measured on- and off-axis x-ray spectra for 100 kV tube voltage. (a) Central axis, (b)  $6^\circ$  cathode side and (c)  $6^\circ$  anode side.

MCNP4C is slightly higher than IPEM in tube voltages lower than 100 kV and this behaviour is reversed for tube voltages greater than 100 kV while the intensity of  $K_{\beta 1}$  (67 keV) and  $K_{\beta 2}$  (69 keV) characteristic photon production by IPEM is higher than MCNP4C for all tube voltages. This is consistent with the observations made by Verhaegen *et al* (1999) using the previous version of the code (MCNP4B). Characteristic photons in MCNP are created by the electron impact ionization (EII) process. However, the model overestimates the total number of EII characteristic photons especially in the mammography energy range. This is regulated by the parameter XNUM on the PHYS:E card, which is used to control the sampling of x-ray photons produced along electron substeps.

Figure 3 compares simulated spectra (2 keV energy bin) with experimental spectra published by Fewell *et al* (1981) and Bhat *et al* (1998) for different tube voltages. The simulated spectra have higher intensity in characteristic x-rays for the reasons mentioned

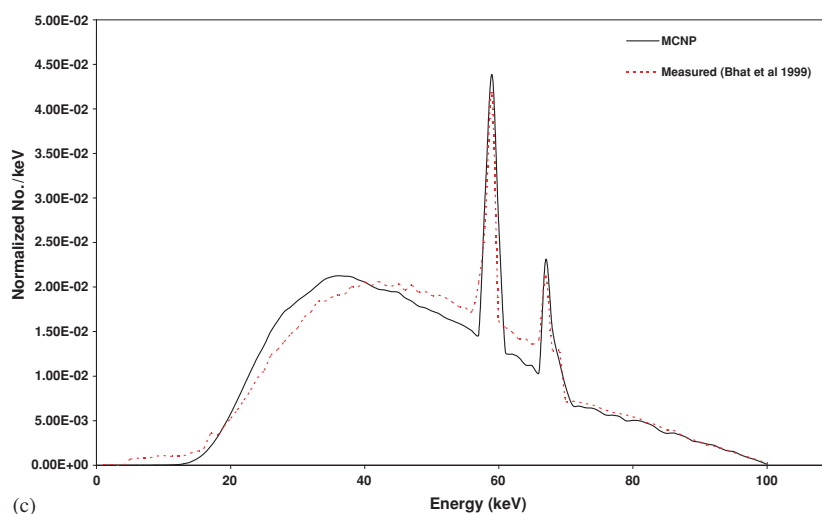
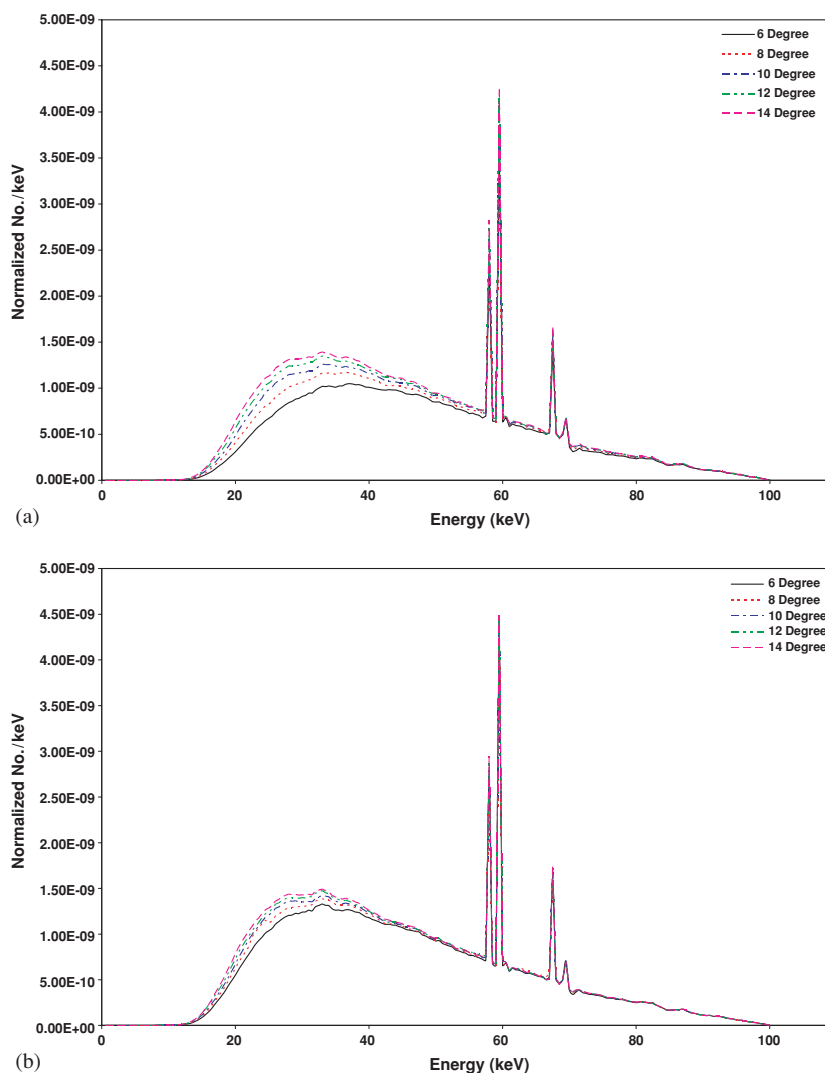


Figure 8. (Continued.)

above. Note that a pure tungsten target was used in our simulation, while the targets used in the experimental measurements have some rhenium and molybdenum impurity. It is worth emphasizing that both el03 and el1 treatments only take into account the highest Z component of the material for production of k-shell x-rays in MCNP (Briesmeister 2000). Thus, the tungsten k-shell masks the x-ray characteristic of added low Z impurities. Figure 4 shows the effect of tube voltage ripple on production of simulated x-ray spectra and its comparison with IPEM report no. 78. Some authors modelled the tube voltage ripple by combining a number of spectra generated at different constant tube potentials, each one being weighted according to the time for which that tube potential occurs (Boone and Seibert 1997, Cranley *et al* 1997). In our experiments, we modelled the tube voltage ripple during Monte Carlo simulation of x-ray spectra by uniformly sampling from the tube voltage waveform (equation (2)). Similar to the results reported above, there is good agreement between simulated and calculated spectra apart from the small shift in characteristic photon energy for the reasons explained above. A 30% ripple is probably higher than most inverter generators as most of them produce ripple factors between 5% and 15% (Boone and Seibert 1997).

Comparisons of the simulated x-ray spectra using MCNP4C with IPEM report 78 for different target/filter material combinations including molybdenum and tungsten as targets and molybdenum, rhodium and aluminium as filters are shown in figure 5. Although there are no statistically significant differences between MCNP4C and IPEM data in Mo target material, the low energy x-ray (<19.5 keV) intensity calculated by IPEM is higher than MCNP4C, which is again the result of the significant overestimation of the intensity of characteristic x-rays in MCNP4C following the normalization procedure. The same observations were reported by Wilkinson *et al* (2001), where the characteristic x-rays in their measured spectrum at 20 keV had a higher intensity in comparison with the IPEM model predictions.

Figure 5(b) shows that the rhodium filter transmits more bremsstrahlung radiation than the Mo filter especially for energies greater than 20 keV, because the attenuation of the Rh filter in this energy range is lower than the attenuation of the Mo filter. Figure 5(c) shows the tungsten target spectra where the spectrum generated by MCNP4C has good agreement with IPEM in the energy range <17 keV, but the intensity of the spectrum in the energy range 17–25 keV is lower than IPEM. This behaviour is reversed for energies >25 keV.



**Figure 9.** Simulated x-ray spectra for 140 kV tube voltage for various target angles. (a) Central axis. (b)  $6^\circ$  cathode side. (c)  $6^\circ$  anode side.

The optimal adjustment of the XNUM parameters in the PHYS:E card to reduce the intensity of characteristic x-ray production proved to be a difficult issue. Figure 6(a) shows the difference between the simulated spectra with different values of XNUM (1 and 0.01) with the set-up used in figure 5(a). It can be shown that the difference between MCNP simulated spectra and IPEM spectra in the low energy range (figures 5(a) and (b)) is the result of the overestimation of characteristic photons following the normalization procedure. Good agreement between the spectra has been achieved (figure 6(b)) after manual adjustment of the characteristic x-ray intensity in the MCNP spectrum (XNUM = 1) to match the value of the IPEM spectra.

The difference in the quality of x-ray spectra produced by MCNP4C and IPEM report no.78 is further illustrated in figure 7 which shows the transmission curves through an aluminium filter computed from various spectra in increments of 1 mm in diagnostic radiology

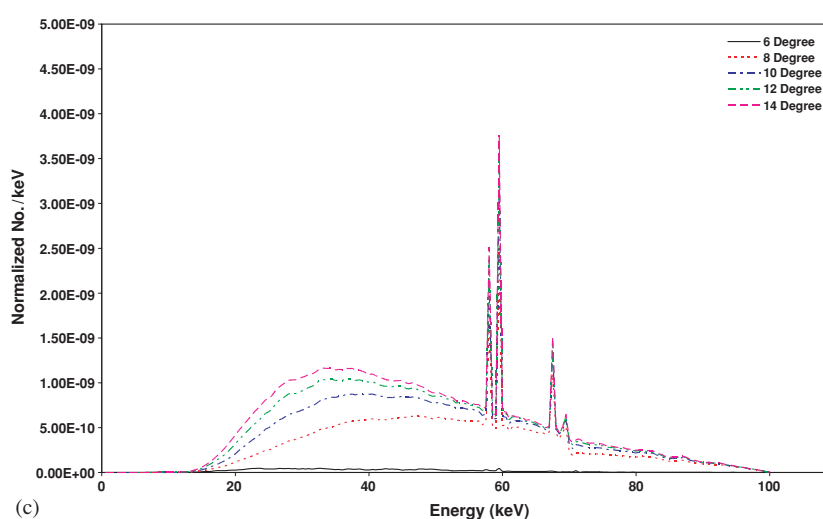


Figure 9. (Continued.)

**Table 2.** Comparison between measured, calculated (IPEM report 78) and simulated (MCNP4C) HVLs and mean spectrum energy for spectra produced using 12° target angle and different tube voltages. The percentage difference between IPEM and MCNP4C estimates is also shown.

kV	Target material	Filter (mm)	Mean spectrum energy (keV)			First HVL (mm Al)				
			IPEM	MCNP	Diff (%)	Bhat (1998)	Fewell (1981)	IPEM	MCNP	Diff (%)
30	Mo	0.5 Be 0.035 Mo	16.8	17.0	-1.2	-	-	0.32	0.35	-9.4
50	W	1.2 Al	29.9	29.4	+1.7	1.32	-	1.19	1.18	+0.8
80	W	1.2 Al	40.5	40.4	+0.3	1.80	1.81	1.97	1.95	+1.0
100	W	1.2 Al	46.9	46.2	+1.5	2.35	2.29	2.64	2.51	+4.9
120	W	1.2 Al	52.6	51.6	+1.9	-	-	3.38	3.17	+6.2
140	W	1.2 Al	57.4	56.3	+1.9	-	-	4.19	3.75	+10.5

and 0.1 mm in mammography. The transmission curves produced by MCNP4C have good agreement with the IPEM report especially for tube voltages of 50 kV and 80 kV. The systematic discrepancy for higher tube voltages is the result of systematic differences between the corresponding spectra (figure 2). The average and maximum differences in transmission curves for energies between 50 and 140 kV (five energies) are -2.7, 3.2, 6, 6.7, 7.31% and -5.9, 3.8, 7.5, 8.4, 9.2%, respectively (figure 7(a)).

Table 2 compares the mean spectrum energy and HVL for different tube voltages as measured by physical experiments and calculated using IPEM and MCNP4C spectra. The percentage differences vary between -1.2% to 1.9% and -9.4% to 10.5% for mean spectrum energy and HVLs, respectively, for all tube voltages and targets/filters investigated. The results indicate that the percentage difference between HVLs calculated from MCNP4C spectra and IPEM spectra increases with increasing tube voltage. Moreover, the mean energy of IPEM spectra in the diagnostic radiology energy range is higher than spectra calculated by MCNP4C. The amplitude of this difference increases with increasing tube voltage, thus increasing the differences between transmission curves. The higher quality of IPEM spectra for tube voltages

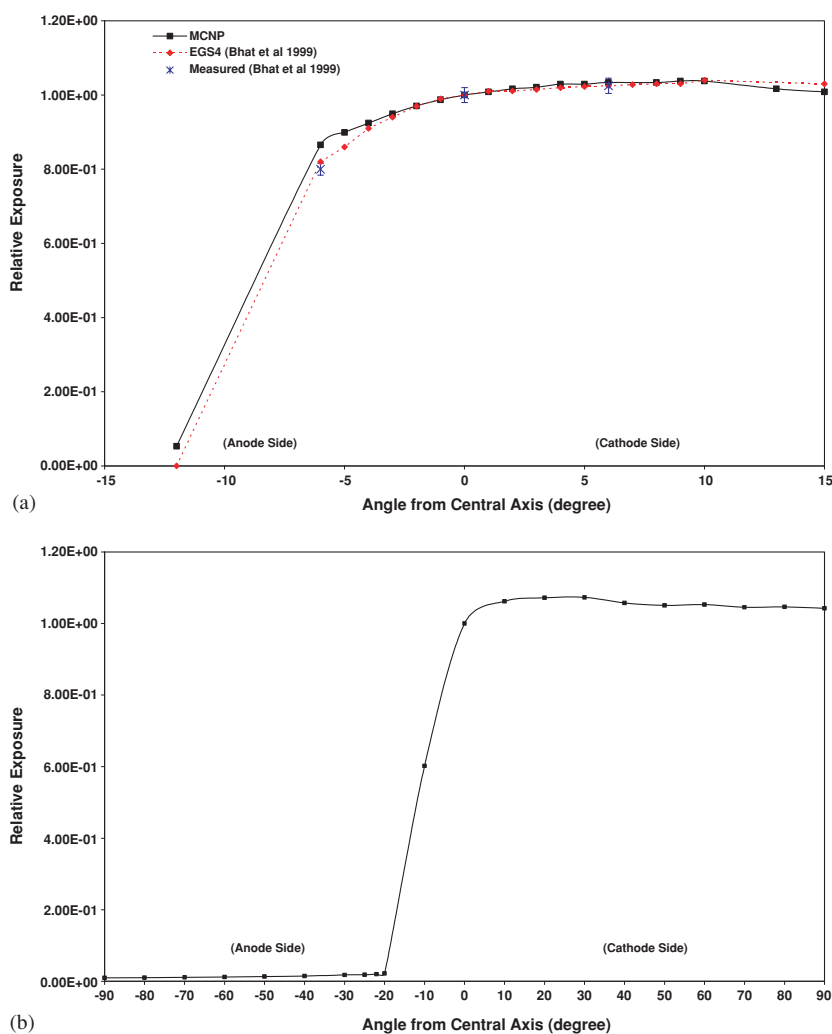
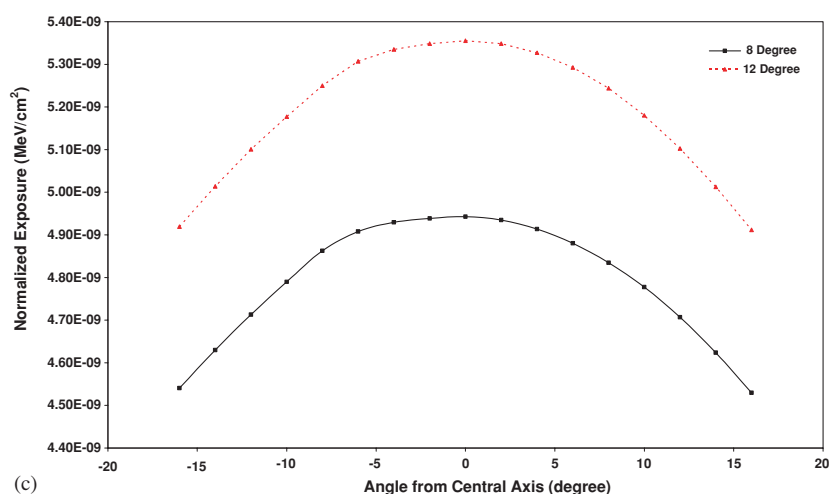


**Figure 10.** (a) Comparison of simulated and measured relative exposure values in different directions relative to the central axis (calculation points B in figure 1). (b) Relative exposure around the target (calculation points A in figure 1). (c) Normalized exposure on the axis perpendicular to the anode–cathode axis.

higher than 80 kV induces higher values in transmission curves in comparison with MCNP4C spectra.

In our simulation of x-ray spectra resulting from the use of different target/filter combinations in mammography, the tube voltage was assumed to be 30 kV. The transmission curve for the spectrum produced from a molybdenum target with 1 mm Be and 0.035 mm Mo additional filter was calculated. An uncertainty of 0.6% was reached by simulating  $3 \times 10^7$  electrons. In the mammography energy range, the quality of MCNP4C spectra is higher than IPEM, thus the IPEM transmission curves have lower values compared to those estimated by MCNP4C. The average and maximum differences observed are  $-7.6\%$  and  $-9.8\%$  at tube voltage 30 kV in mammography (figure 7(b)). To further investigate the validity of our simulation results, we compared our calculated HVL with measured data published by the



(c)

Figure 10. (Continued.)

SSDL laboratory of the IAEA (Pernieka *et al* 1997). They reported 0.348 mm Al for first HVL while we calculated 0.35 mm ( $-0.6\%$  difference). Note that there are some differences between their experimental set-up (0.8 mm Be filter, 0.03 mm Mo filter,  $20^\circ$  Mo target angle) and our simulation set-up (1 mm Be filter, 0.035 mm Mo filter,  $12^\circ$  Mo target angle). According to our estimation, the  $8^\circ$  difference in target angle produces  $3.8\%$  difference in the first HVL.

### 3.2. Assessment of anode heel effect in diagnostic radiology and mammography

Figure 8 shows the on- and off-axis spectra for a tungsten target at  $6^\circ$  anode side and  $6^\circ$  cathode side and compares them with experimental measurements (Bhat *et al* 1999). The shape of the anode side spectrum after passing through the target skewed towards the higher energy with some distortion in the characteristic tungsten x-ray at 69.5 keV (figure 8(c)). Figure 9 shows the central axis and off-axis x-ray spectra for different target angles. The anode side spectrum encounters more attenuation when using small target angles while the cathode side spectra are approximately similar for all target angles except for a slightly higher attenuation for small target angles in the low energy range.

Figure 10(a) shows the variation of relative exposure with respect to the central axis (calculation points B in figure 1) as simulated by the MCNP4C code and compares it with experimental measurements and EGS4-based Monte Carlo simulations published by Bhat *et al* (1999). The average difference between EGS4 and MCNP simulations for 18 different angles is  $0.8\%$ . The maximum difference is  $-5.5\%$  at  $6^\circ$  anode side, while the maximum difference between MCNP and measured data is  $-8.2\%$  in the same position. Generally there is good agreement between the relative exposure estimated by MCNP, EGS4 and the experimental data on the cathode side. A small discrepancy ( $-1.6\%$ ) is, however, visible starting from  $4^\circ$  anode side due in our opinion to differences in target dimensions used in both experiments. The radiation escaping from the x-ray tube housing through areas other than the desired x-ray window increases the dose to the patient and surroundings. Figure 10(b) shows the relative exposure around the target at distance 200 mm from the focal spot, which is useful for calculation of x-ray tube shielding. The exposure has been calculated after attenuation of produced x-ray spectra by a 1.2 mm Al filter (calculation points A in figure 1). Obviously, the

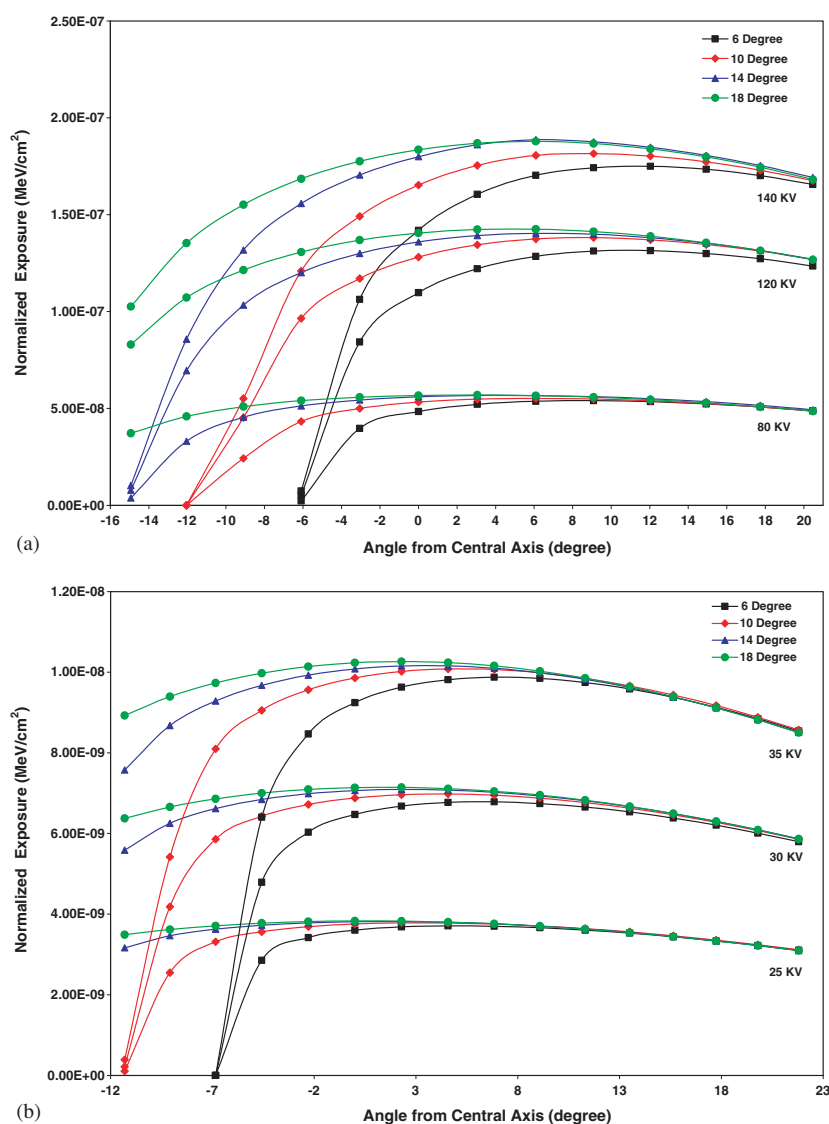


**Figure 11.** Illustration of anode heel effect for different anode angles for (a) tungsten target with tube voltages between 80 and 140 kV and for (b) molybdenum target with the tube voltages between 25 and 35 kV.

relative exposure on the cathode side is higher than that on the anode side owing to attenuation of the x-ray spectra in the target.

Another problem in x-ray imaging is nonuniformity of exposure in the direction perpendicular to the anode–cathode axis, bearing in mind that the field of view is usually rectangular. Figure 10(c) shows the variation of exposure (normalized to  $2 \times 10^7$  simulated electrons) on this axis for  $8^\circ$  and  $12^\circ$  target angles at 100 kV tube voltage. The off-axis exposure is identical on both sides of the central axis and the absorption at small target angles is higher than that at large target angles. In addition, we have calculated the off-axis spectra in both cases. The results show that the off-axis and central axis spectra have approximately the same shape without any distortion similar to data shown in figure 9. Our further investigation

**Table 3.** Variation in radiation exposure for various target angles and tube voltages in the useful x-ray beam.

Tube voltage (kV)	Target material	Difference in radiation exposure in the useful beam <sup>a</sup> (%)			
		Target angle			
		6°	10°	14°	18°
25	Mo	96.0	11.7	3.7	1.3
30	Mo	96.7	15.7	5.7	2.7
35	Mo	97.4	19.8	8.0	4.6
80	W	92.0	21.6	9.5	4.4
120	W	94.2	30.7	14.3	8.4
140	W	94.4	33.2	17.5	11.15

<sup>a</sup> From 6° anode side until 6° cathode side.

of the influence of focal spot size on anode heel effect performed by calculating the heel effect for different focal spot sizes (0.3, 0.6, 1.2 mm) indicated that its effect is negligible.

Figure 11(a) shows the anode heel effect for different target angles and tube voltages. The relative difference in radiation exposure in the useful x-ray beam (6° anode side until 6° cathode side) calculated from figure 11(a) is shown in table 3. To demonstrate the validity of results presented in this table, we have compared our simulated data for 12° target angle and 100 kV with experimentally measured and EGS4 Monte Carlo simulation results published by Bhat *et al* (1999). It turns out that the difference in radiation exposure calculated by MCNP4C is 20.5% while this value is 20.0% for EGS4 and 22.0% for measured data (figure 10(a)).

In theory, the anode heel effect is of considerable importance in mammography. It is expected that the conic shape of breasts would require greater radiation intensity near the chest wall rather than to the nipple side so that near uniform exposure of the image receptor will occur. This could be accomplished by positioning the cathode on the chest wall side. However, in practice this is not necessary because compression of the breast ensures that a uniform thickness of tissue is imaged (Bushong 1998). Figure 11(b) shows the anode heel effect for different target angles and tube voltages for Mo/Mo target/filter combinations. The difference in radiation exposure in the useful x-ray beam calculated from figure 11(b) is shown in table 3. It can be seen that the radiation exposure difference in the mammography energy range increases by increasing the tube voltage and decreasing the target angle.

#### 4. Conclusion

Monte Carlo simulation of x-ray spectra has been used extensively in different medical imaging applications including assessment of image quality, optimization of system design and absorbed dose calculation (Caon *et al* 1998, Dance *et al* 2000, Spyrou *et al* 2002, Zaidi and Sgouros 2002). This study used the MCNP4C general-purpose Monte Carlo code for generating x-ray spectra in diagnostic radiology and mammography. Although the simulation of x-ray spectra using the Monte Carlo method is time consuming, the generated x-ray spectra provide detailed information about particles' interaction with different target and filter combinations. This information is useful for x-ray tube design and development of new target/filter combinations to improve image quality in diagnostic radiology and mammography.

The generated x-ray spectra in this work have been verified against IPEM report number 78, experimental measurements and EGS4 Monte Carlo simulations for validation. Although

the paired *t*-test results show no statistically significant differences between simulated and reference spectra, the intensity of characteristic x-rays in MCNP4C simulated spectra is slightly higher than that in IPEM spectra for tube voltages <100 kV, and this behaviour is reversed for tube voltages >100 kV in the diagnostic radiology energy range. Whereas MCNP produces a significantly higher intensity of characteristic x-rays compared to IPEM in mammography when using a Mo target. This discrepancy can be tackled by appropriate adjustment of the XNUM parameter. The results indicate that the MCNP4C general purpose Monte Carlo code with some small adjustment in the appropriate MCNP cards is a useful tool for generating diagnostic radiology and mammography x-ray spectra and investigation of the heel effect.

### Acknowledgments

This work was supported by the AmirKabir University of Technology, Department of Physics and Nuclear Sciences and the Swiss National Science Foundation under grant SNSF 3152A0-102143. The authors are indebted to M Bhat for providing measured and EGS4 simulated data.

### References

- Acosta E, Liovet X, Coleoni E, Riveros J A and Salvat F 1998 Monte Carlo simulation of x-ray emission by kilovolt electron bombardment *J. Appl. Phys.* **83** 6038–49
- Antonuk L E *et al* 1997 Empirical investigation of the signal performance of a high-resolution, indirect detection, active matrix flat-panel imager (AMFPI) for fluoroscopic and radiographic operation *Med. Phys.* **24** 51–70
- Ay M, Sarkar S, Shahriari M, Sardari D and Zaidi H 2004 Comparative assessment of different computational models for generation of x-ray spectra in diagnostic radiology and mammography *Proc. IEEE Nuclear Science Symposium and Medical Imaging Conference (Rome, Oct 19–22)* at press
- Ben Omrane L, Verhaegen F, Chahed N and Mtimet S 2003 An investigation of entrance surface dose calculations for diagnostic radiology using Monte Carlo simulations and radiotherapy dosimetry formalisms *Phys. Med. Biol.* **48** 1809–24
- Berger M J and Hubbell J H 1987 XCOM: photon cross sections on a personal computer *NBSIR 87-3597* (National Bureau of Standards (US))
- Bhat M, Pattison J, Bibbo G and Caon M 1998 Diagnostic x-ray spectra: a comparison of spectra generated by different computational methods with a measured spectrum *Med. Phys.* **25** 114–20
- Bhat M, Pattison J, Bibbo G and Caon M 1999 Off-axis x-ray spectra: a comparison of Monte Carlo simulated and computed x-ray spectra with measured spectra *Med. Phys.* **26** 303–9
- Birch R and Marshall M 1979 Computation of bremsstrahlung x-ray spectra and comparison with spectra measured with a Ge(Li) detector *Phys. Med. Biol.* **24** 505–17
- Birch R, Marshall M and Ardran G M 1979 Catalogue of spectral data for diagnostic x-rays hospital physicists *Association Scientific Report Series 30*
- Blough M M, Waggener R G, Payne W H and Terry J A 1998 Calculated mammographic spectra confirmed with attenuation curves for molybdenum, rhodium, and tungsten targets *Med. Phys.* **25** 1605–12
- Boone J M 1988 The three parameter equivalent spectra as an index of beam quality *Med. Phys.* **15** 304–10
- Boone J M, Fewell T R and Jennings R J 1997 Molybdenum, rhodium, and tungsten anode spectral models using interpolating polynomials with application to mammography *Med. Phys.* **24** 1863–74
- Boone J M and Seibert J A 1997 An accurate method for computer-generating tungsten anode x-ray spectra from 30 to 140 kV *Med. Phys.* **24** 1661–70
- Briesmeister J F 2000 MCNP—a general Monte Carlo N-particle transport code. version 4C *Los Alamos National Laboratory Report LA-13709-M* (Los Alamos, NM)
- Bushong S C 1998 *Radiologic Science for Technologists: Physics, Biology and Protection* (St. Louis: Mosby Co)
- Caon M, Bibbo G, Pattison J and Bhat M 1998 The effect on dose to computed tomography phantoms of varying the theoretical x-ray spectrum: a comparison of four diagnostic x-ray spectrum calculating codes *Med. Phys.* **25** 1021–7

- Cranley K, Gilmore B J, Fogarty G W A and Desponds L 1997 *IPEM Report 78: Catalogue of Diagnostic X-ray Spectra and Other Data* (CD-Rom Edition 1997) (*Electronic Version prepared by D Sutton*) (York: The Institute of Physics and Engineering in Medicine (IPEM))
- Dance D *et al* 2000 Influence of anode/filter material and tube potential on contrast, signal-to-noise ratio and average absorbed dose in mammography: a Monte Carlo study *Br. J. Radiol.* **73** 1056–67
- Fewell T R and Shuping R E 1977 Photon energy distribution of some typical diagnostic x-ray beams *Med. Phys.* **4** 187–97
- Fewell T R and Shuping R E 1978 *Handbook of Mammography Spectra* (HEW Publication) (FDA) 79-8071
- Fewell T R, Shuping R E and Healy K E 1981 *Handbook of Computed Tomography X-Ray Spectra* (HHS Publication) (FDA) 81-8162 (Washington, DC: US Govt. Printing Office)
- Hughes H G 1997 Status of electron transport in MCNP *Los Alamos National Laboratory LA-UR-97-1368* (Los Alamos, NM)
- ICRU 1989 Tissue Substitutes in Radiation Dosimetry and Measurement *ICRU Report 44* (Bethesda, MD: International Commission on Radiological Units and Measurements (ICRU))
- Kramers H A 1923 On the theory of x-ray absorption and of the continuous x-ray spectrum *Phil. Mag.* **46** 836–71
- Kulkarni R N and Supe S J 1984 Monte Carlo calculations of mammographic x-ray spectra *Phys. Med. Biol.* **29** 185–90
- Laitano R F, Pani R and Pellegrini R 1991 Determination of x-ray spectra and of the scattered component up to 300 kV *Med. Phys.* **18** 934–8
- Mercier J R *et al* 2000 Modification and benchmarking of MCNP for low-energy tungsten spectra *Med. Phys.* **27** 2680–7
- Ng K P, Kwok C S and Tang F H 2000 Monte Carlo simulation of x-ray spectra in mammography *Phys. Med. Biol.* **45** 1309–18
- O'Meara J M, Chettle D R, McNeill F E, Prestwich W V and Svensson C E 1998 Monte Carlo simulation of source-excited *in vivo* x-ray fluorescence measurements of heavy metals *Phys. Med. Biol.* **43** 1413–28
- Pernieka F, Andreo P, Meghziefene A, Czap L and Girzikowsky R 1997 Standards for radiation protection and diagnostic radiology at the IAEA dosimetry laboratory SSDL Newsletter 17 (Vienna: International Atomic Energy Agency)
- Spyrou G, Tzanakos G, Nikiforides G and Panayiotakis G 2002 A Monte Carlo simulation model of mammographic imaging with x-ray sources of finite dimensions *Phys. Med. Biol.* **47** 917–33
- Tucker D M, Barnes G T and Chakraborty D P 1991 Semiempirical model for generating tungsten target x-ray spectra *Med. Phys.* **18** 211–8
- Verhaegen F and Castellano I A 2002 Microdosimetric characterisation of 28 kVp Mo/Mo, Rh/Rh, Rh/Al, W/Rh and Mo/Rh mammography x ray spectra *Radiat. Prot. Dosim.* **99** 393–6
- Verhaegen F, Nahum A E, Van de Putte S and Namito Y 1999 Monte Carlo modelling of radiotherapy kV x-ray units *Phys. Med. Biol.* **44** 1767–89
- Wilkinson L E, Johnston P N and Heggie J C 2001 A comparison of mammography spectral measurements with spectra produced using several different mathematical models *Phys. Med. Biol.* **46** 1575–89
- Zaidi H and Sgouros G (ed) 2002 *Therapeutic Applications of Monte Carlo Calculations in Nuclear Medicine* (Bristol: Institute of Physics Publishing)

# Paper II

*Med Phys* **32**: 1660-1675

© Reprinted with Permission From  
The American Association of Physicists in Medicine

# Assessment of different computational models for generation of x-ray spectra in diagnostic radiology and mammography

M. R. Ay<sup>a)</sup>

*Department of Physics & Nuclear Sciences, AmirKabir University of Technology, Tehran, Iran, and Division of Nuclear Medicine, Geneva University Hospital, 1211 Geneva, Switzerland*

S. Sarkar

*Department of Medical Physics, Tehran University of Medical Science & RCSTIM, Tehran, Iran*

M. Shahriari

*Department of Nuclear Engineering, Shahid Beheshti University, Tehran, Iran*

D. Sardari

*Department of Physics & Nuclear Sciences, AmirKabir University of Technology, Tehran, Iran*

H. Zaidi

*Division of Nuclear Medicine, Geneva University Hospital, 1211 Geneva, Switzerland*

(Received 12 November 2004; revised 8 February 2005; accepted for publication 19 March 2005; published 24 May 2005)

Different computational methods based on empirical or semi-empirical models and sophisticated Monte Carlo calculations have been proposed for prediction of x-ray spectra both in diagnostic radiology and mammography. In this work, the x-ray spectra predicted by various computational models used in the diagnostic radiology and mammography energy range have been assessed by comparison with measured spectra and their effect on the calculation of absorbed dose and effective dose (ED) imparted to the adult ORNL hermaphroditic phantom quantified. This includes empirical models (TASMIP and MASMIP), semi-empirical models (X-rayb&m, X-raytbc, XCOMP, IPEM, Tucker *et al.*, and Blough *et al.*), and Monte Carlo modeling (EGS4, ITS3.0, and MCNP4C). As part of the comparative assessment, the K x-ray yield, transmission curves, and half value layers (HVLs) have been calculated for the spectra generated with all computational models at different tube voltages. The measured x-ray spectra agreed well with the generated spectra when using X-raytbc and IPEM in diagnostic radiology and mammography energy ranges, respectively. Despite the systematic differences between the simulated and reference spectra for some models, the student's *t*-test statistical analysis showed there is no statistically significant difference between measured and generated spectra for all computational models investigated in this study. The MCNP4C-based Monte Carlo calculations showed there is no discernable discrepancy in the calculation of absorbed dose and ED in the adult ORNL hermaphroditic phantom when using different computational models for generating the x-ray spectra. Nevertheless, given the limited flexibility of the empirical and semi-empirical models, the spectra obtained through Monte Carlo modeling offer several advantages by providing detailed information about the interactions in the target and filters, which is relevant for the design of new target and filter combinations and optimization of radiological imaging protocols. © 2005 American Association of Physicists in Medicine.

[DOI: 10.1118/1.1906126]

## I. INTRODUCTION

A detailed knowledge of x-ray spectra is required for the mathematical modeling and optimization of imaging systems in diagnostic radiology. The direct measurement of spectra, however, requires expensive equipment and careful attention and planning during the experimental measurement setup,<sup>1-6</sup> which is generally not practical in a clinical diagnostic radiology department with limited physics support. Since direct measurement of x-ray spectra is time consuming and remains a difficult task, attempts for prediction of x-ray spectra in different energy ranges and various target/filter combinations have begun several decades ago and still represent an active research area. Generally the x-ray prediction models

can be divided into three categories: empirical,<sup>7-11</sup> semi-empirical,<sup>12-17</sup> and Monte Carlo calculations.<sup>4,18-21</sup>

Empirical models are based on the use of measured data for prediction of x-ray spectra. Early attempts by Silberstein<sup>22</sup> relied on the determination of x-ray spectra from measurement of x-ray attenuation curve. Several groups made every effort to analyze the attenuation data as accurately as possible by different mathematical methods such as analytical modeling,<sup>23</sup> Laplace transform,<sup>24</sup> iterative methods,<sup>11,25</sup> matrix manipulation,<sup>26</sup> and neural networks.<sup>27</sup> Nevertheless, the calculation of x-ray spectra from attenuation curves is subject to errors in two respects. First, attenuation measurement with various detectors will yield different values for the same spectrum due to different response of detectors.<sup>28</sup> Second, it would be possible to calculate different spectra from identical attenuation curves. An alternative

method proposed by Boone *et al.*<sup>9,10</sup> fits the highest order polynomial to the measured spectra without any assumption concerning the physics of x-ray production.

Semi-empirical models are based on a theoretical formulation to calculate the x-ray spectra by mathematical derivation followed by some tuning in the equations' parameters using measured spectra. The earliest theoretical model of differential intensity of the bremsstrahlung was introduced by Kramers.<sup>29</sup> This model was modified later on to include the target attenuation.<sup>23</sup> Birch and Marshal<sup>12</sup> adjusted some parameters in the latter model to give good agreement with experimental data. They used Green's formulation<sup>30</sup> for estimating the characteristic radiation with some modifications using experimental measurements. Iles<sup>14</sup> included a term for electron backscatter from the target to this model whereas Tucker *et al.*<sup>15</sup> modified this model by incorporating appropriate modeling for the fact that the bremsstrahlung and characteristic x rays are produced in different depths in the target. They used the Vignes and Dez<sup>31</sup> approach with some modifications to estimate the characteristic radiations and proposed another model for generating molybdenum target x-ray spectra by extending the tungsten target model.<sup>16</sup> Blough *et al.*<sup>17</sup> proposed a model based on Tucker *et al.*'s work using mathematical formulation instead of semi-empirical functions for production of mammography spectra.

On the other hand, Monte Carlo calculations use direct transport of electrons and generated photons in the target and filter for calculation of x-ray spectra. Monte Carlo simulation has proven to be the most suitable theoretical tool for the computation of x-ray spectra in complex geometries. For this purpose, some groups used self-written or in house developed computer codes,<sup>18</sup> while others used public domain general-purpose Monte Carlo codes such as EGS4,<sup>4</sup> MCNP,<sup>19,21,32</sup> and ITS.<sup>20</sup>

The spectra predicted with the aforementioned models do not have the same bremsstrahlung x-ray energy distribution and characteristic x-ray intensity, even for the same tube voltage and target angle. Thus, the accuracy of predicted spectra with these methods should be investigated considering the impact they might have on performance parameters of diagnostic radiological imaging systems and radiation dosimetry calculations. A few publications addressed the issue of comparing various methods proposed for calculating x-ray spectra; however, none of them covered all existing computational models using different target/filter combinations for various tube voltages in diagnostic radiology and mammography energy range.<sup>33</sup> Bissonnette and Schreiner<sup>34</sup> compared Birch and Marshal<sup>12</sup> with the Tucker *et al.*<sup>15</sup> model while Bhat *et al.*<sup>3</sup> compared the same models with spectra measured with a high-purity germanium detector. Caon *et al.*<sup>35</sup> compared four x-ray prediction methods by calculating the resulting absorbed dose to x-ray computed tomography (CT) body and head phantoms. Ng *et al.*<sup>20</sup> compared Boone *et al.*<sup>9</sup> and IPEM spectra with ITS Monte Carlo simulations in mammography energy range whereas Wilkinson *et al.*<sup>6</sup> compared four methods with measured spectra for molybdenum target.

In this study, the accuracy of spectra generated by empirical models (TASMIP and MASMIP), semi-empirical models (IPEM, X-raytbc, X-rayb&m, XCOMP, Tucker *et al.*, and Blough *et al.*), and Monte Carlo calculations (MCNP4C, EGS4, and ITS3.0) in both the diagnostic radiology and mammography energy ranges are assessed through comparison with measured spectra published by Fewell *et al.*<sup>1,2</sup> for different target/filter combinations and tube voltage parameters. The comparative assessment encompassed many figures of merit including qualitative and quantitative assessment of spectra shape, the difference in K x-ray yield, transmission curves, half value layer (HVL) as well as absorbed dose and effective dose imparted to the adult ORNL hermaphroditic phantom.

## II. MATERIALS AND METHODS

### A. Experimental measurement of x-ray spectra

The measured spectra published by Fewell *et al.*<sup>1,2</sup> have been used as the gold standard in this study because of their reliability, availability, and popularity among the diagnostic imaging community. Despite the significant advances made in experimental x-ray spectroscopy, the above referenced reports are still the most complete and exhaustive experimental measurements available today. Moreover, the spectra were measured without added filtration, thus giving the opportunity to the user to modify the spectrum using known attenuation properties of any particular material as additional filter.

*Measurement of x-ray spectra in diagnostic radiology.* The measured spectra used in this study were taken from the Handbook of Computed Tomography X-ray Spectra.<sup>2</sup> The high voltage generator employed in the experiments is the L90-10C Delta ray constant potential with maximum output rating of 180 kV and 10 mA. Published data for the Eimac (B-160-H, A-465) x-ray tube (Ohio Nuclear Inc., Solon, OH) with 12.5° tungsten target angle and nominal inherent filtration of 1.2 mm Al were used. The x-ray spectra were measured with a high-purity germanium detector. The spectrometer was calibrated to give an energy conversion of 0.15 keV per channel. After correction of detector response, the x-ray spectra were tabulated in 2 keV energy bins.

*Measurement of x-ray spectra in mammography.* The measured spectra used in this study were taken from the Handbook of Mammographic X-ray Spectra.<sup>1</sup> The General Electric MSI-1250II high voltage generator was used, which can operate as a three-phase, 12-pulse system in the radiologic mode and as a single phase full rectified system in the fluoroscopy mode. The ripple in high voltage waveform varied from approximately 4% to 6%. The tabulated spectra in the 1 keV energy bin for Dynamax M64 molybdenum and Dynamax 69M tungsten target x-ray tube (Machlett Laboratories, Stamford, CT) with inherent filtration of 0.6 mm Al and 12° target angle were used as reference spectra in this study. Similar to the diagnostic energy range, the x-ray spectra were measured with high-purity germanium detector.

## B. Empirical models

*TASMIP*. This model uses interpolating polynomials to compute the x-ray spectra at 1 keV energy bin for tube voltages between 30 and 140 kV for a tungsten target from a modified version of Fewell's measured spectra as a data source.<sup>7</sup> The highest order polynomial that is practical (depending on the number of data points available in the fit) has been used for fitting the data. The various tube voltage ripples and aluminum filters have been considered in this model.<sup>10</sup>

*MASMP and TASMIP*. These computer models were developed for generating x-ray spectra in the mammographic energy range from 18 to 40 keV through an interpolating polynomial method in 0.5 keV energy bins. The tungsten and molybdenum anode spectral models are named TASMIP and MASMP, respectively.<sup>9</sup> Different sets of polynomials have been used for each anode material (Mo and W). It is worth emphasizing that these models are not able to predict the x-ray spectra for various combinations of targets/filters (and their thicknesses) and anode angles.

## C. Semi-empirical models

*XCOMP*. This computer program can be used for calculation of x-ray spectra, kerma, and HVL for various tube settings (kV, anode angle, distance) and eight absorbing materials (Be, Al, Cu, Sn, Pb, PMMA, water, and oil) with different thicknesses according to Birch and Marshall model.<sup>13</sup> The tube voltage can be selected between 20 and 150 kV in 0.1 keV steps. The energy bin is set to 0.5 keV for voltages less than 50 keV and 1 keV for tube voltages between 50 and 150 keV.

*IPEM Report No. 78*. The original version of the catalog was published in 1979 and provided essential data useful for applications in diagnostic radiology and mammography.<sup>36</sup> The current version uses XCOM program<sup>37</sup> to calculate linear attenuation coefficients for various materials and contains sets of radiology and mammography x-ray spectra with much wider ranges than the previous version. The spectra are presented for tungsten targets at tube voltages from 30 to 150 keV and target angles from 6° to 22° at 1° intervals. Constant potential mammographic spectra are provided from 25 to 32 keV for molybdenum and rhodium targets for target angles ranging between 9° and 23°. Different materials can be used as additional filters. All spectra are provided at an energy interval of 0.5 keV.<sup>38</sup>

*X-raytbc and X-rayb&m*. These models (computer program supplied by Dr. G. Stirling NRL, Christchurch, New Zealand) predict the x-ray spectra, kerma, and HVL for various tube voltages, anode angles, distances, and absorbing materials (Be, Al, Cu, Pb, water, oil, pyrex glass, lexan, concrete, cortical Bone, soft tissue, and acrylic) in the range 10 to 150 keV for constant and two pulse tube voltages. The energy bin is set to 1 keV for both models. Attenuation coefficients are taken from five sources depending on material composition. X-raytbc is based on the Tucker *et al.*<sup>15</sup> model for tungsten-rhenium alloy target (90/10 atomic percent

TABLE I. Summary of computational models used for generation of x-ray spectra in diagnostic radiology and mammography energy range assessed in this study.

Computational model	Category	Target material	Reference
Measurement <sup>a</sup>	Experimental	W	2
Measurement <sup>b</sup>	Experimental	W, Mo, W/Mo	1
TASMIP <sup>a,b</sup>	Empirical	W	10
MASMP <sup>b</sup>	Empirical	Mo	9
X-rayb&m <sup>a,b</sup>	Semi-empirical	W	12
IPEM <sup>a,b</sup>	Semi-empirical	W, Mo, Rh	38
XCOMP <sup>a,b</sup>	Semi-empirical	W	13
X-raytbc <sup>a,b</sup>	Semi-empirical	W	15
Tucker <i>et al.</i> <sup>b</sup>	Semi-empirical	Mo	16
Blough <i>et al.</i> <sup>b</sup>	Semi-empirical	W, Mo, Rh	17
MCNP4C <sup>a,b</sup>	Monte Carlo	All materials	39
EGS4 <sup>a,b</sup>	Monte Carlo	All materials	40
ITS3.0 <sup>a,b</sup>	Monte Carlo	All materials	41

<sup>a</sup>Radiology energy range.

<sup>b</sup>Mammography energy range.

W/Re alloy) while X-rayb&m is based on the Birch and Marshall<sup>12</sup> model for tungsten target.

*Tucker et al. model*. This semi-empirical model generates x-ray spectra in a molybdenum target and takes into account the depth of production for both bremsstrahlung and characteristic x rays.<sup>16</sup> The computer program written by Wilkinson *et al.*<sup>6</sup> was used in this work.

*Blough et al. model*. This analytical model was developed to allow calculation of mammographic spectra in various target and filter combinations.<sup>17</sup> It uses the same formulation of Tucker *et al.*<sup>16</sup> except that a semi-empirical mathematical polynomial derivation was used instead of fitting measured data.<sup>15,16</sup> The spectra published by Wilkinson *et al.*<sup>6</sup> for a molybdenum target were used in this study.

## D. Monte Carlo modeling

*MCNP4C*. The Monte Carlo N-Particle version 4C (MCNP4C) is a general-purpose Monte Carlo code that can be used for neutron, photon, and electron or coupled neutron/photon/electron transport. For simulation of x-ray spectra, MCNP4C was run in photon and electron mode (mode: P,E). A continuous slowing down model is used for electron transport. Photon transport in diagnostic radiology energy range includes photoelectric absorption with creation of K- and L-shell x-ray photons or Auger electrons and coherent and incoherent scattering.<sup>39</sup> An in-depth description of the use of this code for x-ray spectra simulation is given elsewhere.<sup>19</sup>

*EGS4*. The Electron-Gamma Shower version 4 (EGS4) is a general purpose Monte Carlo code for transport of electrons and photons in arbitrary geometry and media for particles with energies from a few keV up to several TeV.<sup>40</sup> The general particle transport physics in this code is the same as MCNP4C except that the latter includes the production of characteristic photons by electron impact ionization.<sup>21</sup> The data simulated by Bhat *et al.*<sup>4</sup> were used in this work.

*ITS3.0*. The Integrated TIGER Series version 3 (ITS3.0)

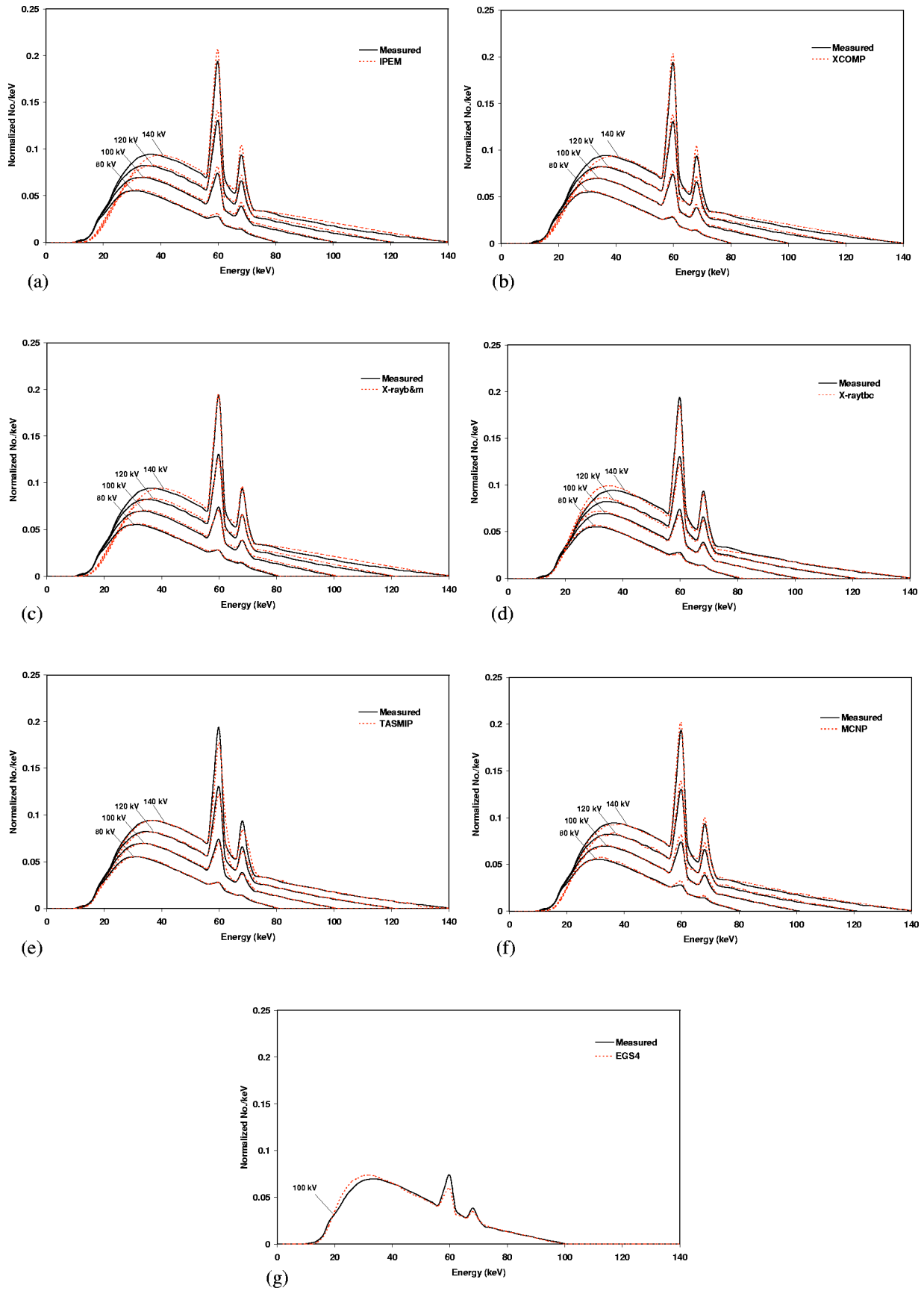


FIG. 1. Comparison of x-ray spectra calculated using the different computational models with measured spectra at tube voltages between 80 and 140 kV for 12.5° tungsten target, 1.2 mm Al<sub>eq</sub> inherent filter, and FSD 127 cm.

TABLE II. Ratios of total tungsten K x rays to sum of bremsstrahlung and K x rays using various computational models for different tube voltages.

Computational model	80 kV		100 kV		120 kV		140 kV	
	Total	Difference <sup>a</sup> (%)	Total	Difference (%)	Total	Difference (%)	Total	Difference (%)
Measured	0.012 50	na <sup>b</sup>	0.046 28	na	0.071 96	na	0.091 13	na
IPEM	0.015 72	-25.7	0.053 96	-16.6	0.081 81	-13.7	0.101 07	-10.9
XCOMP	0.015 01	-20.1	0.051 97	-12.3	0.079 91	-11.0	0.099 69	-9.4
X-rayb&m	0.010 90	12.8	0.040 90	11.6	0.068 35	5.0	0.090 13	1.1
X-raytbc	0.010 67	14.6	0.039 95	13.7	0.064 72	10.1	0.084 62	7.1
TASMIP	0.012 32	1.4	0.043 58	5.8	0.068 69	4.5	0.085 60	6.0
MCNP4C	0.020 97	-67.8	0.055 67	-20.3	0.080 02	-11.5	0.098 50	-8.1
EGS4	...	...	0.033 46	27.7	...	...	...	...

<sup>a</sup>Relative difference with measured spectra.

<sup>b</sup>Not applicable.

of coupled electron/photon Monte Carlo code is a powerful tool for determining state-of-the-art descriptions of the production and transport of the electron/photon cascade in a time-independent, multi-material, and multi-dimensional environment.<sup>41</sup> The ITS-simulated spectra in this study were taken from Ng *et al.*<sup>20</sup>

### E. Comparative assessment strategy

The x-ray spectra calculated by the different computational models summarized in Table I were assessed through comparison with measurement spectra. The criteria and figures of merit used include spectrum shape, attenuation curves, HVLs, K x-ray yield, absorbed dose, and effective dose in the adult ORNL hermaphroditic phantom.<sup>42</sup> Note that the spectrum shape is the best parameter for qualitative visual assessment of potential differences between two spectra owing to the fact that it includes the bremsstrahlung and characteristic x rays. On the other hand, attenuation curves and HVLs are standard indices of beam quality while the K x-ray yield indicates the contribution of characteristic x rays to the total spectrum. Finally, the calculation of the absorbed dose gives an indication of the impact of x-ray spectra on energy imparted to the irradiated phantoms, which is useful for clinical and research applications.

Since the spectra shape and beam quality are a function of tube voltage, filtration, and anode angle, the different computational models were used to simulate spectra with the same parameters used in experimental measurements. The energy bin of the spectra produced by the computational models was changed to 2 keV in radiology and 1 keV in mammography for comparison with measured spectra.<sup>1,2</sup> The calculation of HVLs and transmission curves was performed using the original energy bin. During the rebinning process, the resulting spectra for some computational models do not fall to zero at maximum tube voltage. Quantitative evaluation of the differences between measured spectra and the spectra generated by different models was performed using the root mean square difference (RMSD) metric and statistical student's *t*-test analysis. The transmission curves were calculated by dividing the transmitted air kerma through the filter by the air kerma without the filter being present. The

HVLs and transmission curves calculated for some models in this study have small differences in some cases with the values reported by the original codes. This can be attributed to differences in attenuation coefficients for aluminium, which are derived from XCOM program<sup>37</sup> in our work. The K x-ray contribution is determined by subtracting the bremsstrahlung part of the spectra from total counts in the desired region and normalizing to the total number of photons in the spectra. The bremsstrahlung spectra can be obtained by subtracting the K x-ray yields from the appropriate intervals in the spectra.<sup>2</sup>

The MCNP4C Monte Carlo code was used for calculation of absorbed dose in ORNL hermaphroditic phantom. The predicted spectra using the different computational models at 100 kV were used as input. The x-ray source was set at a distance of 100 cm from the chest of the ORNL hermaphroditic phantom. A field of view (FOV) of 40×40 cm<sup>2</sup> was considered and 1.5×10<sup>7</sup> photons were employed in the simulation to get an uncertainty less than 1% in the calculation of absorbed dose using \*F6 tally, which calculates the energy deposit averaged over a cell. No variance reduction technique was used and all photon interactions were simulated until they are absorbed in the phantom or escape from it. The ED was calculated using appropriate tissue weighting factors.<sup>43</sup> The same simulations were performed for molybdenum and tungsten target mammographic spectra at 30 kV to calculate the mean absorbed dose to the breasts ( $\overline{D_b}$ ) and ED using typical mammography setup (FSD 50 cm, FOV 10×10 cm<sup>2</sup>). The values calculated by Monte Carlo simulation were scaled to mimic typical values encountered in chest and mammography x-ray imaging for measured spectra that is an ED of 40 μSv for x-ray chest imaging and a mean absorbed dose to breasts of 2 mGy in mammography.<sup>44</sup>

## III. RESULTS

### A. Diagnostic radiology

Figure 1 shows the comparison of tungsten x-ray spectra calculated using different computational models with measured spectra for an Eimac x-ray tube at tube voltages between 80 and 140 kV, except the spectra calculated using

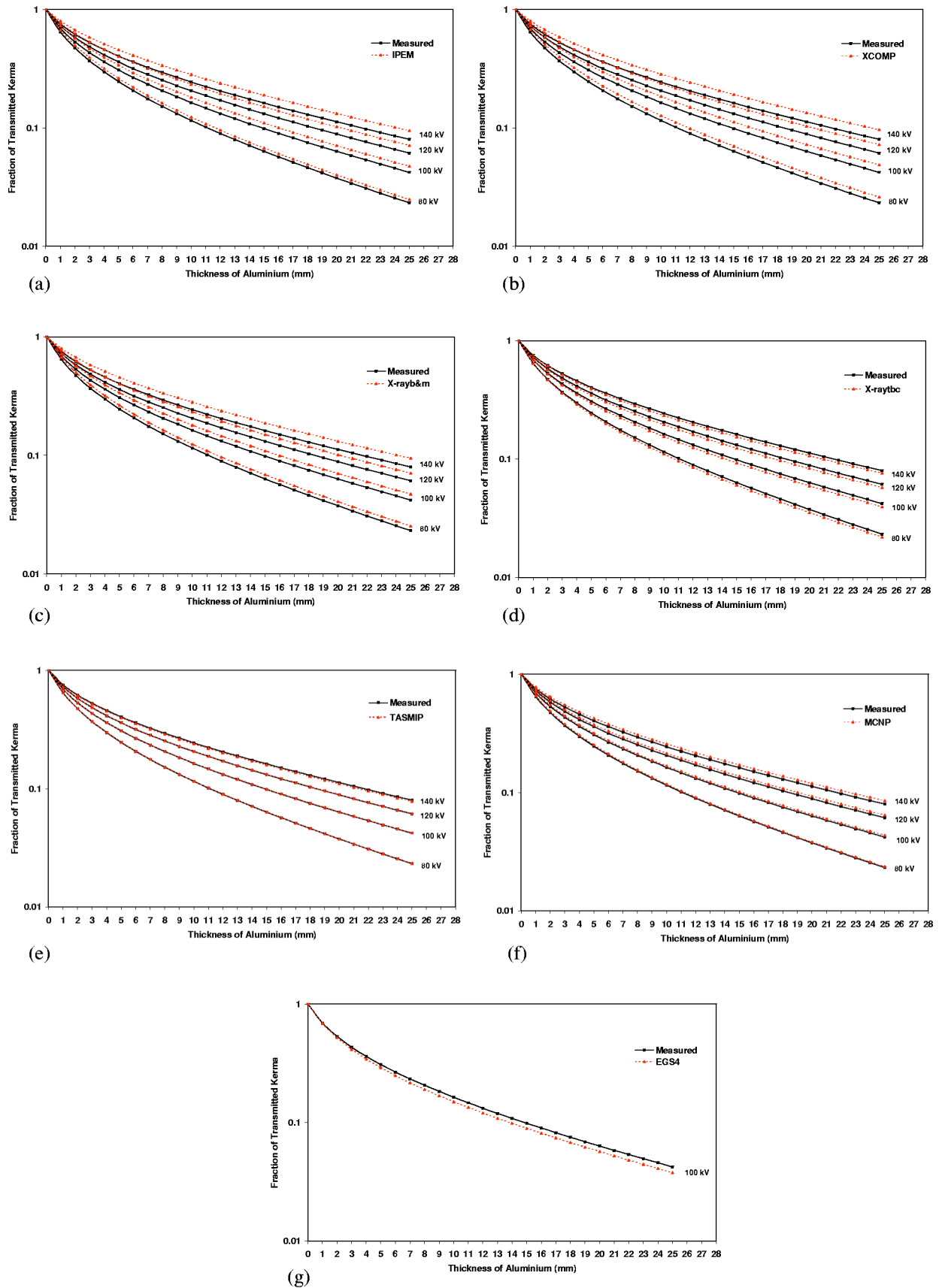


FIG. 2. Comparison of transmission curves produced by different computational models with those calculated from measured spectra at tube voltages between 80 and 140 kV for 12.5° tungsten target, 1.2 mm Al<sub>eq</sub> inherent filter, and FSD 127 cm.

TABLE III. Comparison of maximum and mean absolute relative difference between transmission curves calculated using the different computational models and curves calculated from measured spectra (12.5° tungsten target, 1.2 mm Al<sub>eq</sub> inherent filtration).

Computational model	80 kV		100 kV		120 kV		140 kV	
	Mean (%)	Max (%)						
IPEM	7.6	9.2	10.4	12.7	13.1	16.3	14.9	18.6
XCOMP	9.5	11.9	12.3	15.8	14.4	18.1	16.1	20.6
X-rayb&m	6.2	6.9	9.9	12.4	12.2	15.8	14.6	18.6
X-raytbc	4.1	5.6	4.5	6.1	4.7	6.1	3.7	5.2
TASMIP	0.5	0.8	0.6	1.2	0.5	1.3	1.7	2.4
MCNP	2.0	2.7	3.0	3.5	4.4	5.6	5.5	6.8
EGS4	...	...	7.7	10.3	...	...	...	...

EGS4 which are available only at 100 kV. All spectra were normalized to the total number of photons in each spectrum. The relative difference between measured and calculated total K x rays is summarized in Table II. Good agreement between the bremsstrahlung x rays produced by the TASMIP model with measured spectra can be observed while the characteristic x rays have lower intensity. The relative difference of total K x-ray yields with measured data increase with increasing tube voltage. In comparison with measured spectra, all semi-empirical models based on Birch and Marshal theory<sup>12</sup> have lower intensity at low energies while they have higher intensity in high energies ( $E > 68$  keV) for all tube voltages. Our calculations showed that the K x-ray yield in all peaks ( $K_{\alpha 1}, K_{\alpha 2}, K_{\beta 1}, K_{\beta 2}$ ) in both IPEM and XCOMP is higher than measured spectra while these values are lower in X-rayb&m model. The total K x-ray yield values shown in Table II indicate that these differences decrease with increasing tube voltage. The X-raytbc model based on Tucker *et al.*<sup>15</sup> theory produces more low energy x rays ( $E < 42$  keV) and the intensity of characteristic x rays predicted by this model is lower than measured spectra in all peaks. The calculated spectra by MCNP have higher intensity in low energy photons while this behavior is reversed for energies

$>68$  keV in comparison with measured spectra. The K x-ray yields have higher intensity in all energies. The relative difference of total K x-ray yields decreases by increasing tube voltage. The low energy bremsstrahlung photons have higher intensity in the spectra simulated by EGS4 at 100 kV in comparison with measured spectra, while this behavior is reversed for the intensity of characteristic x rays.

The quality of x-ray spectra calculated with different computational models as compared to measured spectra was assessed in Fig. 2, which shows the transmission curves through aluminum filter for different tube voltages. All models based on Birch and Marshal theory (IPEM, XCOMP, and X-ray&m) result in higher transmission curves in comparison with measured spectra for all tube voltages and the difference increases with increasing the tube voltage. This behavior is reversed for transmission curves calculated using X-raytbc, while the transmission curves calculated using TASMIP spectra have good agreement with the curves calculated from measured spectra. The transmission curves calculated using MCNP spectra have higher values and this difference increases with increasing tube voltage, whereas the EGS4 transmission curve has lower values in comparison with measured spectra. Table III shows the maximum and

TABLE IV. Comparison of root mean square difference (RMSD) between measured and calculated spectra using the different computational models (the original data values have been multiplied by 10<sup>3</sup>).

Computational model	Figure 1				Figure 3		Figure 5		
	80 kV	100 kV	120 kV	140 kV	25 kV	30 kV	30 kV	35 kV	40 kV
IPEM	2.66	3.84	5.17	6.34	5.69	14.87	7.53	8.04	8.10
XCOMP	1.01	1.89	3.18	4.56	...	...	10.09	8.06	9.67
X-rayb&m	2.37	3.31	4.45	5.53	...	...	9.06	14.87	14.24
X-raytbc	0.98	1.83	2.67	3.03	...	...	10.20	16.88	17.44
TASMIP	1.24	2.04	3.40	5.06	...	...	8.64	7.39	9.94
MCNP4C	2.18	2.70	3.20	3.62	27.89	30.47	11.68	8.84	11.64
EGS4	...	3.66	...	...	...	...	...	...	...
Blough <i>et al.</i>	...	...	...	...	20.55	20.61	...	...	...
Tucker <i>et al.</i>	...	...	...	...	11.90	16.50	...	...	...
MASMP	...	...	...	...	4.29	10.67	...	...	...
ITS3.0	...	...	...	...	...	14.18	9.90	...	...

TABLE V. Comparison between measured and computed HVL estimates (in mm Al) using the different computational models for tube voltages in the diagnostic radiology energy range (12.5° tungsten target, 1.2 mm Al<sub>eq</sub> inherent filtration).

Computational model	80 kV		100 kV		120 kV		140 kV	
	HVL	Difference (%)	HVL	Difference (%)	HVL	Difference (%)	HVL	Difference (%)
Measured	1.81	na	2.29	na	2.81	na	3.36	na
IPEM	2.02	-11.6	2.67	-16.5	3.41	-21.3	4.22	-25.5
SCOMP	2.03	-12.1	2.68	-17.0	3.44	-22.4	4.27	-27.1
X-rayb&m	2.01	-11.0	2.65	-15.7	3.39	-20.6	4.20	-25.0
X-raytbc	1.78	1.6	2.22	3.0	2.73	2.8	3.29	2.1
TASMIP	1.81	0	2.29	0	2.81	0	3.30	1.8
MCNP4C	1.86	-2.8	2.40	-4.8	2.95	-5.0	3.62	-7.7
EGS4	...	...	2.15	6.1	...	...	...	...

mean differences between measured and calculated transmission curves. It can be seen that the percentage absolute value of maximum and mean relative errors in transmission curves calculated from XCOMP spectra are higher than the other models for energies between 80 and 140 kV. Table IV summarizes the root mean square difference between measured and calculated spectra for the different computational models in different energies. It can be seen that the RMSD is minimum for the spectra calculated using the X-raytbc model in the diagnostic radiology energy range.

Further comparative assessment of the quality of x-ray spectra calculated by different models is illustrated in Table V, which shows the calculated HVLs and their relative difference with respect to measured data for tube voltages between 80 and 140 kV. Once again, the difference increases with increasing tube voltage and the XCOMP model has the maximum difference with measured spectra. Note that IPEM and X-rayb&m models produce very close estimates to this latter model. Table VI summarizes the impact of the x-ray spectra on the ED imparted to the ORNL hermaphroditic phantom in typical chest x-ray imaging setup, with 1.2 and 3.2 mm aluminum filters at 100 kV. The maximum differences in calculation of ED in comparison with measured

spectra with 1.2 and 3.2 mm Al filters are -3.2% and -5% for IPEM, while the minimum differences are 0% and 0.6% for x-raytbc, respectively.

## B. Mammography

Figure 3 shows the comparison of spectra predicted by different computational models with measured spectra published by Fewell *et al.*<sup>1</sup> for a Dynamax M64 x-ray tube at voltages of 25 and 30 kV. All spectra predicted by computational models have higher intensity in the low energy range ( $E < 15$  keV), although it appears that IPEM and MASMIP produce the same amplitude at low energies compared with measured spectra for 30 kV. The difference in K x-ray characteristic yield was calculated for all peaks; however, only the total value and its relative difference with measured spectra are reported in Table VII. According to these data, MASMIP underestimates the production of characteristic x rays in both tube voltages, while MCNP4C overestimates these values. The maximum difference in production of K x-ray yield with measured spectra are -71.8% and -73.5% at 25 kV and -31.3% and -42.3% at 30 kV for MCNP4C spectra with

TABLE VI. Comparison between MCNP4C-based Monte Carlo calculations of effective dose (ED) in adult ORNL hermaphroditic phantom in typical chest x-ray imaging setup (100 kV, FSD 100 cm, 12.5° target angle) with 1.2 and 3.2 mm Al filter.

Computational model	1.2 mm Al filter		3.2 mm Al filter	
	ED ( $\mu$ Sv)	Difference <sup>a</sup> (%)	ED ( $\mu$ Sv)	Difference (%)
Measured	40.00±1.4	na	29.81±0.3	na
IPEM	41.30±1.4	-3.2	31.29±0.3	-5.0
XCOMP	40.55±1.4	-1.4	30.55±0.3	-2.5
X-rayb&m	41.11±1.5	-2.8	31.11±0.3	-4.3
X-raytbc	40.00±1.6	0	29.63±0.3	0.6
TASMIP	40.37±1.5	-0.9	30.37±0.3	-1.7
MCNP4C	40.74±1.4	-1.8	30.55±0.3	-2.5
EGS4	39.63±1.4	0.9	29.26±0.3	1.9

<sup>a</sup>Relative difference with calculated effective dose from measured spectrum.

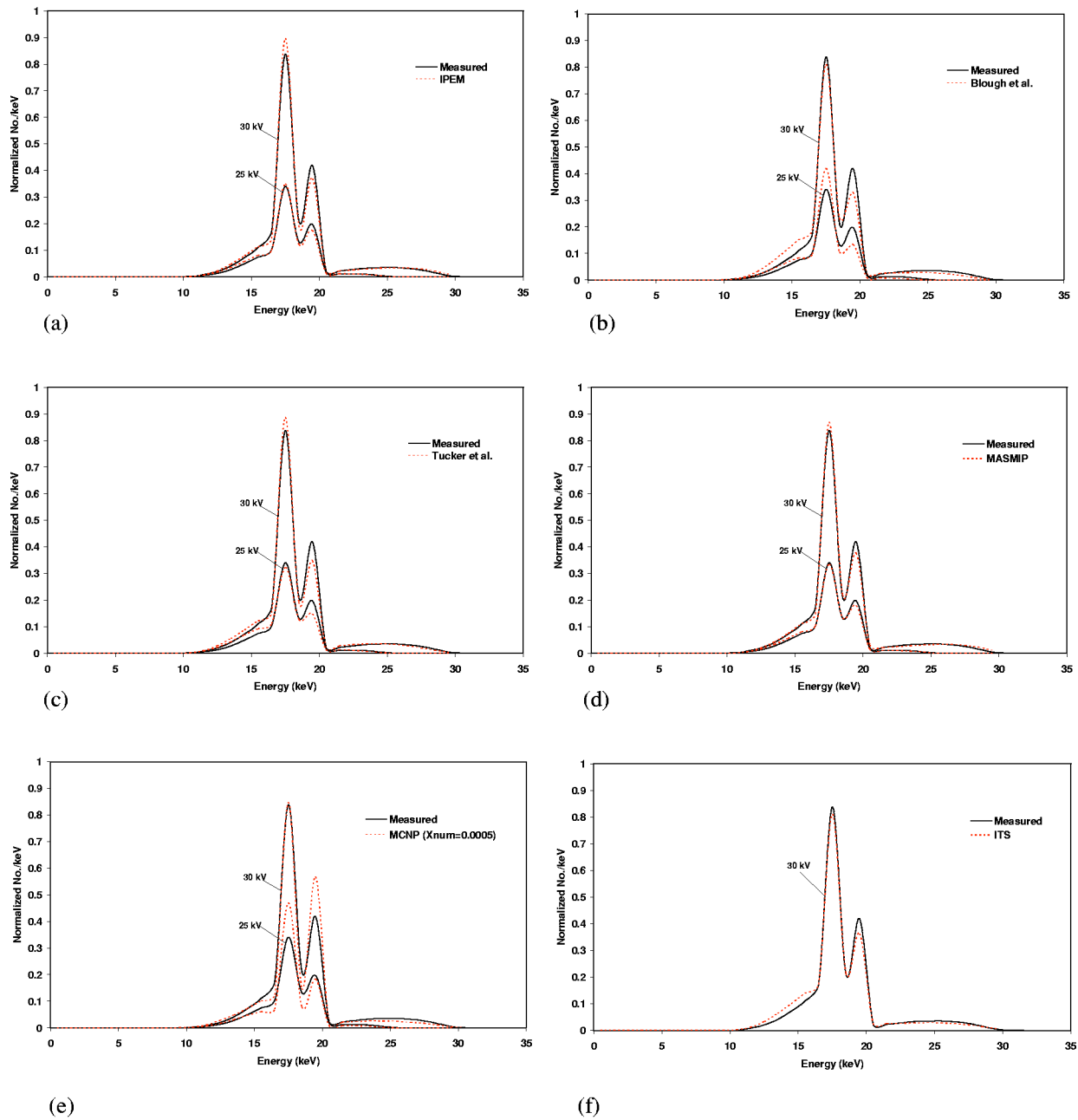


FIG. 3. Comparison of x-ray spectra calculated using different computational models with measured spectra at tube voltages 25 and 30 kV for 12° molybdenum target, 0.6 mm Al<sub>eq</sub> inherent filter, 0.03 mm Mo additional filter, and FSD 100 cm.

XNUM values of 0.0005 and 1, respectively, whereas the minimum difference is 1.1% (at 25 kV) for IPEM and -0.4% (at 30 kV) for the Tucker *et al.* model.

The quality of produced spectra with different models with respect to transmission curves is assessed in Fig. 4. It can be seen that all models underestimate the measured transmission curves in each filter thickness. Figure 5 shows the comparison between the spectra predicted by different computational models and measured spectra for a Dynamax 69M tungsten target x-ray tube at tube voltages of 30, 35, and 40 kV. The peak of calculated spectra for all models occurs at lower energy in comparison with measured spectra and has lower intensity in all tube voltages, whereas the mea-

sured spectra has higher intensity in low and high energies. All transmission curves calculated using different computational models have lower amplitude in comparison with measured spectra at tube voltages 35 and 40 kV while this behavior is reversed at 30 kV, except the curve calculated from ITS (Fig. 6).

The maximum and mean absolute relative differences between measured and calculated transmission curves for molybdenum and tungsten targets are reported in Table VIII. Table IX compares calculated HVLs obtained using the different models with measured spectra at tube voltages 25 and 30 kV for a molybdenum target and 30, 35, and 40 kV for a tungsten target. A maximum difference of 8.6% at 30 kV for

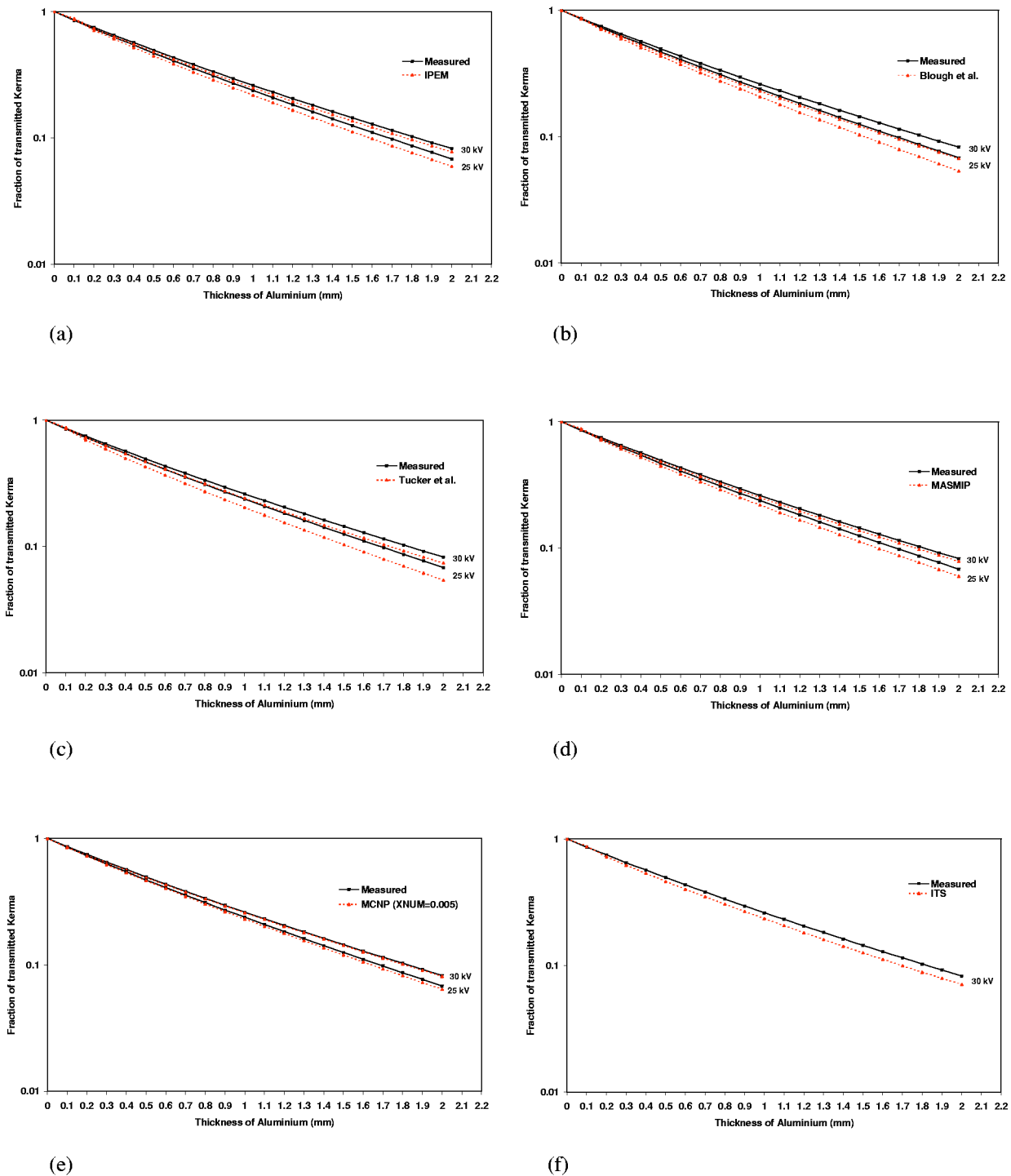


FIG. 4. Comparison of transmission curves produced by different computational models with those calculated from measured spectra at tube voltages 25 and 30 kV for 12° molybdenum target, 0.6 mm  $Al_{eq}$  inherent filter, 0.03 mm Mo additional filter, and FSD 100 cm.

ITS, and 12.6% at 35 kV, and 6.5% at 40 kV for XCOMP were observed. The MCNP4C transmission curve is in good agreement with the curve calculated from measured spectra. The mean and maximum differences are 3%, 5.7%, 1.1%, and 1.8% at tube voltages of 25 and 30 kV, respectively. This good agreement is obvious in calculation of HVLs where the difference with measured data is minimum for MCNP4C spectra, that is, 4.3% and 4% at tube voltages of

25 and 30 kV, respectively. The same observations can be made regarding the RMSD in the mammographic energy range where the MASMIP model for the molybdenum target results in the lowest values owing to the fact that it is based on unpublished spectral data that are similar but more recent than the reference spectra used in this work (Table IV).<sup>9</sup> IPEM performs well compared to other computational models for both molybdenum and tungsten targets.

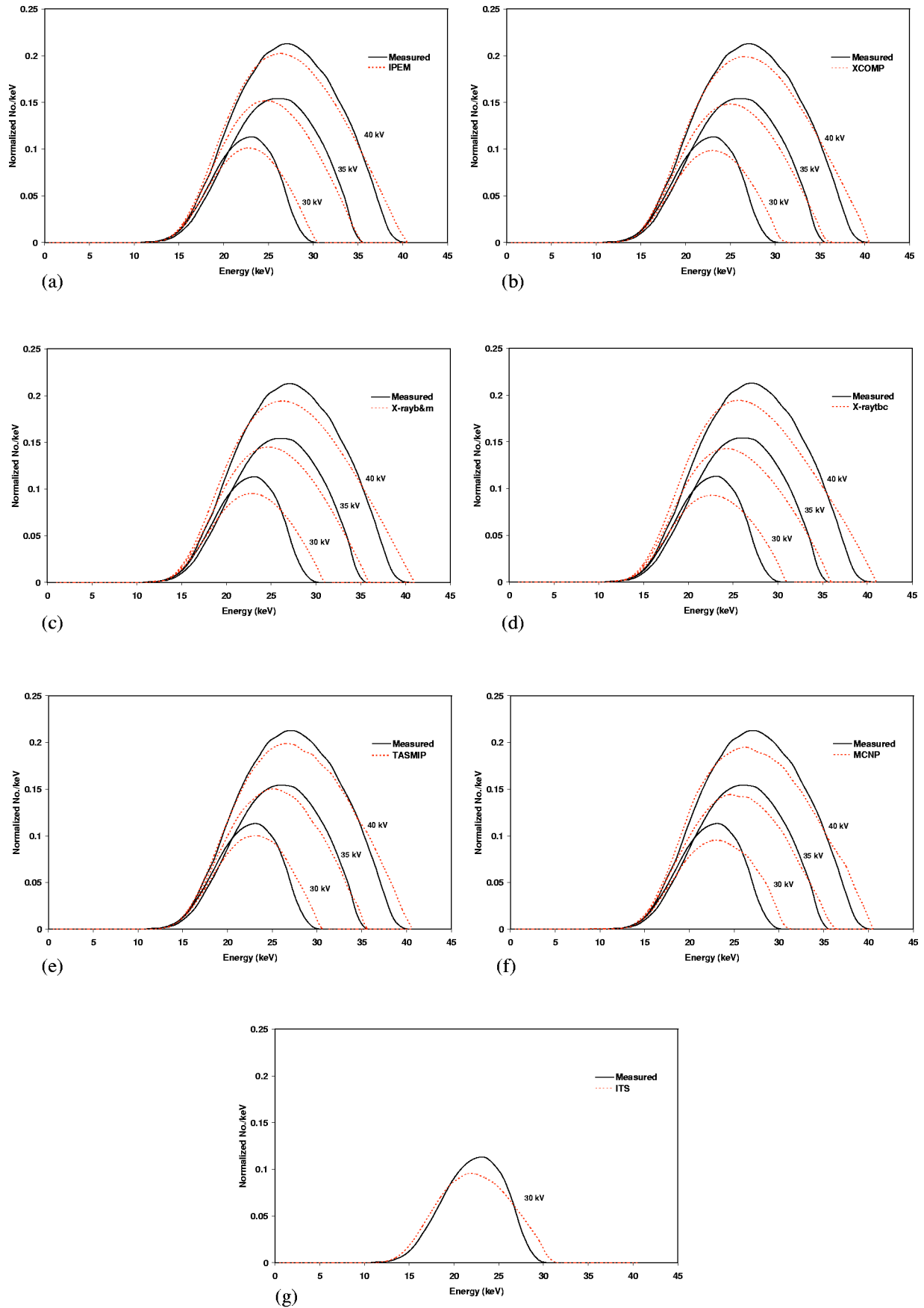


FIG. 5. Comparison of x-ray spectra calculated using different computational models with measured spectra at tube voltages 30, 35, and 40 kV for 12° tungsten target, 0.6 mm  $Al_{eq}$  inherent filter, 1.02 mm Al additional filter, and FSD 100 cm.

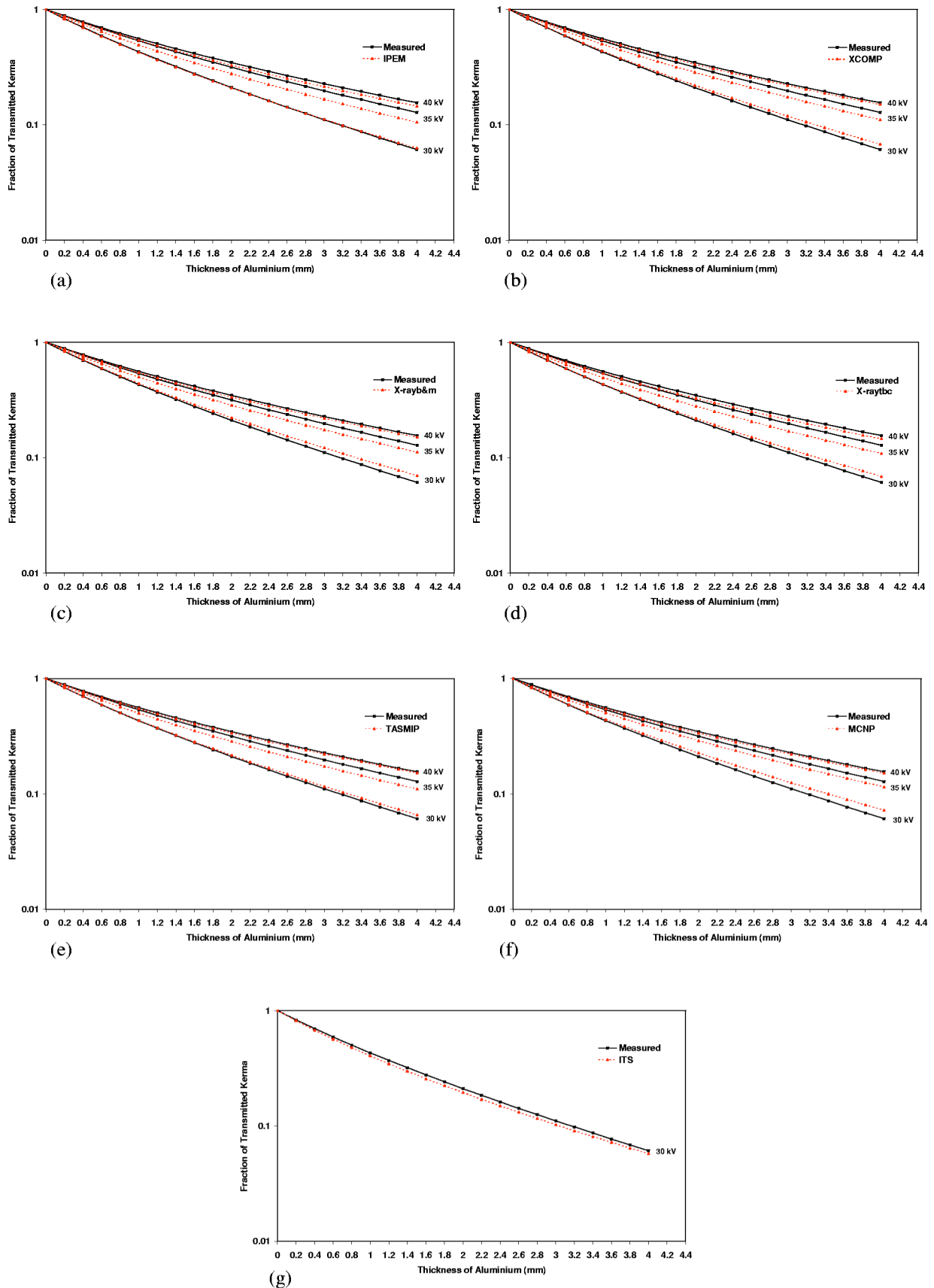


FIG. 6. Comparison of transmission curves produced by different computational models with those calculated from measured spectra at tube voltages 30, 35, and 40 kV for 12° tungsten target, 0.6 mm Al<sub>eq</sub> inherent filter, 1.02 mm Al additional filter, and FSD 100 cm.

TABLE VII. Comparison between ratios of total molybdenum K x rays to sum of bremsstrahlung and K x rays obtained using measured and calculated spectra for different tube voltages. The MCNP4C calculations include results obtained using two values for the XNUM parameter of the PHYS:E card, which is used to control the sampling of x-ray photons produced along electron substeps (the default value XNUM=1 corresponds to the case where an analog number of tracks is sampled).

Computational model	25 kV		30 kV	
	Total	Difference (%)	Total	Difference (%)
Measured	0.2992	na	0.3983	na
IPEM	0.2860	1.1	0.4160	-4.4
Blough <i>et al.</i>	0.3470	-19.9	0.3200	19.6
Tucker <i>et al.</i>	0.2230	22.9	0.4000	-0.4
MASMIP	0.2310	20.1	0.3460	13.1
MCNP4C <sup>a</sup>	0.4970	-71.8	0.5230	-31.3
MCNP4C <sup>b</sup>	0.5020	-73.5	0.5670	-42.3
ITS3.0	...	...	0.3500	12.1

<sup>a</sup>XNUM=0.0005.

<sup>b</sup>XNUM=1.

The Monte Carlo calculations of mean breast absorbed dose ( $\overline{D}_b$ ) and ED in typical mammography imaging setup using different computational models for generating x-ray spectra in the adult ORNL hermaphroditic phantom at 30 kV are summarized in Table X. The maximum difference in calculation of  $\overline{D}_b$  and Ed in molybdenum target is 2.5% and 2.6% when using the Blough *et al.* model, while this value is 1.5% and 1.1% for the X-raytbc tungsten target model.

IV. DISCUSSION

The differences in the bremsstrahlung x-ray energy distribution calculated by different semi-empirical models in comparison with measured spectra can be explained by the differences in the fitting equations derived in these models for prediction of spectra. Different semi-empirical polynomial functions used in these models are the origin of the discrepancy

in the production of bremsstrahlung x-ray intensity. The comparison of these functions shows that the Birch and Marshal models (IPEM, XCOMP, and X-rayb&m) produce less low energy photons and more high energy photons compared to the Tucker *et al.* model (X-raytbc). This behavior is obvious in Fig. 1. The different target geometry used in these models should be considered especially for low energy photons. In the Tucker *et al.* model, the electrons hit the target at angle 90° while this angle is 90-θ (θ is the target angle) in the Birch and Marshal model. Thus, the photons produced in depth x pass through anode thickness  $d=x/\tan \theta$  in the Birch and Marshal model and  $d'=x/\sin \theta$  in the Tucker *et al.* model. The ratio  $d'/d$  shows that the Tucker model overestimates the target attenuation, which varies from 0.7% to 6% for a target angle between 7° and 20° (2.4% in our study with 12.5° target angle). Although the target absorption is an important parameter in the intensity of low energy photons, the difference in the semi-empirical polynomial functions compensate this effect in low-energy photon intensity. The spectra predicted by the TASMIP empirical model are in excellent agreement with measured spectra. The difference in K x-ray intensity is the result of arranging the data in 2 keV energy bins. It should, however, be emphasized that the same measured data were used for fitting interpolating polynomials. During the comparison of the calculated and measured spectra, especially the intensity of low photon energies, it is worth noticing that all models used a perfectly smooth target, while the influence of anode roughness on low energy photons in measured spectra appears to be important, especially at low tube voltages.<sup>45</sup>

The intensity of K x rays in the spectra is another important parameter that should be taken into account when comparing different computational models. Even though the semi-empirical models used an empirical relationship for the intensity of characteristic x rays,<sup>30</sup> they relied on different experimental measurements for adjusting their intensity. The difference in K x-ray yield in comparison with measured

TABLE VIII. Comparison of maximum and mean absolute relative difference between measured and calculation transmission curves in mammography energy range for molybdenum (12° target angle, 0.6 mm Al<sub>eq</sub> inherent and 0.03 mm molybdenum additional filter) and tungsten targets (12° target angle, 0.6 mm Al<sub>eq</sub> inherent and 1.02 mm Al additional filter).

Computational model	Mo target				W target					
	25 kV		30 kV		30 kV		35 kV		40 kV	
	Mean (%)	Max (%)	Mean (%)	Max (%)	Mean (%)	Max (%)	Mean (%)	Max (%)	Mean (%)	Max (%)
IPEM	7.6	12.1	4.0	5.8	1.0	3.3	11.1	17.6	4.2	6.4
Blough <i>et al.</i>	12.1	21.2	11.3	18.7	...	...	...	...	...	...
Tucker <i>et al.</i>	12.6	20.3	6.7	10.1	...	...	...	...	...	...
MASMIP	7.2	11.8	3.3	4.7	...	...	...	...	...	...
MCNP4C	3.0	5.7	1.1	1.8	8.0	18.7	7.2	10.1	2.6	6.2
ITS3.0	...	...	9.1	14.1	5.8	7.6	...	...	...	...
XCOMP	...	...	...	...	5.0	11.8	8.5	13.5	2.5	3.4
X-rayb&m	...	...	...	...	6.4	15.0	8.6	12.8	2.7	3.4
X-raybc	...	...	...	...	4.8	12.8	10.1	14.9	4.6	6.1
TASMIP	...	...	...	...	3.1	8.1	8.8	13.8	1.9	2.5

TABLE IX. Comparison between measured and computed HVL estimates (in mm Al) using the different computational models for tube voltages in mammography energy range for molybdenum (12° target angle, 0.6 mm Al<sub>eq</sub> inherent and 0.03 mm molybdenum additional filter) and tungsten targets (12° target angle, 0.6 mm Al<sub>eq</sub> inherent and 1.02 mm Al additional filter).

Computational model	Mo target				W target					
	25 kV		30 kV		30 kV		35 kV		40 kV	
	HVL	Difference (%)	HVL	Difference (%)	HVL	Difference (%)	HVL	Difference (%)	HVL	Difference (%)
Measured	0.46	na	0.50	na	0.81	na	1.11	na	1.22	na
IPEM	0.42	8.7	0.47	6.0	0.80	1.2	0.98	11.7	1.15	5.7
Blough <i>et al.</i>	0.41	10.9	0.47	6.0	...	...	...	...	...	...
Tucker <i>et al.</i>	0.40	13.0	0.46	8.0	...	...	...	...	...	...
MASMIP	0.42	8.7	0.47	6.0	...	...	...	...	...	...
MCNP4C	0.44	4.3	0.48	4.0	0.82	-1.2	1.07	3.6	1.17	4.1
ITS3.0	...	...	0.44	12.0	0.74	8.6	...	...	...	...
XCOMP			...	...	0.80	1.2	0.97	12.6	1.14	6.5
X-rayb&m					0.84	-3.7	1.01	9.0	1.17	4.1
X-raytbc					0.82	-1.2	0.99	10.8	1.14	6.5
TASMIP					0.81	0	1.00	9.9	1.18	3.2

spectra decreases with increasing tube voltage owing to the fact that all semi-empirical models were adjusted with measured spectra at 140 kV. Even though the same measured data were used for adjusting the characteristic x rays in X-raytbc and X-rayb&m, the lower intensity in X-raytbc is the effect of target absorption discussed above. Characteristic photons in MCNP are created by the electron impact ionization (EII) process. It has been shown that this model overestimates the total number of EII characteristic photons especially in mammography energy range.<sup>19,21</sup> The low characteristic x-ray intensity in the EGS4 spectra can be explained by the fact that the contribution of electron impact ionization had not been included in the EGS4 code system at the time of simulation.<sup>4</sup>

All semi-empirical models based on Birch and Marshal theory (IPEM, XCOMP, and X-rayb&m) produce spectra

with higher quality than measured spectra, while the situation is reversed in the model based on the Tucker *et al.* theory (X-raytbc). This is due to production of softer x-ray spectra in the Tucker *et al.* model. We have considered the aluminum equivalent thickness needed to match TASMIP with the Fewell spectra,<sup>10</sup> so that the attenuation curve calculated from TASMIP spectra is in good agreement. The transmission curves calculated from MCNP4C spectra are higher than those obtained from measured spectra because of the overestimation of K x rays and high energy bremsstrahlung photons ( $E > 68$  keV) in the spectra, while the EGS4 spectra produce a lower transmission curve compared to the measured one because of underestimation of K x rays.

The calculation of absorbed dose and ED in the ORNL hermaphroditic phantom from the spectra generated by different models was used to assess the effect of spectra in the

TABLE X. Comparison between MCNP4C-based Monte Carlo calculations of mean absorbed dose to the breasts ( $\overline{D}_b$ ) and effective dose (ED) in adult ORNL hermaphroditic phantom for typical mammography imaging setup of 30 kV in Mo target (FSD 50 cm, 12° target angle, 0.6 mm Al<sub>eq</sub> inherent filter and 0.03 mm Mo additional filter) and W target (FSD 50 cm, 12° target angle, 0.6 mm Al<sub>eq</sub> inherent and 1.02 mm Al additional filter). The standard deviation (SD) in calculation of mean absorbed dose to the breasts is negligible.

Computational model	Mo target				W target			
	$\overline{D}_b$ (mGy)	Difference (%)	ED ( $\mu$ Sv)	Difference (%)	$\overline{D}_b$ (mGy)	Difference (%)	ED ( $\mu$ Sv)	Difference (%)
Measured	2.00	na	104.37±22.1	na	2.00	na	104.05±13.6	na
IPEM	1.99	0.5	103.70±7.6	0.6	2.00	0.0	104.05±15.7	0.0
Blough <i>et al.</i>	1.95	2.5	101.70±22.2	2.6	...	...	...	...
Tucker <i>et al.</i>	1.97	1.5	103.00±21.3	1.3	...	...	...	...
MASMIP	2.00	0.0	104.40±7.5	0.0	...	...	...	...
MCNP4C	2.00	0.0	104.40±22.1	0.0	2.01	-0.5	104.62±12.9	-0.5
ITS3.0	1.96	2.0	102.30±8.8	2.0	1.98	1.0	102.89±13.1	1.1
XCOMP	...	...	...	...	2.01	-0.5	104.62±12.9	-0.5
X-rayb&m					1.98	1.0	102.89±13.2	1.1
X-raytbc					1.97	1.5	102.89±13.1	1.1
TASMIP					2.01	-0.5	104.62±15.6	-0.5

field of radiation dosimetry. The calculated ED from the X-raytbc model results in lower estimates compared to spectra generated by other models. Similar results were reported by Caon *et al.*<sup>35</sup> The underestimation of ED observed with 3.2 mm aluminium filter is the effect of absorption of soft x rays in the filter. The magnitude of the relative difference increases more substantially with increasing filtration thickness for the spectra generated by the models based on Birch and Marshal theory since they produce less soft x rays than measured spectra.

The comparative assessment of x-ray spectra generated by different computational models to measured spectra for molybdenum target showed that the Blough *et al.* and Tucker *et al.* models produce more soft energy than IPEM for the reasons discussed previously. The discrepancy between the Blough *et al.* model and measured spectra at 25 kV probably is due to the overestimation of the Dyson derivation<sup>46</sup> or to slight differences in the implementation of this model at this energy.<sup>6</sup> The difference between MASMIP and measured spectra is attributed to the fact that different measured spectra were used for interpolating polynomials.<sup>9</sup> Comparison of the MCNP4C spectra with measured spectra showed that the code highly overestimates the production of K x rays with the default setting (XNUM=1). The optimal adjustment of the XNUM parameter in the PHYS:E card proved to be a difficult issue. Further investigation showed that MCNP produces bremsstrahlung energy distribution in good agreement with measured spectra. The discrepancy shown in Fig. 3 results from spectral normalization with overestimated characteristic x-ray peaks.<sup>19</sup> The simulated spectra with ITS3.0 showed that this code gives a better approximation of K x rays in comparison with MCNP4C, although the electron physics enhancement library was intended to make MCNP4C more consistent with ITS 3.0. It is worth emphasizing that the K-shell impact ionization calculation (based upon ITS 3.0) remains unchanged with eI03 evaluation.<sup>39</sup> The latter uses detailed calculations of the electron-nucleus bremsstrahlung cross section for electrons with energies below 2 MeV and above 50 MeV. According to Fig. 5, the spectrum peak in all semi-empirical models occurred in lower energy and with less intensity than the measured spectra. One plausible explanation could be the overestimation of electron penetration in the target in the Thomson-Whiddington relation<sup>30</sup> where the range of electrons is proportional to  $T_0^2$  below 50 keV while it is proportional to  $T_0$  for higher energies ( $T_0$  is the kinetic energy of electron). The systematic discrepancy between measured and calculated transmission curves is the result of systematic differences between the corresponding spectra in both molybdenum and tungsten target spectra in the mammography energy range.

Despite there not being any statistically significant differences between measured and calculated spectra for all computational models considered in this study, the flexibility and robustness of these models with respect to generating the desired spectrum for a variety of parameters such as target material, target angle, additional filter, tube voltage ripple, and energy bin and accurate modeling of more recent x-ray

generator designs should be considered. The empirical models are inherently limited in terms of target angle and filter material as well as tube voltage ripple in the mammography energy range. Although semi-empirical models are more flexible compared to empirical models, they are limited to specific target materials, particular sets, or combinations of additional filters and voltage ripples. Notwithstanding, there is no theoretic limitation in the prediction of x-ray spectra for the different parameters mentioned above using the Monte Carlo method; computer proficiency and computational time remain the challenges for widespread application of Monte Carlo simulations. With the advent of high speed parallel supercomputers, which have much higher execution rates, and recent developments in Grid technology allowing us to subdivide time-consuming simulations on geographically distributed platforms, the field has received increased attention and will certainly live up to its potential in the near future.

## V. CONCLUSION

The spectra generated using a number of different computational models were compared with measured spectra. The comparative assessment showed that the energy distribution and the quality of spectra produced by the Tucker model (X-raytbc) are in better agreement with measured spectra than other models in the diagnostic radiology energy range while IPEM has better agreement in the mammography energy range. The empirical models perform well since they are based on the reference experimental spectra used in this work. It should, however, be emphasized that these models are rather limited in terms of flexibility with respect to target angle and filter material. MCNP4C has good agreement with experimental measurements in the diagnostic radiology energy range, while ITS3.0 reproduces more accurately the measured spectra in the mammography energy range. Although Monte Carlo modeling is time consuming, the simulations provide detailed information about the interactions inside the target and filter, which can be useful for the design of new target/filter combinations, for instance in transmission x-ray tube design.<sup>47</sup>

## ACKNOWLEDGMENTS

This work was supported by the Department of Physics & Nuclear Sciences (AmirKabir University of Technology) and the Swiss National Science Foundation under Grant No. SNSF 3152A0-102143. The authors would like to thank Dr. J. M. Boone, Dr. M. Bhat, Dr. K. P. Ng, Dr. L. E. Wilkinson, Dr. G. Stirling, Dr. R. Nowotny, and Dr. G. W. Allen who shared with us their data and programs.

<sup>a</sup>)Electronic mail: farshid.ay@tpggems.com

<sup>1</sup>T. R. Fewell and R. E. Shuping, "Handbook of mammographic x-ray spectra," HEW publication (FDA) 79-8071, 1978.

<sup>2</sup>T. R. Fewell, R. E. Shuping, and K. E. Healy, "Handbook of computed tomography x-ray spectra," HHS publication (FDA), 81-8162, 1981.

<sup>3</sup>M. Bhat, J. Pattison, G. Bibbo, and M. Caon, "Diagnostic x-ray spectra: a comparison of spectra generated by different computational methods with a measured spectrum," *Med. Phys.* **25**, 114-120 (1998).

<sup>4</sup>M. Bhat, J. Pattison, G. Bibbo, and M. Caon, "Off-axis x-ray spectra: a

- comparison of Monte Carlo simulated and computed x-ray spectra with measured spectra," *Med. Phys.* **26**, 303–309 (1999).
- <sup>5</sup>D. R. Dance *et al.*, "Influence of anode/filter material and tube potential on contrast, signal-to-noise ratio and average absorbed dose in mammography: a Monte Carlo study," *Br. J. Radiol.* **73**, 1056–1067 (2000).
  - <sup>6</sup>L. E. Wilkinson, P. N. Johnston, and J. C. Heggie, "A comparison of mammography spectral measurements with spectra produced using several different mathematical models," *Phys. Med. Biol.* **46**, 1575–1589 (2001).
  - <sup>7</sup>T. R. Fewell and R. E. Shuping, "Photon energy distribution of some typical diagnostic x-ray beams," *Med. Phys.* **4**, 187–197 (1977).
  - <sup>8</sup>B. R. Archer and L. K. Wagner, "Determination of diagnostic x-ray spectra with characteristic radiation using attenuation analysis," *Med. Phys.* **15**, 637–641 (1988).
  - <sup>9</sup>J. M. Boone, T. R. Fewell, and R. J. Jennings, "Molybdenum, rhodium, and tungsten anode spectral models using interpolating polynomials with application to mammography," *Med. Phys.* **24**, 1863–1874 (1997).
  - <sup>10</sup>J. M. Boone and J. A. Seibert, "An accurate method for computer-generating tungsten anode x-ray spectra from 30 to 140 kV," *Med. Phys.* **24**, 1661–1670 (1997).
  - <sup>11</sup>R. G. Wagnere *et al.*, "X-ray spectra estimation using attenuation measurements from 25 kVp to 18 MV," *Med. Phys.* **26**, 1269–1278 (1999).
  - <sup>12</sup>R. Birch and M. Marshall, "Computation of bremsstrahlung X-ray spectra and comparison with spectra measured with a Ge(Li) detector," *Phys. Med. Biol.* **24**, 505–517 (1979).
  - <sup>13</sup>R. Nowotny and A. Hofer, "Ein program für die berechnung von diagnostischen Röntgenspektren," *Fortschr. Röntgenstr.* **142**, 685–689 (1985).
  - <sup>14</sup>W. J. Iles, "The Computation of the bremsstrahlung x-ray spectra over an energy range 15 keV to 300 keV," Report NRPB-R204 National Radiological Protection Board, 1987.
  - <sup>15</sup>D. M. Tucker, G. T. Barnes, and D. P. Chakraborty, "Semiempirical model for generating tungsten target x-ray spectra," *Med. Phys.* **18**, 211–218 (1991).
  - <sup>16</sup>D. M. Tucker, G. T. Barnes, and X. Z. Wu, "Molybdenum target x-ray spectra: A semiempirical model," *Med. Phys.* **18**, 402–407 (1991).
  - <sup>17</sup>M. M. Blough, R. G. Waggener, W. H. Payne, and J. A. Terry, "Calculated mammographic spectra confirmed with attenuation curves for molybdenum, rhodium, and tungsten targets," *Med. Phys.* **25**, 1605–1612 (1998).
  - <sup>18</sup>R. N. Kulkarni and S. J. Supe, "Monte Carlo calculations of mammographic x-ray spectra," *Phys. Med. Biol.* **29**, 185–190 (1984).
  - <sup>19</sup>M. R. Ay, M. Shahriari, S. Sarkar, M. Adib, and H. Zaidi, "Monte Carlo simulation of x-ray spectra in diagnostic radiology and mammography using MCNP4C," *Phys. Med. Biol.* **49**, 4897–4917 (2004).
  - <sup>20</sup>K. P. Ng, C. S. Kwok, and F. H. Tang, "Monte Carlo simulation of x-ray spectra in mammography," *Phys. Med. Biol.* **45**, 1309–1318 (2000).
  - <sup>21</sup>F. Verhaegen, A. E. Nahum, S. Van de Putte, and Y. Namito, "Monte Carlo modeling of radiotherapy kV x-ray units," *Phys. Med. Biol.* **44**, 1767–1789 (1999).
  - <sup>22</sup>L. Silberstein, "Determination of the spectral composition of x-ray radiation from filtration data," *Opt. Soc. Am.* **22**, 265–280 (1932).
  - <sup>23</sup>B. W. Soole, "A determination of x-ray attenuation analysis for approximating the intensity distribution at its point of origin of bremsstrahlung excited in a thick target by incident electrons of constant medium energy," *Phys. Med. Biol.* **21**, 369–389 (1976).
  - <sup>24</sup>B. R. Archer, T. R. Fewell, and L. K. Wager, "Laplace reconstruction of experimental diagnostic x-ray spectra," *Med. Phys.* **15**, 832–837 (1988).
  - <sup>25</sup>P. Huang, T. Chen, and K. R. Kase, "Reconstruction of diagnostic x-ray spectra by numerical analysis of transmission data," *Med. Phys.* **13**, 707–710 (1986).
  - <sup>26</sup>P. Francois, A. Catala, and Ch. Scouarnec, "Simulation of x-ray spectra reconstruction from transmission data by direct resolution of the numeric system  $AF=T$ ," *Med. Phys.* **20**, 1695–1703 (1993).
  - <sup>27</sup>J. M. Boone, "X-ray spectral reconstruction from attenuation data using neural networks," *Med. Phys.* **17**, 647–654 (1990).
  - <sup>28</sup>J. M. Boone, "The three parameter equivalent spectra as an index of beam quality," *Med. Phys.* **15**, 304–310 (1988).
  - <sup>29</sup>H. A. Kramers, "On the theory of x-ray absorption and of the continuous x-ray spectrum," *Philos. Mag.* **46**, 836–871 (1923).
  - <sup>30</sup>M. Green and V. E. Cosslett, "Measurements of K, L and M shell x-ray production efficiencies," *Br. J. Appl. Phys.* **1**, 425 (1968).
  - <sup>31</sup>A. Vignes and G. Dez, "Distribution in depth of the primary x-ray emission in anticathodes of titanium and lead," *Br. J. Appl. Phys.* **1**, 1309–1322 (1968).
  - <sup>32</sup>J. R. Mercier *et al.*, "Modification and benchmarking of MCNP for low-energy tungsten spectra," *Med. Phys.* **27**, 2680–2687 (2000).
  - <sup>33</sup>M. R. Ay, S. Sarkar, M. Shahriari, D. Sardari, and H. Zaidi, "Comparative assessment of different computational models for generation of x-ray spectra in diagnostic radiology and mammography," Proc. IEEE Nuclear Science Symposium and Medical Imaging Conference, 19–22 October, Rome, Italy (2004) (in press).
  - <sup>34</sup>J. P. Bissonnette and L. J. Schreiner, "A comparison of semiempirical models for generating tungsten target x-ray spectra," *Med. Phys.* **19**, 579–582 (1992).
  - <sup>35</sup>M. Caon, G. Bibbo, J. Pattison, and M. Bhat, "The effect on dose to computed tomography phantoms of varying the theoretical x-ray spectrum: a comparison of four diagnostic x-ray spectrum calculating codes," *Med. Phys.* **25**, 1021–1027 (1998).
  - <sup>36</sup>R. Birch, M. Marshall, and G. M. Ardran, Catalogue of Spectral Data for Diagnostic X-Rays Hospital Physicists, Report SRS30, 1979.
  - <sup>37</sup>M. J. Berger and J. H. Hubbell, XCOM: Photon cross sections on a personal computer, National Bureau of Standards (US), Report NBSIR 87-3597, 1987.
  - <sup>38</sup>K. Cranley, B. J. Gilmore, G. W. A. Fogarty, and L. Desponds, IPEM Report 78 Catalogue of Diagnostic X-Ray Spectra and other Data, The Institute of Physics and Engineering in Medicine (IPEM); CD-Rom Edition 1997 (Electronic Version prepared by D. Sutton), 1997.
  - <sup>39</sup>J. F. Briesmeister, "MCNP—A general Monte Carlo N-particle transport code," version 4C, Los Alamos National Laboratory, NM, Report LA-13709-M, 2000.
  - <sup>40</sup>W. R. Nelson, H. Hirayama, and D. Roger, The EGS4 code system, Stanford Linear Accelerator Center, Report SLAC-256, 1985.
  - <sup>41</sup>J. A. Halbleib *et al.*, "ITS Version 3.0: The Integrated TIGER," series of coupled Electron/Photon Monte Carlo Transport Codes, Sandia National Laboratories, Report SAND91-1634, 1992.
  - <sup>42</sup>M. Cristy and K. F. Eckerman, "Specific Absorbed Fractions of Energy at Various Ages from Internal Photon Source," Report ORNL/TM-8381/V1-7, Oak Ridge National Laboratory, 1987.
  - <sup>43</sup>ICRP Report 60, Recommendations of the International Commission on Radiological Protection, International Commission on Radiological Protection, 1991.
  - <sup>44</sup>NRPB, A National Survey of Doses to Patients Undergoing a Selection of Routine X-ray Examination in English Hospitals. Report R200, National Radiological Protection Board, 1986.
  - <sup>45</sup>R. Nowotny and Kh. Meghzifene, "Simulation of the effect of anode surface roughness on diagnostic x-ray spectra," *Phys. Med. Biol.* **47**, 3973–3983 (2002).
  - <sup>46</sup>N. A. Dyson, *X-ray in Atomic and Nuclear Physics*, 2<sup>nd</sup> ed. (Cambridge University Press, Cambridge, 1990).
  - <sup>47</sup>L. M. N. Tavora, E. J. Morton, and W. B. Gilboy, "Design considerations for transmission x-ray tubes operated at diagnostic energies," *J. Phys. D* **33**, 2497–2507 (2000).

# Paper III

*Phys Med Biol* **50**: 4863-4885

© Reprinted with Permission From  
Institute of Physics and IOP Publishing

# Development and validation of MCNP4C-based Monte Carlo simulator for fan- and cone-beam x-ray CT

Mohammad Reza Ay and Habib Zaidi

Division of Nuclear Medicine, Geneva University Hospital, CH-1211 Geneva 4, Switzerland

E-mail: [habib.zaidi@hcuge.ch](mailto:habib.zaidi@hcuge.ch)

Received 29 April 2005, in final form 1 July 2005

Published 5 October 2005

Online at [stacks.iop.org/PMB/50/4863](http://stacks.iop.org/PMB/50/4863)

## Abstract

An x-ray computed tomography (CT) simulator based on the Monte Carlo N-particle radiation transport computer code (MCNP4C) was developed for simulation of both fan- and cone-beam CT scanners. A user-friendly interface running under Matlab 6.5.1 creates the scanner geometry at different views as MCNP4C's input file. The full simulation of x-ray tube, phantom and detectors with single-slice, multi-slice and flat detector configurations was considered. The simulator was validated through comparison with experimental measurements of different nonuniform phantoms with varying sizes on both a clinical and a small-animal CT scanner. There is good agreement between the simulated and measured projections and reconstructed images. Thereafter, the effects of bow-tie filter, phantom size and septa length on scatter distribution in fan-beam CT were studied in detail. The relative difference between detected total, primary and scatter photons for septa length varying between 0 and 95 mm is 11.2%, 1.9% and 84.1%, respectively, whereas the scatter-to-primary ratio decreases by 83.8%. The developed simulator is a powerful tool for evaluating the effect of physical, geometrical and other design parameters on scanner performance and image quality in addition to offering a versatile tool for investigating potential artefacts and correction schemes when using CT-based attenuation correction on dual-modality PET/CT units.

(Some figures in this article are in colour only in the electronic version)

## 1. Introduction

X-ray computed tomography (CT) images inherently have the tendency to produce physics-related artefacts compared to conventional planar radiography owing to the fact that the images are reconstructed from a large number of independent detector elements. The reconstruction algorithm often assumes that all these measurements are consistent; consequently any error of

measurement will usually be reflected as an error in the reconstructed images. There are several sources of error and artefact that affect clinical image quality in x-ray CT (Tofts and Gore 1980). It is therefore necessary to assess their significance and effect on the resulting images to reduce their impact either by optimizing the scanner design or by devising appropriate image correction and reconstruction algorithms. Recent advances in the design of fan- and cone-beam CT scanners rely on a detailed analysis of the influence of different physical and geometrical parameters on overall scanner performance, clinical image quality and patient absorbed dose. This could be achieved through costly physical experiments and development of test prototypes (Drangova and Fenster 1994, Lee *et al* 2003, Meinel *et al* 2003), analytical mathematical modelling (Siewerdsen and Jaffray 2000, De Man 2001, Chen and Ning 2002, De Francesco and Da Silva 2002, Hsieh 2003) or sophisticated Monte Carlo simulations (Colijn and Beekman 2004, Colijn *et al* 2004, Khodaverdi *et al* 2005). Although the investigation of imaging design parameters using the Monte Carlo method is time consuming compared to relatively simple mathematical modelling, the widespread availability of high performance parallel computing and more recently Grid technology in addition to the popularity of variance reduction techniques spurred the use of Monte Carlo calculations especially when modelling complex geometries. It should be noted that the accuracy of Monte Carlo simulations is well established in the area of CT dosimetry (Atherton and Huda 1995, Caon *et al* 1997, 1998, Wang *et al* 1999, Boone *et al* 2000, Jarry *et al* 2003, Lucas *et al* 2004).

One of the most important parameters in x-ray CT imaging is the bias induced by scattered radiation, which depends on the geometry of the CT scanner and the object under study. The amount and spatial distribution of the scatter component should be corrected for before or during the reconstruction process. Since the corruption of collected data with scattered photons decreases low contrast detectability, reduces CT number (Kanamori *et al* 1985) and introduces cupping and streak artefacts in the reconstructed images (Colijn and Beekman 2004), thorough knowledge of scatter distribution is essential for optimization of scanner design geometry (Siewerdsen and Jaffray 2000) and development of scatter correction techniques (Ohnesorge *et al* 1999).

The general practice of developing theoretical scatter models involves experimental physical measurements and mathematical modelling (Tofts and Gore 1980, Glover 1982, Johns and Yaffe 1982, Joseph and Spital 1982, Merritt and Chenery 1986, Siewerdsen and Jaffray 2001) whereas most recent publications focus on the use of Monte Carlo simulations (Kanamori *et al* 1985, Endo *et al* 2001, Malusek *et al* 2003, Colijn and Beekman 2004, Colijn *et al* 2004). It has long been recognized that the ideal research tool (gold standard) for scatter modelling and evaluation of scatter correction techniques is the Monte Carlo method. However, it should be emphasized that most studies were carried out using in-house developed dedicated Monte Carlo programs. The advantages offered by widely used and extensively tested state-of-the-art general-purpose Monte Carlo codes such as MCNP in terms of versatility, published reports and long-term technical support and maintenance are well established.

In this work, we have developed a Monte Carlo x-ray CT simulator for fan- and cone-beam geometries with single-slice, multi-slice and flat detector configurations based on the Monte Carlo N-particle (MCNP4C) radiation transport computer code. A user-friendly interface running under Matlab 6.5.1 (The MathWorks Inc., Natick, MA, USA) creates the geometry of the scanner in different views as MCNP4C input file. Detailed simulation of x-ray tube, collimator, bow-tie filter, phantom, detector geometry and material were considered. The simulator was validated through comparison with experimental measurements of different nonuniform phantoms with various sizes on both a clinical GE HiSpeed X/iF (General Electric Healthcare Technologies, Waukesha, WI, USA) fan-beam CT scanner and a small-animal SkyScan 1076 (SkyScan, Aartselaar, Belgium) cone-beam CT scanner. The accelerated

Monte Carlo simulator (AMCS) developed by Colijn *et al* (2004) was also used as a benchmark for validation of parameters difficult or impossible to measure experimentally. This paper addresses particularly some aspects not sufficiently covered in the literature, namely the assessment of scatter distribution in fan-beam scanners and the effect of scatter media (phantom size) and septa length up to 95 mm on the spatial distribution of scattered radiation. The aim is to exploit this tool for development and evaluation of scatter modelling and correction techniques in CT and assessment of potential sources of artefacts and their compensation when using CT-based attenuation correction in dual-modality PET/CT imaging (Hasegawa and Zaidi 2005).

## 2. Materials and methods

### 2.1. Description of the MCNP4C-based Monte Carlo CT simulator

*2.1.1. The MCNP4C code.* The x-ray CT simulator was built on top of the MCNP4C general-purpose Monte Carlo code, which serves as a core layer giving the opportunity to the developer to construct application-specific modules in a hierarchical layer architecture. MCNP is a general-purpose, continuous-energy, generalized-geometry, time-dependent, coupled neutron/photon/electron Monte Carlo transport code. For photon transport, the code takes into account photoelectric absorption, with the possibility of K- and L-shell fluorescent emission or Auger electron, coherent and incoherent scattering and pair production. The photoelectric cross sections are based on Storm and Israel (1967) whereas the scattering cross sections are taken from ENDF tabulations (Hubbell *et al* 1975). The continuous slowing down approximation energy loss model is used for electron transport. To improve the efficiency of electron and photon transport, two cards (PHYS:P and PHYS:E) are implemented in MCNP for biasing some physical parameters such as upper energy limit for electrons and photons (EMAX and EMCPE), production of secondary electrons by photons (IDES), coherent scattering (NOCOH), production of photons by electrons (IPHOT) and production of characteristic x-rays (XNUM).

In the first step, the user should create an input file which contains information about the problem such as geometry specification, description of materials, type of answer or tally and variance reduction techniques to be used. The geometry of MCNP treats an arbitrary three-dimensional configuration in Cartesian coordinate system. The number of cells in this code should be less than  $10^5$ . If this limit is exceeded when using cell geometry, the lattice geometry should be used. The lattice uses a smaller number of cells but adds somewhat to the MCNP execution time. Important standard features that make MCNP very versatile and easy to use include a powerful general source and surface source, both geometry and output tally plotters, a rich collection of variance reduction techniques, a flexible tally structure and an extensive collection of cross-section data. For the purpose of decreasing computation time, MCNP takes advantage of parallel computer architectures. It is supported in multitasking mode on some mainframes and in multiprocessing mode on a cluster of workstations where the distributed processing uses the Parallel Virtual Machine (PVM) software (Briesmeister 2000).

*2.1.2. User interface.* The creation of input file in the MCNP4C code using first and second degree surfaces is not an easy task, especially when dealing with the complex geometries typical of an x-ray CT scanner requiring an extremely large number of plans to create detector cells and septa. The user interface running under Matlab 6.5.1 is realized by an easy to use concept. Basically, the user is asked to choose the x-ray CT scanner design parameters.

According to the information provided and options selected by user, the interface program creates the scanner geometry as input file for MCNP4C. Since MCNP is not able to simulate gantry rotation, the geometry of each view is created in separate files. To increase the performance of the simulator for investigation of different design parameters, the input file is created according to the parameters selected by the user, some of which are summarized in table 1. It should be emphasized that the number of detector rows were chosen to mimic typical geometry of prototype and commercially available CT scanners. There are two reasons for setting the number of detector elements in each row less than 1000 in the simulator. Firstly, the number of detector elements in all commercial single- and multi-slice fan-beam x-ray CT scanners is less than this value (between 800 and 900 elements) and secondly, as we aim at simulating the geometry of multi-slice scanners up to 64 slices and considering the limitation of MCNP4C in terms of number of cells (99'999), we made every effort to save the maximum number of cells for septa plates, voxel-based phantoms and other elements such as collimators and filters. It is, however, also possible to use more than 1000 elements per row in some cases if needed.

After simulation of all views, the sinogram is created from detector outputs after blank scan correction in all views by the user interface program. The filtered back-projection reconstruction algorithm was used for image reconstruction of the simulated data sets (Kak and Slaney 1999). Beam hardening effect, usually integrated in commercial software supplied by scanner manufacturers, was removed from the projections according to the method described by Kanamori *et al* (1985).

**2.1.3. CT simulator features.** The simulation process starts from the x-ray tube where the user interface offers two options for simulation of x-ray spectra. In the full simulation case, all electrons emitted from the filament are fully tracked into the target for the calculation of bremsstrahlung and produced characteristic photons (Ay *et al* 2004). Since tracking a large number of electrons into the target is time consuming, a pre-calculated spectra option offering the possibility of using spectra generated by different computational methods (Ay *et al* 2005) with varying focal spot size was implemented in the user interface program. In addition, the creation of simple shape-based and more complicated adult ORNL hermaphroditic mathematical phantoms (Cristy and Eckerman 1987) was also considered. The use of voxel-based phantoms as input to the simulator is still under development. One of the possibilities would be to use Scan2MCNP commercial program (White Rock Science, Los Alamos, NM, USA) to convert anatomical patient-specific CT or MRI data and other software phantoms (e.g. VIP-Man (Xu *et al* 2000)) to an input file for MCNP/MCNPX by paying special attention to the number of cells. For dosimetry purposes, the default value of PHYS:P and PHYS:E cards should be used to enable full electron and photon transport, while these parameters could be modified for imaging systems modelling purposes to speed-up the simulation process. The user interface program can create the input file as individual cells or as a lattice. This capability solves the limitation of MCNP in terms of number of cells especially for the cone-beam geometry with an extremely large number of detector elements. Different types of detector elements' output such as energy distribution of pulses created in each element (\*F8 in MeV), photon fluence (F4 in  $\text{cm}^{-2}$ ) and energy fluence (\*F4 in  $\text{MeV cm}^{-2}$ ) which pass through each element with various energy bins were considered in the simulator. The energy deposit per unit mass in each phantom's cell could be calculated using cell energy deposit tally (F6 in  $\text{MeV g}^{-1}$ ) for dosimetry purposes. The four classes of variance reduction techniques (truncation, population control, modified sampling and partially deterministic methods) implemented in MCNP4C could be used depending on the objectives and expected outcome of the simulation.

**Table 1.** Summary of x-ray CT scanner design parameters used for creation of model geometry as MCNP4C input file.

Gantry		Detector		X-ray tube		Phantom	
Parameter	Option	Parameter	Option	Parameter	Option	Parameter	Option
Source-to-isocentre distance	– <sup>a</sup>	Detector configuration	Single-slice multi-slice, flat panel	X-ray spectra	Full simulation, pre-computed	Phantom type	Shape based, voxel based <sup>b</sup>
Source-to-detector distance	– <sup>a</sup>	Number of detector rows	1, 2, 4, 8, 12, 16, 32, 64	Target angle	– <sup>a</sup>	Phantom shape	– <sup>a</sup>
Source to primary collimator distance	– <sup>a</sup>	Number of detector elements per row	<sup>a</sup> (<1000)	Target material	– <sup>a</sup>	Phantom dimensions	– <sup>a</sup>
Source to secondary collimator distance	– <sup>a</sup>	Detector element dimensions	– <sup>a</sup>	Inherent filtration	Al, Cu, <sup>a</sup>	Phantom material	– <sup>a</sup>
Secondary collimation aperture	Circular, rectangular	Ratio of detector element to septa pitch	– <sup>a</sup>	Additional filter	Al, Cu, <sup>a</sup>	Non-homogeneous phantoms	Yes
Bow-tie filter size	– <sup>a</sup>	Septa element size	– <sup>a</sup>	Spectrum energy bin	– <sup>a</sup>		
Bow-tie filter material	Teflon, PMMA, ... etc	Detector material	Highlight, GOS, CdWO <sub>4</sub> , CSI	Focal spot size	– <sup>a</sup>		
Beam geometry	Fan-beam, cone-beam	Detector output	Energy deposit, flux				
Beam angle	– <sup>a</sup>	Detector cells geometry	Individual cells, lattice				
Rotation angle	Full, partial rotation						
Number of views	– <sup>a</sup>						

<sup>a</sup> Adjustable.<sup>b</sup> Under development.

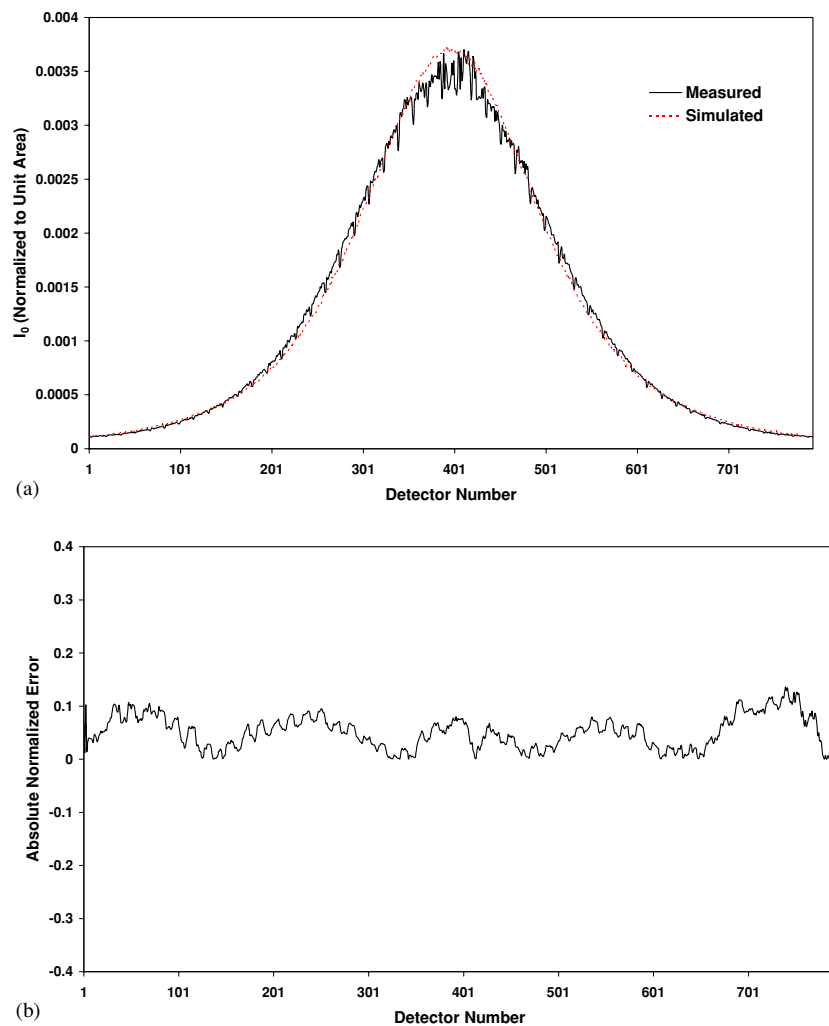


**Figure 1.** (a) Comparison of simulated and measured bow-tie filter profiles for the GE HiSpeed X/iF CT scanner at tube voltage 120 kV, slice thickness 10 mm and focal spot 1.2 mm. (b) Plot of the absolute normalized error (NE) for the profile shown in (a).

## 2.2. CT simulator evaluation and validation

The validity of MCNP4C-based Monte Carlo simulator was verified by comparing the simulated and measured distributions from various uniform and non-uniform phantoms on both a fan- and a cone-beam x-ray CT scanner.

**2.2.1. Fan-beam human CT scanner.** The single-slice GE HiSpeed X/iF CT scanner with Highlight ( $\text{Y}_2\text{Gd}_2\text{O}_3:\text{Eu}$ ) ceramic scintillator was used. This third generation CT scanner has 541 mm source-to-isocentre and 949 mm source-to-detector distances, 816 detector elements (793 active elements) with a physical dimension of 0.8 mm. The Highlight scintillator combined with 0.2 mm septa results in a geometrical efficiency of 80%. The actual shape and size of the Teflon bow-tie filter was measured directly on the scanner and used as input to the

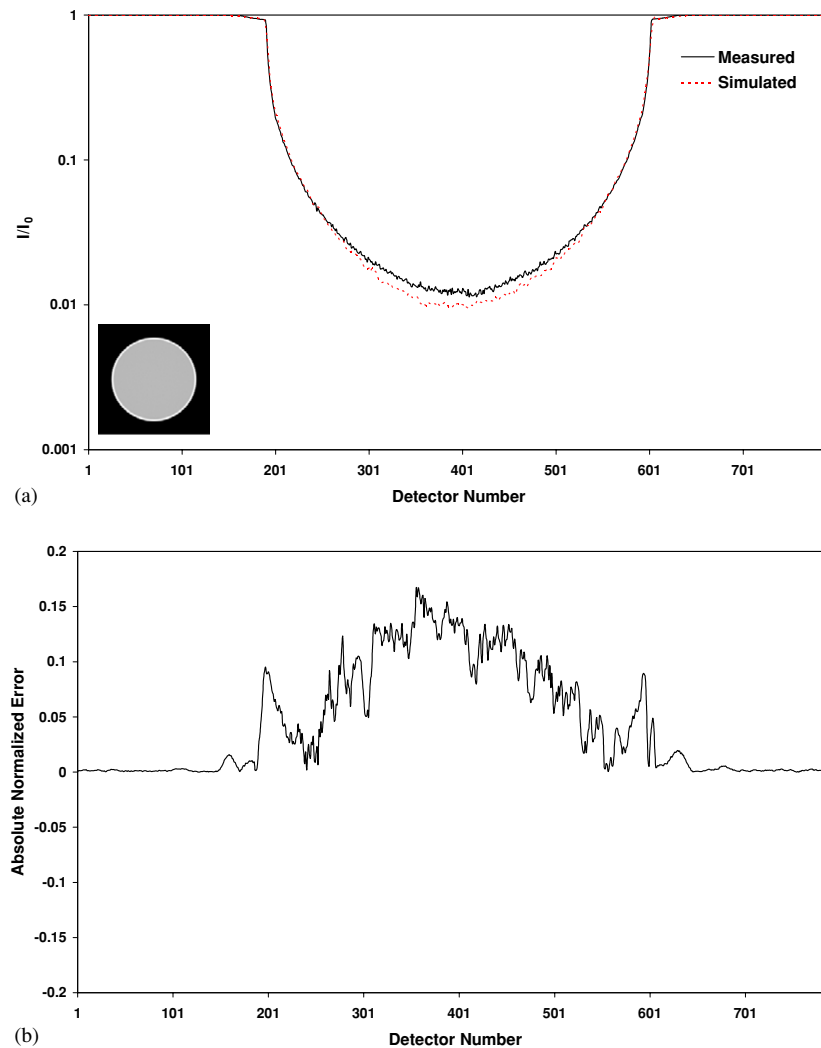


**Figure 2.** Comparison between simulations and experimental measurements for the GE HiSpeed X/iF CT scanner using the same set-up as in figure 1. (a) Profile of the water phantom. (b) The absolute normalized error of the profile shown in (a). (c) The scatter to primary ratio limited to the field of view.

simulator. The CT scanner is equipped with Solarix x-ray tube with  $61.5^\circ$  fan-beam angle,  $7^\circ$  target angle and minimum inherent filtration of  $1.2 \text{ mm Al}_{\text{eq}}$  at 140 kV.

**2.2.2. Cone-beam small-animal CT scanner.** The cone-beam small-animal CT scanner is the SkyScan 1076 with 172 mm source-to-detector and 51 mm isocentre-to-detector distances. The x-ray tube is L8032 micro-focus (Hamamatsu Photonics K. K., Iwata City, Japan) with  $100 \mu\text{m}$  Be window and  $500 \mu\text{m}$  aluminium additional filter. The emission cone angle is  $39^\circ$ , the fan angle or angle of the beam in the transaxial plane is  $32^\circ$  while it reduces to  $8^\circ$  in the axis of scanner (cone angle). The scanner uses GOS ( $\text{Gd}_2\text{O}_2\text{S}$ ) scintillator crystal with 0.025 mm thickness and  $100 \times 25 \text{ mm}^2$  detector area with pixel size of  $12.5 \times 12.5 \mu\text{m}^2$ .

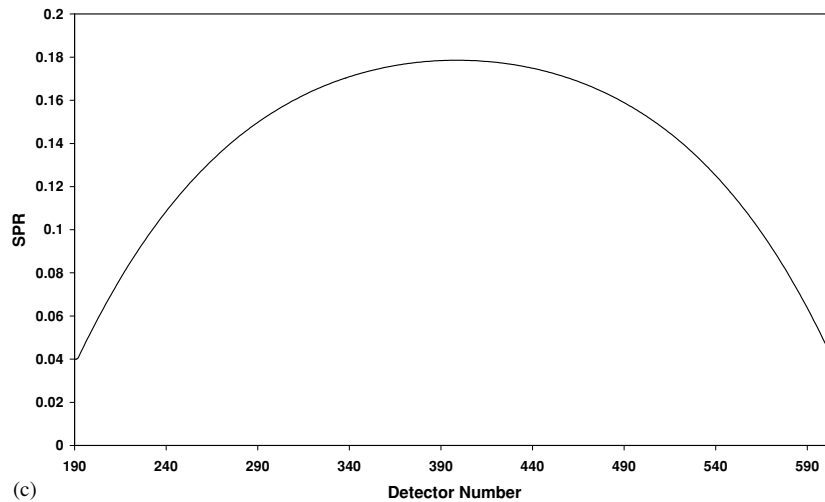


Figure 2. (Continued.)

The experimental measurements used in this work were taken from a recent paper by Colijn *et al* (2004) related to the validation of their rapid Monte Carlo-based Micro-CT simulator.

**2.2.3. Phantoms.** Two cylindrical phantoms were constructed specifically for experimental measurements on the clinical fan-beam CT scanner: (i) a homogenous cylindrical water phantom ( $\phi 266 \pm 0.5$  mm) with 16 mm acrylic case and (ii) a polyethylene cylindrical phantom ( $\phi 200 \pm 0.5$  mm) containing two centred air ( $\phi 50 \pm 0.5$  mm) and steel ( $\phi 10 \pm 0.5$  mm) cylinders. Another non-uniform software phantom was specifically designed to study the capability of the simulator to produce typical expected profiles when using different materials. This water-filled elliptical cylinder with 220 mm and 80 mm long and short axes, respectively, and 200 mm height contains nine cylinders ( $\phi 10$  mm) filled with air ( $\rho = 0.0012$  g cm<sup>-3</sup>), inflated lung ( $\rho = 0.296$  g cm<sup>-3</sup>), deflated lung ( $\rho = 1.092$  g cm<sup>-3</sup>), soft tissue ( $\rho = 1.04$  g cm<sup>-3</sup>), cartilage ( $\rho = 1.1$  g cm<sup>-3</sup>), trabecular bone ( $\rho = 1.3$  g cm<sup>-3</sup>), cortical bone ( $\rho = 1.92$  g cm<sup>-3</sup>), dental implant ( $\rho = 4.42$  g cm<sup>-3</sup>) and hip implant ( $\rho = 4.52$  g cm<sup>-3</sup>).

Three cylindrical phantoms were used for experimental validation of the cone-beam CT scanner (Colijn *et al* 2004): (i) a cylindrical water phantom ( $\phi 60$  mm), (ii) the same cylindrical water phantom containing four Teflon rods with 10 mm and 3 mm diameters and (iii) again the same cylindrical water phantom containing two 10 mm Teflon rods and two 3 mm stainless steel rods. The casing of the phantoms was 1 mm polystyrene. The rods were placed along the axial direction of the phantom with equal distance from the cylinder centre.

The normalized error (NE) calculated for each detector element was used as a figure of merit to assess discrepancies between measured and simulated projections using the following formulation (Colijn *et al* 2004):

$$NE(u, v) = \frac{P_{\text{Measured}}(u, v) - P_{\text{Simulation}}(u, v)}{P_{\text{Measured}}(u, v)} \quad (1)$$

where  $u$  and  $v$  are detector element's coordinates,  $P_{\text{Measured}}(u, v)$  and  $P_{\text{Simulation}}(u, v)$  are the measured and simulated projection data for each detector element. To reduce statistical

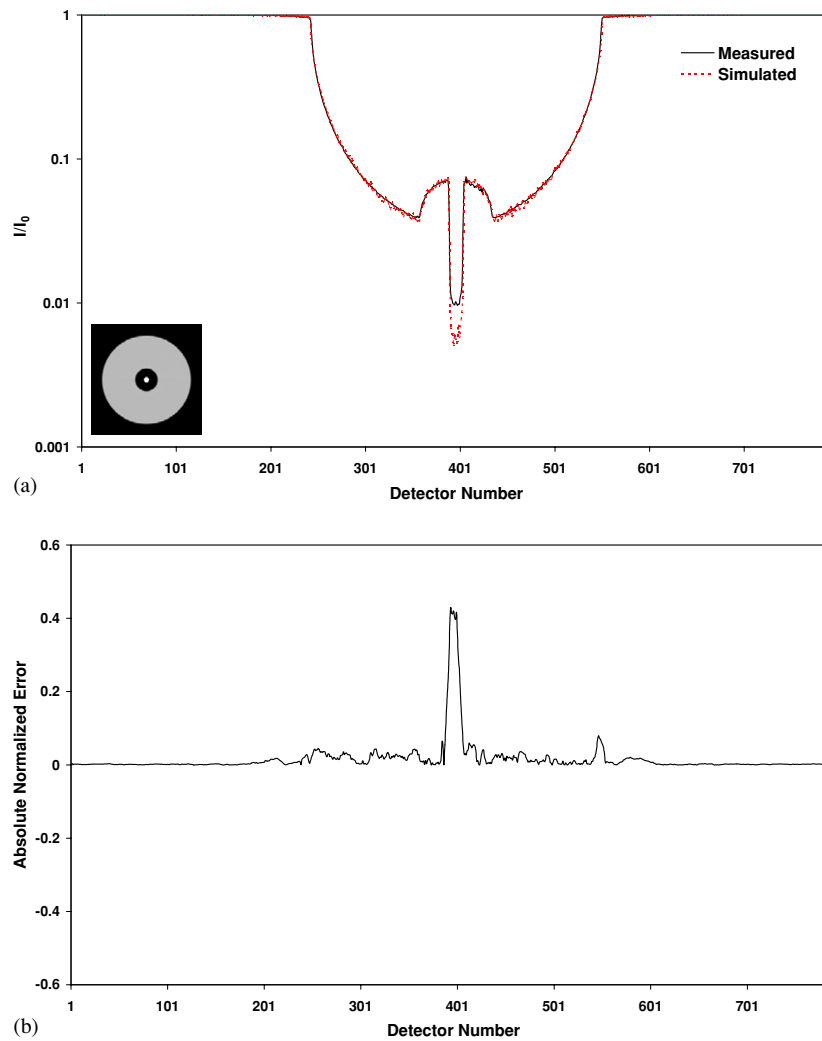


**Figure 3.** Comparison between simulations and experimental measurements for the GE HiSpeed X/iF CT scanner using the same set-up as in figure 1. (a) Profile of the polyethylene inhomogeneous phantom. (b) The absolute normalized error of the profile shown in (a). (c) The scatter-to-primary ratio limited to the field of view.

fluctuations and quantum noise, the normalized errors were smoothed using eight neighbouring points averaging.

### 2.3. Characterization of scatter distribution

The corruption of projection data in fan-beam CT scanners with scattered photons was investigated qualitatively by assessing the distribution of scattered photons as a function of phantom size and quantitatively by calculating scatter-to-primary ratio (SPR) for each detector element. Moreover, the effect of septa length on the scatter profile using full transport of photons inside the septa plates was studied. Statistical fluctuations in the scatter projections were removed for visualization using least-square polynomial fits having

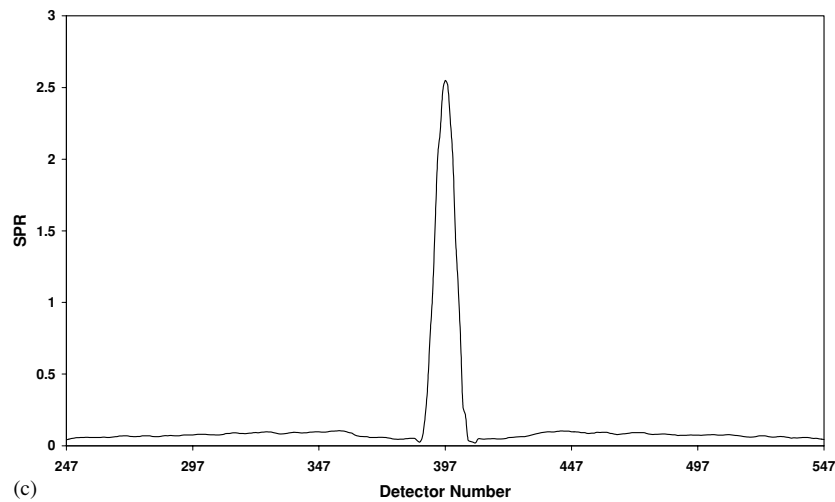


Figure 3. (Continued.)

the highest order polynomial that was practical by means of the XPlot software (European Synchrotron Radiation Facility, France). In all cases,  $\sim 1.9 \times 10^9$  photons were simulated from the focal spot where  $\sim 4.4 \times 10^7$  photons could pass through the bow-tie filter, primary and secondary collimator blades. Increasing the number of photon histories will decrease the statistical fluctuations and quantum noise in the simulated profiles and thus decrease the standards deviations of the estimates. We made every effort to match the simulated statistical fluctuations to the range found in measured results.

### 3. Results

#### 3.1. Validation

*3.1.1. Fan-beam human CT scanner.* Figure 1 shows the comparison between measured and simulated blank scan profiles (detector elements output without phantom being present) from the GE HiSpeed X/iF scanner. The bell shape of the profile is due to photons attenuation on the edges by the Teflon bow-tie filter. This profile was used for blank scan correction to compensate for detectors response non-uniformity in the results presented in the following figures. The absolute normalized error for each detector element is also shown. The maximum of absolute normalized error and average normalized errors in the blank scan profile are 13% and 1.1%, respectively.

The comparison of simulated and measured cylindrical water-filled phantom profiles is shown in figure 2. Both measured and simulated profiles were divided by the corresponding blank scan illustrated in figure 1 (blank scan correction). The log-linear scale was used to magnify the differences between simulated and measured profiles in the central area of the phantom where attenuation lengths are maximum (figure 2(a)). Likewise, the absolute normalized error for each detector element is also shown (figure 2(b)). The noticeable peaks on the borders of the phantom are due to slight misalignment between simulated and measured phantoms (maximum = 16.3%). The central region in the scatter-to-primary ratio plot for detector elements covered by the phantom is larger owing to the smaller number of detected primary photons in this area (figure 2(c)).

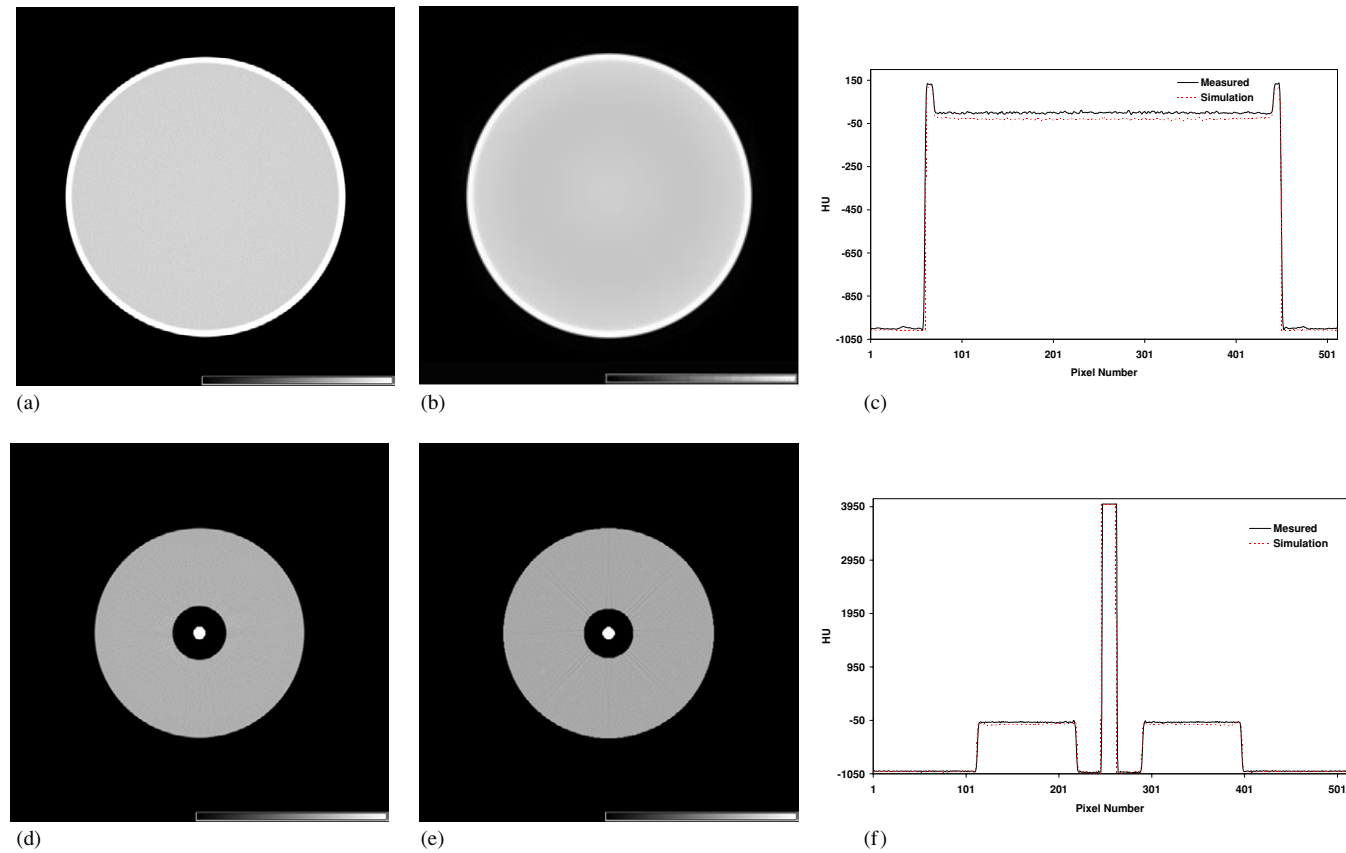


**Figure 4.** Representative images of the measured cylindrical water phantom reconstructed using commercial software (a) and simulated cylindrical water phantom reconstructed using *ifanbeam.m* FBP Matlab routine (b) together with a comparison of central horizontal profiles between measured and simulated image are shown (c). Same as above for the inhomogeneous polyethylene phantom illustrating measured (d) and simulated (e) images and horizontal profiles (f). The window level and width were set at  $-200$  and  $600$  HU, respectively, for both images.

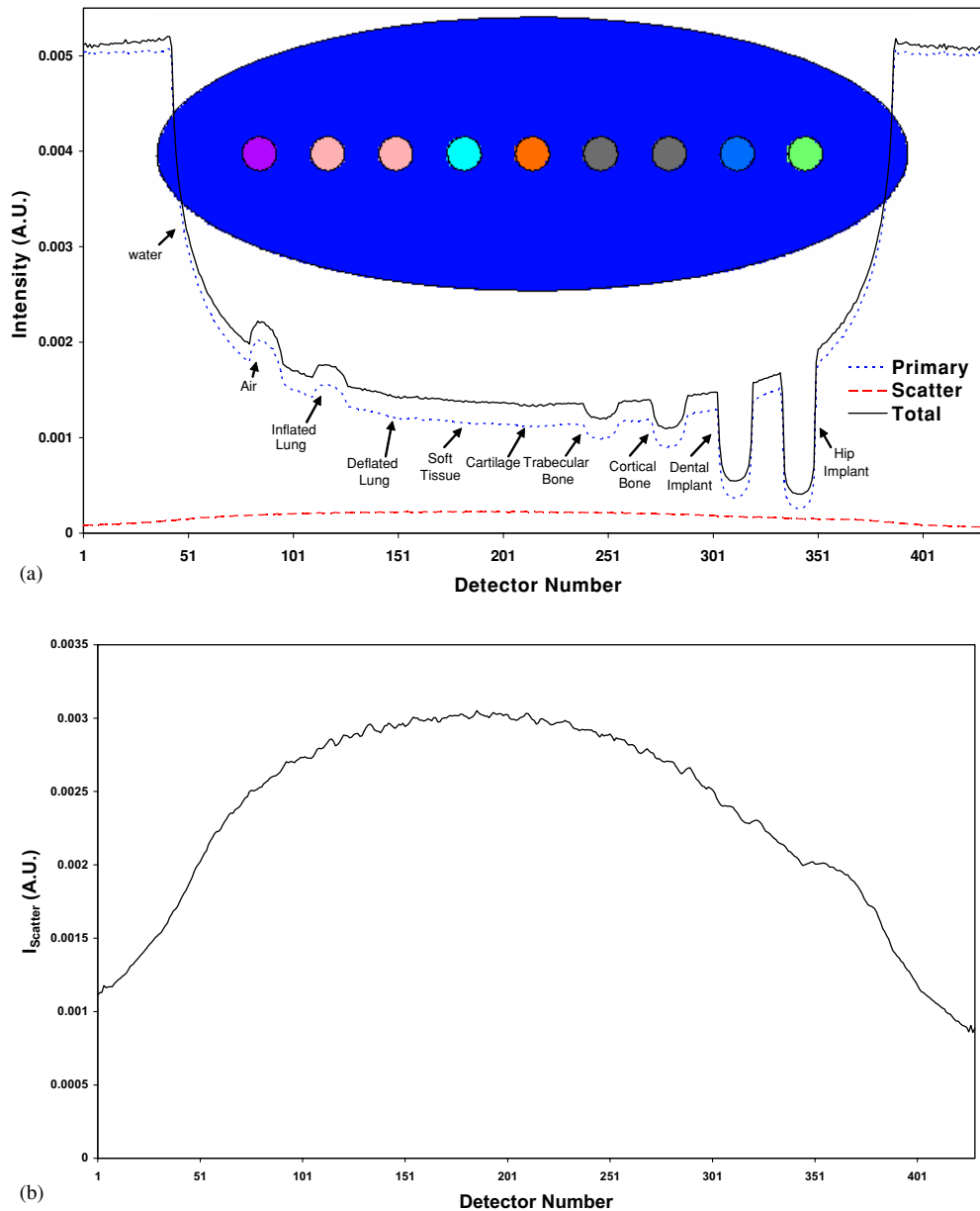


**Figure 5.** Simulated profiles of the water-filled elliptical phantom containing nine cylindrical inserts filled with different materials showing (a) total detected events (full line) separated into different contributions due to primary (dotted line) and scattered (dashed line) photons. (b) Magnified spatial distribution of scattered photons is shown for clarity.

Figure 3 shows the comparison between simulated and measured profiles of the polyethylene cylindrical phantom containing air and steel cylinders after blank scan correction. Good agreement between the simulated and measured profiles can be observed in the polyethylene and air regions of the phantom (figure 3(a)). The maximum absolute normalized error (42%) occurs in the area corresponding to the central steel rod (figure 3(b)). The

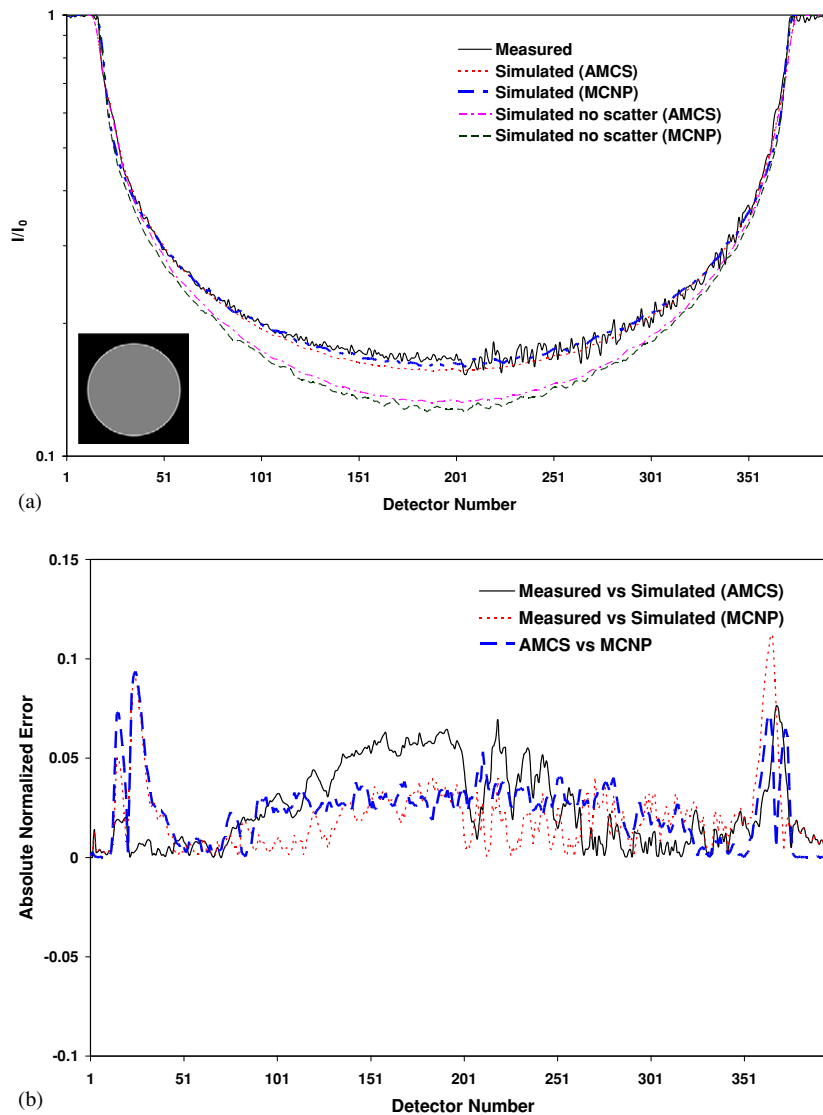


**Figure 6.** Comparison between MCNP and AMCS simulated profiles and experimental measurements of the water phantom (Colijn *et al* 2004) using the SkyScan small-animal x-ray CT scanner at tube voltage 100 kV showing (a) total and primary profiles; (b) the absolute normalized error of the profiles shown in (a); and (c) the scatter-to-primary ratio for the simulated data.

high scatter-to-primary ratio peak (maximum = 255%) observed in the central part could be explained by the high absorption of primary photons in the steel rod (figure 3(c)).

The images of the real and simulated water and polyethylene phantoms reconstructed using filtered back-projection reconstruction algorithm as implemented in commercial software incorporating beam hardening and scatter correction and Matlab's *ifanbeam.m* routine after beam hardening removal from the projections (Kanamori *et al* 1985), respectively, together with a central horizontal profile from reconstructed images are shown in figure 4. The

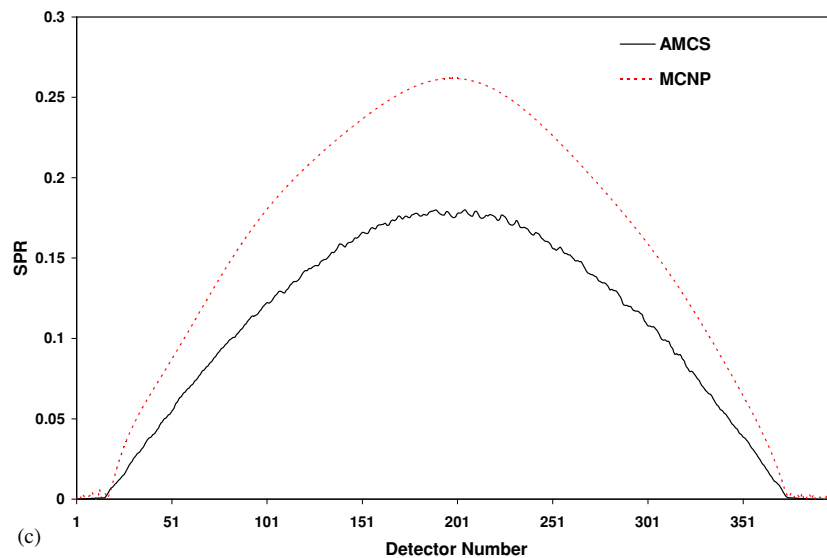
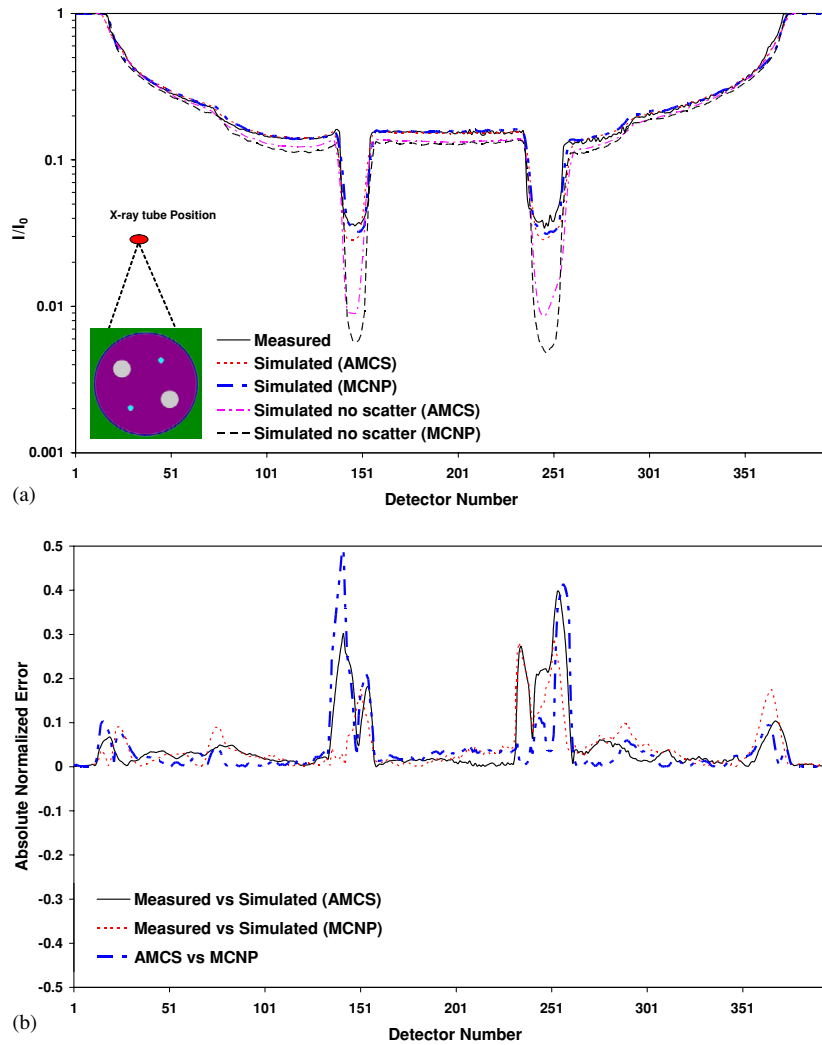


Figure 6. (Continued.)

underestimation of CT numbers in simulated images is due to contribution from scattered radiation, which is corrected for during the reconstruction process in measured images using software supplied by scanner manufacturers. The contrast detectability of MCNP4C-based simulator was further investigated in figure 5, which shows the total, primary and scatter profiles of simulated elliptical water-filled cylindrical phantom containing nine cylinders filled with different materials. The magnified scatter profile is also shown separately. It should be emphasized that a CT geometry with 430 detector elements,  $60^\circ$  fan angle, 5 mm septa length and 80% geometrical efficiency was used for the calculation of these profiles by simulating  $10^9$  photon histories sampled from the 140 kV spectrum with 2 mm Al filter. Although the effect of deflated lung, soft tissue and cartilage is not clearly distinguishable on the profiles, it is expected that the simulation of a large number of photon histories would help us to resolve materials having small differences in electronic density.

**3.1.2. Cone-beam small-animal CT scanner.** Figures 6–8 show the comparison of MCNP4C simulated and measured profiles from the SkyScan 1076 cone-beam small-animal CT as well as the simulated profiles using the AMCS micro-CT simulator (Colijn *et al* 2004). The simulated flat detector configuration was considered as a  $400 \times 100$  grid of  $250 \times 250 \mu\text{m}^2$  detector elements area. The profiles were calculated from the central row of detector matrix. The unscattered profiles were calculated by removing the scattered photons contribution from the simulated profiles. There is generally good agreement between both MCNP4C- and AMCS-based simulations and experimental results. The calculated absolute normalized error for each detector element shows that the MCNP4C-based simulator is in better agreement with measured profiles in comparison to AMCS with a maximum absolute normalized error of 4% in the area covered by the phantom (figure 6(b)). The maximum scatter-to-primary ratios calculated using MCNP4C and AMCS are 26% and 18%, respectively (figure 6(c)). The discrepancy between MCNP4C and AMCS simulation results appears to be due to underestimation of the scattered component and overestimation of primary component by AMCS in comparison with MCNP4C.



**Figure 7.** Comparison between MCNP and AMCS simulated profiles and experimental measurements from water phantom containing steel and Teflon rod inserts (Colijn *et al* 2004) using the SkyScan small-animal x-ray CT scanner at tube voltage 100 kV showing (a) total and primary profiles; (b) the absolute normalized error of the profiles shown in (a); and (c) the scatter-to-primary ratio for the simulated data.

Figure 7 shows the comparison of measured and simulated profiles from water phantom containing Teflon and steel rods presented in log-linear scale in order to magnify the differences between simulated and measured results. It appears that MCNP4C has better agreement with the measured profile compared to AMCS (figure 7(b)). The high absolute normalized error in the area covered by steel rods is due to the high attenuation of steel and probably small geometrical misalignment between simulated and experimental set-ups. The comparison between calculated SPR further illustrates the discrepancy between AMCS and MCNP4C in the region corresponding to steel rod location for the reasons discussed above (figure 7(c)). Figure 8 shows the comparison of simulated and measured profiles, absolute normalized error

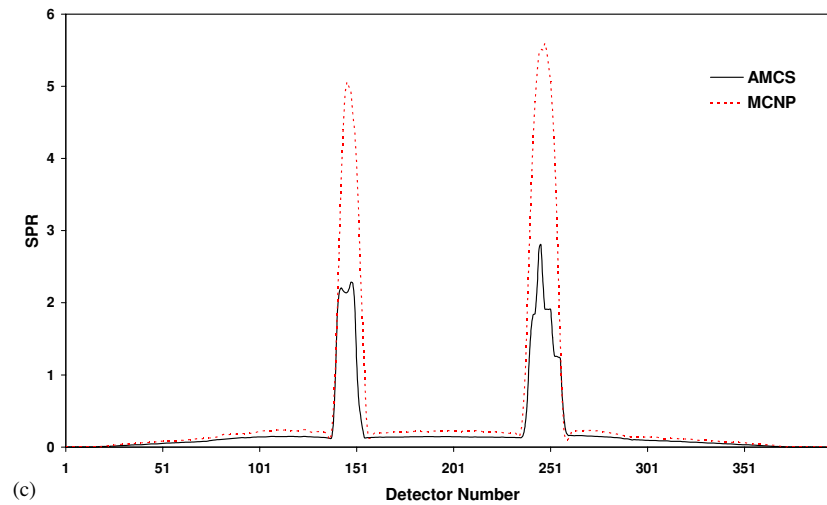


Figure 7. (Continued.)

and SPR for the water-filled phantom containing four Teflon rods. There is generally good agreement between MCNP4C-simulated profiles and measured and AMCS-simulated profiles whereas the same conclusions regarding the SPR still hold.

### 3.2. Scatter characterization

To characterize the spatial distribution of scattered photons from the bow-tie filter and objects of different size, corresponding scatter profiles calculated using the Monte Carlo simulator for the geometry of the fan-beam GE HiSpeed X/iF CT scanner are shown in figure 9. The scatter profile of the blank scan illustrates the detected photons following interaction within the bow-tie filter only whereas the remaining profiles reflect different combinations of detected scattered radiation from the water-filled phantom and bow-tie filter. It can be seen that the scatter profile follows closely the phantom size in the presence of Teflon bow-tie filter (figure 9(b)). The scatter profile in the region corresponding to the phantom decreases with increasing the phantom size as a result of increasing the attenuation length compared to the photons' mean free path.

In fan-beam CT scanners, the collimator (septa) in the detector housing directed towards the focal spot is generally used to decrease the contribution of scattered radiation. The corruption of x-ray projection data with scattered radiation decreases by increasing septa length. Figure 10 shows the effect of septa length on the scatter profile obtained by simulating a cylindrical water phantom ( $\phi 266$  mm) in presence of bow-tie filter together with the relative number of detected total, primary and scattered photons. The relative difference between detected total, primary and scatter photons for septa length varying between 0 and 95 mm is 11.2%, 1.9% and 84.1%, respectively, whereas the scatter-to-primary ratio decreases by 83.8%.

## 4. Discussion

The MCNP4C-based x-ray CT simulator developed in this work is in good agreement with both experimental measurements performed on clinical and small-animal CT scanners and

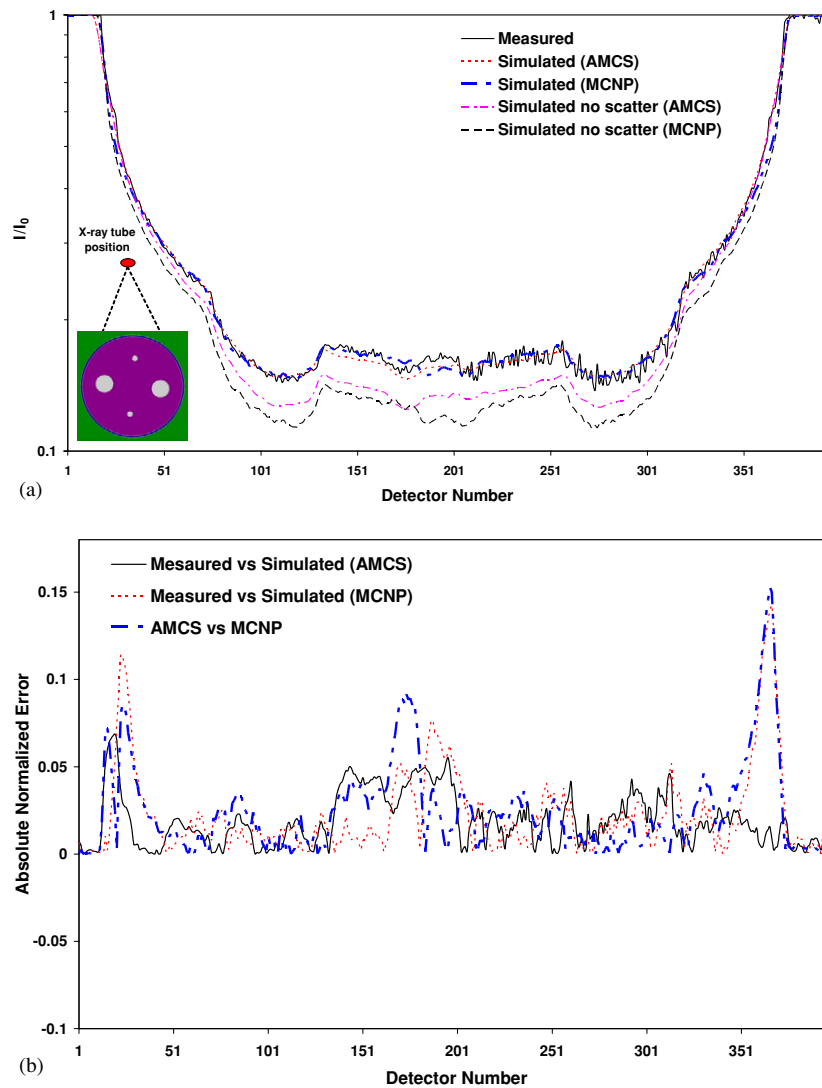


**Figure 8.** Comparison between MCNP and AMCS simulated profiles and experimental measurements from water phantom containing 4 Teflon rods (Colijn *et al* 2004) using the SkyScan small-animal x-ray CT scanner at tube voltage 100 kV showing (a) total and primary profiles; (b) the absolute normalized error of the profiles shown in (a); and (c) the scatter-to-primary ratio for the simulated data.

similar simulated results obtained using an independent dedicated simulator. Therefore, it could serve as an excellent tool for detailed investigation of the effect of different scanner design parameters and data correction techniques on resulting image quality. In the following paragraphs, the origins of small discrepancies between simulated and measured results are discussed.

The discrepancy observed in the blank scan profiles (figure 1) can be explained by apparent differences between the real complex shape of the scanner's bow-tie filter and that used as input to the simulator modelled using combinations of ellipsoidal and cubic surfaces. Although the

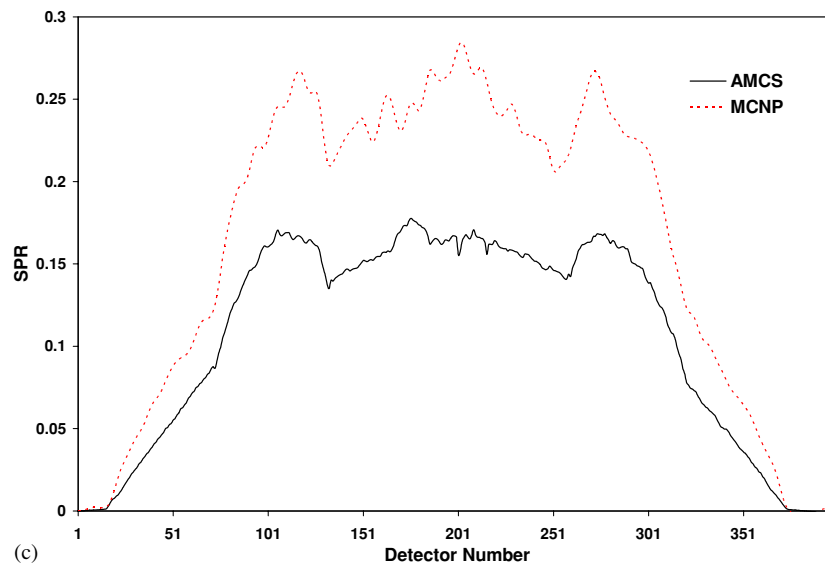
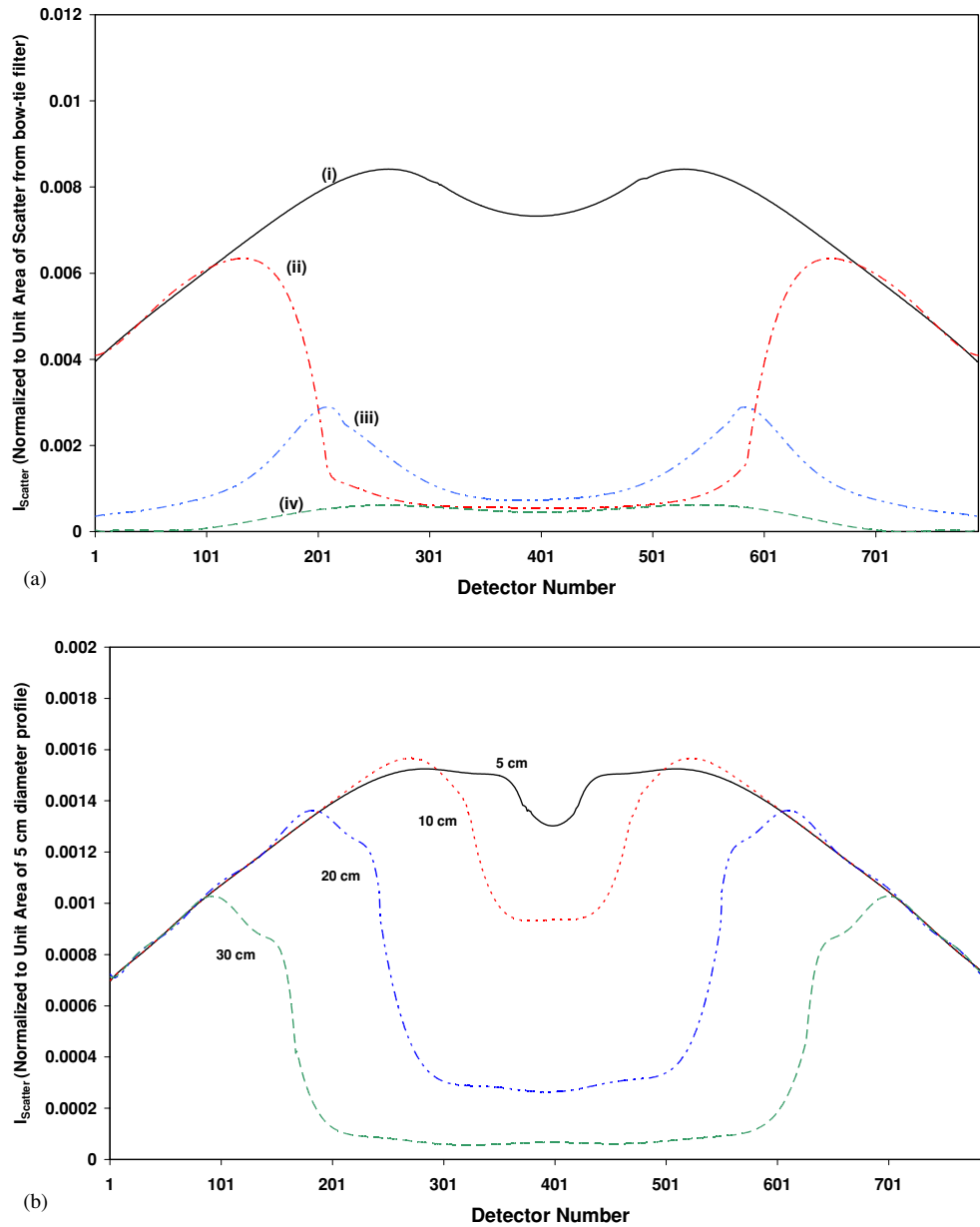


Figure 8. (Continued.)

average normalized error in the blank scan profile is  $\sim 1.1\%$ , the maximum is close to 13%, which can bias somehow the generated data since each simulated x-ray projection data should be divided by the blank scan to compute attenuation profiles. More elaborate modelling of the bow-tie filter should help decreasing the discrepancy, thus preventing error propagation to the simulated projections. Likewise, the small discrepancy between the measured and simulated projections of the cylindrical water phantom (figure 2) is due to differences in the central area of the corresponding measured and simulated blank scans. It has been shown that the distribution of scattered photons in the cylindrical water phantom is approximately uniform. The curvature of SPR (figure 2(c)) is due to the variable probability of primary photons transmission, which is significantly lower in the region corresponding to longer path lengths (central area). The discrepancy between the simulated and measured profiles of the polyethylene phantom (figure 3(a)) arises from two crucial factors: firstly the density and chemical composition of the simulated and commercially available (mixed) steel were not similar (pure steel was simulated); and secondly the high attenuation of steel in the x-ray spectra energy range decreases the probability of photons transmission, thus increasing the statistical uncertainty in the region covered by steel. The high value of SPR in the steel area (figure 3(c)) is due to the high absorption of primary photons in the steel since the scatter distribution is approximately uniform.

The good agreement between simulated and measured images is an additional proof of the accurate modelling of x-ray CT imaging physics incorporated in the Monte Carlo simulator and associated user interface program (figure 4). It should be noted that the simulated projection data were reconstructed without performing scatter correction in contrary to the experimentally measured data where the commercial reconstruction software supplied by the manufacturer was used to effectively remove scatter artefacts. The central horizontal profiles revealed slight underestimation of CT numbers in simulated images as compared to the measured images, which is due to contribution of scattered photons. The low and high contrast detectability of the x-ray CT simulator was also investigated demonstrating modest performance for low contrast detectability depending on the collected statistics (figure 5).



**Figure 9.** Simulated scatter profiles for the GE HiSpeed X/iF CT scanner using the same set-up as in figure 1 for (a) blank scan with bow-tie filter (without water phantom) (i), water phantom and bow-tie filter (ii), water phantom without bow-tie filter (iii), and only Compton scattering in the water phantom (in the presence of bow-tie filter) (iv); (b) cylindrical water phantoms with different size.

There is generally good agreement between measured and simulated results using both MCNP4C and AMCS for the cone-beam small-animal CT scanner (figures 6–8). The absolute normalized error plots for different phantoms demonstrated that MCNP4C has better agreement with measured projections in comparison to AMCS. Although the SPR estimates using both

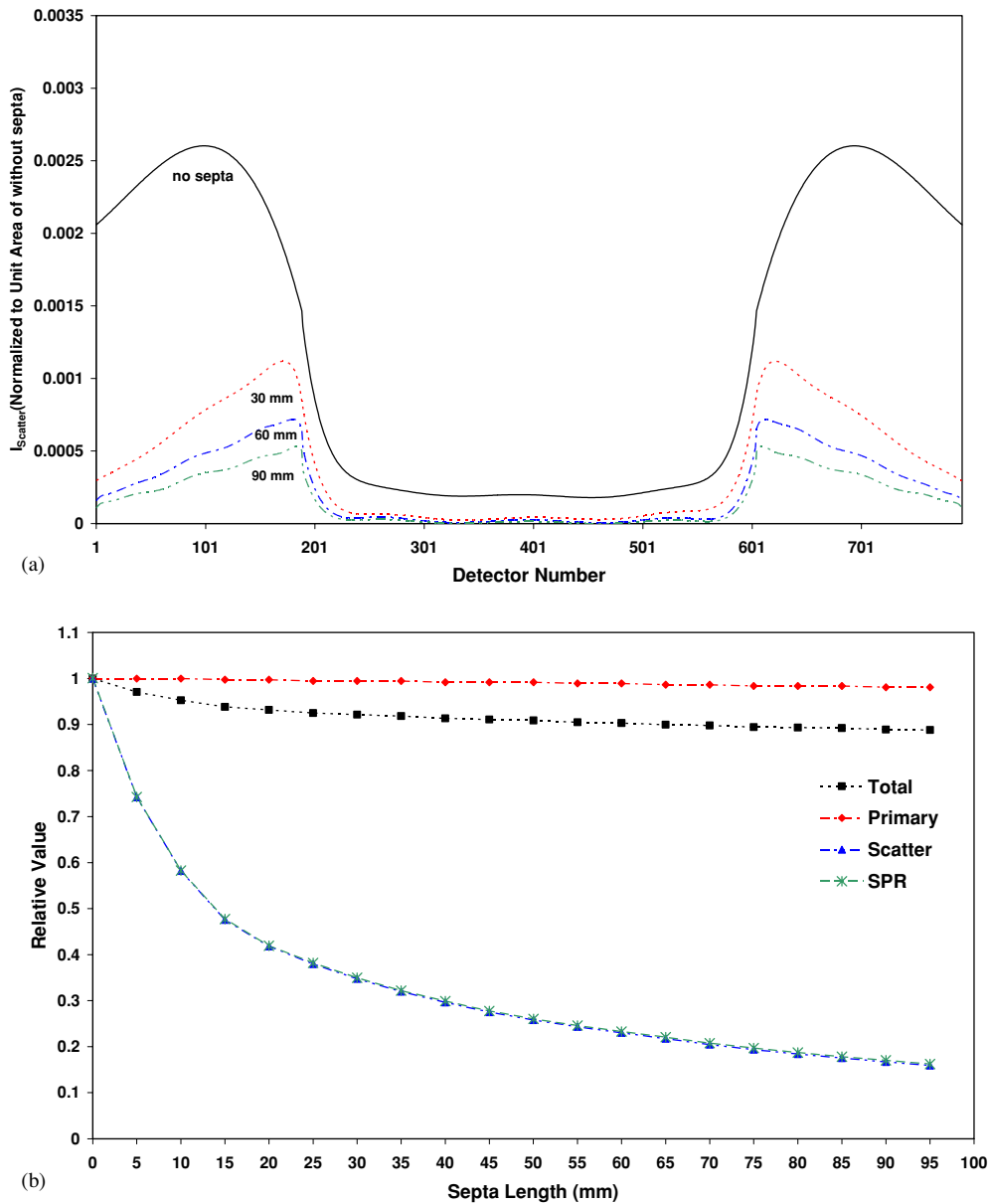


**Figure 10.** Monte Carlo simulations of the cylindrical water phantom for the GE HiSpeed X/iF CT scanner using the same set-up as in figure 1 showing both (a) simulated scatter profiles and (b) relative SPR, total, primary and scattered photons, as a function of septa length.

simulation programs have the same shape, there is a substantial discrepancy in the magnitude of the profile which can be explained by the underestimation of the scattered component and overestimation of primary component by AMCS. In the absence of gold standard with respect to the contribution of primary and scattered photons to the projection data, it is difficult to judge the validity of both computational codes. However, the better agreement of the MCNP4C-based CT simulator with experimental measurements could be an indicator of its

improved performance. It should also be emphasized that AMCS uses XCOM photon cross section libraries (Berger and Hubbell 1987) whereas the scattering cross sections in MCNP are taken from ENDF tabulations (Hubbell *et al* 1975). In addition, AMCS combines short Monte Carlo simulation with data fitting and other acceleration techniques to generate noise-free scatter projections (Colijn and Beekman 2004), which might introduce an additional uncertainty.

It has been shown that scatter in the bow-tie filter used in fan-beam CT scanners to reduce dynamic range requirements for the detector and to decrease the radiation dose to the patients contributes significantly to the scatter component (figure 9). The two peaks in the scatter profile are due to the trade-off between increasing the probability of Compton scattering while decreasing the transmission probability of scattered photons from the bow-tie filter with increasing the attenuation length. It should be noted that the lower scattered photons at the centre of the profile covered by the phantom (whose diameter is large compared to the mean free path of photons) is the result of either absorption of incoming photons before undergoing Compton scattering or their absorption after undergoing Compton scattering. The set-up used to assess the scatter profile without bow-tie filter being present corresponds to the configuration adopted by Johns and Yaffe (1982) to measure experimentally the scatter profile. Consistent with the observations made by Glover (1982), the bow-tie filter decreases the scatter component in the region covered by the phantom. Increasing the septa length could effectively reduce the contribution of scattered radiation, thus decreasing the scatter-to-primary ratio (figure 10). The optimal septa length to be used in the design of multi-slice CT scanners is still an open research question, which requires further research and development efforts.

It should be noted that the x-ray CT simulator described in this paper is still time consuming ( $\sim 1$  h per view—depending on complexity of the geometry—on a medium performance single processor PC), which is not a major concern in a research environment where massively parallel computers, PC clusters and Grid technology are generally available. Recently, we attempted to generate images using a combination of techniques including pure Monte Carlo and analytic models resulting in a hybrid approach namely numerical approaches using Monte Carlo data which seems to be reliable thus allowing us to reduce significantly the computation time.

## 5. Conclusion

An MCNP4C-based Monte Carlo simulator for fan- and cone-beam x-ray CT with single-slice, multi-slice and flat detector configurations has been developed. A user interface program running under Matlab 6.5.1 was designed to create the geometry of the actual CT scanner as MCNP's input file and perform image reconstruction of the simulated projection data. The simulated projections of various phantoms for both human and small-animal CT scanners were in good agreement with experimentally measured and published simulated data. Likewise, the reconstructed images were also comparable to the images obtained from the measured projections. The developed x-ray CT simulator is a powerful tool for evaluating the effect of physical, geometrical and other design parameters on the performance of new generation CT scanners and image quality in addition to offering a versatile tool for optimizing the absorbed dose to the patients and investigating potential artefacts and optimal correction schemes when using CT-based attenuation correction on dual-modality PET/CT units (Hasegawa and Zaidi 2005) in connection with ongoing research in our lab related to PET quantification using a dedicated PET Monte Carlo simulator (Zaidi *et al* 1999).

## Acknowledgments

This work was supported by the Swiss National Science Foundation under grant SNSF 3152A0-102143. The authors would like to thank W Zbijewski, H Ghadiri and H Moosavi for providing some of the data used in this work, F Schoenahl and M Adib for their support in programming and D Keidel from GE Healthcare Technologies for supplying design parameters of the HiSpeed X/iF CT scanner.

## References

- Atherton J V and Huda W 1995 CT dose in cylindrical phantoms *Phys. Med. Biol.* **40** 891–911
- Ay M R, Shahriari M, Sarkar S, Adib M and Zaidi H 2004 Monte Carlo simulation of x-ray spectra in diagnostic radiology and mammography using MCNP4C *Phys. Med. Biol.* **29** 4897–917
- Ay M R, Sarkar S, Shahriari M, Sardari D and Zaidi H 2005 Assessment of different computational models for generation of x-ray spectra in diagnostic radiology and mammography *Med. Phys.* **32** 1660–75
- Berger M J and Hubbell J H 1987 *XCOM: Photon Cross Sections on a Personal Computer* National Bureau of Standards (US)
- Boone J M, Cooper V N, Nemzek W R, McGahan J P and Seibert J A 2000 Monte Carlo assessment of computed tomography dose to tissue adjacent to the scanned volume *Med. Phys.* **27** 2393–407
- Briesmeister J F 2000 *MCNP—A General Monte Carlo N-Particle Transport Code Version 4C* (Los Alamos, NM: Los Alamos National Laboratory)
- Caon M, Bibbo G and Pattison J 1997 A comparison of radiation dose measured in CT dosimetry phantoms with calculations using EGS4 and voxel-based computational models *Phys. Med. Biol.* **42** 219–29
- Caon M, Bibbo G, Pattison J and Bhat M 1998 The effect on dose to computed tomography phantoms of varying the theoretical x-ray spectrum: a comparison of four diagnostic x-ray spectrum calculating codes *Med. Phys.* **25** 1021–7
- Chen B and Ning R 2002 Cone-beam volume CT breast imaging: feasibility study *Med. Phys.* **29** 755–70
- Colijn A P and Beekman F J 2004 Accelerated simulation of cone beam x-ray scatter projections *IEEE Trans. Med. Imaging* **23** 584–90
- Colijn A P, Zbijewski W, Sasov A and Beekman F J 2004 Experimental validation of a rapid Monte Carlo based micro-CT simulator *Phys. Med. Biol.* **49** 4321–33
- Cristy M and Eckerman K F 1987 *Specific Absorbed Fractions of Energy at Various Ages from Internal Photon Source* Rep. ORNL/TM-8381/V1-7, Oak Ridge National Laboratory
- De Francesco D and Da Silva A 2002 Multislice spiral CT simulator for dynamic cardiopulmonary studies *SPIE Medical Imaging 2002: Physiology and Function from Multidimensional Images (San Diego, CA, USA)* SPIE vol 4683 pp 305–16
- De Man B 2001 Iterative reconstruction for reduction of metal artifact in computed tomography *PhD Thesis* Leuven University, Belgium
- Drangova M and Fenster A 1994 A laboratory CT scanner for dynamic imaging *Med. Phys.* **21** 731–40
- Endo M, Tsunoo T, Nakamori N and Yoshida K 2001 Effect of scatter radiation on image noise in cone beam CT *Med. Phys.* **28** 469–74
- Glover G H 1982 Compton scatter effects in CT reconstructions *Med. Phys.* **9** 860–7
- Hasegawa B H and Zaidi H 2005 Dual-modality imaging: more than the sum of its components *Quantitative Analysis in Nuclear Medicine Imaging* ed H Zaidi (New York: Springer) pp 35–81
- Hsieh J 2003 Analytical models for multi-slice helical CT performance parameters *Med. Phys.* **30** 169–78
- Hubbell J H, Veigele W J, Briggs E A, Brown R T, Cromer D T and Howerton R J 1975 Atomic form factors, incoherent scattering functions, and photon scattering cross-sections *J. Phys. Chem. Ref. Data* **4** 471–538
- Jarry G, DeMarco J J, Beifuss U, Cagnon C H and McNitt-Gray M F 2003 A Monte Carlo-based method to estimate radiation dose from spiral CT: from phantom testing to patient-specific models *Phys. Med. Biol.* **48** 2645–63
- Johns P C and Yaffe M 1982 Scattered radiation in fan beam imaging systems *Med. Phys.* **9** 231–9
- Joseph P M and Spital R D 1982 The effects of scatter in x-ray computed tomography *Med. Phys.* **9** 464–72
- Kak A C and Slaney M 1999 *Principles of Computerized Tomographic Imaging* (New York: IEEE Press)
- Kanamori H, Nakamori N, Inoue K and Takenaka E 1985 Effect of scattered x-ray on CT images *Phys. Med. Biol.* **30** 239–49
- Khodaverdi M, Chatziioannou A F, Weber S, Ziemons K, Halling H and Pietrzyk U 2005 Investigation of different microCT scanner configurations by GEANT4 simulations *IEEE Trans. Nucl. Sci.* **52** 188–92

- Lee S C, Kim H K K, Chun I K, Cho M H, Lee S Y and Cho M H 2003 A flat-panel detector based micro-CT system: performance evaluation for small-animal imaging *Phys. Med. Biol.* **48** 4173–85
- Lucas P A, Dance D R, Castellano I A and Vano E 2004 Monte Carlo simulations in CT for the study of the surface air kerma and energy imparted to phantoms of varying size and position *Phys. Med. Biol.* **49** 1439–54
- Malusek A, Sandborg M P and Carlsson G A 2003 Simulation of scatter in cone beam CT: effects on projection image quality *SPIE Medical Imaging 2003: Physics of Medical Imaging (San Diego, CA, USA) SPIE* vol 5030 pp 740–51
- Meinel J F, Wang G, Jiang M, Ferei T, Vannier M and Hoffman E 2003 Spatial variation of resolution and noise in multi-detector row spiral CT *Acad. Radiol.* **10** 607–13
- Merritt R B and Chenery S G 1986 Quantitative CT measurements: the effect of scatter acceptance and filter characteristics on the EMI 7070 *Phys. Med. Biol.* **31** 55–63
- Ohnesorge B, Flohr T and Klingenberg-Regn K 1999 Efficient object scatter correction algorithm for third and fourth generation CT scanners *Eur. Radiol.* **9** 563–9
- Siewerdsen J H and Jaffray D A 2000 Optimization of x-ray imaging geometry (with specific application to flat-panel cone-beam computed tomography) *Med. Phys.* **27** 1903–14
- Siewerdsen J H and Jaffray D A 2001 Cone-beam computed tomography with flat-panel imager: magnitude and effects of x-ray scatter *Med. Phys.* **28** 220–31
- Storm E and Israel H I 1967 *Photon Cross-Section from 0.001 to 100 MeV for Elements 1 through 100* LA-3753, Los Alamos Scientific Laboratory
- Tofts P S and Gore J C 1980 Some sources of artefact in computed tomography *Phys. Med. Biol.* **25** 117–27
- Wang L, Lovelock M and Chui C S 1999 Experimental verification of a CT-based Monte Carlo dose-calculation method in heterogeneous phantoms *Med. Phys.* **26** 2626–34
- Xu X G, Chao T C and Bozkurt A 2000 VIP-MAN: an image-based whole-body adult male model constructed from color photographs of the visible human project for multi-particle Monte Carlo calculations *Health Phys.* **75** 476–86
- Zaidi H, Scheurer A H and Morel C 1999 An object-oriented Monte Carlo simulator for 3D cylindrical positron tomographs *Comput. Methods Prog. Biomed.* **58** 133–45

# **Paper IV**

*European Journal of Nuclear Medicine and Molecular Imaging*  
Under revision (2005)

## Assessment of errors caused by x-ray scatter and use of contrast medium when using CT-based attenuation correction in PET

Mohammad Reza Ay and Habib Zaidi

Division of Nuclear Medicine, Geneva University Hospital, CH-1211 Geneva 4, Switzerland

### Abstract

*Purpose:* Quantitative image reconstruction in positron emission tomography (PET) requires an accurate attenuation map of the object under study for the purpose of attenuation correction. Current dual-modality PET/CT systems offer significant advantages over stand-alone PET, including decreased overall scanning time and increased accuracy in lesion localization and detectability. However, the contamination of CT data with scattered radiation and misclassification of contrast medium with high density bone in CT-based attenuation correction (CTAC) is known to generate artefacts in the attenuation map and thus the resulting PET images. The purpose of this work is to quantitatively measure the impact of scattered radiation and contrast medium on the accuracy of CTAC. *Methods:* Our recently developed MCNP4C-based Monte Carlo x-ray CT simulator for modelling both fan- and cone-beam CT scanners and the *Eidolon* dedicated 3D PET Monte Carlo simulator were used to generate realigned PET/CT data sets. The impact of x-ray scattered radiation on the accuracy of CTAC was investigated through simulation of a uniform cylindrical water phantom for both a commercial fan-beam multi-slice and prototype cone-beam flat panel detector-based CT scanner. The influence of contrast medium was studied by simulation of a cylindrical phantom containing different concentrations of contrast medium. Moreover, an experimental study using an anthropomorphic striatal phantom was conducted for quantitative evaluation of errors arising from the presence of contrast medium by calculating the apparent recovery coefficient (ARC) in presence of different concentrations of contrast medium. *Results:* The analysis of attenuation correction factors (ACFs) for the simulated cylindrical water phantom in both fan- and cone-beam CT scanners showed that the contamination of CT data with scattered radiation in the absence of scatter removal underestimates the true ACFs, namely by 7.3% and 28.2% in the centre for both geometries, respectively. The ARC was 190.7% for a cylindrical volume of interest located in the main chamber of the striatal phantom containing contrast medium corresponding to 2000 Hounsfield units (HU), whereas the ARC was overestimated by less than 5% for the main chamber and ~2% for the left/right putamen and caudate nucleus compared to the absence of contrast medium. *Conclusions:* Without x-ray scatter compensation, the visual artefacts and quantitative errors in flat panel detector-based cone-beam geometry are substantial and propagate cupping artefacts to PET images during CTAC. Likewise, contrast-enhanced CT images may create considerable artefacts during CTAC in regions containing high concentrations of contrast medium.

**Key Words:** PET, x-ray CT, attenuation correction, scattered radiation, contrast medium.

## 1. Introduction

Diagnostic, monitoring and follow-up in clinical oncology traditionally are based on high resolution anatomical computed tomography (CT) images. In recent years, functional positron emission tomography (PET) imaging using dedicated radiopharmaceuticals has been recognized as an important imaging modality and adjunct to CT by providing complementary metabolic information. To overcome the challenges of aligning PET and CT images, which are acquired in different conditions, hybrid PET/CT units have been designed and are commercially available since 2000 [1]. The PET/CT scanner combines premier technology from two imaging modalities, making it possible to reveal both anatomical and functional information in a single procedure. PET/CT systems offer significant advantages over stand-alone PET, including decreased overall scanning time and increased accuracy in lesion localization and detectability [2]. However, the use of CT images for attenuation correction of PET data is known to generate visible artefacts in the resulting PET images in some cases [3]. Several investigators tried to characterize quantitatively the effect of physical and physiological parameters such as oral and intravenous contrast medium [4-11], metallic implants [12-15] and respiratory motion [16,17] on the accuracy of CT-based attenuation correction (CTAC) in PET. Likewise, the contamination of CT data with scattered radiation, which depends on the geometry of the CT scanner and object under study, reduces reconstructed CT numbers [18] and introduces cupping artefacts in the reconstructed images [19]. This effect is more pronounced in the next generation of CT scanners with flat panel detector-based cone-beam configurations, which are much less immune to scatter than fan-beam CT scanners [20]. The magnitude and spatial distribution of scattered radiation in x-ray CT for both fan- and cone-beam geometries should be accurately quantified for optimization of scanner design geometry and development of robust scatter correction techniques [21,22]. This problem has been historically addressed by different groups in the context of using CT for quantitative measurements using experimental studies, mathematical modelling and Monte Carlo simulations for both fan- [18,23-27] and cone-beam [20,21,28,29] geometries. It should be noted that most published papers assessing the distribution of scattered radiation in the fan-beam geometry used either

straightforward experimental measurements or in-house developed Monte Carlo simulators modelling old CT scanner technologies based on gaseous (Xenon) detectors, whereas the characterization of scattered radiation in current generation CT scanners with accurate modelling of single- and multi-row scintillation detectors technology has been addressed recently by our group [30]. In addition, to the best of our knowledge, the assessment of the impact of scattered radiation in CT images on the accuracy of CT-based attenuation correction has never been addressed before, neither in the fan-beam geometry with multi-row detector configuration nor in the cone-beam geometry with flat panel detectors. It is worth emphasizing that a limited number of studies addressed the contribution of scattered radiation in radionuclide transmission scans for stand-alone PET systems [31,32]. It has been shown that the acceptance of scattered radiation can be minimized by setting lower energy discriminator thresholds owing to the fact that PET detectors work in pulse mode [33]. Such a technique is unpractical in x-ray CT imaging since the detectors operate in current mode.

Although diagnostic quality CT relies on the administration of oral or intravenous contrast agents to allow improved lesion delineation, the presence of positive contrast agents in dual-modality PET/CT systems significantly overestimates the attenuation map in some cases and may generate artefacts during CTAC [4,5,10,11]. This is due to the high attenuation coefficient of these materials at the low effective energy of the corresponding x-ray spectra which results in high CT numbers in the region of contrast agent accumulation through misclassification with high density cortical bone [8]. Currently available algorithms for conversion from CT numbers to linear attenuation coefficients at 511 keV are based on the assumption that image contrast in the CT data is contributed by mixtures of air, soft tissue, and bone [34]. The presence of contrast medium complicates this process since two regions that have the same image contrast may indeed have different compositions, for example contributed by bone and soft tissue in one case and iodine/barium contrast and soft-tissue in another situation [2]. These artefacts are most severe in cases where the contrast media is concentrated, for example in abdominal imaging after the patient swallows a bolus of oral contrast. In this case, the higher densities contributed by the oral contrast

media can lead to an overestimation of PET activity concentration [3]. The limited number of publications assessing the impact of contrast medium using phantom studies where the ground truth is known and their limitations in terms of complexity of simulated shapes, usually restricted to simple uniform cylindrical phantoms [8,9,11], spurred the research presented in this paper where a more realistic anthropomorphic striatal phantom and accurate modelling of contrast medium through Monte Carlo simulations combined with partial volume correction for accurate quantitative analysis were used.

One can account for attenuation differences between iodine versus bone using a technique that generates a calibration curve for contrast media, using a method similar to that referenced above for soft tissue and bone alone where separate calibration curves are generated for each material (i.e., iodine vs. bone) for different x-ray potentials used to acquire CT scans, and for different photon energies [35]. Some investigators have proposed using image segmentation methods of converting CT numbers to attenuation coefficients that correctly scale contrast enhanced CT images for intravenous [35] and oral [36] agents. In addition, other strategies including the acquisition of both pre-contrast and post-contrast CT scans can be used to minimize possible artefacts contributed by the presence of contrast media when the CT scan is to be used as an attenuation map for correction of the PET data [1]. More recently, a segmented contrast correction (SCC) method was proposed by Nehmeh *et al.* [8] to correct for oral contrast medium artefact in CTAC PET images. This method was evaluated using both phantom and clinical studies and proved to accurately recover lesion size and uptake.

The aim of this study is to investigate the impact of x-ray scatter and contrast medium in CT images on the accuracy of CTAC at different levels including raw data acquisition, attenuation maps, attenuation correction factors (ACFs) and reconstructed PET emission images using dedicated x-ray CT [30] and 3D PET [37] Monte Carlo simulations combined with experimental phantom studies. Both commercially available fan-beam multi-slice and future generation cone-beam flat panel detector-based CT scanners were considered. For the latter, a hypothetical cone-beam CT mimicking the geometry of a prototype flat panel detector-based

CT scanner [21] adjusted to the dimensions of large area panel PET detectors under development by CPS Innovations (Knoxville, TN) [1] for next generation PET/CT systems was simulated. Moreover, the SCC method discussed above for oral contrast agents was extended and generalized for intravenous contrast medium.

## **2. Materials and Methods**

### *2.1 Monte Carlo simulations*

The MCNP4C-based Monte Carlo x-ray CT simulator [30] was used for simulation of LightSpeed four-slice CT scanner (GE Healthcare Technologies, Waukesha, WI) and cone-beam panel detector-based CT scanner based on the geometry of a prototype flat panel detector-based CT scanner [21] modified to fit the size of LSO detector modules proposed for a flat panel-based PET scanner [1] for similar axial coverage. Full simulation of x-ray spectra including tracking the electrons into the x-ray tube target for the calculation of bremsstrahlung and produced characteristic photons was considered [38]. All photon interaction processes such as photoelectric absorption, incoherent and coherent scatterings as well as full primary and secondary electrons transport were considered during Monte Carlo simulations of x-ray CT since the MCNP4C code was run in E/P (electron and photon) mode. The collimator inside the detector housing (septa) in the LightSpeed scanner was accurately modelled through full photons transport inside the septa plates. It should be noted that antiscatter grids were not considered during simulation of the cone-beam geometry to replicate current prototype flat panel detector-based CT scanners [21]. After simulation of all views, a filtered backprojection reconstruction algorithm was used for image reconstruction of the simulated data sets. Likewise, the *Eidolon* 3D PET Monte Carlo simulator [37] was used to acquire emission data corresponding to the geometry of the ECAT ART PET scanner (CTI/Siemens, Knoxville, TN). Experimental and/or clinical validation of the PET and CT simulators is described elsewhere [30,37,39].

### *2.2 Experimental measurements*

A polyethylene cylindrical phantom ( $250\pm 0.5$  mm diameter) containing 16 cylindrical holes ( $20\pm 0.5$  mm diameter) was constructed. Fourteen syringes were filled with a solution of  $K_2HPO_4$  and water with concentrations varying between  $50\text{ mg/cm}^3$  and  $900\text{ mg/cm}^3$  to simulate cortical bone with different densities. The prepared syringes and two additional syringes containing water and air were inserted into the polyethylene phantom's holes. Thereafter, the phantom was scanned using the LightSpeed four-slice CT scanner to calculate the calibration curve for conversion from CT numbers to linear attenuation coefficients at 511 keV according to the method proposed by Bai *et al.* [34]. The XCOM photon cross section library [40] was used for calculation of the linear attenuation coefficients of the inserted solutions at 511 keV.

To investigate the effect of contrast medium on CTAC, experimental measurements of the anthropomorphic striatal phantom (Radiology Support Devices Inc., Long Beach, CA) were performed. This phantom consists of four small cavities that can be filled independently representing the left and right caudate and left and right putamen. In addition, there is a larger main chamber surrounding the four small cavities representing the rest of the brain. The main chamber itself is embedded in a bone like structure representing the skull. This arrangement provides properties similar to the human head suitable for mimicking PET studies of the presynaptic and postsynaptic dopaminergic system. For an activity concentration ratio of 1:8 between the main chamber and small cavities, 2.94 MBq of  $^{18}\text{F}$  (in 0.9 ml, 0.9% NaCl) were diluted in distilled water. A total activity of 13.2 MBq  $^{18}\text{F}$  diluted into 1.1 ml NaCl was filled into the main chamber. Subsequently, the main chamber was totally filled with distilled water. The fully 3D emission study lasted 25 minutes whereas the CT data of the same phantom were acquired using the Aquilion CT scanner (Toshiba Medical Systems Corporation, Tokyo, Japan) at 120 kVp and 240 mA.

### *2.3 Attenuation correction and image reconstruction*

The reconstructed CT images ( $512\times 512$  matrix size) were down-sampled to  $128\times 128$  to match the resolution of PET images followed by Gaussian smoothing using a 6 mm kernel. The calculated bi-linear calibration curve was used to

convert CT pixel values in Hounsfield units (HU) to an attenuation map ( $\mu$ map) at 511 keV. The resulting  $\mu$ map was forward projected according to the PET scanner geometry to generate ACFs. The ECAT 7.2.1 software was used for attenuation and scatter corrections and reconstruction of the emission data using the 3DRP reprojection algorithm with a maximum acceptance angle corresponding to 17 rings and a span of 7. The default parameters used in clinical routine were applied (Ramp filter, cut-off frequency 0.35 cycles/pixel). The reconstructed images consist of 47 slices with  $128 \times 128$  resolution and a voxel size set to  $1.72 \times 1.72 \times 3.4$  mm<sup>3</sup>. Since the PET and CT data used in this study were acquired on separate PET and CT scanners, PET to CT image coregistration was performed using the commercial Hermes multi-modality fusion software (Nuclear Diagnostics AB, Stockholm, Sweden). In order to increase the accuracy of quantitative analysis of reconstructed PET images, correction for partial volume effect was performed using the popular geometric transfer matrix (GTM)-based method proposed by Rousset *et al.* [41] which allows to compute corrected estimates without *a priori* knowledge on any activity level. Figure 1 shows a flow-chart describing the different steps of the study design.

#### 2.4 Scattered radiation modelling

To evaluate the impact of scattered radiation on CT images during CTAC in both fan-beam multi-slice and cone-beam panel detector-based CT, a cylindrical water phantom (200 mm diameter) was simulated for both geometries. Likewise, PET data of the same phantom with uniformly distributed activity of <sup>18</sup>F were simulated using *Eidolon*. The scatter contribution during the simulation of CT data was separated from the primary component using the surface source method implemented in the MCNP4C Monte Carlo code. In this method, a virtual plane is considered after the scatter medium (water phantom) and the direction, energy and history of each photon passing through this plane is registered. In the next step, the scatter component is calculated by considering only photons which had at least one interaction before hitting this plan toward the detection system. The unscattered component is calculated using the same method by considering only photons which had no interaction before hitting the virtual plane. The beam

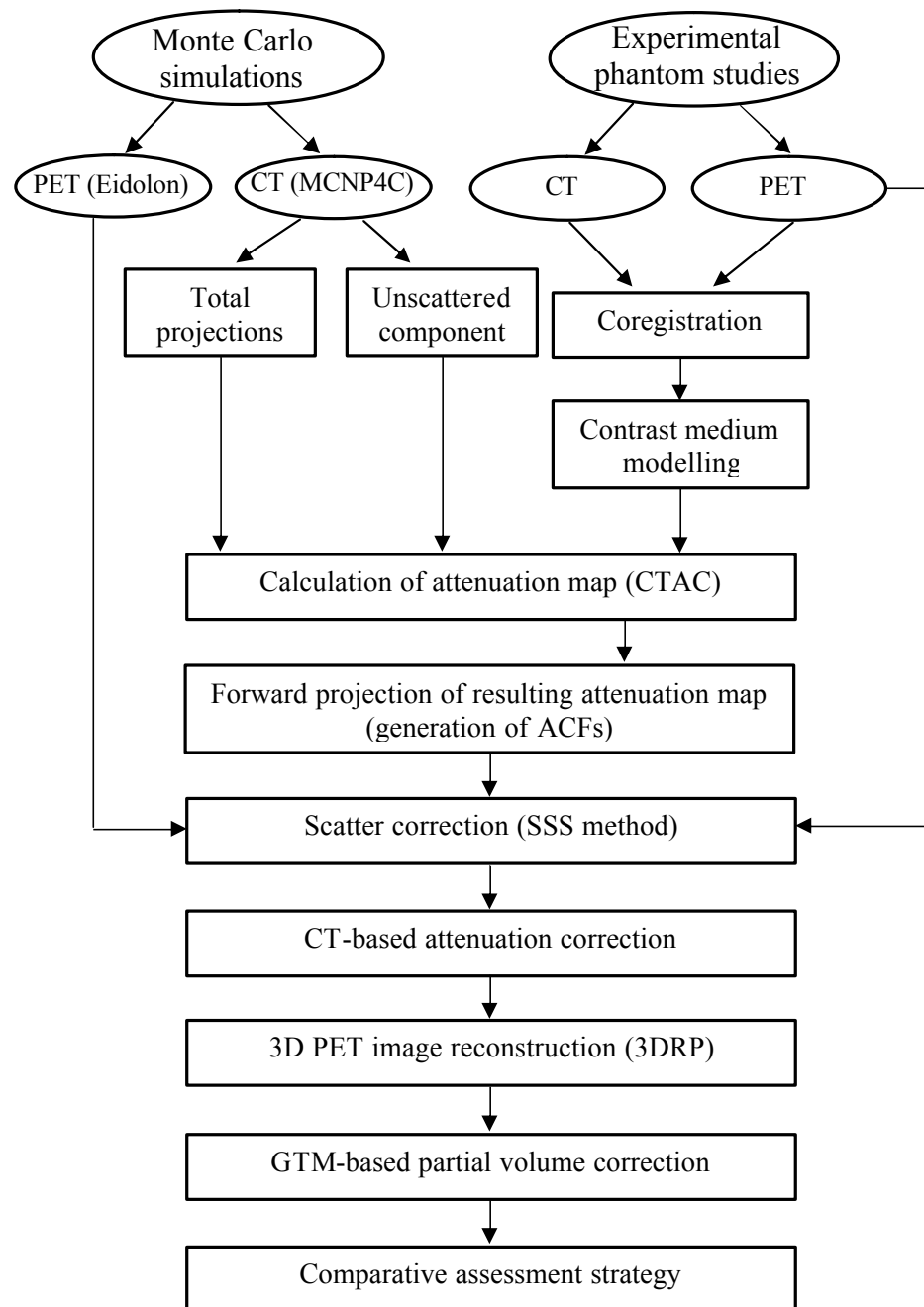


**Fig. 1.** Flow-chart illustrating the different steps of study design used to investigate the impact of x-ray scatter and contrast medium on CT-based attenuation correction in PET using both Monte Carlo simulations and experimental phantom studies.

hardening effect was removed from the projections according to the method described by Kanamori *et al.* [18] to isolate its effects from scatter. The accuracy of beam hardening removal was validated by comparing corrected profiles with those simulated using monoenergetic photons with the effective CT energy (72 keV for the LightSpeed CT scanner operated at 120 kVp). The latter was

calculated using experimental measurements based on the method proposed by Bai *et al.* [34]. Scatter correction of the simulated CT data was not performed for both fan- and cone-beam geometries to allow the assessment of the impact of x-ray scatter on the accuracy of CTAC in the absence of antiscatter grids and robust scatter correction algorithms. However, the physical scatter rejection components (septa) always present in multi-slice CT scanners were accurately modelled during the simulation. Thereafter, the simulated primary and total (sum of primary and scattered photons) projections were reconstructed using a filtered backprojection algorithm.

To assess the differences between the energy-dependent scatter components when using x-ray CT and radionuclide-based transmission scanning at 511 keV (e.g.  $^{68}\text{Ga}/^{68}\text{Ge}$ ), the  $\mu\text{map}$  was generated for both conditions, i.e. using the polyenergetic x-ray spectra and monoenergetic 511 keV photons as input to the Monte Carlo CT simulator. To avoid the effect of using different imaging geometries and source configurations, the projections were simulated for both energies using the same scanner (LightSpeed CT).

### *2.5 Contrast medium modelling*

Two experiments were carried out to assess the impact of contrast medium on CTAC. Firstly, CT scans of a cylindrical water phantom (200 mm diameter) containing a centred cylinder (50 mm diameter) filled with different concentrations of iohexol (Omnipaque 350, Nycomed, Princeton, NJ) were simulated. Iodine concentrations of  $0.7 \text{ mg/cm}^3$ ,  $3.5 \text{ mg/cm}^3$ ,  $7 \text{ mg/cm}^3$  and  $70 \text{ mg/cm}^3$  were considered for simulation of contrast agent solution (dilution of 1:500, 1:100, 1:50 and 1:5 of iohexol, respectively). This simple configuration aims to emulate typical concentrations of oral contrast media into the colon in clinical studies. Iohexol contrast media was used as reference to validate simulated CT images by comparison to similar published experimentally measured CT numbers [9] for the chosen concentrations. Thereafter, the reconstructed CT images were used for attenuation correction of the equivalently simulated PET data sets.

In the second experiment, CT images of the anthropomorphic striatal phantom

were modified by inserting a cylindrical region (20 mm diameter) in the main chamber to simulate the presence of positive contrast agents with various concentrations corresponding to CT numbers of 50, 100, 200, 500, 1000, 1500 and 2000 HU. This choice was motivated by considering that in clinical studies, CT numbers for regions where the contrast media is concentrated can range from a few HU to the maximum CT number (~4000 HU), depending on the contrast media concentration [8]. Thereafter, the resultant CTAC  $\mu$ map was calculated and used for attenuation correction of emission data. To correct artefacts caused by contrast media in the modified striatal phantom images, the SCC method originally proposed by Nehmeh *et al.* [8] for oral contrast agents was extended and generalized to intravenous contrast agents. In this method, the CT numbers of pixels belonging to the region containing contrast medium are substituted with their equivalent effective bone CT numbers since the commonly used bi-linear calibration curve is calculated based on the assumption that positive CT numbers are contributed by a mixture of tissue and bone. The related bi-linear calibration curve was calculated for the Aquilion CT scanner using different concentrations of intravenous contrast agent.

### 3. Results

#### 3.1 Impact of scattered radiation

Figure 2 shows Monte Carlo simulated scatter profiles for the cylindrical water phantom (200 mm diameter) calculated for CT (x-ray spectra, 120 kVp) and PET (511 keV) energies. A total number of  $1.9 \times 10^9$  photons were simulated. The fan-beam angle was adjusted to cover the water phantom in order to increase the simulation efficiency. The magnitude and spatial distribution of the scatter component for the x-ray spectra is quite different from the scatter component at 511 keV owing to the difference in terms of dominations by photoelectric and Compton interactions occurring in different energy ranges, which might preclude application of scatter correction algorithms developed for radionuclide transmission scanning to CT data even with appropriate rescaling [42].

The comparison of simulated attenuation profiles for primary and total projection data of the cylindrical water phantom in both fan- and cone-beam CT

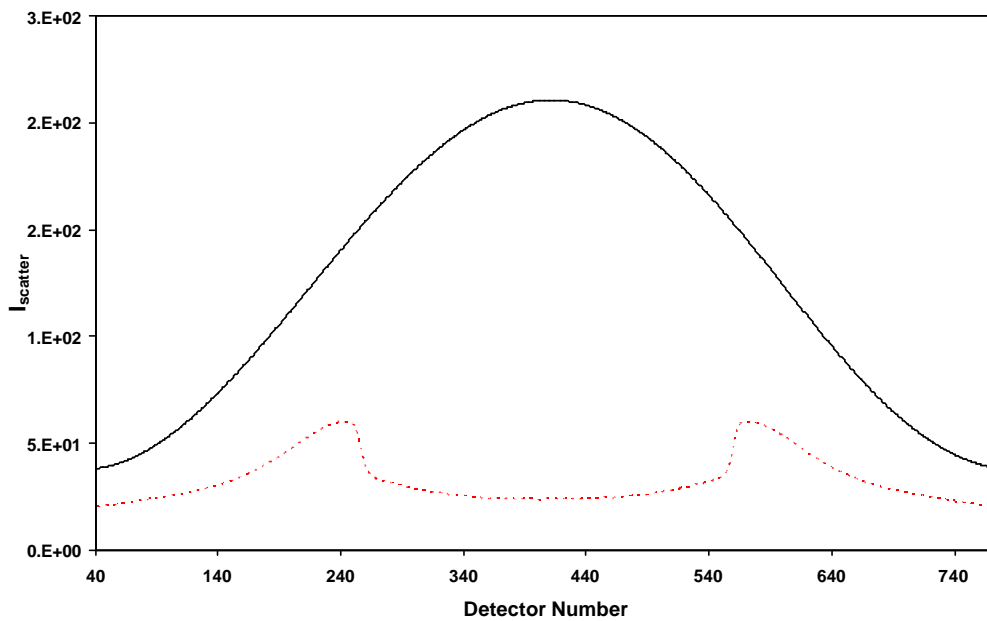


**Fig. 2.** Simulated scatter profiles for a cylindrical water phantom (200 mm diameter) in both 120 kVp x-ray spectra (dotted line) and monoenergetic 511 keV photons (solid line) using a dedicated Monte Carlo x-ray CT simulator.

geometries is shown in Figure 3a. It should be noted that the total profile for the cone-beam CT was taken from the central elements of the flat panel detector for comparison with the fan-beam geometry. The maximum value for primary and total fan- and cone-beam profiles is 4.26, 4.13 and 3.61, respectively. The underestimation of attenuation profiles for the cone-beam geometry is the consequence of substantial contribution of scattered radiation. The central profile of the corresponding reconstructed CT images is shown in Figure 3b. The typical cupping artefact apparent on the reconstructed images for the cone-beam geometry illustrates the important influence of scattered radiation on the quality of reconstructed CT images. It should be noted that the effect of beam hardening was removed from the profiles before reconstruction [18]. The central profile of the corresponding CTAC-based  $\mu$ map of the cylindrical water phantom at monoenergetic 511 keV photons is shown in Figure 3c. The calculated linear attenuation coefficient in the central region of  $\mu$ maps created from the primary, total fan-beam and cone-beam CT images is 0.0958, 0.0926 and 0.0782  $\text{cm}^{-1}$ , respectively. The latter value deviates considerably from the theoretical linear attenuation coefficient in water at 511 keV (0.096  $\text{cm}^{-1}$ ). Figure 3d compares central profiles (view 23/47) of ACFs computed using calculated AC (CAC)

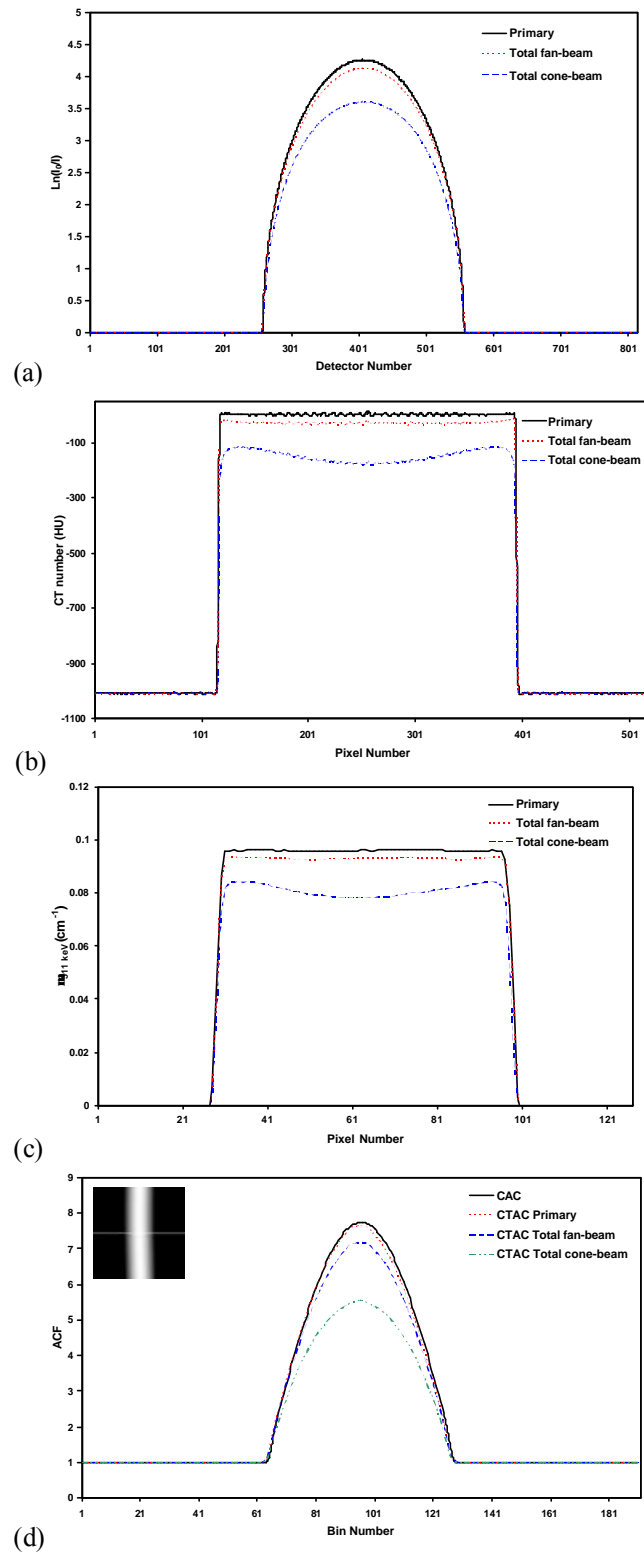
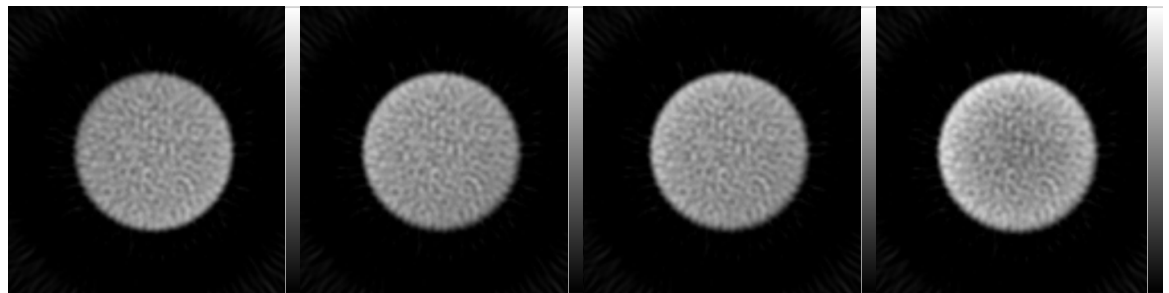


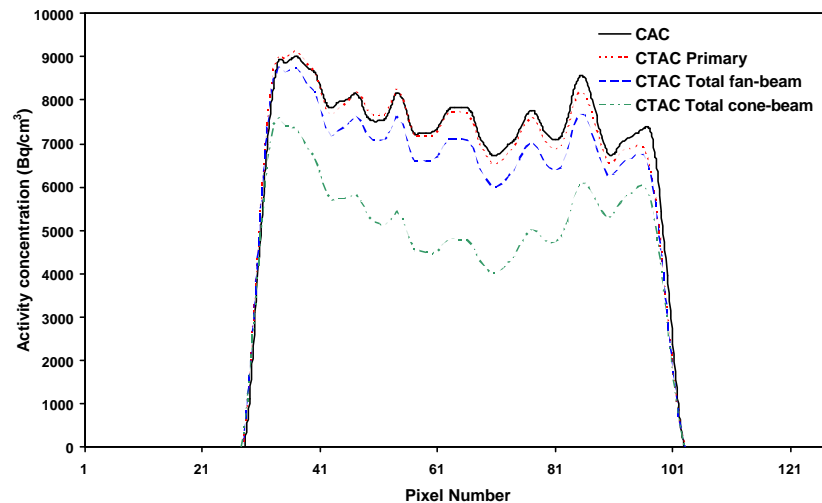
**Fig. 3.** Monte Carlo simulations of the cylindrical water phantom (200 mm diameter) in both fan- and cone-beam CT geometries showing: (a) Attenuation profiles of primary and total photons; (b) Central profiles through reconstructed CT images; (c) Central profiles through attenuation maps at 511 keV generated using the bi-linear transformation method; and (d) Central profiles through ACF sinograms calculated from attenuation maps shown in (c).

based on the theoretical value of the linear attenuation coefficient of 511 keV photons in water and the generated  $\mu$ maps using CTAC. The maximum ACF in the central part is 7.73, 7.64, 7.18 and 5.55 when using CAC and CTAC primary, total fan-beam and total cone-beam, respectively.

The reconstructed images after attenuation correction of simulated emission data using the ACF sinograms calculated with different methods are shown in Figure 4a. Figure 4b shows central profiles of activity concentration from the reconstructed images. The average relative difference between the profiles drawn on images reconstructed using the different methods for deriving the CT-based attenuation map and CAC serving as gold standard is 1.58%, 7.98% and 30.18%, respectively.



(a)



(b)

**Fig. 4.** (a) Reconstructed images of Monte Carlo simulated emission data corrected for attenuation using from left to right: CAC, CTAC primary, CTAC total fan-beam and CTAC total cone-beam. (b) Central profile through images shown in (a).

### 3.2 Impact of contrast medium

As an illustration of the effect of the presence of positive contrast medium in a circular region located at the centre of a water-filled cylinder, Figure 5a-b shows Monte Carlo generated attenuation profiles and scatter to primary ratios (SPR) using different concentrations of contrast medium for both x-ray spectra and 511 keV. The attenuation profiles illustrate the significant difference in photons attenuation by contrast media between the two energies. The SPR is a good indicator of the scatter component's magnitude in the acquired data. The corresponding central profiles of the derived  $\mu$ maps from reconstructed images and computed ACFs in both energies and for two extreme cases of Iodine concentration (maximum of 70 mg/cm<sup>3</sup> and minimum of 0.7 mg/cm<sup>3</sup>) are also shown (Fig. 5c-f) to illustrate the impact of using contrast media on generated  $\mu$ maps and ACFs. The computed ACF sinograms were used for attenuation correction of simulated emission data. Figure 6 illustrates the  $\mu$ maps and corresponding reconstructed emission images corrected for attenuation using CTAC (Fig. 6a) and 511 keV-based simulations (Fig. 6b) for different concentrations of Iodine. The percentage relative difference between central profiles of the PET images is shown in Figure 6c. As expected, the difference increases by increasing the concentration of contrast medium. The simulated attenuation profiles for both energies are further validated by comparing average CT numbers in the contrast region of the uniform cylindrical phantom with published experimentally measured values [9] and theoretical linear attenuation coefficients computed using the XCOM photon cross section library [40] at 511 keV (Table 1).

Figure 7a shows  $\mu$ maps resulting from the conversion of CT images of the RSD striatal phantom modified by inserting positive contrast medium in a cylindrical region (20 mm diameter) in the main chamber containing different concentrations of contrast medium. The corresponding emission data corrected for attenuation using the generated  $\mu$ maps and reconstructed using a filtered backprojection algorithm are also shown (Fig. 7b). Figure 7c illustrates the overestimation of activity concentration in the region containing contrast medium on horizontal profiles drawn at the level of this region. A more rigorous

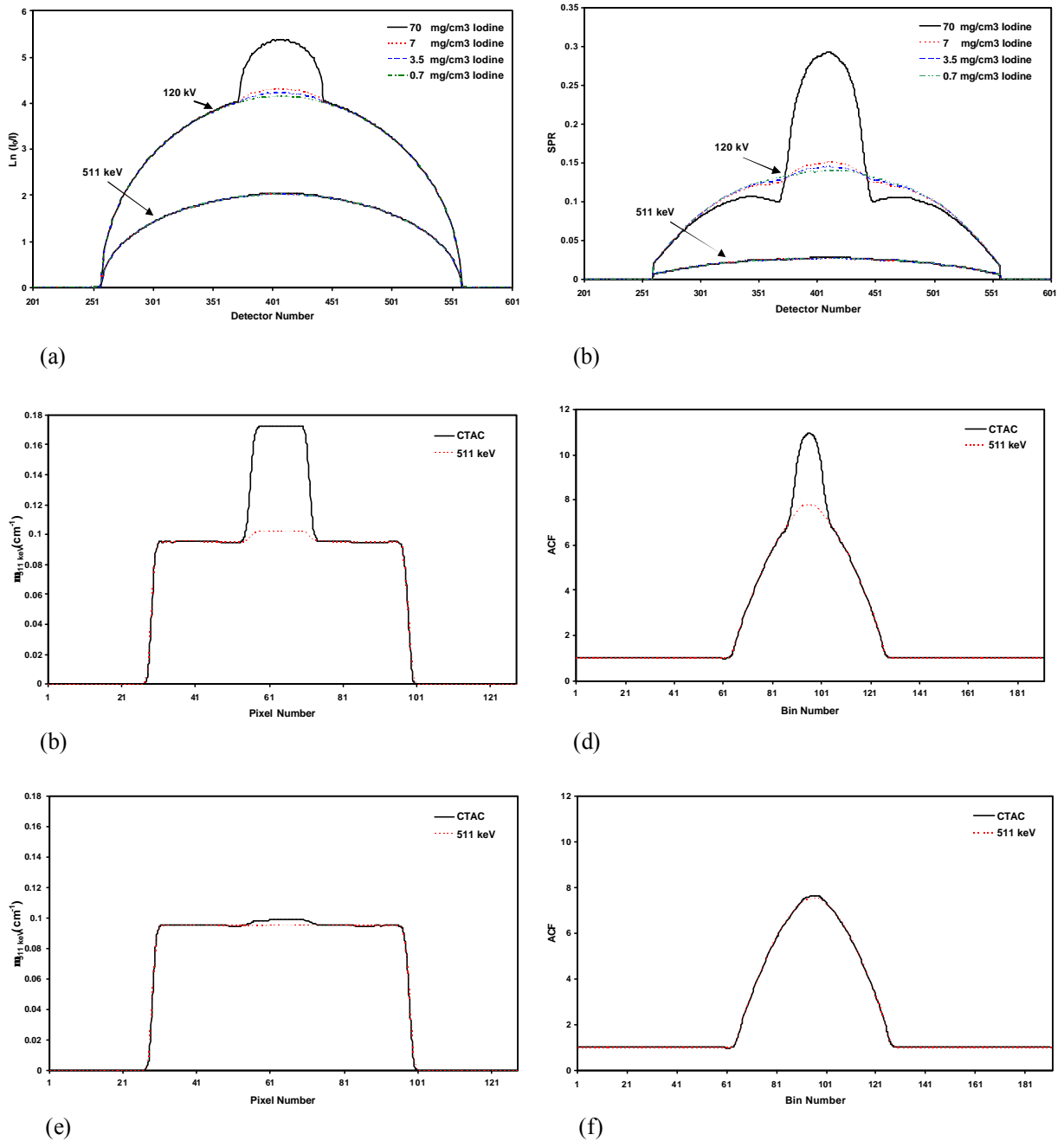
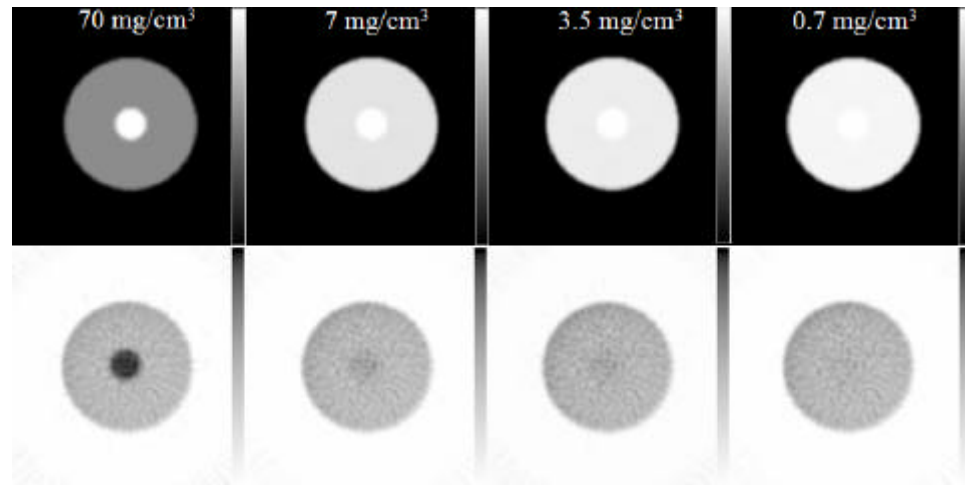
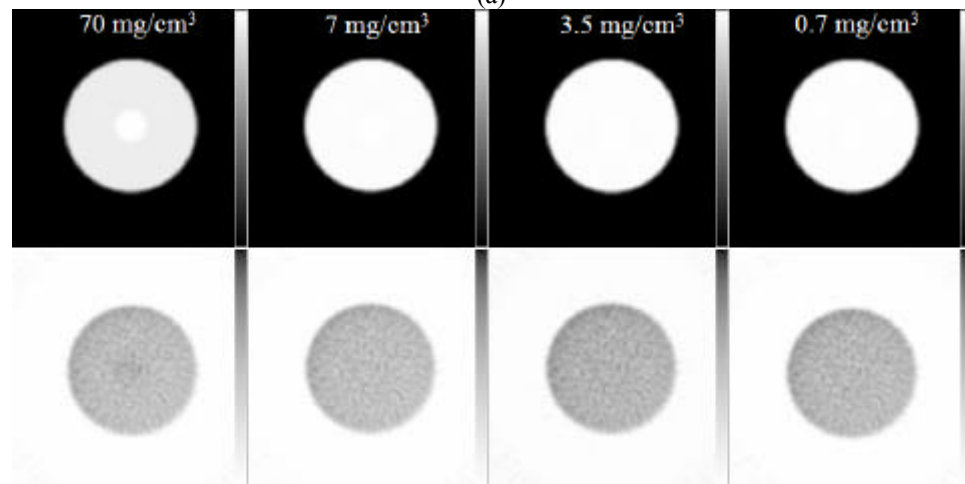


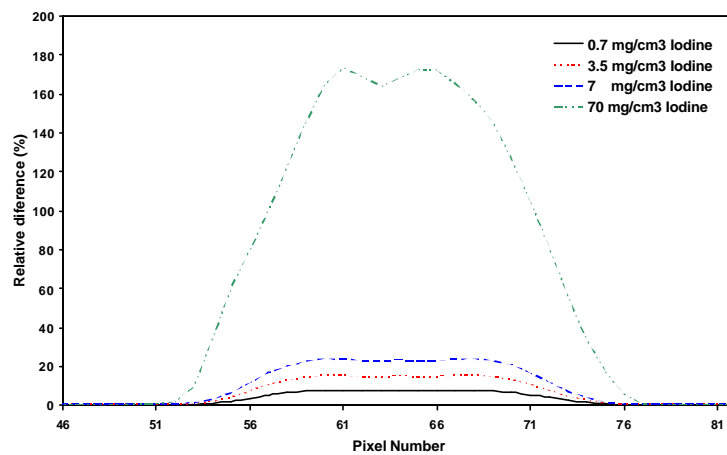
**Fig. 5.** Monte Carlo study of the impact of contrast medium in a cylindrical water phantom (200 mm diameter) containing centred cylinder (50 mm diameter) having different concentrations of iohexol for both CT and monoenergetic 511 keV energies showing: (a) Attenuation profiles; (b) Scatter to primary ratios; (c and d) Central profiles through attenuation maps and ACFs for maximum concentration (70 mg/cm<sup>3</sup> Iodine) of contrast medium; (e and f) same as c and d for minimum concentration (0.7 mg/cm<sup>3</sup> Iodine) of contrast medium.



(a)



(b)



(c)

**Fig. 6.** Representative slice of calculated attenuation maps and reconstructed emission images for different concentrations of contrast medium at CT energy (a) and 511 keV monoenergetic photons (b). (c) Relative percentage difference between the activity concentrations in the central profile for images corrected using (a) and (b).

quantitative measure of the effect of contrast medium is also given in Table 2, which shows the apparent recovery coefficients (ARCs) calculated for six different regions in the RSD striatal phantom after partial volume correction using the GTM-based method [41]. The ARC represents the apparent (observed or partial volume corrected) regional radioactivity concentration to true activity ratio.

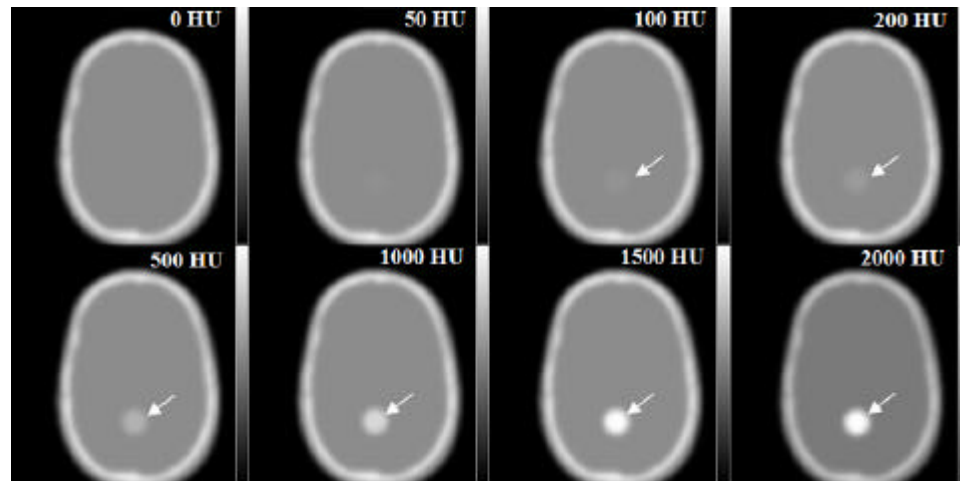
**Table 1.** Comparison of average simulated and published measured CT numbers and simulated and theoretical linear attenuation coefficients in both CT (120 kVp) and 511 keV monoenergetic energies.

Concentration of Iodine in solution	Measured CT Number (HU) [9]	Simulated CT Number (HU)	Theoretical $\mu_{511 \text{ keV}} (\text{cm}^{-1})$ XCOM [41]	Simulated $\mu_{511 \text{ keV}} (\text{cm}^{-1})$ MCNP4C
70 mg/cm <sup>3</sup>	1445.3	1434.8	0.1026	0.1028
7 mg/cm <sup>3</sup>	205.7	193.2	0.0965	0.9677
3.5 mg/cm <sup>3</sup>	128.2	118.2	0.0962	0.0964
0.7 mg/cm <sup>3</sup>	65.3	50.2	0.0959	0.0961
0 mg/cm <sup>3</sup>	9.7	1.3	0.0958	0.0960

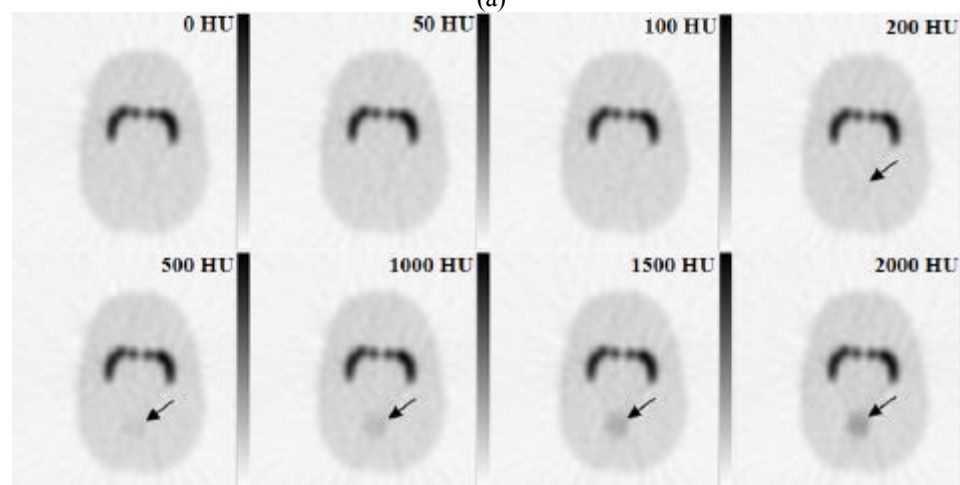
**Table 2.** Apparent Recover Coefficients (ARCs) for different VOIs after partial volume effect correction in the modified RSD anthropomorphic striatal phantom by inserting a cylindrical VOI containing contrast medium in CT images.

Volume of interest (VOI)	Volume (cm <sup>3</sup> )	CT number in the cylindrical VoI							
		0	50	100	200	500	1000	1500	2000
Main chamber	1290	109.6	109.7	109.9	110.1	110.9	112.2	113.5	114.9
Left putamen (LPU)	6	95.4	95.5	95.5	95.5	95.6	95.9	96.1	96.3
Right putamen (RPU)	6	101.9	101.9	101.9	102.1	102.2	102.5	102.8	103.1
Left nucleus caudate (LCN)	4.9	95.3	95.3	95.4	95.5	95.7	96.1	96.5	96.9
Right nucleus caudate (RCN)	4.9	100.5	100.5	100.6	100.7	100.8	101.1	101.4	101.7
Contrast medium region	79.3	109.9	111.8	113.7	117.4	128.8	148.4	169.0	190.7

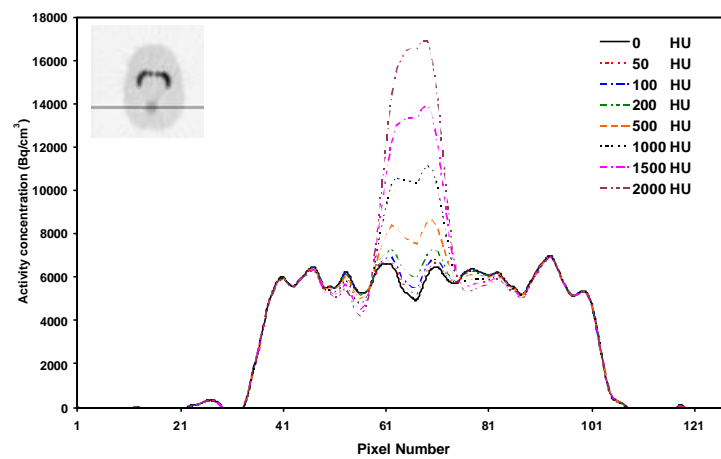
The segmented contrast correction (SCC) method proposed by Nehmeh *et al.* [8] was extended for intravenous contrast medium using calculated calibration curves for both bone-water and intravenous contrast medium-water assumptions (Fig. 8a). Thereafter, the SCC algorithm was applied to the  $\mu$ map corresponding to the maximum concentration of contrast medium (2000 HU) (Fig. 7a). Figure 8b shows the  $\mu$ maps and reconstructed images before and after correction using *a priori* knowledge of the presence of contrast medium. The ARCs after partial volume correction in the region containing contrast medium before and after applying the SCC algorithm are 190.7% and 115.8%, respectively. It should be



(a)

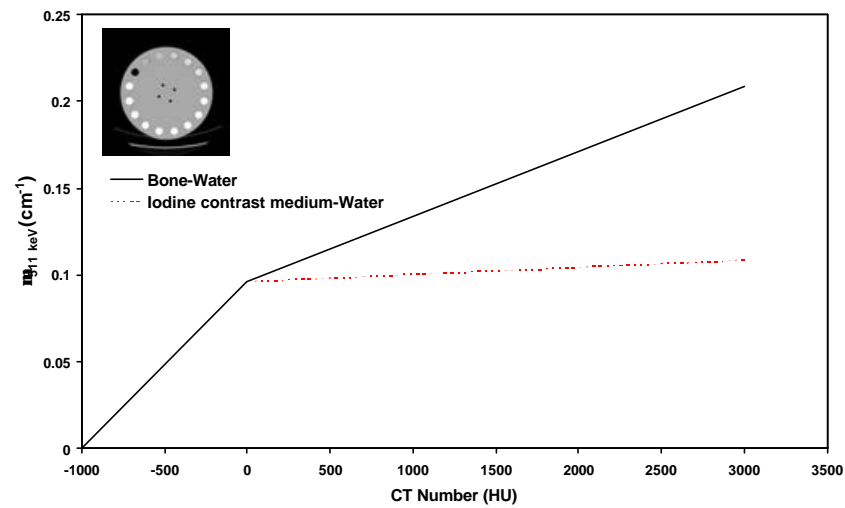


(b)

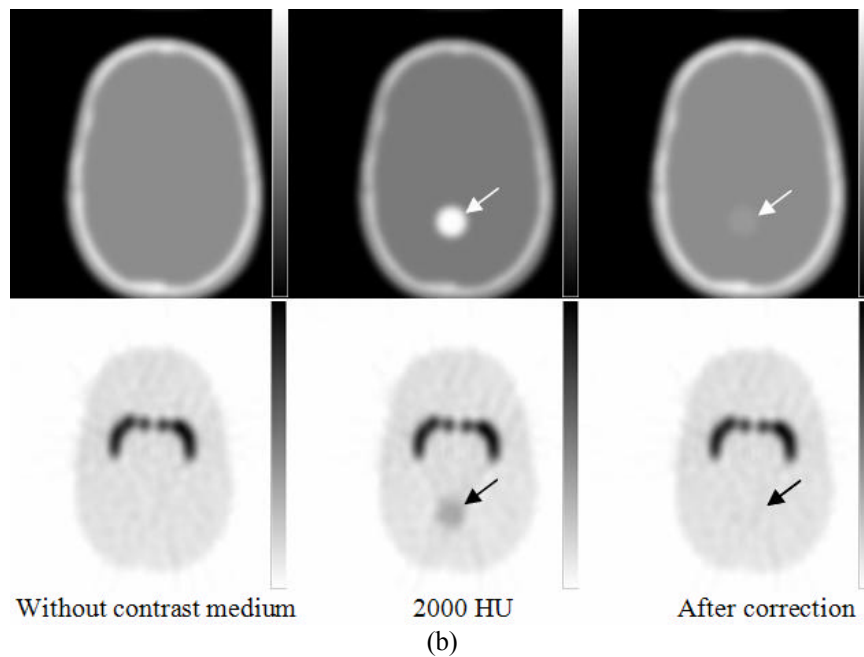


(c)

**Fig. 7.** (a) Calculated attenuation map of the modified striatal phantom by inserting a cylindrical area containing different concentrations of contrast medium. (b) Reconstructed emission images of the same phantom. (c) Horizontal profiles at the level of the circular region concentrating contrast medium through PET images shown in (b).



(a)



(b)

**Fig. 8.** (a) Plot of the calculated bi-linear calibration curve for the Toshiba Aquilion CT scanner. (b) Validation of SCC algorithm for intravenous contrast medium.

noted that the ARC in the same region in the absence of contrast medium is 109.9%, which could be explained in part by neglecting the scatter component during the derivation of calibration curves and application of the CTAC procedure.

#### 4. Discussion

PET/CT now has emerged as an important and cost-effective method of

performing anatomical-functional correlations in a way that improves patient management. The adoption of this technology has been rapid, and it is anticipated that the next phase of PET/CT likely will combine 3-D PET with volumetric cone-beam CT. This study revealed that the contamination of CT data with scattered radiation could generate some additional uncertainties during quantitative analysis of PET images when using CTAC if the CT images are not corrected for scatter [42]. The magnitude of propagated errors resulting from contribution of scatter in CT images depends on the object size and its chemical composition and more importantly on the geometry of the CT scanner. The scatter component in the next generation of cone-beam CT scanners based on flat panel detector geometry is significant and should be addressed to keep technology moving forward. The detailed scatter characterization made possible through simulation further asserts that the ideal research tool for scatter modelling and evaluation of scatter correction strategies is the Monte Carlo method. The later approach gives further insight and might offer a possible correction procedure analogous to approaches reported for PET [39].

The bell shape of the scatter profile at 511 keV (Fig. 2) is due to the fact that the dominant interaction in this energy is Compton forward scattering. The higher value in the centre of the profile is the consequence of increased probability of Compton scattering with increasing the attenuation length in the central area of the cylindrical water phantom. The two peaks visible on the scatter profile at CT energy are the result of increasing the transmission probability of scattered photons with decreasing the attenuation length on the edges of the water phantom. It is worth to emphasize that the lower number of scattered photons in the centre of the profile for the CT energy is the result of either photoelectric absorption of incoming photons before undergoing Compton or coherent scattering or their absorption after scattering. Although the amplitude of the scatter profile for 511 keV is higher, the acceptance of scattered photons in conventional radionuclide transmission scanning can be minimized by setting an appropriate energy discrimination window to reject scattered photons [33].

The underestimation of attenuation profiles for the cone-beam geometry is due to the high contamination of projection data with scattered radiation (Fig. 3). The

magnitude of this contamination is rather small for the fan-beam geometry owing to the fact that scattered photons are either absorbed in septa plates placed between the detector elements or do not hit the detector elements because of limited detector's aperture in the  $z$ -axis (4 cm in multi-slice scanners). The underestimation of attenuation profiles reduces CT numbers in the central area of reconstructed images and creates cupping artefacts. Consequently, cupping artefacts in CT images will result in the underestimation of linear attenuation coefficients in the central area of  $\mu$ maps generated using CTAC and thus the ACFs to be used for attenuation correction of the emission data. The underestimation of ACFs will induce underestimation of activity concentration in the central area of PET images (Fig. 4). In this study, the magnitude of the scatter component in both commercial multi-slice and prototype flat panel detector geometries was assessed. Moreover, the contribution of scattered radiation during CTAC of PET images was quantified and used to identify correction strategies for better management of deleterious scatter effect, especially for the new generation of flat panel detector-based cone-beam CT scanners that may be combined with future generation panel-based PET scanners [1] to bring in a new design for large axial field-of-view PET/CT.

The effects related to the use of contrast media likely are the same for current PET/CT systems versus those that would be obtained with volumetric CT imaging chains. Several articles have reported perturbations contributed by iodinated contrast media in PET/CT studies [4-11]. However, in a realistic clinical setting, these perturbations appear to have a relatively minor impact on diagnostic interpretation. In addition, challenges introduced by the use of contrast media certainly have not impeded the clinical adoption of PET/CT. The impact of the presence of positive contrast agents on the accuracy of CTAC was investigated in both the effective energy of the x-ray tube and monoenergetic 511 keV photons at the level of CT images, resulting  $\mu$ maps, ACF sinograms, and finally the reconstructed emission images (Fig 5.). The first objective was reached through Monte Carlo simulations to confirm that the behaviour of contrast medium with respect to photon absorption and scattering is completely different between CT and 511 keV energies. The remaining experiments aimed to study the impact of

contrast medium quantitatively by calculating ARCs in different regions of the RSD striatal phantom corrected for attenuation using CTAC for different concentrations of contrast medium (Table 2). The difference between attenuation profiles for different concentrations of contrast medium at CT energy (120 kVp) and 511 keV is due to the difference between the photon interaction cross sections at these energy ranges (Fig. 5a). The difference between attenuation profiles calculated at 511 keV for different concentrations of contrast medium is insignificant whereas there is significant difference between attenuation profiles calculated at CT energy. The high value of SPR in the region containing contrast medium at CT energy (Fig. 5b) is due to the high absorption of primary photons by the contrast medium since the scatter distribution is approximately uniform. The curvature of SPR at 511 keV is due to the variable transmission probability of primary photons, which depends on the angle-dependent pathlength of attenuating media. It should be noted that the presence of contrast medium in the central area of the phantom has negligible impact on the SPR profile at 511 keV while its effect is significant at CT energy. The difference between  $\mu$ maps and ACF sinograms generated using simulated CT images at CT energy and 511 keV (Fig. 5c-f) for minimum ( $0.7 \text{ mg/cm}^3$  Iodine) and maximum ( $70 \text{ mg/cm}^3$  Iodine) concentrations of contrast medium is a nice illustration of extreme imaging conditions and the propagation of errors in attenuation correction factors to the emission data during attenuation compensation (Fig. 6). The overestimation of activity concentration in the central area of PET images corrected using  $\mu$ maps derived at CT energies (Fig. 6a) is due to overestimation of ACFs in the related region whereas the effect of contrast medium at 511 keV is negligible (Fig. 6b), even with the highest concentration of Iodine ( $70 \text{ mg/cm}^3$ ). The same observations were made using the RSD striatal phantom's data corrected for attenuation using CTAC for different concentrations of contrast medium in a cylindrical region (Fig. 7). The overestimation of activity in the cylindrical region is significant when using high concentration of contrast medium (90% for 2000 HU). However, it produces negligible effect on the far away located brain regions, namely less than 2% for the small regions (LPU, RPU, LCN and RCN) and 6% in the main chamber (Table 2).

The SCC algorithm proposed by Nehmeh *et al.* [8] for correction of oral contrast agents was extended for intravenous contrast agents using suitable calibration curves calculated for related materials (Fig. 8a). In this approach, the CT numbers of pixels belonging to contrast medium region are substituted with their equivalent effective bone CT numbers (Fig. 8b). The SCC algorithm is efficient but still limited to simple shapes reflecting the spatial distribution of contrast medium. For wider applicability, the algorithm needs to be improved by developing an automatic segmentation algorithm for classification of irregular shapes of regions containing contrast medium usually found in clinical studies.

Consistent with other studies, it was observed that the presence of contrast medium (oral or intravenous) in CT images can be misclassified with high-bone density and can result in building an incorrect  $\mu$ map [3]. Subsequently, this misclassification and overestimation of attenuation coefficients results in overestimation of the activity concentration in the region containing high concentration of contrast medium. The issue of whether the use of contrast medium in dual-modality PET/CT scanning produces medically significant artefacts is still controversial with some studies corroborating [5,6,10,11] and others contradicting [8,9,43] the fact that the presence of contrast medium can be a source of errors and artefacts when the CT data are used for attenuation correction of PET images. The quantification of a lower concentration threshold below which the use of contrast medium is risk-free proved to be a difficult task. The optimal quantity and route of administration of contrast medium and potential correction schemes are still open questions which require further research and development efforts.

## 5. Conclusion

The impact of contrast medium and x-ray scatter in CT images on the accuracy of CT-based attenuation correction in PET was studied using Monte Carlo simulations combined with experimental phantom studies. The latter aspect has not been addressed before to the best of our knowledge. The contribution of x-ray scatter during the CTAC procedure was quantified for commercially available fan-beam multi-slice CT and prototype large area flat panel detector-based cone-beam

CT scanners. The magnitude of scatter in CT images for the cone-beam geometry is significant and might create cupping artefacts in reconstructed PET images during CTAC; however, its effect is small for current generation multi-slice fan-beam CT scanners using septa between detector elements, but should preferably be corrected during CT reconstruction to avoid quantification bias. These results substantiate the important role of antiscatter collimation and robust scatter correction algorithms which certainly will be implemented in future generation flat panel-based PET/CT scanners when used for quantitative measurements. Contrast-enhanced CT images may create visible artefacts in regions containing high concentrations of contrast medium. This study reports results from a limited set of computer simulations of realistic PET and CT systems combined with experimental measurements using validated techniques. Further research using experimentally measured whole-body dynamic anthropomorphic phantoms on operational PET/CT systems (64-slice CT) to be installed in our department with a broader range of contrast medium concentrations, as well as more realistic geometries and sizes of the opacified structures representative of those imaged in clinical settings is guaranteed.

### **Acknowledgements**

This work was supported by the Swiss National Science Foundation under grant SNSF 3152A0-102143. The authors would like to thank Dr O.G. Rousset for providing the PVC software and F. Schoenahl, T. Ruest and N. Andreini, for their valuable support.

## References

1. Townsend DW, Carney JPJ, Yap JT, Hall NC. PET/CT today and tomorrow. *J Nucl Med* 2004; 45:4s-14s.
2. Hasegawa BH, Zaidi H. Dual-modality imaging: more than the some of its components. In: Zaidi H, ed. *Quantitative analysis in nuclear medicine imaging*. New York: Springer, 2005:35-81.
3. Zaidi H, Hasegawa BH. Determination of the attenuation map in emission tomography. *J Nucl Med* 2003; 44:291-315.
4. Antoch G, Freudenberg LS, Stattaus J, Jentzen W, Mueller SP, Debatin JF, et al. Whole-body positron emission tomography-CT: optimized CT using oral and IV contrast materials. *AJR Am J Roentgenol* 2002; 179:1555-1560.
5. Antoch G, Freudenberg LS, Beyer T, Bockisch A, Debatin JF. To enhance or not enhance? 18F-FDG and CT contrast agents in dual-modality 18F-FDG PET/CT. *J. Nucl. Med.* 2004; 45:56S-95S.
6. Antoch G, Kuehl H, Kanja J, Lauenstein TC, Schneemann H, Hauth E, et al. Dual-modality PET/CT scanning with negative oral contrast agent to avoid artifacts: introduction and evaluation. *Radiology* 2004; 230:879-885.
7. Dizendorf EV, Treyer V, Von Schulthess GK, Hany TF. Application of oral contrast media in coregistered positron emission tomography-CT. *AJR* 2002; 179:477-481.
8. Nehmeh SA, Erdi YE, Kalaigian H, Kolbert KS, Pan T, Yeung H, et al. Correction for oral contrast artifacts in CT attenuation-corrected PET images obtained by combined PET/CT. *J Nucl Med* 2003; 44:1940-1944.
9. Nakamoto Y, Chin BB, Kraitchman DL, Lawler LP, Marshall LT, Wahl RL. Effects of nonionic intravenous contrast agents in PET/CT imaging: phantom and canine studies. *Radiology* 2003; 227:817-824.
10. Yau Y-Y, Chan W-S, Tam Y-M, Vernon P, Wong S, Coel M, et al. Application of intravenous contrast in PET/CT: does it really introduce significant attenuation correction error? *J Nucl Med* 2005; 46:283-291.
11. Dizendorf E, Hany TF, Buck A, von Schulthess GK, Burger Cl. Cause and magnitude of the error induced by oral CT contrast agent in CT-based attenuation correction of PET emission studies. *J Nucl Med* 2003; 44:732-738.
12. DiFilippo FP, Brunken RC. Do implanted pacemaker leads and ICD leads cause metal-related artifact in cardiac PET/CT? *J Nucl Med* 2005; 46:436-443.

13. Goerres GW, Hany TF, Kamel E, von Schulthess GK, Buck A. Head and neck imaging with PET and PET/CT: artefacts from dental metallic implants. *Eur J Nucl Med Mol Imaging* 2002; 29:367-370.
14. Goerres GW, Ziegler SI, Burger C, Berthold T, Von Schulthess GK, Buck A. Artifacts at PET and PET/CT caused by metallic hip prosthetic material. *Radiology* 2003; 226:577-584.
15. Kamel E, Burger C, Buck A, Von Schulthess GK, Goerres G. Impact of metallic dental implants on CT-based attenuation correction in a combined PET/CT scanner. *Eur. Radiol.* 2003; 13:724-728.
16. Goerres GW, Burger C, Kamel E, Seifert B, Kaim AH, Buck A, et al. Respiration-induced attenuation artifact at PET/CT: Technical considerations. *Radiology* 2003; 226:906-910.
17. Osman MM, Cohade C, Nakamoto Y, Wahl RL. Respiratory motion artifacts on PET emission images obtained using CT attenuation correction on PET-CT. *Eur J Nucl Med Mol Imaging* 2003; 30:603-606.
18. Kanamori H, Nakamori N, Inoue K, Takenaka E. Effect of scattered x-ray on CT images. *Phys. Med. Biol.* 1985; 30:239-249.
19. Colijn AP, Beekman FJ. Accelerated simulation of cone beam X-ray scatter projections. *IEEE Trans. Med. Imaging* 2004; 23:584-590.
20. Siewerdsen JH, Jaffray DA. Cone-beam computed tomography with flat-panel imager: Magnitude and effects of x-ray scatter. *Med. Phys.* 2001; 28:220-231.
21. Ning R, Tang X. X-ray scatter correction algorithm for cone beam CT imaging. *Med. Phys.* 2004; 31:1195-1202.
22. Ohnesorge B, Flohr T, Klingenberg-Regn K. Efficient object scatter correction algorithm for third and fourth generation CT scanners. *Eur Radiol* 1999; 9:563-569.
23. Tofts PS, Gore JC. Some sources of artefact in computed tomography. *Phys Med Biol* 1980; 1
24. Glover GH. Compton scatter effects in CT reconstructions. *Med Phys* 1982; 9:860-867.
25. Johns PC, Yaffe M. Scattered radiation in fan beam imaging systems. *Med Phys* 1982; 9:231-239.
26. Joseph PM, Spital RD. The effects of scatter in x-ray computed tomography. *Med Phys* 1982; 9:464-472.

27. Merritt RB, Chenery SG. Quantitative CT measurements: the effect of scatter acceptance and filter characteristics on the EMI 7070. *Phys. Med. Biol.* 1986; 31:55-63.
28. Endo M, Tsunoo T, Nakamori N, Yoshida K. Effect of scatter radiation on image noise in cone beam CT. *Med. Phys.* 2001; 28:469-474.
29. Malusek A, Seger MM, Sandborg M, Alm Carlsson G. Effect of scatter on reconstructed image quality in cone beam computed tomography: evaluation of a scatter-reduction optimisation function. *Radiat Prot Dosimetry* 2005; 114:337-340.
30. Ay MR, Zaidi H. Development and validation of MCNP4C-based Monte Carlo simulator for fan- and cone-beam x-ray CT. *Phys. Med. Biol.* 2005; 50:4863-4885.
31. Digby WM, Hoffman EJ. An investigation of scatter in attenuation correction for PET. *IEEE Trans Nucl Sci* 1989; 36:1038-1042.
32. Wegmann K, Adam L-E, Livieratos L, Zaers J, L. BD, Brix G. Investigation of the scatter contribution in single photon transmission measurements by means of Monte Carlo simulations. *IEEE Trans Nucl Sci* 1999; 46:1184-1190.
33. Dahlbom M, Hoffman E. Problems in signal-to-noise ratio for attenuation correction in high resolution PET. *IEEE Trans. Nucl. Sci.* 1987; 34:288-293.
34. Bai C, Shao L, Da Silva AJ, Zhao Z. A generalized model for the conversion from CT numbers to linear attenuation coefficients. *IEEE Trans Nucl Sci* 2003; 50:1510-1515.
35. Tang HR, Brown JK, Da Silva AJ, Matthay KK, Price DC, Huberty JP, et al. Implementation of a combined X-ray CT-scintillation camera imaging system for localizing and measuring radionuclide uptake: experiments in phantoms and patients. *IEEE Trans Nucl Sci* 1999; 46:551-557.
36. Carney J, Beyer T, Brasse D, Yap JT, Townsend DW. CT-based attenuation correction for PET/CT scanners in the presence of contrast agent. *IEEE Nuclear Science Symposium Conference Record*, 2002; 3:1443-1446.
37. Zaidi H, Scheurer AH, Morel C. An object-oriented Monte Carlo simulator for 3D cylindrical positron tomographs. *Comput. Methods Programs Biomed.* 1999; 58:133-145.
38. Ay M, Shahriari M, Sarkar S, Adib M, Zaidi H. Monte Carlo simulation of x-ray spectra in diagnostic radiology and mammography using MCNP4C. *Phys. Med. Biol.* 2004; 49:4897-4917.
39. Zaidi H. Comparative evaluation of scatter correction techniques in 3D positron emission tomography. *Eur J Nucl Med* 2000; 27:1813-1826.

40. Berger MJ, Hubbell JH, Seltzer SM, Chang J, Coursey JS, Sukumar R, *et al.* XCOM: photon cross sections database. NBSIR 87-3597. 1998;  
*<http://physics.nist.gov/PhysRefData/Xcom/Text/XCOM.html>*
41. Rousset OG, Ma Y, Evans AC. Correction for partial volume effects in PET: principle and validation. *J Nucl Med* 1998; 39:904-911.
42. Zaidi H, Koral KF. Scatter modelling and compensation in emission tomography. *Eur J Nucl Med* 2004; 31:761-782.
43. Berthelsen AK, Holm S, Loft A, Klausen TL, Andersen F, Hojgaard L. PET/CT with intravenous contrast can be used for PET attenuation correction in cancer patients. *Eur J Nucl Med Mol Imaging* 2005; 32:1167-1175.

# **Paper V**

*Nuclear Medicine Communications*  
Submitted for Publication (2005)

## CT-based attenuation correction in neurological PET: evaluation of the effect of x-ray tube voltage on quantitative analysis

Mohammad Reza Ay and Habib Zaidi

Division of Nuclear Medicine, Geneva University Hospital, CH-1211 Geneva 4, Switzerland

### Abstract

The advent of dual-modality PET/CT imaging has revolutionized the practice of clinical oncology by improving lesions localization and facilitating treatment planning for radiation therapy. In addition, the use of CT images for CT-based attenuation correction (CTAC) allows to decrease the overall scanning time and to create a noise-free attenuation map ( $\mu$ map). The most common procedure requires a piece-wise linear calibration curve acquired under standard imaging conditions to convert the patient's CT image from low effective CT energy into an attenuation map at 511 keV. The aim of this work is to evaluate the effect of tube voltage on the accuracy of CTAC. As different tube voltages are used in current PET/CT scanning protocols depending on patients size and the region under study, the impact of using a single calibration curve on the accuracy of CTAC for images acquired at different tube voltages was investigated through quantitative analysis of created  $\mu$ maps, generated attenuation correction factors and reconstructed neurological PET emission data using anthropomorphic experimental phantom and clinical studies. For CT images acquired at 80 and 140 kVp, an average relative difference of -2.9% and 0.7% with the images acquired at 120 kVp, respectively, was observed between absolute activity concentrations in five regions of the anthropomorphic striatal phantom when CT images are converted using a single calibration curve derived at 120 kVp. Likewise, an average relative difference of 1.9% and -0.6% was observed when CT images are acquired at 120 kVp and CTAC uses calibration curves derived at 80 and 140 kVp, respectively. It was concluded that the use of a single calibration curve acquired under standard imaging conditions does not affect to a visible or measurable extent neurological PET images reconstructed using CT-based attenuation correction when CT images are acquired in different conditions.

**Key Words:** PET/CT, attenuation correction, brain imaging, tube voltage, quantification.

## 1. Introduction

The advent of combined Positron Emission Tomography (PET)/Computed Tomography (CT) units is considered as a major advance in medical imaging technology and health care. As the name implies, PET/CT combines the information produced by two sophisticated imaging modalities: the functional information from PET with the anatomical information from CT into a single procedure [1]. Dual-modality imaging correlates functional and anatomical data to improve disease localization and facilitates treatment planning for radiation oncology or surgery [2]. PET/CT systems offer significant advantages over stand alone PET including decreased overall scanning time and increased accuracy in lesions localization. The high-resolution anatomical information from PET/CT improves the differentiation of physiological (normal) uptake of  $^{18}\text{F}$ -fluorodeoxyglucose (FDG) and other radiopharmaceuticals from that associated with disease, and thereby can reduce false positive errors in comparison to lesion characterization when PET imaging is used alone.

Several physical factors can degrade image quality and quantitative accuracy of PET, the most important is photon attenuation in tissues, which can affect both visual interpretation and quantitative accuracy of PET data [3]. Several methods have been devised to correct for attenuation in neurological PET studies that do not require an always noisy transmission scan [4-7]. One of the advantages of PET/CT is the ability to generate a noise-free attenuation map ( $\mu\text{map}$ ) to be used for attenuation correction purposes. With the introduction of hybrid PET/CT systems in clinical setting, precise conversion from CT numbers derived from low-energy polyenergetic x-ray spectra to linear attenuation coefficients at 511 keV became essential in order to apply accurate CT-based attenuation correction (CTAC) to the PET data. Several CT-based attenuation correction strategies have been developed including scaling [8], segmentation [9], hybrid segmentation/scaling [10], piece-wise linear scaling [11,12], and dual-energy decomposition methods [13]. Most commercially available PET/CT scanners use the bi-linear calibration curve method, which is generally calculated at a preset tube voltage (120-140 kVp) and current. Kamel *et al.* [14] investigated the effect of varying tube current and showed that a low-current CT is sufficient for CTAC

using comparative quantitative analysis of reconstructed clinical PET images. Since patient CT images may be acquired at different tube voltages and currents depending on patient size and region under study and considering the fact that the CT number of a particular tissue is tube voltage dependent, it was hypothesized that the use of a single calibration curve calculated at a specific tube voltage for CT images acquired under different scanning conditions might propagate a significant uncertainty during the CTAC procedure. Bai *et al.* [12] argued that the slope of the bi-linear calibration curve for CT numbers higher than 0 Hounsfield units (HU) is tube voltage dependent. Other studies reported on the relevance of deriving tube voltage dependent CTAC schemes for PET/CT [15]. These topical developments combined with the lack of detailed studies investigating the effect of tube voltage on the quantitative analysis of non-clinical PET data where the ground truth is known motivated the work presented in this paper.

This study was designed to provide answers to the legitimate question of the clinician or physicist: “what is the magnitude of error due to acquiring CT at e.g. 80 kVp when the calibration curve would be the manufacturer’s standard of 120 or 140 kVp?” and vice versa, that is, acquiring CT images at specific tube voltages and varying the voltage for derivation of calibration curves. The assessment was carried out through quantitative analysis of created  $\mu$ maps, generated attenuation correction factors (ACFs) and reconstructed neurological PET emission data using experimental anthropomorphic phantom and clinical studies.

## **2. Materials and Methods**

### *2.1 Phantom and clinical studies*

Our department is in the process of installing a commercial PET/CT scanner which was not available during the actual study design which relied on the use of PET and CT data acquired on separate PET and CT scanners. One of the motivations behind the choice of brain imaging is that automated multimodality coregistration algorithms work relatively well (in contrary to whole-body imaging) and can be applied most successfully to neurological studies, where the skull provides a rigid structure that maintains the geometrical relationship of structures within the brain. An anthropomorphic head phantom (Radiology

Support Devices Inc., Long Beach, CA) designed specifically for the assessment of quantitative imaging capabilities of the striatum relevant for PET studies of the presynaptic and postsynaptic dopaminergic system was used in order to quantitatively assess the effect of using a single calibration curve on the accuracy of CTAC when CT images are acquired in different tube voltages. The phantom has five compartments which can be filled separately: left and right caudate nucleus (LCN and RCN), left and right putamen (LPU and RPU), and the rest of the brain (main chamber). The main chamber itself is embedded in a bone like structure to provide properties similar to the human head.

For an activity ratio of 1:8 between the main chamber and small cavities, 2.942 MBq of  $^{18}\text{F}$  (in 0.9 ml, 0.9% NaCl) were diluted in distilled water and used to fill the striatum. A total activity of 13.2 MBq diluted into 1.1 ml NaCl was filled into the main chamber. Subsequently, the main chamber was totally filled with distilled water. The fully 3-D emission study lasted 25 minutes whereas a 2-D pre-injection transmission scan (10 minutes) was acquired using  $^{137}\text{Cs}$  single-photon point sources on the ECAT ART PET scanner (CTI/Siemens, Knoxville, TN). The measured transmission scan was scaled for the difference between 662 keV and 511 keV energies by normalizing to a slab phantom scan and correcting for scatter and cross section variation using a log-linear transformation of the attenuation factors. Thereafter, CT data of the same phantom were acquired on the Aquilion CT scanner (Toshiba Medical Systems Corporation, Tokyo, Japan) at 240 mA in order to apply the CTAC procedure to the emission data. Calibration curves calculated at 80, 120 and 140 kVp were used to create sets of  $\mu$ maps from images acquired at 80, 120 and 140 kVp. The emission data were corrected for attenuation using the measured transmission method (MTM) as well as the set of  $\mu$ maps generated using CTAC. Apparent recovery coefficients (ARCs), representing the apparent (observed or partial volume corrected) regional radioactivity concentration to true activity ratio, and absolute activity concentrations were calculated for the five compartments of the striatal phantom as figures of merit for the quantitative analysis of reconstructed neurological PET images.

A polyethylene cylindrical phantom ( $\phi 250 \pm 0.5$  mm) containing 16 cylindrical holes ( $\phi 20 \pm 0.5$  mm) was made in order to calculate the bi-linear calibration curves required for application of the CTAC procedure. Fourteen syringes were filled with a solution of  $K_2HPO_4$  and water with concentrations varying between 50 mg/cc and 900 mg/cc to simulate cortical bone with different densities. The prepared syringes together with two additional syringes containing water and air were inserted into the polyethylene phantom's holes (see Fig. 1). Subsequently, the phantom was scanned on the HiSpeed X/iF CT scanner (GE Healthcare Technologies, Waukesha, WI) using three different tube voltages (80 kVp, 120 kVp and 140 kVp). The bi-linear calibration curves at different tube voltages for both CT scanners were calculated according to the method proposed by Bai *et al.* [12]. Patient brain CT scans acquired at 120 kVp on the HiSpeed X/iF CT scanner were selected from the database and used for clinical evaluation of the effect of tube voltage.

### *2.2 Attenuation correction and image reconstruction*

The computation of ACFs derived from CTAC involved down-sampling the CT image matrix to  $128 \times 128$  followed by Gaussian smoothing using a 6 mm kernel to match the spatial resolution of the PET scanner used in this study. CT numbers (in HU) were then transformed to linear attenuation coefficients at 511 keV using the calculated bi-linear curve. The created  $\mu$ maps were forward projected to generate 47 ACF sinograms. The attenuation corrected projections were reconstructed using the 3DRP reprojection algorithm implemented within the ECAT 7.2.1 software (CTI Molecular Imaging Inc., Knoxville, TN) with a maximum acceptance angle corresponding to 17 rings and a span of 7. The default parameters used in clinical routine were applied (Ramp filter, cut-off frequency 0.35 cycles/pixel). The reconstructed images consist of 47 slices with  $128 \times 128$  resolution and a voxel size set to  $1.72 \times 1.72 \times 3.4$  mm<sup>3</sup>.

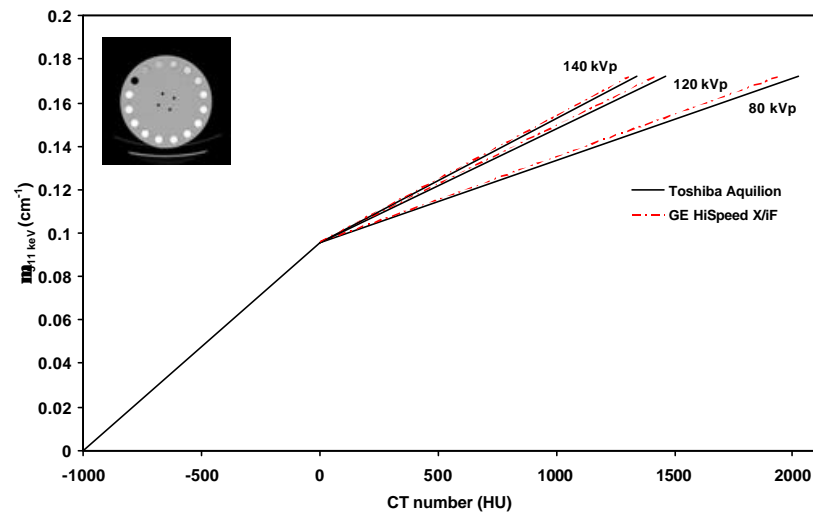
The acquired CT and preliminary PET images reconstructed using calculated attenuation correction were coregistered using the commercial Hermes multi-modality fusion software (Hermes multi-modality fusion software, Nuclear Diagnostics AB, Stockholm, Sweden) to limit potential artefacts arising from

misalignment of images during the CTAC procedure. The slice thickness of CT images was adjusted during the coregistration to match the thickness of PET images. To increase the accuracy of quantitative analysis, partial volume effect correction of the striatal phantom's PET images was performed using the geometric transfer matrix (GTM)-based method [16] where the regions of interest (ROIs) were delineated on the CT images to allow computing corrected estimates without *a priori* knowledge on any activity level. Briefly, the algorithm directly computes the degradations introduced by the limited spatial resolution of the PET scanner, as well as smoothing introduced during image backprojection, and further modulation during extraction of regional tracer concentration. In practice, these partial volume factors are computed from simulation of noise-free regional spread function images and sampling with a user-defined set of ROIs.

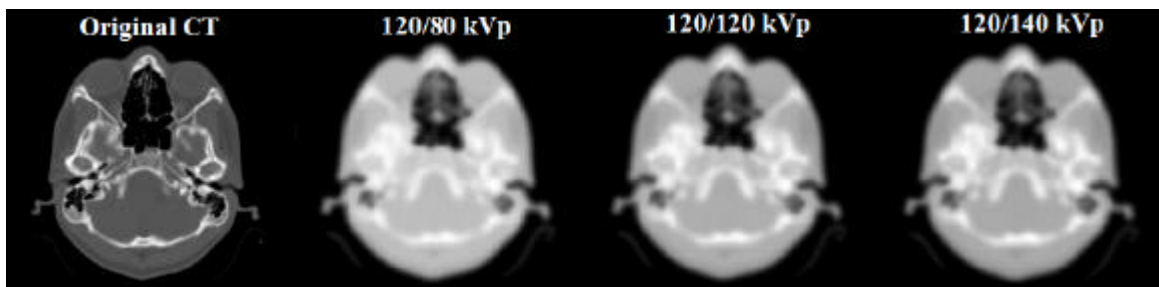
### 3. Results

Figure 1 shows the calculated bi-linear calibration curves for both CT scanners used in this study at different tube voltages (80 kVp, 120 kVp and 140 kVp). The XCOM photon cross sections database [17] was used for calculation of the corresponding linear attenuation coefficients of the inserted solutions at 511 keV. The slope of calibration curves for CT numbers greater than 0 HU increases with increasing tube voltage. It is worth noting that these curves have slightly different slopes for different scanners for the same tube voltage. A typical slice of the original clinical brain CT image (512×512 matrix) acquired at 120 kVp is shown in Figure 2. Three  $\mu$ maps (128×128 matrix) were calculated from the same data set using calibration curves calculated at different tube voltages (Fig. 2). It was considered unethical to scan the patients with varying tube voltages owing to the additional radiation dose and the absence of any direct clinical benefit to the patients. Figure 3 shows the difference in calculated  $\mu$ maps and ACFs by displaying horizontal profiles through the middle of the same slice to demonstrate quantitatively the differences when using different calibration curves. Both  $\mu$ maps and ACFs are overestimated when using a calibration curve derived from a tube voltage (140 kVp) higher than the one used during actual CT scanning (120 kVp)

of the patient. The behaviour is reversed when using the calibration curve derived from a lower tube voltage (80 kVp).



**Fig. 1.** Calculated bi-linear calibration curves for conversion of CT numbers (HU) into linear attenuation coefficients at 511 keV at different tube voltages for both Aquilion and HiSpeed X/iF CT scanners. The in-house designed polyethylene cylindrical phantom containing 16 cylindrical holes is shown in the upper left corner.



**Fig. 2.** Effect of using different calibration curves during the CTAC procedure. From left to right, original clinical CT image acquired at 120 kVp, derived  $\mu$ map at 511 keV using calibration curves calculated at tube voltages of 80 kVp, 120 kVp and 140 kVp, respectively.

Figure 4 shows the RSD striatal phantom's  $\mu$ map obtained through transmission scanning using  $^{137}\text{Cs}$  sources as well as the  $\mu$ maps calculated by CTAC when CT images are acquired at 120 kVp and scaled using calibration curves derived at different tube voltages (80, 120 and 140 kVp) and also when CT images are acquired at different tube voltages (80, 120 and 140 kVp) and scaled using a single calibration curve derived at 120 kVp. The difference between the  $\mu$ maps and ACFs calculated by the different methods is shown in Figure 5. A small but noticeable difference is visible on the horizontal profiles of the ACFs as

a result of overestimation/underestimation of attenuation coefficients depending on the combination of tube voltages for acquisition/calibration curves derivation.

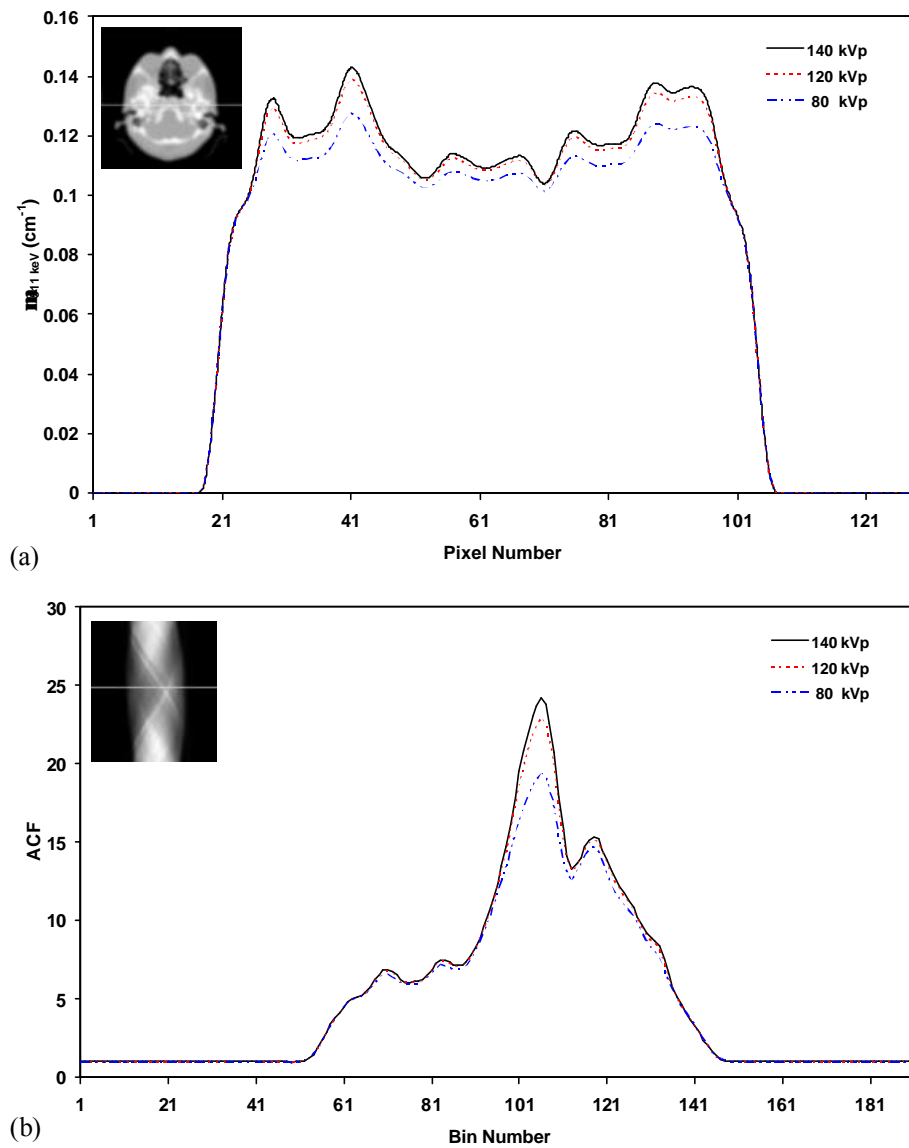


**Fig. 3.** (a) Horizontal profiles through the  $\mu$ maps shown in Fig. 2 and (b) central profiles through generated ACF sinogram (view 23/47).

The created  $\mu$ maps based on different methods (Fig. 4) were used for attenuation correction of emission data shown in Figure 6. There is no visually significant difference between the images corrected for attenuation using CTAC with different combinations of tube voltages for CT image acquisition/calibration curves derivation. It should be noted that the illustrated  $\mu$ maps are for different slices than the striatal images used for evaluation and shown in Figure 6 where the

differences between  $\mu$ maps generated using different conditions are small in the central region corresponding to the brain compartment (data not shown).

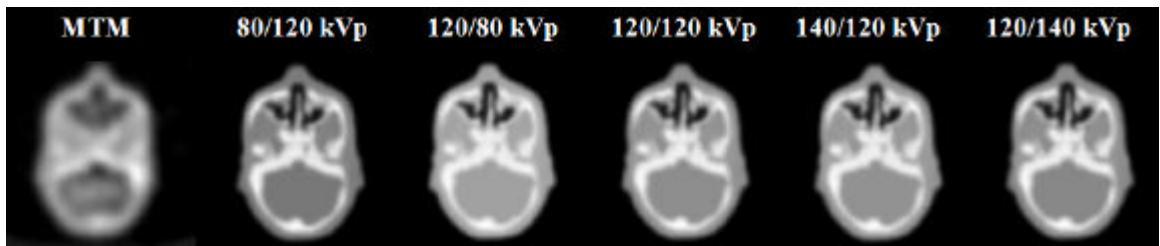
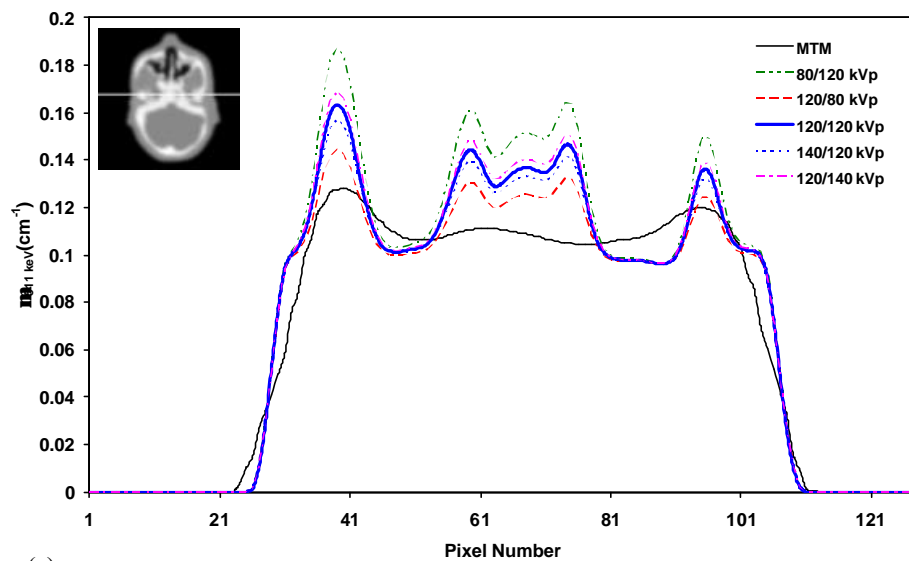
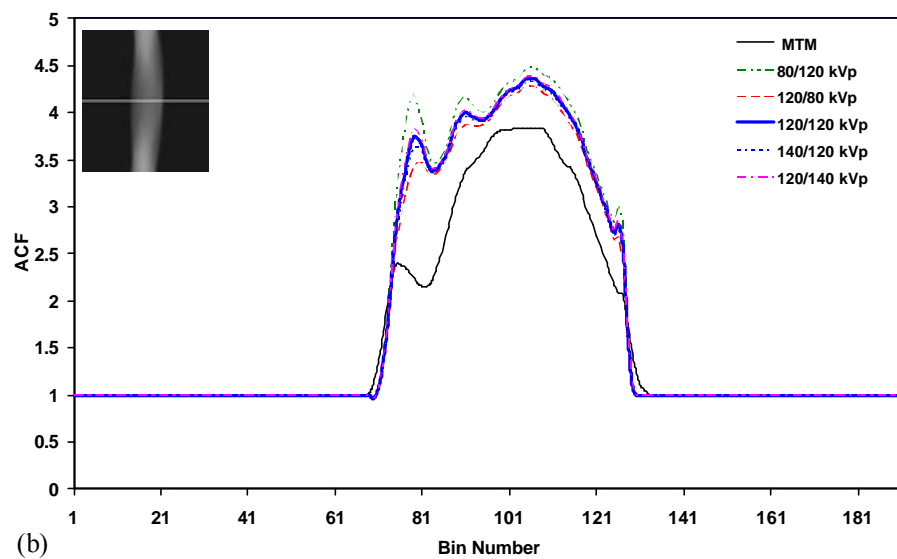


**Fig. 4.** Attenuation maps at 511 keV of the anthropomorphic striatal phantom calculated using different methods. From left to right, measured transmission method (MTM) using  $^{137}\text{Cs}$  single-photon sources, CTAC method using different combinations of tube voltages for image acquisition and calculation of calibration curves.



(a)



(b)

**Fig. 5.** (a) Horizontal profiles through the  $\mu$ maps shown in Fig. 4 and (b) central profiles through generated ACF sinogram (view 23/47).

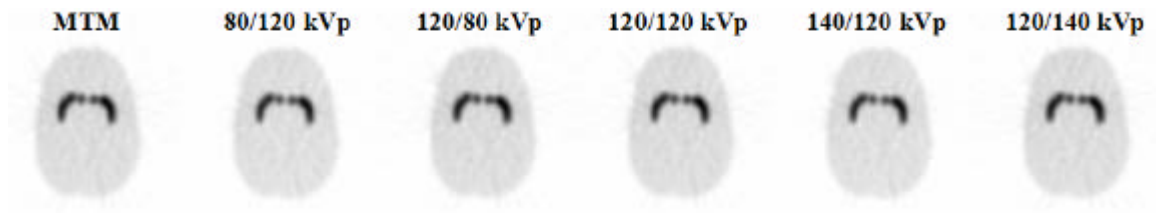


**Fig. 6.** Reconstructed emission PET images of the anthropomorphic striatal phantom corrected for attenuation using different methods. From left to right, MTM, CTAC method using different combinations of tube voltages for image acquisition and calculation of calibration curves.

However, the ACFs are created using 3-D forward projection of  $\mu$ maps and thus the noticeable differences in the bony regions might bias the ACF estimates in the striatal regions. Figure 7 shows absolute activity concentrations estimated from the reconstructed PET emission images before and after partial volume correction for five individual compartments of the anthropomorphic striatal phantom. The ARCs for each compartment calculated before and after partial volume correction are also shown in Tables 1 and 2, respectively.

#### 4. Discussion

The advent of dual-modality PET/CT imaging had great impact on improving the value of diagnostic PET in localizing, evaluating and therapeutic monitoring of head and neck cancer and may be equally valuable for other localizations that are difficult to pinpoint. [18]. The reduction of examination time owing to the use of low noise CT data for attenuation correction is another benefit of combined scanners. PET/CT systems have demonstrated their ability to facilitate attenuation correction using an x-ray based patient-specific attenuation map that can be produced faster and more accurately than attenuation maps generated with external radionuclide sources [2].

The general feasibility of CTAC was already proven [10] but some practical technical issues remained to be explored. A high tube current improves CT image quality at the expense of increasing patient dose. It was reported that effective doses of 8.81 mSv and 18.97 mSv are delivered to the patient for a whole body scan in high-speed and high-quality mode, respectively [19]. This is in contrast to relatively low effective doses of 0.15 mSv and 0.08 mSv for thoracic and whole-

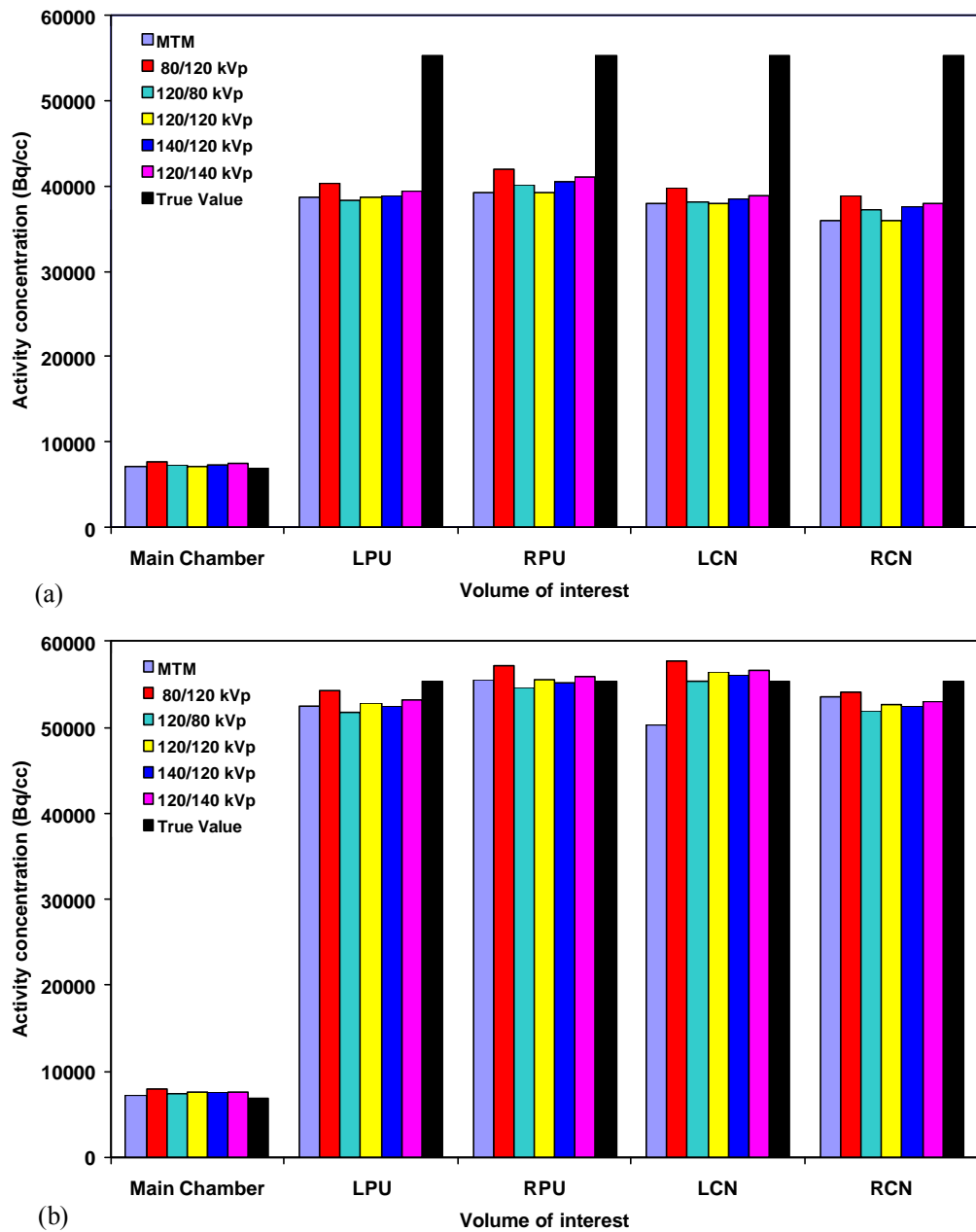


**Fig. 7.** Comparison between the true and calculated absolute activity concentrations in different brain structures of the striatal phantom when using the different attenuation correction methods before (a) and after (b) partial volume correction.

body transmission scans using positron emitting  $^{68}\text{Ga}/^{68}\text{Ge}$  and single-photon emitting  $^{137}\text{Cs}$  radionuclide sources, respectively [3]. This study was designed to assess the impact of using a single calibration curve on the accuracy of CTAC when CT images are acquired in different tube voltages and vice versa, that is, acquiring CT images at specific tube voltages and varying the voltage for

derivation of calibration curves. The feasibility of using a single calibration curve during practical application of CTAC for CT images acquired in different tube voltages was investigated through quantitative analysis of created  $\mu$ maps, generated ACFs and reconstructed neurological PET emission data using experimental phantom and clinical studies. Moreover, the possibility of using a low-dose CT for the purpose of attenuation correction was investigated for two commercial scanners to confirm the validity of results reported in the literature using only clinical data (data not shown) [14]. More recently, a new pre-processing algorithm was proposed to use a single ultra-low dose CT scan for both attenuation map construction and lesion localization [20].

The difference between the slopes of calibration curves calculated at various tube voltages (Fig. 1) is due to the fact that the probability of photoelectric interaction increases with decreasing tube voltage, particularly in materials with high atomic numbers. Consequently, CT numbers in these regions increase with decreasing tube voltage. Since the calculation of calibration curves is based on CT numbers of air, water and cortical bone, the tube voltage dependency of cortical bone's CT number is the reason of the difference in the slope of calibration curves obtained at different tube voltages. Likewise, the difference between calibration curves at a particular tube voltage for different scanners can be explained by possible differences in detector calibration procedures, x-ray spectra shape and reconstruction algorithms used by different scanner manufacturers. As the x-ray tube spectra is polyenergetic, with the exact energy spectra being determined by physical factors including characteristics of tubes, filters, ... etc, the spectra for a specific tube voltage may differ slightly between different devices. It should be emphasized that even for a particular CT scanner and fixed tube voltage; there might be changes in calibration curves obtained in different periods of time.

The underestimation of clinical  $\mu$ maps and ACFs when using a calibration curve derived at 80 kVp is due to the lower slope of the calibration curve in comparison with the one obtained at 120 kVp (Figs. 2-3). The same behaviour was observed when using the anthropomorphic striatal phantom (Figs. 4-5). Generally, the difference between the  $\mu$ maps and ACFs when using different calibration curves seems to be significant. Evidently, using a calibration curve

calculated at a tube voltage higher than the one used during CT scanning tend to overestimate the  $\mu$ maps and ACFs. The behaviour is reversed when using a calibration curve derived at a lower tube voltage. On the other hand, the  $\mu$ maps and ACFs are overestimated when using a calibration curve calculated at tube voltages higher than the voltage used to acquire the CT image. This behaviour is reversed when the calibration curve is derived at tube voltage lower than the voltage used during CT acquisition (Fig. 5). The underestimation of ACFs calculated by MTM in comparison to CTAC is the consequence of the underestimation of bone's linear attenuation coefficients at 511 keV when using low count, low resolution transmission scans [4,5]. In contrast, the differences between reconstructed PET emission images corrected using CTAC with different combinations of tube voltages for image acquisition/calibration curves are not qualitatively (Fig. 6) and quantitatively (Fig. 7b and Table 2) significant. One possible explanation is that the difference of ACFs varies at different projections but is small on average. Likewise, the backprojection procedure averages the differences observed in the ACFs in projection space during the reconstruction process. The noticeable underestimation of absolute activity concentrations (Fig. 7a) and ARCs (Table 1) for the small brain structures (LPU, RPU, LCN and RCN) within the RSD striatal phantom is the result of partial volume effect [16].

After partial volume correction of the emission images corrected for attenuation using CT images acquired at 80 and 140 kVp, an average relative difference of -2.9% and 0.7% with the images acquired at 120 kVp was observed between absolute activity concentrations in five regions of the anthropomorphic striatal phantom when CT images are converted to  $\mu$ maps using a single calibration curve derived at 120 kVp, respectively. Likewise, an average relative difference of 1.9% and -0.6% was observed when CT images acquired at 120 kVp and calibration curves derived at 80 and 140 kVp were used during CTAC, respectively. We conclude that using a single calibration curve for application of the CTAC procedure to images acquired at different tube voltages does not significantly affect visual qualitative interpretation and quantitative analysis of neurological PET emission images.

**Table 1.** Apparent recovery coefficients for different VOIs corresponding to different structures within the anthropomorphic brain phantom before partial volume correction. ( $\alpha/\beta$  kVp denotes CT image acquired at  $\alpha$  kVp scaled using a calibration curve calculated at  $\beta$  kVp).

Volume of interest (VOI)	Volume (cc)	MTM 662 keV	CTAC 80/120 kVp	CTAC 120/80 kVp	CTAC 120/120 kVp	CTAC 140/120 kVp	CTAC 120/140 kVp
Main chamber	1290	101.74	111.87	105.00	107.79	106.76	108.62
Left putamen (LPU)	6	70.01	72.78	69.30	70.67	70.14	71.10
Right putamen (RPU)	6	71.00	75.90	72.33	73.73	73.18	74.16
Left nucleus caudate (LCN)	4.9	68.69	71.79	68.73	69.95	69.49	70.33
Right nucleus caudate (RCN)	4.9	65.08	70.10	67.14	68.32	67.87	68.69

**Table 2.** Same as Table 1 after partial volume correction.

Volume of interest (VOI)	Volume (cc)	MTM 662 keV	CTAC 80/120 kVp	CTAC 120/80 kVp	CTAC 120/120 kVp	CTAC 140/120 kVp	CTAC 120/140 kVp
Main chamber	1290	103.36	113.83	106.76	109.63	108.58	110.49
Left putamen (LPU)	6	94.86	98.26	93.62	95.45	94.74	96.02
Right putamen (RPU)	6	96.97	103.44	98.66	100.52	99.79	101.11
Left nucleus caudate (LCN)	4.9	100.32	104.47	100.20	101.90	101.24	102.42
Right nucleus caudate (RCN)	4.9	90.79	97.68	93.73	95.31	94.70	95.80

Despite the fact that increasing tube current increases signal-to-noise ratio and decreases statistical fluctuations in reconstructed CT images thus improving image quality, CT numbers and the derived attenuation maps are tube current (mA) independent (data not shown). The statistical fluctuations of CT numbers in the low current CT images are removed during the down-sampling and smoothing procedures inherent to the CTAC procedure. Consistent with the observations reported by Kamel *et al.* [14], it appears that the tube current used during CT scanning does not affect significantly the quantification of clinical PET images for the purpose of calculating tumour uptake. As discussed above, it might happen that some slight differences are observed at the level of  $\mu$ maps and ACFs when using different tube currents and a fixed tube voltage. These differences will, however, not induce significant differences during quantitative analysis of reconstructed neurological PET emission images.

Since this study was carried out using separate PET and CT systems for the reasons mentioned in section 2, it was limited to the use of a neurological research brain phantom and clinical brain images, rather than an anthropomorphic whole-body phantom and whole-body clinical images, which might impose a far greater challenge to the accuracy of attenuation correction due to the much larger attenuating volume, larger bony structures and more complex juxtapositions of media with different attenuating properties, e.g. lung/soft tissue/bone in the thorax. It is hard to predict whether the answers necessarily will be equivalent or the same conclusions will be reached in the clinical challenging situations mentioned above. Further investigation using whole-body data is guaranteed when the inline PET/CT system will be fully operational in our department. Given the increasing use of CT contrast media and the severe challenge that such media present for accurate attenuation correction in PET/CT, this paper does not consider the effects that might be observed in the presence of contrast media or other non-human tissue (metallic implants etc), which are addressed in a separate paper [21].

## 5. Conclusion

The impact of tube voltage (kVp) on the accuracy of CT-based attenuation correction in neurological PET studies was investigated in detail using experimental phantom and clinical studies. It was concluded that using a single calibration curve derived under standard scanning conditions during the CTAC procedure to images acquired at different tube voltages does not affect significantly the visual qualitative interpretation and quantitative analysis of neurological PET emission images. The same behaviour was observed when calibration curves are derived at different tube voltages and used for conversion of CT images acquired at fixed tube voltage. These results might contribute to alleviate the quality assurance procedures required for daily operation of PET/CT scanners in a clinical environment.

### **Acknowledgements**

This work was supported by the Swiss National Science Foundation under grant SNSF 3152A0-102143. The authors would like to thank Dr O.G. Rousset for providing the PVC software and F. Schoenahl, T. Ruest and N. Andreini, for their valuable support.

## References

- [1] Townsend DW, Beyer T, Blodgett TM. PET/CT scanners: A hardware approach to image fusion. *Semin Nucl Med* 2003; **33**: 193-204.
- [2] Hasegawa BH, Zaidi H. Dual-modality imaging: more than the some of its components. In: Zaidi H, ed. *Quantitative analysis in nuclear medicine imaging*. New York: Springer, 2005, 35-81.
- [3] Zaidi H, Hasegawa B. Determination of the attenuation map in emission tomography. *J Nucl Med* 2003; **44**: 291-315.
- [4] Weinzapfel BT, Hutchins GD. Automated PET attenuation correction model for functional brain imaging. *J Nucl Med* 2001; **42**: 483-491.
- [5] Zaidi H, Montandon ML, Slosman DO. Magnetic resonance imaging-guided attenuation and scatter corrections in three-dimensional brain positron emission tomography. *Med Phys* 2003; **30**: 937-948.
- [6] Zaidi H, Montandon ML, Slosman DO. Attenuation compensation in cerebral 3D PET: effect of the attenuation map on absolute and relative quantitation. *Eur J Nucl Med Mol Imaging* 2004; **31**: 52-63.
- [7] Montandon M-L, Zaidi H. Atlas-guided non-uniform attenuation correction in cerebral 3D PET imaging. *Neuroimage* 2005; **25**: 278-286.
- [8] Beyer T, Kinahan PE, Townsend DW, Sashin D. The use of X-ray CT for attenuation correction of PET data. *Proc. IEEE Nuclear Science Symposium and Medical Imaging Conference* 1994; **4**: 1573-1577.
- [9] Kinahan PE, Hasegawa B, Beyer T. X-ray-based attenuation correction for positron emission tomography/computed tomography scanners. *Semin Nucl Med* 2003; **34**: 166-179.
- [10] Kinahan PE, Townsend DW, Beyer T, Sashin D. Attenuation correction for a combined 3D PET/CT scanner. *Med Phys* 1998; **25**: 2046-2053.
- [11] Burger C, Goerres G, Schoenes S, Buck A, Lonn AH, Von Schulthess GK. PET attenuation coefficients from CT images: experimental evaluation of the transformation of CT into PET 511-keV attenuation coefficients. *Eur J Nucl Med Mol Imaging* 2002; **29**: 922-927.

- [12] Bai C, Shao L, Da Silva AJ, Zhao Z. A generalized model for the conversion from CT numbers to linear attenuation coefficients. *IEEE Trans Nucl Sci* 2003; **50**: 1510-1515.
- [13] Guy MJ, Castellano-Smith IA, Flower MA, Flux GD, Ott RJ, Visvikis D. DETECT-dual energy transmission estimation CT-for improved attenuation correction in SPECT and PET. *IEEE Trans Nucl Sci* 1998; **45**: 1261 -1267.
- [14] Kamel E, Hany TF, Burger C, Treyer V, Lonn AHR, Von Schulthess GK, *et al.* CT vs 68Ge attenuation correction in a combined PET/CT system: evaluation of the effect of lowering the CT tube current. *Eur. J. Nucl. Med.* 2002; **29**: 346-350.
- [15] Rappoport V, Carney JPJ, Townsend DW. CT tube-voltage dependent attenuation correction scheme for PET/CT scanners. *Proc. IEEE Nuclear Science Symposium and Medical Imaging Conference* 2004; **6**: 3853-3857.
- [16] Rousset OG, Ma Y, Evans AC. Correction for partial volume effects in PET: principle and validation. *J Nucl Med* 1998; **39**: 904-911.
- [17] Berger MJ, Hubbell JH, Seltzer SM, Chang J, Coursey JS, Sukumar R, *et al.* XCOM: photon cross sections database. NBSIR 87-3597. 1998; <http://physics.nist.gov/PhysRefData/Xcom/Text/XCOM.html>.
- [18] Branstetter BF, IV, Blodgett TM, Zimmer LA, Snyderman CH, Johnson JT, Raman S, *et al.* Head and neck malignancy: Is PET/CT more accurate than PET or CT alone? *Radiology* 2005; **235**: 580-586.
- [19] Wu TH, Huang YH, Lee JJS, Wang SY, Wang SC, Su CT, *et al.* Radiation exposure during transmission measurements: comparison between CT- and germanium-based techniques with a current PET scanner. *Eur J Nucl Med* 2004; **31**: 38-43.
- [20] Li J, Hsieh J, Colsher J, Stearns C, Lonn AHR. Towards single ultra-low dose CT scan for both attenuation map creation and localization in PET-CT application. *Proc. IEEE Nuclear Science Symposium and Medical Imaging Conference* 2004; **4**: 2396-2398.
- [21] Ay MR, Zaidi H. Assessment of errors caused by x-ray scatter and use of contrast medium when using CT-based attenuation correction in PET. *Submitted (2005)*.